

NANOCRYSTALLINE SILICON AND SILICON OXIDE CONTACT LAYERS FOR SILICON HETEROJUNCTION SOLAR CELLS

VORGELEGT VON
M.Sc. ING.
LUANA MAZZARELLA
GEB. IN NAPOLI

VON DER FAKULTÄT IV – ELEKTROTECHNIK UND INFORMATIK
DER TECHNISCHEN UNIVERSITÄT BERLIN
ZUR ERLANGUNG DES AKADEMISCHEN GRADES

DOKTORIN DER INGENIEURWISSENSCHAFTEN
- DR.-ING. -
GENEHMIGTE DISSERTATION

PROMOTIONS-AUSSCHUSS:

VORSITZENDER: PROF. DR.-ING ROLAND PLATH
GUTACHTER: PROF. DR. BERND RECH
GUTACHTER: PROF. DR. RUTGER SCHLATMANN
GUTACHTER: PROF. DR. PERE ROCA I CABARROCAS

TAG DER WISSENSCHAFTLICHEN AUSSPRACHE: 13.02.2017

BERLIN 2017

Abstract

Crystalline-silicon solar cells are presently the main technology to supply the rapidly growing market for competitive photovoltaic electricity. To drive conversion efficiency of such cells further up, silicon heterojunction (SHJ) solar cells are promising.

This thesis addresses strategies to improve the efficiency of such cells by the integration of nanocrystalline silicon (nc-Si:H) and nanocrystalline silicon oxide (nc-SiO_x:H) contact layers grown by plasma enhanced chemical vapor deposition, replacing the commonly used amorphous silicon (a-Si:H) contact layers. The aim is to take advantage of both the improved charge carrier transport and contact resistance and a reduced parasitic absorption. The key challenge is to develop very *thin*, highly crystalline layers that require fast nucleation.

As prerequisite, we first had to establish a reference process with p-doped a-Si:H with a high degree of reproducibility. With this we reached a conversion efficiency of 21.3%.

We investigated the relation between deposition gas composition, optoelectronic material properties and structural features of (p)nc-Si:H films on cell stacks. The a-Si:H passivation layer growth regime (slight epitaxial or fully amorphous) is relevant for the nanocrystalline evolution and critically influences the fill factor (*FF*) and open circuit voltage of completed solar cells. Furthermore, nc-Si:H layers exhibited the ability to enhance surface passivation similarly to what was found with post-deposition hydrogen plasma treatment. A CO₂ plasma treatment of the (i)a-Si:H surface prior to the emitter deposition was optimized as method to fast nucleate the *thin* nc-Si:H films without deteriorating the underlying passivation. The combination of optimized deposition parameters, plasma treatments and film thickness resulted in solar cells exhibiting an open circuit voltage of 727 mV, a short circuit current density of 38.9 mA/cm², a *FF* of 74.6% and a conversion efficiency of 21.1%.

The optical interaction between the incoming light and the multilayer stack placed on the illuminated side of the c-Si absorber was simulated varying the doped contact material (a-Si:H, nc-Si:H, nc-SiO_x:H and doping type) in stack with (i)a-Si:H passivation and In₂O₃:Sn layers. We identified the optimal film thickness and refractive index as function of the substrate texture to maximize the generated current. The use of a tailored nc-SiO_x:H layers allowed for the creation of a stack with refractive indexes that consecutively decreases from silicon to the ambient air resulting in a high short circuit current density of 40.4 mA/cm² with a gain of 2 mA/cm² as compared to using the (p)a-Si:H reference, but with limited *FF* of 72.9%. The causes of the *FF* limitations experimented were ascribed to both the poor contact to the front transparent conductive oxide and the initial stage of growth of the *thin* nc-Si:H emitter. Finally, an alternative procedure showed the potential to overcome both problems by passivating the silicon wafer surfaces with an ultra-thin amorphous silicon oxide film growth by PECVD. An exceptionally high crystalline volume fraction of 72% was measured in a thin layer on a cell stack. Preliminary cells exhibited a high *FF* and reduced current loss but a low open circuit voltage due to insufficient passivation. However, the approach opens up perspectives to further exploit the full potential of nc-Si:H contact layers.

Kurzfassung

Kristalline Silizium-Solarzellen sind derzeit die wichtigste Technologie, um den schnell wachsenden Markt für wettbewerbsfähigen Photovoltaik-Strom zu bedienen. Um den Wirkungsgrad dieser Solarzellen weiter zu steigern, sind Solarzellen basierend auf einem Silizium Heteroübergang (SHJ) vielversprechend.

Diese Doktorarbeit befasst sich mit Strategien zur Effizienzsteigerung dieses Zelltyps. Dafür werden nanokristalline Silizium- (nc-Si:H) und nanokristalline Siliziumoxid- ($\text{nc-SiO}_x\text{:H}$) Kontaktschichten, welche mittels plasmaunterstützter chemischer Gasphasenabscheidung (PECVD) abgeschieden werden, verwendet. Diese Schichten ersetzen die für gewöhnlich verwendeten Kontaktschichten aus amorphem Silizium (a-Si:H). Das Ziel ist, von dem verbesserten Ladungsträgertransport und Kontaktwiderstand als auch der reduzierten parasitären Absorption zu profitieren. Die Hauptherausforderung ist die Entwicklung sehr *dünn*er, hoch kristalliner Schichten, welche eine schnelle Nukleation aufweisen.

Zunächst war es notwendig einen Referenzprozess für SHJ Solarzellen mit p-dotierten a-Si:H Emittern mit einem hohen Grad an Reproduzierbarkeit zu etablieren. Damit erzielten wir einen Wirkungsgrad von 21,3%.

Wir untersuchten daraufhin den Zusammenhang zwischen der Zusammensetzung des Depositionsgases, den optoelektronischen Materialeigenschaften und strukturellen Eigenschaften von (p) nc-Si:H Schichten auf Zellstapeln. Das Wachstumsverhalten der a-Si:H Passivierungsschicht (entweder epitaktisch oder vollständig amorph) ist ausschlaggebend für die nanokristalline Entwicklung und beeinflusst wesentlich den Füllfaktor und die Leerlaufspannung der Solarzelle. Ähnlich der Nachbehandlung mit einem Wasserstoffplasma führt die Abscheidung nanokristalliner Schichten zu einer verbesserten Oberflächenpassivierung. Eine CO_2 Plasmabehandlung der (i) a-Si:H Oberfläche wurde vor der Emitter-Abscheidung durchgeführt. Diese Behandlung wurde im Hinblick auf die Emitter Nukleation optimiert, wobei die Qualität der Passivierung der darunterliegenden Schicht unverändert bleiben sollte. Die Kombination aus optimierten Depositionsparametern, Plasmabehandlungen und Filmdicken resultierte in Solarzellen, welche eine Leerlaufspannung von 727 mV, eine Kurzschlussstromdichte von $38,9 \text{ mA/cm}^2$, einen Füllfaktor von 74,6% und einen Wirkungsgrad von 21,1% aufwiesen.

Der Schichtstapel auf der beleuchteten Seite des c-Si Absorbers wurde optisch simuliert. Dabei wurde das dotierte Kontaktmaterial (a-Si:H , nc-Si:H , $\text{nc-SiO}_x\text{:H}$ und Dotiertyp) im Stapel mit (i) a-Si:H Passivierung und der ITO Schichten variiert. Wir ermittelten die optimale Filmdicke und den optimalen Brechungsindex als Funktion der Substrattextur in Hinblick auf eine maximale Stromstärke.

Die Verwendung geeigneter $\text{nc-SiO}_x\text{:H}$ Schichten erlaubte die gezielte Reduktion des Brechungsindex-Übergangs vom Silizium zur Luft. Damit konnte eine im Vergleich zur (p) a-Si:H Referenz um 2 mA/cm^2 höhere Kurzschlussstromdichte von $40,4 \text{ mA/cm}^2$ erreicht werden, wobei der Füllfaktor auf 72,9% begrenzt war. Diese Füllfaktorbegrenzung wurde

einer schlechten Kontaktierung des Vorderseiten-TCOs und dem unzureichenden initialen Wachstumsverhaltens (Nukleation) des dünnen Emitters zugeschrieben.

Die Passivierung der Silizium-Waferoberfläche mit einer ultradünnen, amorphen PECVD Siliziumoxid-schicht bietet potentiell die Möglichkeit beide o.g. Probleme zu umgehen. Ein sehr hoher kristalliner Volumenanteil von 72% konnte in dünnen Schichten auf Zellstapeln gemessen werden. Erste Solarzellen weisen einen hohen Füllfaktor und einen verringerten Stromverlust auf. Allerdings ist die Leerlaufspannung aufgrund einer geringen Passivierungsqualität niedrig. Dennoch eröffnet dieser Ansatz neue Perspektiven, um das Potential von nc-Si:H basierten Kontaktschichten vollständig auszuschöpfen.

Contents

Abstract.....	III
Kurzfassung	IV
1. Introduction.....	1
2. Fundamentals	5
2.1. Basic Operational Principles of a Solar Cell	5
2.1.1. Semiconductor Materials	5
2.1.2. Fundamental Limitations and Recombination Mechanisms.....	6
2.2. a-Si:H/c-Si Heterojunction Solar Cells.....	10
2.2.1. Band Diagram to Describe a-Si:H/c-Si Contact.....	10
2.2.2. TCO/(p)Emitter Contact.....	12
2.2.3. Design of Silicon Heterojunction Solar Cells.....	14
2.3. Hydrogenated Amorphous and Nanocrystalline Silicon Material	17
2.3.1. PECVD Process.....	17
2.3.2. Silicon Material Growth and Properties.....	18
2.4. Specific Limitations in SHJ Solar Cells Fabrication	25
3. Experimental Methods	27
3.1. Cell Preparation Process.....	27
3.1.1. Silicon Wafer Preparation	28
3.1.2. Silicon Deposition by PECVD	29
3.1.3. TCO and Metal Contact Deposition.....	32
3.2. Characterization Methods	34
3.2.1. Thin Film Characterization.....	34
3.2.2. Device Characterization	41
4. Reference Process Development for Silicon Heterojunction Solar Cells	49
4.1. a-Si:H Passivation Layer	50
4.2. p-doped Emitter	54
4.3. Front TCO.....	58
4.4. Rear TCO	61

4.5. Discussion and Conclusions	63
5. Nucleation of p-doped Nanocrystalline Silicon Layers for SHJ Solar Cells.....	67
5.1. Nanocrystalline Material Optimization	68
5.1.1. Effect of the Gas Composition.....	68
5.2. Integration of Thin nc-Si:H Layers in SHJ Cells.....	72
5.2.1. Nanocrystalline Silicon Nucleation	73
5.2.2. Impact on the Passivation	75
5.2.3. Variation of the (i)a-Si:H Passivation Film Thickness and Morphology	84
5.2.4. Effect of the Doping Gas Dilution	85
5.3. Discussion and Conclusions	87
6. Nanocrystalline Silicon Oxide Window Layers	89
6.1. Optical Simulation Model	90
6.2. Nanocrystalline Silicon Oxide Material.....	94
6.2.1. Introduction.....	94
6.2.2. p-doped Layers	94
6.2.3. n-doped Layers	96
6.2.4. Comparison of nc-Si:H and nc-SiO _x :H	98
6.3. Integration of (p)nc-SiO _x :H in Front Emitter Cells.....	100
6.3.1. Simulation Results	100
6.3.2. Photocurrent Analysis	103
6.3.3. Solar Cell Results.....	105
6.3.4. Charge Carrier Transport at the TCO/(p)nc-SiO _x :H Contact	109
6.4. Integration of (n)nc-SiO _x :H in Rear Emitter Cells.....	112
6.4.1. Simulation Results	113
6.4.2. Solar Cell Results.....	116
6.5. Discussion and Conclusions	121
7. Exploratory Study on Thin Silicon Dioxide Passivation Layers	123
7.1. Introduction	123
7.2. Material Optimization.....	124
7.2.1. Optical and Structural Properties.....	126
7.2.2. Passivation Performances	131
7.3. Integration in SHJ Solar Cells	133
7.3.1. Nanocrystalline Growth Enhancement	133
7.3.2. Cell Results on Polished Wafers	134

7.4. Discussion and Conclusions	137
8. Conclusions and Outlook	139
List of Acronyms and Symbols	143
Bibliography	145
List of Publications	163
Acknowledgments	165

1. Introduction

At the *United Nation Climate Change Conference (COP21)* that took place in Paris in 2015, more than 170 countries officially recognized the need of a global response to the urgent long-term climate change caused by greenhouse gas emission. They committed to the goal to limit global warming with the specific aim to “...pursuing efforts to limit the temperature increase to 1.5 °C above pre-industrial levels, recognizing that this would significantly reduce the risks and impacts of climate change.” (art.2) [1].

Despite these binding obligations, developed countries reduced investment in renewable energy by 8% in 2015, with Europe as the leading region in this negative trend [2].

On the contrary, global investment for solar power saw an increase of 12% in 2015, the highest for renewable energies [2]. In particular, the cost-competitiveness of photovoltaic (PV) has increased, reaching levelized cost of electricity (LCOE) well below 0.10 €/kWh and an energy payback time (EPBT) of about 1 year for monocrystalline silicon modules under 1700 kWh/m² global irradiation (southern European conditions), that is estimated to further decrease by half [3].

Silicon wafer based solar cells dominate the PV market with 93% of the total global production in 2015 [4]. This technology benefits firstly from using silicon as raw material, which is abundant, non-toxic and long-term stable. Moreover, it takes advantage of the mature research background in common with the semiconductor microelectronics industry. The main drawback is the cost of Si wafers and the energy usage that are still high. Therefore, the wafer thickness has been progressively thinned to reduce material consumption and wafers of about 180 µm are currently used in mass production [5].

Monocrystalline silicon solar cells and modules have shown progressive improvements in conversion efficiency [6]. In 1999, the remarkable conversion efficiency of 25.0% on c-Si wafer was reached by the PERL cell concept (Passivated Emitter Rear Locally diffused) [7]. In the same decade, a hybrid device concept consisting in amorphous silicon (a-Si:H) films deposited on monocrystalline silicon wafers (c-Si) drew interest [8].

This device is known as a-Si:H/c-Si heterojunction (SHJ) solar cell. It combines the established standard wafer technology with low temperature processing from the thin-film technology ($T < 200$ °C). The distinctive property of this device concept is the exceptionally high open circuit voltage up to 750 mV [9], achieved thanks to the excellent surface

1. INTRODUCTION

passivation. The higher voltages implicate also a lower temperature coefficient than other silicon solar cells. This characteristic improves the output power under higher temperature operating conditions [10]. Finally, the low process temperature together with the symmetric device structure allow for the use of wafer with a thickness of down to 50 μm [11].

The potential of the SHJ concept led to a world record conversion efficiency of 25.6% [12], recently reached 26.3% [13]. Sanyo was the company to patent the SHJ concept and in 1997 entered the PV market commercializing solar modules. Attracted by the simple fabrication process, the possible upscaling due to the extensive experience gained by the thin-film industries and the demonstrated high efficiencies, several companies (such as Kaneka [14] and Mitsubishi Electric [15]) and research institutes showed their interest in SHJ solar cells.

Besides the improvements in cell processing technology, the main limitation to the conversion efficiency is from photocurrent losses. Consequently, a great deal of effort has been dedicated to further increase the current extracted at the cell terminals.

A first method involves cell design optimization to minimize the fraction of light that does not enter the cell due to shadow losses. Typically, it involves front grid electrodes design to match resistive and optical losses. Recently, the interdigitated back contact scheme has been proposed where both contacts are placed on the rear side, leading to the conversion efficiency record of 25.6%. It has the advantage of completely eliminating shadow losses but as a drawback, increases fabrication complexity due to intricate patterning technology. Additionally, the use of light management schemes, such as textured substrates and rear reflectors [16], drastically reduce the light lost by primary reflection or transmission, thus enhancing the probability of the light to be absorbed and to generate carriers.

A second approach is the careful choice of materials and tailoring of their properties to reduce the light that is parasitically absorbed in the illuminated stack on top of the absorbing wafer. Improvements concerned the development of layers that are placed on the illuminated side of the device to enhance transparency with comparable or higher electrical features.

The universally used tin-doped indium oxide ($\text{In}_2\text{O}_3:\text{Sn}$, ITO) as transparent conductive oxide (TCO) film is under development by testing for example, new doping elements [17]. However, the largest fraction of parasitic optical losses in a SHJ cells is due to the a-Si:H films that provide passivation and charge separation at the junction.

Consequently, attempts to widen the band gap of those films are under intensive investigation by alloying them with oxygen or carbon and/or using nanocrystalline films with the aim to minimize parasitic absorption. The challenge is to develop thin layers with reduced refractive index and suitable crystalline fraction embedded in the amorphous matrix to provide an efficient carrier transport.

This approach forms the basis of this thesis that focuses on the development of silicon based material fabricated by plasma enhanced chemical vapor deposition (PECVD) for application in a-Si:H/c-Si heterojunction solar cells. The extensive knowledge at Helmholtz-

Zentrum-Berlin (PVcomB) concerning material properties and plasma deposition techniques on thin-film devices, were transferred to the SHJ concept.

The thesis begins with fundamentals of solar cell device in chapter 2, with a specific discussion on the main limitations, recombination mechanisms and design issues that contribute to the SHJ cell performance. Then, the amorphous and nanocrystalline silicon materials are introduced describing the film growth, properties and structure.

In *chapter 3*, the experimental techniques used for devices fabrication are described together with methods for material and device characterizations.

Chapter 4 is focused on the development of a reference process for silicon heterojunction solar cells using large-area production type tools. Both PECVD and PVD processes are developed and/or re-optimized to obtain stable and reproducible reference device fabrication, as a prerequisite to study the implementation of the novel contact materials.

In *chapter 5* we investigate the growth of thin p-doped hydrogenated nanocrystalline silicon films addressing the specific requirements for integration as emitter in SHJ solar cells. A crucial question is how to nucleate nc-Si:H films on different a-Si:H substrates without deteriorating the underlying intrinsic passivation layer. The influence of PECVD deposition parameters and substrate selectivity, on optoelectronic and structural properties of thin nc-Si:H films, is investigated both in dedicated layer stacks and completed devices. The progressive improvements in conversion efficiency are discussed in comparison to the in-house reference cells with amorphous (p)a-Si:H emitters.

Chapter 6 addresses the benefits of using oxygen alloyed nanocrystalline silicon films as window contact layers, to minimize current losses. As for the (p)nc-Si:H in chapter 5, we investigate material properties of the p- and n-doped nc-SiO_x:H material first, and then their potential in completed solar cell devices. The optical properties of the multilayer stack placed on the front side of the c-Si absorber are simulated to enabling easier layer optimization. Simulation are compared to experimental results.

Chapter 7 explores the use of a silicon dioxide passivation layer based on the results from nucleation enhancement made in chapter 5. PECVD deposited SiO₂ is used as passivation layer to promote the growth of nc-Si:H films with higher crystalline fraction to enhance carrier transport and reduce parasitic absorption.

Chapter 8 summarizes the main results, draws conclusions from them and gives an outlook for future experiments and studies.

2. Fundamentals

This chapter lays the theoretical foundation for the experimental research done in this thesis and supports the hypotheses and methodologies used for the investigations. First, a description of the silicon heterojunction device concept, followed by a review of the most promising design strategies to improve cell efficiency by enhancing photon absorption into the crystalline silicon are presented in sections 2.1 and 2.2, respectively. Finally in section 2.3, the characteristics of hydrogenated amorphous and nanocrystalline silicon materials (a-Si:H and nc-Si:H) relatively to deposition, properties of doped and alloyed films are discussed.

2.1. Basic Operational Principles of a Solar Cell

The photovoltaic effect is the basic principle of any solar cell device and consists of process that convert the solar energy into electrical energy. Firstly, photons are absorbed in the semiconductor material creating photogenerated charge carriers. The electron-hole pairs are separated by an electric field and, finally, collected at the terminal contacts (electrical energy).

2.1.1. Semiconductor Materials

The conduction in semiconductor material takes place by energy states (or bands) separated by a forbidden gap (band gap, E_g) where no electrons are allowed [18]. To participate to the conduction, electrons have to absorb an amount of energy that permits them to overcome the band gap between the valence band (VB) and the conduction band (CB). Photons with energy equal or greater than the E_g excite electrons into to the CB, while photons with energy less than the E_g are not absorbed and are transmitted by the semiconductor. Each promoted electron leaves behind a vacancy, called a hole, that is assumed to be positively charged.

The intrinsic carrier concentration (n_i) in a semiconductor depends on the specific material and the temperature. The number of electrons or holes can be varied by doping. At the

2. FUNDAMENTALS

thermal equilibrium, the product of the majority and minority carrier concentration is a constant and this is mathematically expressed by the fundamental equation, $n_0 p_0 = n_i^2$, where n_0 and p_0 are the electron and hole equilibrium carrier concentrations, respectively.

2.1.2. Fundamental Limitations and Recombination Mechanisms

The fundamental limitation of the conversion efficiency of a solar cell, firstly, depends on the intrinsic properties of the absorber material, such as the band gap. To increase the maximum value of the voltage, semiconductors with wider E_g might be chosen. Conversely, the current density is negatively affected since photons with higher energy are required to promote electrons in the conduction band. This implies that an optimum E_g for semiconductors exists to allow the highest conversion efficiency. The peak occurs in the range 1.4 - 1.6 eV and crystalline silicon (c-Si) exhibits a E_g which is below the optimum ($E_{g,c-si} = 1.12$ eV) [19].

Under illumination, a certain amount of charged carriers are generated in the absorber as a function of the light intensity. The photogenerated electron-hole pairs are in a metastable state thus the system tends to restore the equilibrium condition through different mechanisms, which are introduced below with focus on c-Si solar cells. It is worth distinguishing between intrinsic recombination mechanisms (that occur also in the ideally perfect c-Si material) and recombination that is caused by defects and impurities that act as recombination centers. Radiative recombination [18] and Auger recombination [20] are of the first type whereas the Shockley-Read-Hall (SRH) recombination [21] belongs to the latter. The ultimate effect of the recombination process is a limitation on the maximum voltage available from the device and thus to reduce the cell efficiency.

In the assessment of the efficiency limit of a solar cell, a consideration of the specific illumination spectra and the intrinsic charge carrier recombination properties is important. In the detailed balance limit, Shockley and Queisser [22] determined the theoretical limit for the efficiency at 30% for a crystalline silicon (c-Si) solar cell at the temperature of 300 °K and exposed to a blackbody sun at temperature of 6000 °K. In their discussion, only the radiative recombination is taken into account. That is not the only possible and the most probable recombination mechanism in c-Si. In fact, its indirect band gap makes the non-radiative recombination mechanisms considerably more efficient than the radiative. Hence, considering the so-called Auger recombination in addition to the radiative losses, the limit efficiency for a perfect absorber is calculated to be 29.8% under one-sun illumination (AM 1.5) [23]. Recently Richter *et al.* [24] reassessed the upper efficiency limit at 29.4% for a 110 μm thick undoped c-Si using revised parameters for their calculations.

Recombination Mechanisms

The *radiative recombination* mechanism involves a band-to-band electron-hole recombination and can be seen as the inverse process of the absorption. An electron situated in the CB recombines with a hole in the VB by a radiative process that releases a

photon with an energy level close to the E_g (see Figure 2.1 (a)). This mechanism is dominant in direct band gap materials while it is less probable for indirect E_g ones as c-Si.

The Auger recombination process involves three carriers. The energy released from an electron that recombines by direct band transition is transferred to a third carrier (electron or hole) that then thermalizes back to band edge (see Figure 2.1 (b)). This recombination mechanism is more efficient for high doping levels in c-Si and becomes more dominant with increasing the injection level.

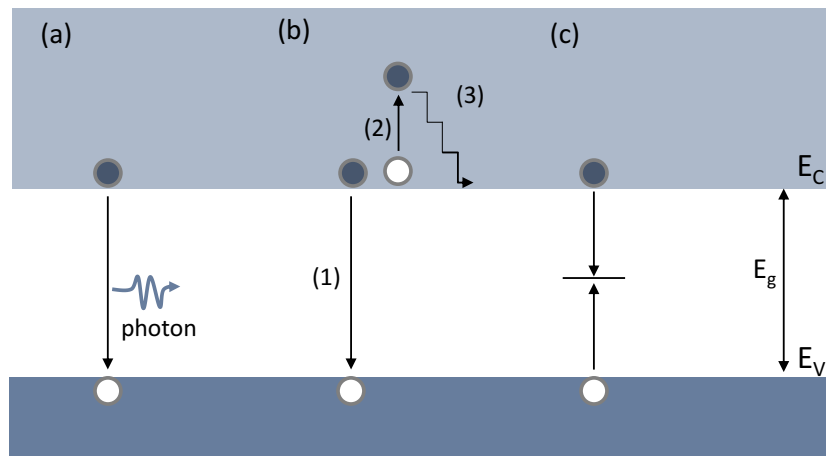


Figure 2.1. (a) Radiative, (b) Auger and (c) Shockley-Read-Hall recombination mechanisms.

The *SRH recombination* is classified as an extrinsic process because it is related to the presence of defect states in the forbidden gap, caused by lattice defects or contaminants (impurities and doping). SRH is a two-step process that involves an electron and a hole that move and are trapped in the same defect state as depicted in Figure 2.1 (c). Such defects can be situated close to the band edge (trap states) or to the mid-gap (recombination centers). The latter one results in more effective SRH recombination. As an example, if the defect is close to the conduction band, there is a higher probability that a charge (i.e. electron) moves to the CB again rather than recombines with a hole that moves from the VB towards the same trap state. There are two sources of SRH recombination, the bulk contribution is mainly related to impurities/doping, whereas the wafer surface presents a net disruption of the crystal network that leads to recombination with a high rate. Methods to control the surface recombination are discussed below.

Effective Minority Carrier Lifetime and Surface Passivation

The effective minority carrier lifetime τ_{eff} depends on all the recombination mechanisms discussed above both for the bulk and surface and is defined as:

$$\tau_{eff} = \frac{\Delta n}{U}, \quad \frac{1}{\tau_{eff}} = \frac{1}{\tau_{rad}} + \frac{1}{\tau_{Auger}} + \frac{1}{\tau_{SRH}} + \frac{1}{\tau_{surf}} \quad (2.1)$$

where U is the sum of all the recombination rate contributions and Δn is the excess minority carrier density.

Figure 2.2 shows how the different limiting mechanisms influence the carrier lifetime variation as a function of the excess carrier concentration (or injection level) [25], simulated with the PV lighthouse software [26]. The radiative and Auger contribution to the total carrier lifetime in the higher injection level scales with the excess carrier concentration with a power of -1 and -2, respectively [18]. Contrarily, the SRH recombination is dominant in the lower injection range.

The quality of the c-Si wafer affects the bulk contribution of the SRH recombination. In the standard technologies for fabricating single crystal silicon wafers, the Float Zone process (FZ) [27] produces a higher level of purity than the Czochralski process (CZ). The monocrystalline FZ ingot is formed by locally melting the silicon via induction heating without any contact with crucible walls that lead to oxygen contamination. However, the FZ wafers are more expensive.

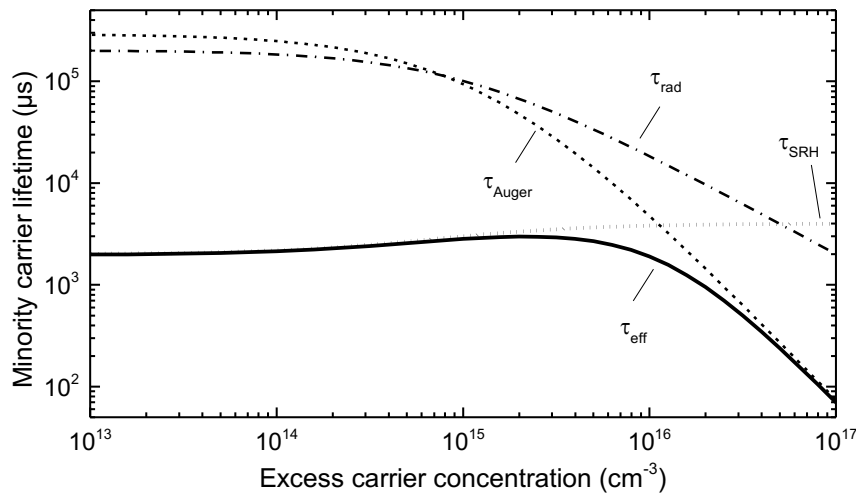


Figure 2.2. Simulated minority carrier lifetime τ_{eff} of a (n)c-Si wafers as function of the excess carrier concentration from different recombination mechanisms. Simulation performed with PV Lighthouse recombination calculator [26] with the following input parameters: phosphorus doping, dopant concentration of 10^{15} cm^{-3} and temperature 300 °K.

2.1. Basic Operational Principles of a Solar Cell

Furthermore, the doping type plays a role. The p-type wafers historically dominate the PV market over n-type silicon material. Fabrication of p-type silicon is in comparison to n-type easy and less expensive. Despite that, n-type material allows much higher minority carrier lifetimes (and consequently V_{oc}) since metal impurities have larger capture cross section for electrons [28]. Additionally, p-doped c-Si degrades after illumination due to metastable oxygen-boron complexes and metal contaminations have a greater detrimental impact on boron doped material resulting in a reduction of initial device efficiency [29].

Since the bulk silicon mono-crystal has a high electronic quality, recombination takes place predominantly at the wafer surfaces where the periodic Si crystal lattice abruptly ends. Particularly, the break of the four covalent bond structure of Si leads to the formation of unpaired electrons that are called dangling bonds (DB). The surface contribution to the SRH recombination rate can be drastically reduced by saturation of the DBs on the c-Si surfaces [30]. This process is commonly referred to as chemical passivation and reduces the interface defect density D_{it} by filling the unoccupied state of the Si atom.

Both wet-chemical treatments and cleaning procedures of the silicon surface are able to reduce D_{it} . The c-Si dipping in HF is well-known as a method to remove the native oxide allowing the formation of H-terminated surfaces [31]. On the other hand, the deposition of intrinsic hydrogenated amorphous silicon ((i)a-Si:H) layer enables excellent surface passivation [32,33] and high voltage potential, by saturation of DBs with hydrogen. The properties and deposition conditions for (i)a-Si:H material used to enhance film quality and passivation are discussed in section 2.3.

Additionally, another mechanism, called field-effect passivation, can reduce the recombination at the c-Si interfaces. By inducing a band bending at the absorber surface, a built-in electrical field repels either electrons or holes from the surface states. Consequently, the avoided accumulation of charge carriers of one type reduces the recombination probability and leads to improvement in minority carrier lifetime. Field-effect passivation has been successfully achieved by introducing fixed negative or positive charges growing for example Al_2O_3 [34] or SiO_2 [35] films, respectively on silicon. The drawback of using non-conductive materials is the necessity to open the film to gain a direct contact between the metal electrodes and the silicon absorber (which then are no longer passivated at these points). Alternatively, a highly doped layer at the Si surface might lead to reduced recombination rate. An example is the creation of p/p⁺ or n/n⁺ areas (by diffusion or deposition of doped film) which is commonly applied as a back surface field layer (BSF, to be discussed in the next section) in silicon homo- [36] or heterojunction [37] solar cells. The role and the consequences of passivation and doped layers in the device operation are given in the next section 2.2.

2.2. a-Si:H/c-Si Heterojunction Solar Cells

Historically, the first direct conversion of solar radiation into electrical power with Si wafer based solar cells was demonstrated by Chapin *et al.* [38] in 1954 with Si wafer based solar cells. The p-n junction was created by diffusion of dopant species from the surface into the wafer (homojunction). The p-n junction formed within the same material facilitates the electron-hole pair separation thanks to the internal electric field formed. On the contrary, the term heterojunction is used when two materials with different composition or morphology create the junction. The device concept under investigation in this work is composed of an amorphous/crystalline silicon (a-Si:H/c-Si) material and it is known as a silicon heterojunction solar cell (SHJ). One of the earliest reports on SHJ cell was by Fuhs *et al.* [39], but nowadays this cell concept is associated to the Sanyo-Panasonic Corporation that developed and patented the HIT™ (*Heterojunction with Intrinsic Thin layer*) technology [8]. A comprehensive review of the crystalline silicon solar cells can be found in the recent paper from Battaglia *et al.* [40] and specifically on SHJ devices in [41,42].

2.2.1. Band Diagram to Describe a-Si:H/c-Si Contact

Figure 2.3 depicts the band lineup scheme of a heterojunction cell for a device with an n-doped c-Si absorber and of a standard homojunction for comparison. The electron-hole pair, photogenerated in the absorber, is separated instantaneously and diffuses across the absorber until it is collected at the terminals or recombines.

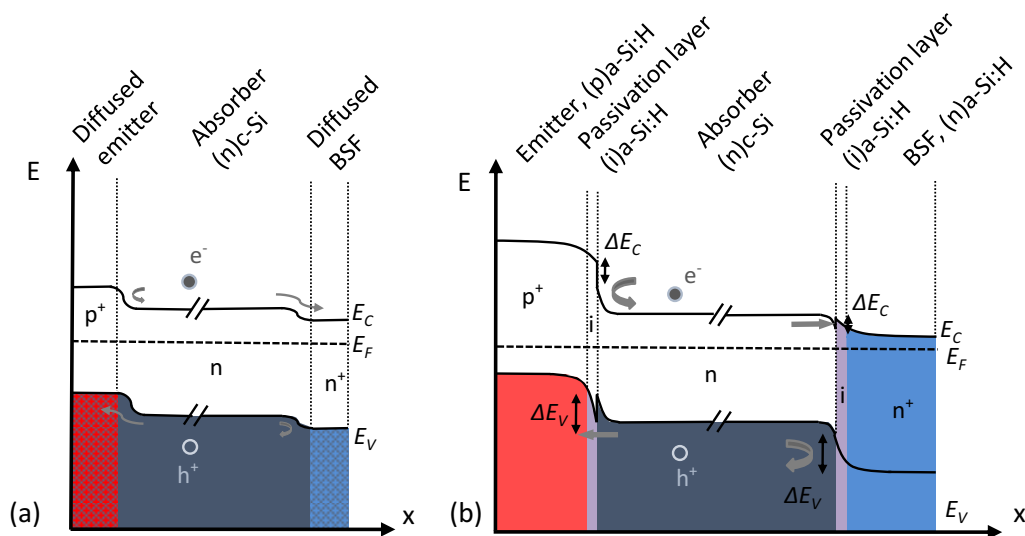


Figure 2.3. Schematic band diagram of (a) p⁺/n/n⁺ homojunction and (b) (p)a-Si:H/(n)c-Si/(n)a-Si:H SHJ illuminated via the emitter side. A schematic band diagram is embedded the cell sketch: E_F , E_C and E_V are Fermi level-, conduction- and valence band edge- energy levels, respectively. The arrows indicate the collection direction and repelling of the electron or hole generated in the absorber. Additionally, the arrow dimensions indicate the effectiveness of the specific mechanisms. Layers are not in scale and acronyms used here are explained in the text.

In the homojunction, the doped contacts are obtained by thermal diffusion of boron or phosphorus, respectively, with a distribution of dopant impurities that is assumed to have an exponential decay profile from the c-Si surfaces. Both doped layers take an active role in the carrier collection process. The ability to promote the selective carrier collection depends on the band structure of the film. Considering the specific case depicted in Figure 2.3 (a), the p⁺ doped layer (emitter) at the p/n junction is a membrane for holes (higher hole conductivity) whereas, it repels the electrons that are in proximity of the interface. Contrarily, the n⁺ doped layer (BSF) at the n⁺/n junction lets only electrons pass across and blocks the holes (higher electron conductivity). It can be concluded that emitter and BSF behave as electron and hole selective contacts, respectively.

The a-Si:H/c-Si heterojunction scheme typically consists of an (i)a-Si:H passivation film and a-Si:H doped contact grown on the absorber surface by plasma enhanced chemical vapor deposition (PECVD). The doping profile is abrupt at the interface and commonly schematized with box-shaped functions. The difference in band gap between the amorphous/crystalline leads to large discontinuities (called band offsets) as displayed in Figure 2.3 (b) by the double arrows. Anderson developed a model to describe the junction between two dissimilar semiconductor material [43]. This model considers the formation of band offsets at the interface as consequence of the electron affinity rule, but no interface defects are assumed. The exact experimental determination of the band offset at the valence band (ΔE_V) and conduction band (ΔE_C) is still an open question and the values reported in literature vary over a wide range [41]. Furthermore, the hydrogen content in the amorphous film can vary while the interface properties can differ from the bulk. Indicative values for the ΔE_V and ΔE_C might be 0.54 and 0.14 eV as reported by [41] and obtained assuming an $E_{g\text{ a-Si:H}} = 1.8$ eV for the amorphous film and $E_{g\text{ c-Si}} = 1.12$ eV for the absorber.

The selectivity control of charges, discussed for the homojunction, is enhanced in heterojunction thanks to suitable band offset at the CBs and VCs. Looking at the band diagram in Figure 2.3 (b), it can be seen that the band offsets influence strongly the charge carrier transport across the interfaces. It results in a drastic reduction in recombination thus, together with the insertion of the (i)a-Si:H passivation layer, very high open circuit voltage (V_{oc}) up to 750 mV can be achieved [9]. Nevertheless, the band offsets have to be carefully tailored to avoid undesired negative effects that was identified as one of the possible reason of reduced cell performance with appearance of S-shape in J - V curve [44]. Specifically, at the p-n contact, besides the useful band offset at the conduction edge (that repels electrons from that interface), a ΔE_V appears as a narrow spike at the valence band edge. Here, holes accumulate and they can overcome the potential barrier only if the discontinuity is not too large through a combination of different transport paths [45] (e.g. by thermionic emission or tunneling process¹). Another advantage of using material with

¹ Thermionic emission: Flow of carriers thermally induced over the potential energy barrier. Tunneling process is the quantum-mechanical phenomenon by virtue of which the electron (described as a wavefunction) can penetrate (tunnel) into the potential barrier of a finite height and width with a probability not equal to zero. Both definitions are taken from the Ref. [18].

2. FUNDAMENTALS

large band gap at the illuminated side is to increase the fraction of incoming light transmitted through the doped material and hence enhance the number of photons that can be absorbed into the c-Si. This aspect is further discussed below.

2.2.2. TCO/(p)Emitter Contact

Due to its high resistivity, the doped amorphous contact layers cannot provide a suitable electronic conductivity for lateral transport of the carriers towards the metal contacts. Thus, an additional conductive layer needs to be placed on the front of the SHJ solar cell. Besides the electrical properties, such film has to fulfill optical requirements depending on the specific position in the device.

Among the transparent conductive oxides (TCOs) materials available, the most employed in SHJ devices is sputtered tin-doped indium oxide ($\text{In}_2\text{O}_3:\text{Sn}$, ITO) because of its superior features such as excellent stability, low resistivity and high transparency. In addition, aluminum-doped zinc oxide ($\text{ZnO}:\text{Al}$, AZO) can be a candidate to replace ITO. The advantages of AZO are the low costs since its production does not depend on scarce materials [46]. Such materials allow very high doping levels (electron density $> 10^{20} \text{ cm}^{-3}$) that results in a shift of the Fermi level above the conduction band edge (*degenerated* semiconductors).

Here, we focused on the TCO/(p)emitter contact properties, while more details concerning the optical features are given in the following section 2.2.3.

Models to Describe the TCO/Emitter Contact

The role of the TCO is not merely providing a contact since its electrical properties can significantly influence the band line up when it is in contact with a-Si:H films.

Classically, the TCO/a-Si:H contact is described as a metal/semiconductor contact in agreement with the Schottky (or rectifying) contact model [47,48]. When the two materials are in contact, a barrier forms at the interface and it is responsible for controlling the current transport. In agreement with [18], the height of the barrier is given by $q\phi_B = E_g - q(\phi_{\text{TCO}} - \chi_{(p)\text{a-Si:H}})$. This value depends on the work function² of the TCO (ϕ_{TCO}) and the electron affinity of the semiconductor $\chi_{(p)\text{a-Si:H}}$. The band diagram deduced from the Schottky contact model is depicted in Figure 2.4 (a), whereas the one simulated in [49] and given in Figure 2.4 (b) considers both layers as semiconductors. Therefore, the band bending is allowed also in the ITO layer and the intensity of bending depends on the ϕ_{TCO} values (see Figure 2.4 (b)).

² The work function is the energy difference between the vacuum level and the Fermi level as depicted in Figure 2.4 [18].

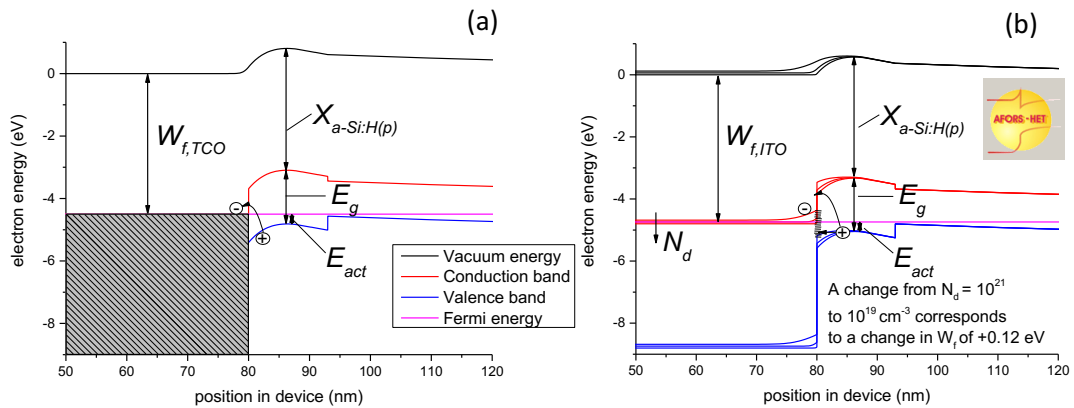


Figure 2.4. Band diagram of the ITO/(p)a-Si:H contact (a) in agreement with the Schottky contact model and (b) where both layers are treated as semiconductors. N_d is the free-carrier density, W_f are the work function of the ITO layer. The plots are taken from [49]. More details about the simulation parameters can be found in the same reference.

Looking at the band structure of the n-type SHJ cell in Figure 2.3 (b) and Figure 2.4 (b), the photogenerated holes in the c-Si have to overcome the two potential barriers (ΔE_V s) in their flow. As discussed in the previous section, the first one occurs at the (n)c-Si/(p)a-Si:H junction, then the holes approach the (p)/ITO interface and are stopped by the high potential barrier (Figure 2.4 (b)). Thus, the cell can be depicted as composed of two consecutive junctions: (n)ITO/(p)emitter and (p)emitter/(n)c-Si [50] that results in two diodes in series that are polarized opposite. This results in a J - V characteristic with a kink that is known with the term S-shaped curve as simulated considering the thermionic emission as the only allowed recombination mechanisms [50]. Consequently, the open circuit voltage and lastly the cell performance can be severely reduced even if the ΔE_V is reduced.

Since the first reports of working SHJ solar cells were reported in literature [9], alternative transport mechanisms have been suggested. Recent studies report more realistic models that introduce a carrier tunneling process in their numerical simulations [50–52]. Kanevce and Metzger [50] showed that the presence of the additional transport path across the TCO/a-Si:H interface mitigates the barrier problems leading to well-shaped cell characteristic as experimentally measured in SHJ solar cells [9].

As described before, the most relevant parameter that electrically describes the contact is the relative work function between TCOs and p-doped films. For ITO a range of values are suggested in literature $\varphi_{ITO} \sim 4.2 - 5.3$ eV [53], whereas for the (p)a-Si:H emitter a value of $\varphi_{(p)a-Si:H} = 5.2$ eV is generally accepted. Both values should be tailored to reduce the work function mismatch and consequently help to mitigate the negative effects on the J - V curve. Thus band offset can be reduced by either increasing the doping efficiency for the p-doped layer and/or the thickness [52] or tuning the ITO work function [47,51,54]. In particular, the

emitter should be thicker than the sum of the depletion regions at the two junctions to avoid their overlapping [51]. Nevertheless, a too thick a-Si:H film also leads to reduced cell performance via parasitic absorption of photons. Bivour *et al.* [55] reported a critical emitter thickness of ~ 4 nm to maximize conversion efficiencies for a simulated structure with highly doped emitter ($\varphi_{(p)\text{a-Si:H}} = 5.4$ eV). On the other side, the simulations mentioned above suggest that the φ_{ITO} has to be above 4.8 eV to avoid detrimental effects on the cell efficiency.

2.2.3. Design of Silicon Heterojunction Solar Cells

In section 2.1.2, the fundamental causes of performance limitations have been described, whereas, here, other relevant aspects in the design of a solar cell are discussed. Among them, the minimization of resistive and photocurrent losses are crucial to controlling the conversion efficiency of the device.

Optical Losses and Light Management

Photocurrent losses quantify the fraction of the incoming light that is prevented from reaching the active layer reducing the electron-hole pair generation. The most relevant optical losses in a SHJ device are shading by the top metal grid coverage and surface reflection at the front side of the device due to coherent light interference.

A *metal grid* is placed on the surface to conduct away the current photogenerated by the absorber. The design of the front contact is a compromise between resistive and optical losses. The two aspects depend on the specific properties of the metal and shadowing of the cell area that prevent the incoming light from reaching the absorber and can require optimization of metal high-to-width aspect ratio and the fingers/busbar pattern.

Light management consists of all the strategies that actively manipulate the interaction between the incident radiation and the device with the aim of minimizing optical losses as much as possible. The most effective light management is by controlling layer characteristics such as refractive index (n) and thickness in multilayer structures. Since the optical properties of a material are function of the wavelengths, the optimization process should take account of the relevant wavelength (λ) range for each layer.

Another efficient approach is the light confinement into the absorber layer by multiple internal reflections. Without any precaution, a single light path occurs and the unabsorbed radiation leaves the device by transmission. The enhancement of the path length is obtained by introducing designed patterns or films at the relevant interface [56].

In a SHJ device, light management techniques are applied in:

- *Front TCO film.* Bare silicon surface reflects about 35% of the light due to the differences in refractive index to the adjacent medium³. The presence of the TCO ensures the reduction of the primary reflectance acting as an antireflection coating (ARC) for λ of 600 nm. The two parameters to be optimized are refractive index and thickness: n is adjusted to be the geometric mean of that of the adjacent media, whereas the optical thickness is a quarter of the wavelength of the incoming light:

$$n_{ARC} = \sqrt{n_{air}n_{c-Si}} \quad \text{and} \quad t_{ARC} = \frac{\lambda}{4n_{ARC}} \quad (2.2)$$

If the ARC is well designed, the two waves reflected at the two interfaces are out of phase and interfere destructively.

- *TCO/Ag stack* at the rear side. The stack is tailored as a back reflector (or mirror) with the aim to reduce losses by transmission and reflect the unabsorbed photons back into the silicon wafer.
- *Silicon surface texturing* can drastically reduce reflectance down to about 10% [57] by increasing the light path of the refracted light into the cell as function the angle of incidence but also by multiple reflection of the reflected portion of the incoming light. The most common surface morphology employed in the silicon technology is a pyramidal random texture even if different geometries and patterns are possible [56].

Parasitic Absorption

The incoming light is partially absorbed in each encountered film resulting in current losses. The term *parasitic absorption* includes both absorption that does not produce electron-hole pairs and recombination of generated carriers before they can be collected at the cell terminals. A complete analysis of current losses in a SHJ solar cell simulated and compared to experimental results is given in [58] and [59] relatively to the front and rear side, respectively. Considering the front emitter cell in Figure 2.3, the ITO, the (p)a-Si:H emitter and the (i)a-Si:H passivation layer contribute to losses for wavelength below 600 nm of 0.3, 1.2 and 0.6 mA/cm², respectively [58]. The a-Si:H films, despite their limited thicknesses, contribute to a large percentage of losses in the high energetic wavelength range as demonstrated by some studies [8,60]. The doping in a-Si:H layer is responsible for adding defects in the layer and increases the parasitic absorption if compared to the intrinsic film.

³ The reflectance, $R(\lambda)$, between two materials of different refractive indices (air and silicon) is determined by: $[(n_{air}-n_{c-Si})/(n_{air}+n_{c-Si})]^2$.

In the infrared region of the spectrum, the losses amount to 0.7 mA/cm^2 and are even more pronounced for thinner wafer thickness. This leads to more potential gains in terms of current density for rear light management optimization. Increasing parasitical optical absorption in both front and rear TCOs reduces the response of the cell at higher wavelengths [59]. The optimized rear TCO thickness should be in range of 150 – 200 nm, for acceptably low absorption, high transmittance and effective antireflection on silicon.

High Efficiency Device Schemes

On the way to improve cell efficiency, different device schemes have been studied:

- Front emitter (FE) cell (schematic sketch in Figure 2.3): The window stack requires a careful design both in terms of optical and electrical properties of each layer. Efforts to reduce parasitic absorption consists of optimization of each layer applied at the illuminated side: more transparent TCOs [61], wider band gap materials both for the doped and intrinsic layers [62] which include alloyed a-Si:H and nc-Si:H films or the use of ultra-thin SiO_2 tunnel oxide film as passivation layer [63]. Dopant-free materials as transition metal oxides have recently drawn attention to higher band gap and reduced defects formation in the doped film [64].
- Rear emitter (RE) cell: The device scheme is similar to the one reported in Figure 2.3 but doped layers have an inverted position [15]. For an n-doped c-Si absorber, placing the p-doped emitter remote from the illuminated side (i.e. at the rear) helps to more freely optimize the electrical and contact properties of the emitter with less optical constraints. The n-doped layer in this configuration assumes the role of front surface field (FSF). Simulations lead to the conclusion that, additionally, less stringent restrictions on the optoelectronic properties of the front TCO are required [65].
- Interdigitated back contact cell (IBC): In this configuration, both the emitter and BSF are placed on the rear side using an inter-digitated finger configuration that requires chemical (photolithography) [66] or mechanical patterning [67]. It has the advantage of (i) maximizing the light into the substrate by totally removing shadow losses (no metal grid on the front side), (ii) removing the highly absorbent a-Si:H films at the illuminated side and (iii) a wider degree of freedom in designing the front side since no conductive properties are necessary.

At the moment, the IBC scheme holds the word record efficiency in the category of SHJ solar cells [12]. The performance parameters for the best cells with the different device scheme discussed above are summarized in Table 2.1.

2.3. Hydrogenated Amorphous and Nanocrystalline Silicon Material

Table 2.1. Best cell parameters on n-type CZ (Czochralski) and FZ (Float Zone) c-Si wafers. (IBC: interdigitated back contact, FE: front emitter, TOPCon: Tunnel Oxide Passivated Contact and RE: rear emitter). For Ref. [13] no cell parameters are available.

Ref.	Wafer type (thickness)	Device scheme	Area (cm ²)	J_{sc} (mA/cm ²)	V_{oc} (mV)	FF (%)	η (%)
[13]	n-CZ	IBC	180.4	42.25	744	83.8	26.3
[12]	n-CZ (150 μ m)	IBC	143.7	41.8	740	82.7	25.6
[14]	n-CZ (160 μ m)	FE	151.9	40.8	738	83.5	25.1
[68]	n-FZ (200 μ m)	TOPCon	4.0	42.1	718	83.2	25.1
[9]	n-CZ (98 μ m)	FE	101.8	39.5	750	83.2	24.7
[15]	n-CZ (130-150 μ m)	RE	100.3	39.2	743	80.7	23.4

2.3. Hydrogenated Amorphous and Nanocrystalline Silicon Material

This section reviews the literature concerning amorphous and nanocrystalline silicon material with focus on the film growth by plasma enhanced chemical vapor deposition (PECVD) and the relevant material properties for solar cell applications. The aim is to emphasize the advantages of using a-Si:H and nc-Si:H films but also to deal with challenges and drawbacks concerning the implementation of such layers in devices. The reader is referred to the books by Shah [69], van Sark [41] and Kasap [27], as well as to the references [70–72] for a deep analysis on both materials and their applications in thin film solar cells devices. More details about the PECVD deposition technique and relevant process parameters are given in the next chapter, section 3.1.2.

2.3.1. PECVD Process

Chemical Vapor Deposition (CVD) involves the dissociation and/or chemical reactions of gaseous species activated by a source of energy. The reaction products can promote the deposition of films or coatings. An exhaustive and comparative overview about the process principles, advantages/drawbacks, scientific and technological significance is given in [73].

Among the different variants of CVD methods available to fabricate coating layers, the one that has become relevant in silicon based thin film technology is the plasma enhanced chemical vapor deposition (PECVD) technique. It has the advantages of material fabrication with the opportunity of structural control of the growing film in the nanometer range. Moreover, the method can provide tuning of layer chemistry and thus properties in a wide range at relatively low processing temperatures. PECVD also offers flexibility in that single layers, multilayers and graded films can be grown by controlling the gas species involved in the plasma.

2. FUNDAMENTALS

In a capacitively coupled PECVD system, the glow discharge (plasma) is created by applying an electric field alternating at high frequency between two parallel electrodes. The resulting excited electrons can interact with the precursor gas species forming neutral radicals and ions. A fraction of the radical species are absorbed onto the heated substrate where a reaction occurs at the gas–solid interface resulting in film deposition. To grow dense material, heterogeneous gas-solid interface reactions are preferred over the homogeneous ones that occur in the gas phase which contribute to powder formation. PECVD is a complex process dominated by chemical kinetics and mass transport phenomena. Plasma chemistry studies for the material relevant in this work can be found in the following papers [74–76].

Deposition of Amorphous and Nanocrystalline Silicon Films

Hydrogenated amorphous (a-Si:H) and nanocrystalline silicon (nc-Si:H) can be grown as thin layers on a substrate. Among the methods available, PECVD remains the most widely used. Some of the earliest reports on PECVD deposition of silicon material are those by Sterling and Swann [77] in 1965 for a-Si:H layer and Usui and Kikuchi [78] reported in 1979 for nc-Si:H layer. The deposition occurs by the dissociation of a gaseous silicon source, typically silane SiH₄ (pure or diluted in hydrogen H₂), in a plasma glow discharge. The precursor molecules are subjected to several reactions when they collide with electrons accelerated by an electric field. An extensive analysis of the dissociation species is given in references [74,79,80] with the deduction that the most abundant species in the plasma are SiH₃ radicals. For nc-Si:H growth, the presence of atomic H is essential to allow the formation of nanocrystals. More precisely, with increasing atomic hydrogen (H) within the plasma, a higher crystalline fraction results, indicating that H plays a decisive role in the nc-Si:H evolution [81]. It is common to define the hydrogen dilution ratio (H₂-dilution = H₂/SiH₄) as a relevant parameter for the film growth since both gases are involved and are in a mutual reliance.

2.3.2. Silicon Material Growth and Properties

Hydrogenated Amorphous Silicon

Amorphous silicon material lacks a long-range ordered structure and the atomic arrangement deviates from the crystalline silicon (c-Si) lattice in bonding angles and lengths. It consists of a continuous random network where so-called dangling bonds (DB) or broken Si-Si bonds are formed when some Si atoms or vacancies thereof, disrupt the tetrahedral bonded structure.

Such defective structure strongly affects both electrical and optical properties. While in c-Si, the perfect crystalline lattice causes a well-defined band gap ($E_g = 1.12$ eV), the unsaturated DBs in the amorphous silicon lead to a continuous distribution of energy states (mid-gap states) that act as recombination centers. Consequently, no well-defined band

2.3. Hydrogenated Amorphous and Nanocrystalline Silicon Material

gap exists (forbidden gap) between the VB and CB causing a continuous distribution of density of states. To describe this system, the band gap concept is not properly valid anymore, thus the reduction of mobility within such mid-gap state are used to describe the so called mobility gap of a-Si:H. Typical values are between 1.7 and 1.8 eV depending on film structure and hydrogen content.

As a consequence of the absence of long-range order, the amorphous material becomes a direct band gap material (no- k -selection rule), thus the absorption coefficient of a-Si:H results to be significantly higher than c-Si in the low wavelength region ($\lambda < 700$ nm).

Usually, the PECVD deposition from SiH₄ allows hydrogen incorporation in the growing layer with saturation of DBs [82]. This process is called *passivation of DBs*, hence the material is referred to as hydrogenated amorphous silicon (a-Si:H) to emphasize the crucial role of hydrogen. Nevertheless, even device quality a-Si:H has a residual DBs (10^{15} - 10^{17} cm⁻³). Their density increases after exposure to light and can be partially reversed by annealing treatment under controlled temperatures [83].

PECVD Parameters to Grow High Quality (i)a-Si:H Films

Structural investigations disclosed that PECVD parameters are responsible for (i)a-Si:H quality that leads to reduced passivation performance of c-Si [84]. Several elements can influence the a-Si:H passivation quality with the development of an epitaxial⁴ interface during the amorphous layer growth [85]. The undesirable epitaxial growth of the a-Si:H is enhanced more by <100> c-Si oriented surfaces than by the <111> ones [86–88], consequently the latter should be preferred. Generally, a highly H₂ diluted SiH₄ source gas promotes the transition from fully amorphous to poor quality a-Si:H film [89]. Moreover, the processing temperature is a determinant parameter both as substrate temperature during the deposition (T_{sub}) and as post annealing temperature (T_{ann}). Higher T_{sub} increases the absorption fraction and the diffusion length of the species from the gas onto the film-growing surface. Therefore, the thermal H removal process increases the defect density formation during the film growth [27]. However exposing the a-Si:H material to a post annealing treatment may significantly improve the surface passivation performance of epitaxial free a-Si:H [90] because of defect reduction in the film close to the interface. It is probably caused by atomic hydrogen effusion thanks to the temperature that helps to passivate the unsaturated DBs [91]. On the contrary, a film of a poor quality degrades when it is thermally treated [92]. Finally, the incorporation of hydrogen by careful post deposition hydrogenated plasma treatments [33] or layer-by-layer technique [32] may improve the passivation of high quality films drastically. These aspects will be further discussed in the experimental section 4.1.

⁴ The term epitaxy is usually referred to the formation of a crystalline overlayer that develops on a crystalline substrate. In this work, the presence of epitaxy in the a-Si:H film, has a negative context since leads to reduced passivation quality in a-Si/c-Si HJ cells [84].

Hydrogenated Nanocrystalline Silicon and Nanostructure

Hydrogenated nanocrystalline silicon has a complex structure composed of a crystalline phase embedded in an amorphous phase (a-Si:H) and may sometimes include voids [93]. The original application of this layer is as an absorber in thin film solar cells and complete overviews are given in [70,71]. In literature, the material is often referred to as microcrystalline silicon ($\mu\text{c-Si:H}$) and more recently as nanocrystalline silicon (nc-Si:H). In the following, we refer to the latter term since the nano size is closer to the structure experimentally fabricated in the a-Si:H/c-Si device. The optoelectronic properties strongly depend on the phases and the relative fractions among them.

Similarly to the a-Si:H, hydrogen atoms play an important role in the growth of and quality of nc-Si:H material. They are preferentially located in the amorphous phase or at the grain boundaries due to the low solubility of H into the crystalline phase [94], contributing to passivation of dangling bonds.

Depending on the deposition parameters, the material can show a wide range of structure evolution from fully amorphous to highly crystalline [93,95,96]. Figure 2.5 shows the growth model of nc-Si:H film on a substrate based on a four stages approach as suggested by Cabarrocas *et al.* [97] and later confirmed by *in situ* ellipsometry studies [98,99]. They identified a critical a-Si:H film thickness which is believed to control the transition from amorphous to nanocrystalline regime. This critical layer is commonly referred to as the incubation zone (IZ) and it affects the evolution and, consequently, the properties of the entire film. Afterwards, the nanocrystalline phase increases progressively until the growth becomes stationary.

The nanocrystalline evolution depends on several interdependent factors:

- *Deposition parameters*: the H_2 -dilution is the most relevant deposition parameter for nc-Si:H evolution. It has been found that the thickness of the IZ decreases for increasing the H_2 -dilution ratio. Koh *et al.* [98] reported a case in which the IZ extended for hundreds of nanometers.
- *Substrate selectivity*: The substrate chemical nature has a strong influence on the IZ and therefore on the properties of the entire film. Several substrates have been investigated in literature such as c-Si [97,100], glass [100,101], (i)a-Si:H [97,98,100,101], SiO_2 [98,100,102], TCOs [102–104], Si_3N_4 [105] and polymer [106].
- *Thickness of the film*: As mentioned above, the strong directional growth of nc-Si:H film makes the crystalline fraction variable along the film thickness. This aspect also influences the electrical and optical properties of the layer until the incubation/nucleation zone has been overcome [101,107,108].
- *Doping gas*: p- or n- doped nc-Si:H films can be obtained by adding doping gases to the precursor mixture. Different doping gases have a different effect on the structural properties [109] as well as on the optical characteristics [110].

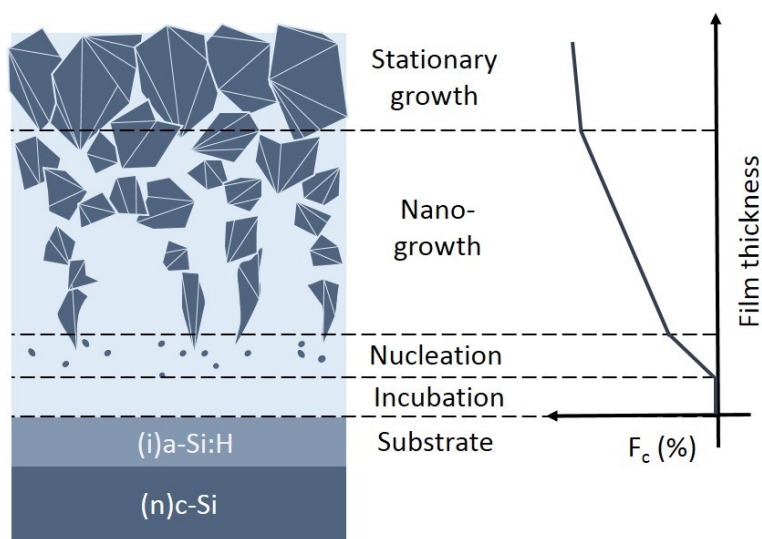


Figure 2.5. Schematic view of the structure of nanocrystalline silicon adapted from [97]. In this case, depicting the growth of nc-Si:H on an (i)a-Si:H template covering a c-Si wafer. The evolution of the nc-Si:H phase (F_c) is depicted as function of the film thickness.

For HJ solar cell application, the film is required to have a reduced thickness (typically in the range of 10 - 50 nm). Due to the directional evolution and the initial stages of growth, the material properties can widely vary within such reduced thickness. Moreover, the film has to grow on the (i)a-Si:H passivation layer that represents the substrate in the cell structures as depicted in Figure 2.5. It was demonstrated that (i)a-Si:H induces a thicker IZ and, subsequently, delays the stationary growth and reduces crystalline fraction in the bulk of the film [97].

In the literature, various strategies have been suggested with the aim of controlling the IZ thickness and the properties of the growing nc-Si:H layer to obtain fast nucleation. Alternative precursors gas have been proposed in literature, such as the use of SiF_4 or Si_2H_6 as silicon source instead of SiH_4 or deuterium in addition to H_2 [111]. To further enhance the development of the crystalline phase, some studies proposed an insertion of an undoped thin nc-Si:H that acts as “seed” layer to reduce the IZ thickness [15,112,113]. Others report on (i)a-Si:H treatment to modify the surface and facilitate the start of the nucleation regime. The most common method is by means of H_2 plasma treatment (HPT) [110,114]. The H presence leads to disorder-to-order transitions via hydrogen-induced crystallization [115]. Nevertheless CO_2 plasma treatment (CO_2PT) or air exposure have been applied at the amorphous/nanocrystalline interface [114] and the beneficial effect has been reported in thin film silicon devices [114,116–118]. Such treatment results in SiO_x formation as indicated by Pernet *et al.* [119].

For SHJ devices, the choice of the appropriate method depends on different aspects such as possible damage of the thin amorphous layer or the interface to the c-Si due to etching and/or ion bombarding. Moreover, the use of an undoped seed layer can lead to additional current losses when the stack is applied on the illuminated side of a cell device whereas the post deposition plasma treatment only changes the i-layer interface without the necessity to deposit additional film.

Growth Models

In literature, the mechanisms to explain the nanocrystalline evolution are usually classified as surface and sub-surface models as discussed below.

The most commonly accepted mechanism for the a-Si:H growth is the surface diffusion model [81,120] that identifies SiH₃ radicals as the leading chemical precursor for a-Si:H growth due to their high density in the plasma [74,79,80]. A certain fraction of SiH₃ in the gas phase interacts with the growing surface by means of adsorption⁵ and afterwards they diffuse across it experimenting different reactions. Some SiH₃ radicals might react over the surface by hydrogen abstraction or by dimerization of two radicals forming SiH₄ and Si₂H₆ molecules, respectively. Both reactions do not contribute to the film growth directly since the silicon leaves the surface creating vacancy terminated site called dangling bond (DB). Such open terminations are necessary for the layer growth. Once the SiH₃ reaches the opened termination, a Si-Si bond is formed contributing to the layer deposition. The diffusion model is often extended to nc-Si:H growth with the following additional hypothesis: (i) the H₂-dilution ensures a sufficient H supply for a full H coverage of the substrate surface and (ii) hydrogen reactions contribute to a local heating. The effect is an improved surface diffusion of the SiH₃ precursor onto the surface with higher probability of nuclei formation in energetically favorable sites [121].

The *etching model* was proposed by Tsai *et al.* [122] to explain the experimental observation that the dilution of silane in hydrogen is related to the growth of nanocrystalline material accompanied by a reduced deposition rate with increasing H₂-dilution. The hydrogen atoms are supposed to impinge on the growing surface with a sufficient energy to break weak Si-Si bonds in the amorphous structure. An arriving SiH₃ precursor reacts in this site forming a stable Si bond. Interestingly, this model indicates a simultaneous interaction of two processes: etching of the a-Si:H phase and nc-Si:H deposition.

The *chemical annealing model* suggested by Nakamura *et al.* [123] is based on the role of atomic hydrogen in the nc-Si:H growth. The chemical annealing model has been experimentally supported by the layer-by-layer technique that involves alternating of thin a-Si:H film and a subsequent hydrogen plasma treatment (HPT). The HPT contributes to the

⁵ *Adsorption* is a surface-based phenomenon and involves adhesion of species from a gas, liquid, or dissolved solid to a surface. This process creates a film of the adsorbate on the surface of the adsorbent. The reverse process is called *desorption*.

permeation of H into the subsurface region with crystallization of the amorphous network and without any etching process. The atomic-scale mechanism that results in H-induced crystallization is explained by [115]. Hydrogen atoms are involved in an induced disorder-to-order transformation by chemical reaction of H with Si-Si bonds followed by rearrangements and strain reduction in the a-Si:H network.

Doped and Alloyed a-Si:H and nc-Si:H

a-Si:H can be defined as an isotropic material, whereas nc-Si:H has a strong anisotropic character due to the coexistence of two phases (see Figure 2.5). This implies that the material properties are influenced by the specific microstructure and they can be tuned by the relative fraction of amorphous/crystalline phase.

Device quality intrinsic a-Si:H ((i)a-Si:H) exhibits an insulator character with a dark electrical conductivity (σ) less than 10^{-10} S/cm. Nevertheless, Spear and Le Comber [124] demonstrated that a-Si:H can be doped by adding phosphorus or boron gas to the precursor mixture during deposition. Both a-Si:H and nc-Si:H are easily n-type or p-type doped. The doping level depends on type and amount of impurity atoms inserted into the network that are responsible of increase in defects [125]. Typical σ values measured in dark for a n-type a-Si:H material are up to 10^{-1} S/cm and for p-type a-Si:H 10^{-2} S/cm [124].

The doping impurities in nc-Si:H films are preferentially located in the crystalline phase, since the doping efficiency of the c-Si is higher than the a-Si:H. The resulting σ increases up to several orders of magnitude. It is worth mentioning that for nc-Si:H, one should distinguish between parallel and perpendicular σ [126] as consequence of the nanostructure depicted in Figure 2.5.

N-doped amorphous and nanocrystalline films exhibit higher conductivities than the p-doped ones. This depends on the following observation that can be considered valid both for amorphous and nanocrystalline films. Substitutional boron can only coordinate three Si atoms, so the fourth creates a dangling bond. H would then passivate the unsaturated bonds with formation of the B-H-Si complex leading to an electrically inactive dopant [127].

Optical properties are relevant in device application and they can be varied in a wide range by hydrogen content, doping and/or alloying with atoms such as oxygen or carbon [128–131]. Figure 2.6 shows experimental extracted absorption curves for four hydrogenated silicon films compared with the c-Si (taken from Ref. [132]). a-Si:H absorbs more the light, whereas nc-Si:H exhibits optical properties closest to the c-Si especially in the visible part of the spectrum (higher photon energy). The doping atoms usually shift the optical band gap to lower energies for a-Si:H films [133], whereas the presence of oxygen widens the band gap (see Figure 2.6).

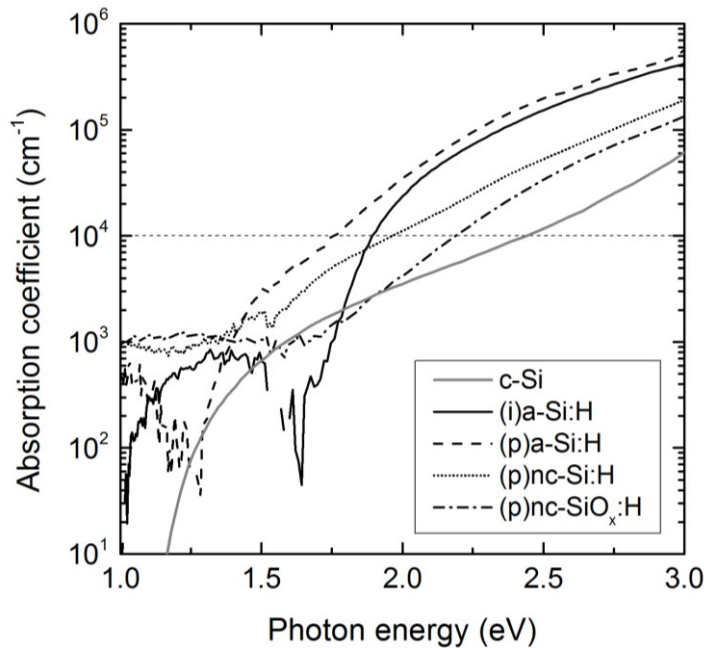


Figure 2.6. Absorption coefficient as function of photon energy for (i)a-Si:H, (p) a-Si:H, (p)nc-Si:H and (p)nc-SiO_x:H. The curves were experimentally determined as described in section 3.2, whereas the data for the c-Si reference are taken from literature [132].

Silicon-Oxygen Alloys

Silicon-oxygen alloy films are fabricated using PECVD by adding a source of oxygen (e.g. CO₂ or N₂O) to the gas mixture. By adjusting the deposition parameters, the material structure and the stoichiometry can be tuned in a wide range. In a fully amorphous film (a-SiO_x:H), the oxygen content is responsible for the widening of the optical band gap but with a consequently reduced conductivity. The main drawback of oxygen addition is that the reduced doping efficiency giving lower σ for a-SiO_x:H than the a-Si:H as reported by Janssen *et al.* [129]. Alloying is often related to an increase in defect density associated to enhanced dangling bond concentration [134].

As compared to the non-alloyed material, nc-SiO_x:H combines two functions: enhanced optical properties due to the oxygen into the matrix and a sufficient electrical conductivity given by the crystalline fraction [135]. The possibility to combine both characteristics makes this material suitable for application as a window layer for solar cells. The microstructure model is similar to the one discussed above for the nc-Si:H [136] with the difference that the amorphous matrix is composed by a-Si:H and/or a-SiO_x:H phase as suggested by Richter *et al.* [137].

2.4. Specific Limitations in SHJ Solar Cells Fabrication

In order to fabricate SHJ, the a-Si:H/c-Si device interface is extremely sensitive to subsequent depositions and/or harsh treatments that can jeopardize it:

- *Effect of temperature exposure:* Post annealing treatments are known to significantly improve the passivation performance of device quality a-Si:H and the open circuit voltage. The T_{ann} and time of treatment have to be chosen carefully. The thermal energy allows H to migrate (H effusion) within the silicon [91] and passivate DBs (as discussed above). However, temperatures above 250 °C are detrimental for the film as they rupture the Si–H bond but also doping and film thickness are relevant parameters [90,91]. This limit implies that any further process performed to the complete device has to be set accordingly.
- *Effect of plasma treatment:* PECVD processes involve both deposition and (unintentional) etching. An appropriate example can be given by the HPT discussed above where a careful choice of plasma parameters can result in a reduced DB density at the (i)a-Si:H/c-Si interface. The etching process can be detrimental for passivation and a minimum (i)a-Si:H film thickness is required to shield the c-Si surface from plasma damage [138].
- *Effect of TCO sputtering:* The sputtering of the TCOs can impact the (i)a-Si:H/c-Si interface and the carrier transport. The reasons seem to be multiple and not fully understood yet but the damage appears to be mostly reversible under annealing at low temperature [139]. On the contrary, other experimental evidence suggests that the causes may reside in the TCO/a-Si:H contact that further varies with the doping type of the layer underneath. Specifically, the mere removal of the TCO layer and cyclic annealing treatments have been reported to result in complete recover of the passivation quality [139].

3. Experimental Methods

This chapter describes the processes and tools used for thin-film deposition and the device structures explored in this work (section 3.1). Section 3.2 describes the methods used for layer and device characterization.

3.1. Cell Preparation Process

Heterojunction solar cells fabrication requires several subsequent process steps starting with the choice of the silicon wafer until the metal grid contacts. The schematic process flow is depicted in Figure 3.1.

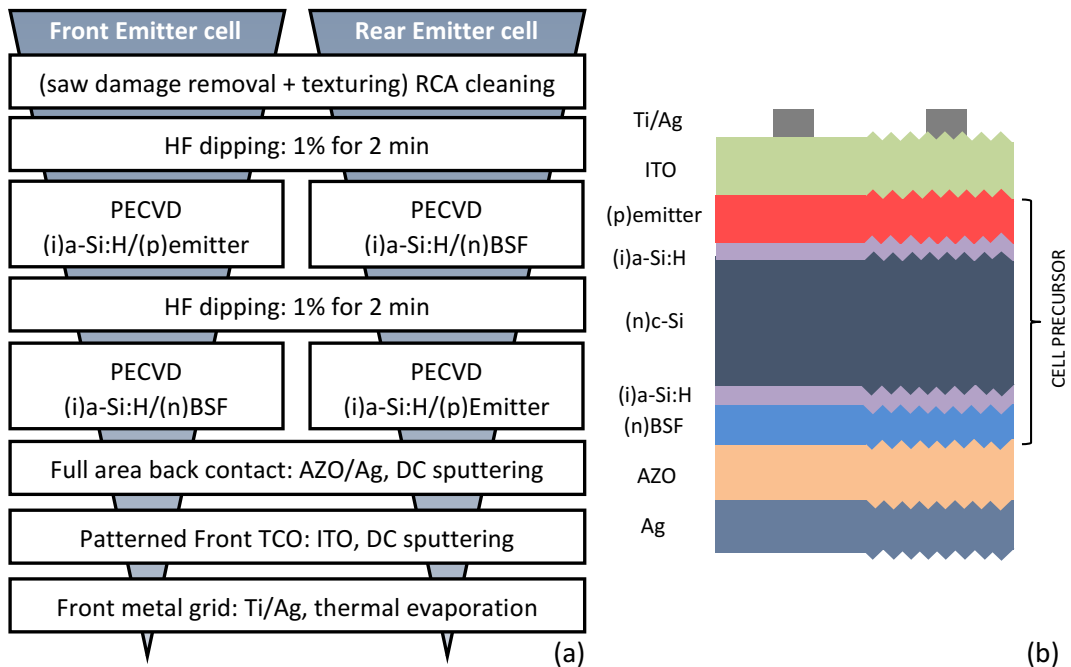


Figure 3.1. (a) Fabrication process flow for front and rear emitter devices. (b) Cross-sectional view of a solar cell in front emitter configuration (not to scale).

3. EXPERIMENTAL METHODS

Single layers or multi-layer stacks were fabricated on two types of substrates: glass substrates for single-layer characterization and silicon wafers. Usually 30 x 30 cm² float glass panels (3.2 mm) or 10 x 10 cm² corning glass (1.1 mm) were previously cleaned with a detergent and deionized water to remove grease and loose particles. c-Si wafers were conditioned as described in the next section for device fabrication.

3.1.1. Silicon Wafer Preparation

All solar cells were fabricated on wafers based on n-type monocrystalline silicon produced by the Float Zone (FZ) growth process. Both as-cut and double-side polished wafers were used in this work. The material specifications are summarized in Table 3.1.

Table 3.1. Specifications of silicon wafers used for this work (supplier: TopSil).

Fabrication process	Float Zone
Size	4 inch
Doping	n-type
Crystal orientation	<100> and <111>
Thickness	270 μm
Specific resistivity	3 $\Omega\text{ cm}$
Bulk lifetime	> 6 ms
Surface morphology	Polished and as-cut

The as-cut wafers were further processed to create a surface texture for light trapping (section 2.2.3). The most common surface morphology in the silicon solar cell technology is a random pyramidal texture. It involves a wet-chemical process composed of two steps: (1) saw-damage removal in KOH and (2) texturing using a proprietary IPA-free KOH solution ("Alkatex Zero" by GP Solar). Further details concerning the experimental procedures used in our laboratory are in Ref. [140]. The resulting pyramids had a height of up to 5 μm with a <111> facet orientation. The wafer thickness was reduced down to about 230 μm . Figure 3.2 shows the appearance of a typical wafer surface after the texturing process.

After texturing a conditioning (cleaning) of the silicon surfaces is crucial to avoid recombination losses of charge carriers at the hetero-interfaces, as discussed in section 2.1.2. Prior to the first PECVD process, the wafers were cleaned by the RCA [141] procedure and dipped in 1% HF for few minutes to remove the native oxide. Wet-chemical conditioning of wafer surfaces influences the electronic interface properties is reported in [41] both for textured and polished silicon wafers.

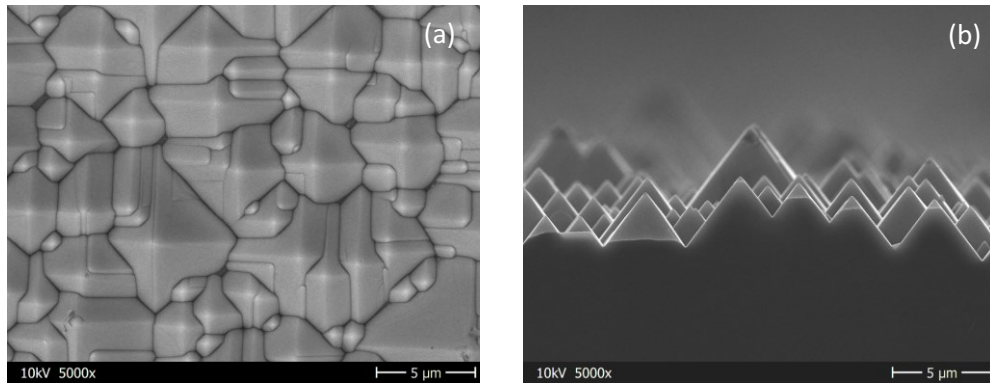


Figure 3.2. SEM images of a textured wafer surface (a) top and (b) cross sectional view.

3.1.2. Silicon Deposition by PECVD

The PECVD system (AKT1600, by Applied Materials) used for the work described here is an industrial multi substrate processing system with three independent chambers (Ch A, B and D) arranged around a central transfer module accessed by a loading chamber equipped with six substrate slots (Figure 3.3 (a) [142]). The plasma excitation radio frequency (RF) is 13.56 MHz. The tool allows a high degree of automation and simultaneous deposition processes. The software permits the definition of deposition sequences for growing several subsequent layers on the same substrate/carrier and additionally pre- and post-deposition to avoid cross contamination (this aspect is further discussed below). The use of carriers is necessary to allow for deposition on samples with size smaller than the 30 x 30 cm², such as wafers. Aluminum carriers were designed to carry up to four wafers of 4 or 5-inch size or glass substrates of equivalent area in one processing run.

Figure 3.3 (b) depicts a schematic cross-sectional view of the PECVD chamber made of two parallel electrodes [142]. The top electrode (area of 2500 cm²) is powered by an RF generator via a matchbox. In the course of this work RF power density is related to this area. The grounded bottom electrode (susceptor) with an area of 1600 cm² carries the substrate and is heated in the range of room temperature to 400° C. It can be vertically moved in order to vary the electrode spacing. The source gases enter the deposition chamber via the RF showerhead electrode to ensure a homogeneous gas distribution.

3. EXPERIMENTAL METHODS

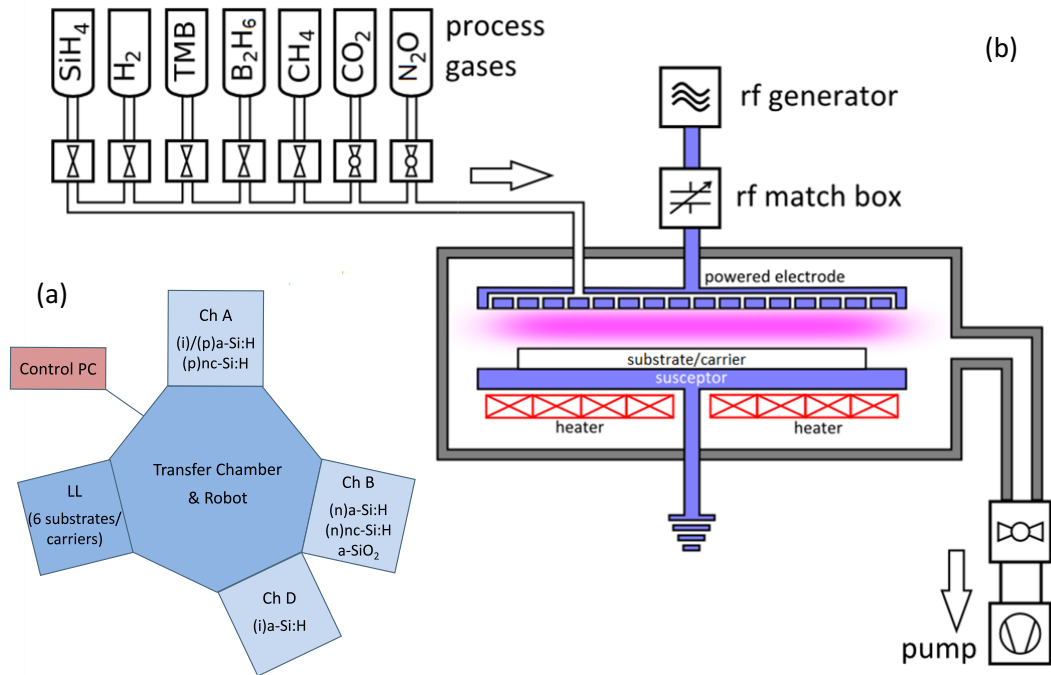


Figure 3.3. (a) Schematic view of the 3-chambers AKT1600 tool and (b) cross sectional view of a PECVD process chamber [142].

Contamination is critical problem in PECVD processes and can originate from previous depositions on chamber walls, electrodes and the carrier/sample surfaces. The deposition conditions specifically required for the nanocrystalline growth involve a high plasma power and hydrogen dilution which causes etching from surfaces. Therefore, pre-conditioning of chamber walls and carriers is a method to minimize incorporation of undesired species into the growing film. The standard procedure before each deposition of both chambers and carriers is: to “clean” with a mixture of nitrogen trifluoride (NF₃) and argon (Ar) until the previously deposited layers are etched away and subsequently to “season” it with a covering film. Usually the carrier is seasoned with an intrinsic a-Si:H layer and the chamber with the layer we intend to deposit afterwards. Studies on the importance of chamber conditioning and effect of cross-contaminations on devices can be found in references [142,143].

To avoid the presence of impurities due to different doping precursors, an additional method is to dedicate, when possible, each deposition chamber for a dedicated type of material (i.e. intrinsic and p- or n-doping type) as indicated in Table 3.2 in our deposition tool.

A summary of the precursor mixtures used to grow different types of materials used in this thesis are listed in Table 3.2. Alloy and doping gases were diluted in H₂ at 2%. Initially, reference emitter film, doped with diborane (B₂H₆) precursor gas, were grown in a separate PECVD tool manufactured by FAP GmbH operating at 60 MHz with an electrode size of 531 cm². The AKT1600 tool was later upgraded with a B₂H₆ gas line.

Table 3.2. Process gas mixture to grow by PECVD the amorphous and nanocrystalline materials used in this thesis.

Material	Process gas mixture			Chamber
	Basic gas	Alloy gas	Doping gas	
(i)a-Si:H, (i)nc-Si(O _x):H	SiH ₄ + H ₂	CO ₂	/	D, A
(p)a-Si:H, (p)nc-Si:H	SiH ₄ + H ₂	-	B(CH ₃) ₃ or (B ₂ H ₆)	A
(p)nc-SiO _x :H		CO ₂		
(n)a-Si:H, (n)nc-Si:H	SiH ₄ + H ₂	-	PH ₃	B
(n)nc-SiO _x :H		CO ₂		
a-SiO _x	SiH ₄ + H ₂	N ₂ O	/	B

Since both sides of a wafers have to be passivated and contacted, two deposition runs were carried out, one on each side, i.e. the (i)a-Si:H passivation layer and the n- or p-doped contact film (Figure 3.1 (a)). For each side, the (i)/(n) and (i)/(p) layer stack is deposited without vacuum break, which would expose the buffer layer surface to the atmosphere and thus lead to oxidation. The reference PECVD process consisted of the i/n stack deposition first and, after a second HF dip, the wafer was processed with the i/p films on the other side. For the processing of each wafer side two different carriers were used, cleaned and seasoned as described above. Samples with both sides coated in this way are defined as *cell precursors* in this work.

Table 3.3 provides an overview of the layers optimized in this work. The deposition time of layers was adjusted to reach the desired thickness. For the textured morphology, a geometrical correction factor of 1.7 with respect to deposition on flat substrates was used to account for the lower growth rate due to the layer deposition on the tilted pyramidal facets.

3. EXPERIMENTAL METHODS

Table 3.3. Overview of intrinsic and doped silicon layer PECVD deposition sequences with process details and nominal thickness calculated on textured substrates with a corrective factor of 1.7.

Deposition sequence	Chamber	Temperature (°C)	Material	Thickness (nm)
1	A (or D)	205 (or 190)	(i)a-Si:H	7 (or 5)
	B	185	(n)a-Si:H	8
			(n)nc-Si:H	15
			(n)nc-SiO _x :H	20-40
2	A (or D)	205 (or 190)	(i)a-Si:H	7 (or 5)
	A	205	(p)a-Si:H	8
			(p)nc-Si:H	15
			(p)nc-SiO _x :H	30

3.1.3. TCO and Metal Contact Deposition

The next steps are the cell electrode fabrication as depicted in Figure 3.1. Transparent conductive oxides (TCOs) and Ag films were grown by using a large-area, inline DC sputtering tool (Model A600V7) from Leybold Optics.

At first, a 80-nm thick aluminum-doped zinc oxide (ZnO:Al, AZO) film was sputtered at room temperature from a ceramic AZO target (1-wt.% Al₂O₃ doped ZnO) in an argon/oxygen mixture. Afterwards, an Ag film was grown by means of the same technique using pure argon with a thickness of 200 nm. This layer stack acted both as reflector and as back contact. Then, the front TCO layer was deposited from a 10 wt.% SnO₂ doped (In₂O₃:Sn, ITO) sputter target at a set temperature of 220 °C with a nominal thickness of 80 nm.

The front electrode was patterned using either shadow masks or by photolithography. In the first technique, the ITO layer was deposited through a shadow mask placed on the wafer defining 7 squared cells with an area of 2 x 2 cm². With photolithography, the ITO layer covered the full wafer surface first and, subsequently, 12 cells with an area of 1 x 1 cm² each were defined by wet etching the TCO layer.

Finally, the front contact consisted of a Ti/Ag grid deposited by thermal evaporation through a shadow mask followed by a thermal annealing at 160 °C. The schematic picture of both grid schemes is presented in Figure 3.4. Depending on the structuring procedure used, one of the following grid design was selected:

- 2 x 2 cm² cells: 16 equally spaced fingers and a central tapered busbar (Figure 3.4 (a-c)) with the Ag layer being 3 μm thick.

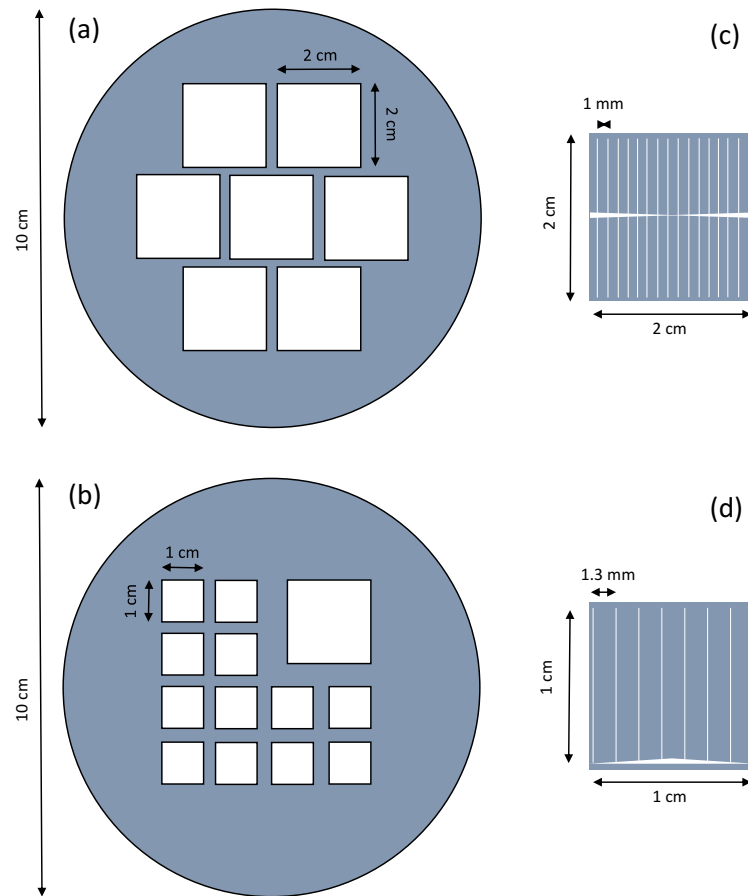


Figure 3.4. (a-b) Top view of a 4 inch wafer with two types cells design. (c-d) show the front metal grid design for $2 \times 2 \text{ cm}^2$ and $1 \times 1 \text{ cm}^2$ cell sizes, respectively.

- $1 \times 1 \text{ cm}^2$ cells: 8 equally spaced fingers and a single busbar (Figure 3.4 (b-d)) with an Ag film thickness of $1.5 \mu\text{m}$.

The analysis of cell parameters for both grid schemes and optimization of the $2 \times 2 \text{ cm}^2$ design are reported in [144].

For rear emitter device, a rear-side patterning was required. For that purpose, a double-sided mask was designed to allow for the alignment of the cell-area patterning of the rear AZO/Ag stack and the front ITO layer.

3.2. Characterization Methods

This section describes the methods used to characterize materials and solar cells. Section 3.2.1 addresses characterization techniques to investigate optical, electrical and structural properties of single layers and film stacks. Section 3.2.2 gives an overview on the used methods to characterize solar cells and cell precursors.

Table 3.4 gives an overview on the different types of single and multi-layer stack samples fabricated with details about substrate type, film thickness and characterization method.

Table 3.4. Overview of the different types of samples fabricated for material characterization and optimization. Details concerning substrates, layers structure and thicknesses are specified. Additional information is given in the experimental chapters.

Substrate type	Layer structure	Thickness (nm)	Characterization technique
Float glass	Single	150-300	UV-Vis spectroscopy Raman spectroscopy Conductivity
Float glass	Single or stacks	< 50	Raman spectroscopy Conductivity
c-Si	Single	150-250	FTIR spectroscopy
c-Si	Single or stacks	< 50	Carrier lifetime Spectral Ellipsometry UV-Vis spectroscopy

3.2.1. Thin Film Characterization

Thickness Measurements

The precise determination of film thickness is relevant for several practical aspects, such as the calculation of the deposition rate and material properties that depend on that parameter (i.e. optical and electrical properties). The easiest way to evaluate the thickness of a layer is by profilometer where a stylus is moved in contact with the sample surface and then moved across it. The presence of the needle in contact with the film surface could damage it especially when the layer is only a few tens of nanometers thick. Additionally, the sample preparation could be problematic since a stepped edge

(substrate/substrate + film) has to be created, for example by covering a small part of the substrate with a tape stripe before the layer deposition or etching away part of the film. Both methods could alter either the layer, due to the etching solution, or reduce accuracy, due to incomplete removal of the film under study. Among the drawbacks, it should also be mentioned that in case of a stack of layers the method is only suitable for measuring the sum of them and not the thickness of each film.

A more reliable and practical method for determining film thickness in case of many samples is by optical measurements, for instance ultraviolet–visible spectroscopy and ellipsometry. The method is non-destructive, fast and both thickness and optical properties can be extracted on the same measured spot (see next section for more details about tools and model used). Moreover, a wider range of film thickness is accessible (down to a few nanometers). The measured data has to be further analyzed by fitting with a proper model, as described below. Since the available methods and equipment were only suitable for flat surfaces, a corrective geometric factor of 1.7 was assumed [145] to deposit the film with the same nominal thickness on textured c-Si morphology.

Optical Measurements

Optical properties determination is crucial for thin film semiconductor development and their characterization may be achieved by numerous methods. The choice of the specific technique depends on material category, layer thickness, substrate nature and properties of interest.

In this thesis, optical characterization of amorphous or nanocrystalline material was performed by ultraviolet–visible-near infrared (UV-Vis-NIR) spectroscopy on single layers grown on glass substrates.

Two spectrophotometer setups are available at PVcomB:

- Avantes spectrometer equipped with deuterium and halogen lamps. The main advantages of this tool are the opportunity to measure reflectance $R(\lambda)$ and transmittance $T(\lambda)$ on the same spot and to monitor the layer homogeneity by mapping large area samples (substrates up to 30 x 30 cm²) measuring up to 9 points consecutively.
- Perkin Elmer spectrophotometer (Lambda 1050) equipped with deuterium and halogen lamps, a monochromator and an integrating sphere allowing measurements from 170 to 3300 nm wavelength. This tool gives higher accuracy.

Spectral ellipsometry (SE) using an instrument (model type SE 850 from Sentech) was instead used for the amorphous silicon oxide films due to the ultra-thin layer deposited and the requirement of c-Si wafer as a substrate and to detect the etching rate of plasma treatments performed on (i)a-Si:H films. This technique detects the change in polarization

3. EXPERIMENTAL METHODS

state of light after reflection on the surface of study performed at variable angles on incidence.

Since both methods (spectrophotometry and SE) are indirect techniques, models are needed to interpret the measured spectra and to extract the physical parameters of the layers (i.e. thickness, optical properties, optical constants and absorption coefficient) using the analysis software SCOUT [146] and SpectraRay3, respectively. Optical functions of the materials investigated are parametrized using the transfer matrix algorithm to describe the interactions of light in multilayer structures [147]. The fitting procedure of simulated optical transmittance and reflectance curves to the experimental data allows the extraction of both thickness and optical properties. A specific optical model had to be chosen depending on the material to be analyzed: the Tauc-Lorentz (TL) model is typically applied to amorphous and nanocrystalline silicon semiconductors and the Cauchy model to dielectric materials.

Several methods are proposed in literature for deriving the optical gap energy from the absorption coefficient α [69]. Among them, the most common used are the Tauc optical band gap E_{Tauc} by extrapolation procedure, described elsewhere [148], and the empirical optical band gap E_{04} [69]. The latter is defined as the photon energy where the absorption coefficient is equal to 10^4 and was used in this work as approximated value for the optical gap.

Conductivity Measurements

The electrical conductivity (σ) of thin semiconductor layers was measured by depositing coplanar metallic contacts of defined geometry onto the film surface. For this purpose, thicker films (in the range of 150 - 300 nm) were deposited on glass substrate and two mercury stripes (with defined length and relative distance) temporarily covered the sample area under investigation. The samples were in the dark and at room temperature during the measurements.

Fourier Transform Infrared Spectroscopy (FTIR)

Fourier transform infrared (FTIR) spectroscopy was used to investigate silicon oxides film developed in this thesis and to obtain information about the influence of the PECVD gas precursors on the film stoichiometry and material quality. Single layers were grown on polished wafers with a thickness of 150 - 250 nm.

Transmission spectra were measured under nitrogen purging at room temperature with a spectral resolution of 4 cm^{-1} and with 32 scans averaged per spectrum by using a Bruker Tensor 27. The measured data were corrected for atmospheric absorption using the OPUS 7 software and the transmittance curves were fitted using an optical model that simulates the samples stack to extract the absorption coefficient using SCOUT software [146] (Figure 3.5 (a)). Library data were chosen for c-Si and native oxide, while the investigated layer was modeled as a constant dielectric background overlaid with Brendel oscillators to

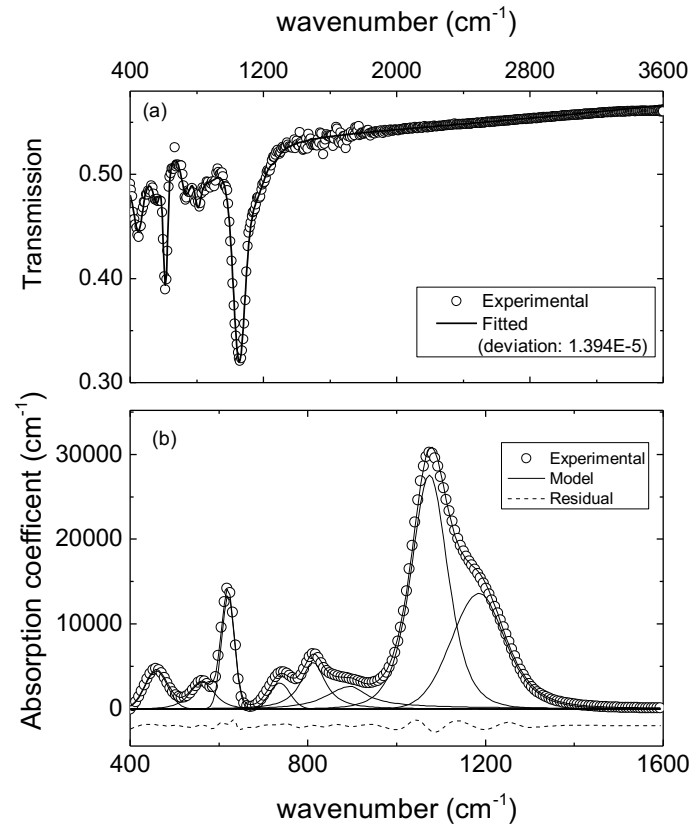


Figure 3.5. (a) Measured FTIR transmission (symbols) and corresponding fits (solid line) as a function of wavenumber for the a-SiO_x:H. (b) Absorption coefficient curve (symbol) for the same a-SiO_x:H layer, modeled curve (solid line) and fitting residual (dashed line, shifted for clarity). The thin lines are the corresponding contributions of the Pearson7 peaks. Details about deposition parameters are given in section 7.2.

describe the different vibrational modes. Thereafter, each peak component of the modeled curve was fitted with a function (Pearson7) using the Fityk software [149] to extract the peak positions as well as the peak area integrals (Figure 3.5 (b)). The last part of the analysis involved identifying the vibration modes for the relevant molecular groups by comparing to literature data (Table 3.5).

The IR absorption intensity (I) of each modes was calculated using the following relationship [150]:

$$I = \int \frac{\alpha(\omega)}{\omega} d\omega \quad (3.1)$$

where α is the absorption coefficient and ω the wavenumber.

3. EXPERIMENTAL METHODS

I is proportional to the bond densities associated to each molecular group ([Si-O], [Si-N], [Si-H] or [Si-N]) through experimental proportionality constants A , as reported in [150–155] and summarized in Table 3.5.

Table 3.5. Molecular bonds and relative vibration modes of interest, assigned peak position (cm^{-1}) and proportionality constants A (cm^{-2}).

Molecular bond (vibration modes)	Peak position (cm^{-1})	Proportionality const. A (cm^{-2})	[Ref]
Si-O-Si (rocking)	465	-	[153]
Si-H, SiH ₂ (wagging)	640	2.10E+19	[150],[155]
Si-O-Si (bending)	781-800	-	[153]
Si-O (bending)	800, 805	-	[153]
Si-H ₂ (bending)	840, 890	2.00E+20	[155]
Si-N (stretching)	830-900, 970	2.07E+19	[151],[154]
Si-O (stretching)	1070	1.48E+19	[152],[153]
Si-O (asym. stretching)	1100	1.48E+19	[153]
N-H wag rock	1150, 1170	2.07E+19	[151]
N-H ₂ (bending)	1530-1550	3.80E+20	[151]
Si-H (isolated stretching)	2000	9.00E+19	[150],[155]
(Si-H) _n , cluster stretch	2100	2.20E+20	[150],[155]
Si-H(N ₂ Si)	2260-2356	2.00E+20	[151]
Si-H(N ₃)	2300	2.00E+20	[151]
N-H, stretching	3300-3340	1.20E+20	[151]

Structural Properties

Several techniques are available for investigating the structural properties of a material. In the following, three of them used during this work are presented.

Raman Spectroscopy is used to investigate structural properties of nanocrystalline layers. The technique is based on the interaction of incoming photons with the bonds of the material causing vibrations (phonons). The difference in energy between the incoming/escaping photons is detected and results in an energy shift (Raman shift). For monocrystalline silicon, a sharp peak at shift of 520 cm^{-1} dominates the Raman spectrum, whereas for amorphous silicon material a broad Raman scattering signal centered at 480 cm^{-1} is detected. As discussed previously in section 2.3.2, nanocrystalline material is a two phase system therefore this leads to a superposition of both peaks [156].

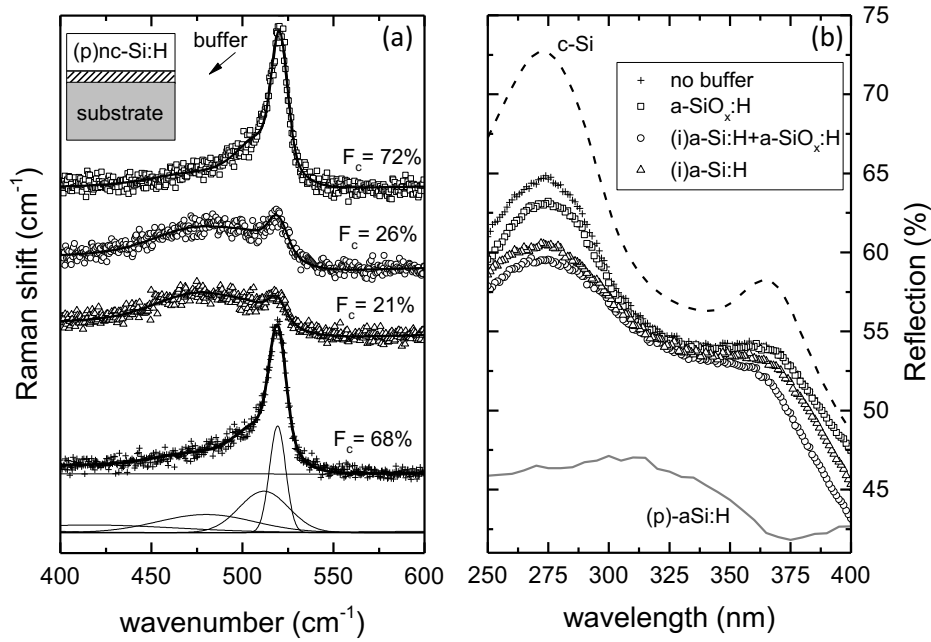


Figure 3.6. (a) Measured Raman spectra (symbols) and fitted curves (thick lines) for four layers stacks as function of wavenumber. The films were deposited on glass substrates coated with a variable buffer layer and a nominally 25 nm thick (p)nc-Si:H film. The correspondent crystalline fraction F_c is also reported for each spectra. The curves are vertically shifted for easier comparison. Hairlines are an example of the Gaussian peaks for the sample without buffer layer. Experimental setting used were laser wavelength 442 nm, 120 s exposure time and 5 accumulations. (b) Reflection spectra for the same layer stacks reported in (a) deposited on polished c-Si substrates. (p)-a-Si:H and c-Si curves are also reported for comparison. A sketch of the samples is depicted in (a). Additional information concerning the layer properties and discussion is given in section 7.3.

The measured Raman spectra were deconvoluted into six Gaussian peaks to calculate the intensity of the wide distributed peak at 480 cm⁻¹ I_a (deconvolution of four peaks) and the crystalline peak at 520 cm⁻¹ (deconvolution of two peaks) as shown in Figure 3.6 (a). The Raman crystalline volume fraction F_c follows from the intensity ratio equation:

$$F_c = \frac{I_c}{I_a + mI_c} \quad (3.2)$$

where m is a corrective factor which was recently determined by [157] and fixed at 1 in this work.

The excited volume of the investigated sample depends both on the laser light used and film composition. At wavelength of 520 nm, for example, the absorption depth of c-Si and a-Si:H are 1 μ m and 100 nm, respectively (see absorption coefficient spectra depicted in Figure 2.6). This leads to a Raman collection depth between 500 nm (c-Si phase) and 50 nm (amorphous phase) depending on the F_c of the layer investigated [102,158,159].

3. EXPERIMENTAL METHODS

In this work, single nanocrystalline layers of 150-250 nm thick were deposited on glass substrates and were analyzed with a Spectrometer equipped with a 532 nm DPSS Laser (SP-2500i MonoVista Imaging). Furthermore, dedicated layer stacks were fabricated with drastically lower thickness (between 5 and 25 nm) with the aim of mimicking the device film structure. The latter type of samples were investigated by micro-Raman backscattering (TriVista triple-monochromator) using a neodymium-cadmium laser of 442 nm, operating at a power of 0.2 mW. The intensity power of the blue laser was carefully calibrated to avoid additional crystallization of the nanocrystalline layers; this aspect is more critical for samples with thin layer thicknesses.

Reflectance measurements are a useful method to support the structural characterization of nc-Si:H material and they can give an indication of the nanocrystalline fraction within the layer. As depicted in Figure 3.6 (b), the reflectance spectrum of c-Si shows two prominent maxima at 275 nm and 365 nm due to singularity that are also visible for nanocrystalline reflectance curves [97,160]. The intensity, shape and position of these peaks is related to the crystalline fraction embedded into the amorphous matrix. Among the advantages, of this method is the opportunity to use polished c-Si as substrate that is the closest condition to the device structure.

Transmission Electron Microscopy (HR-TEM) is a powerful technique for investigating structural properties of nanocrystalline material [93] (i.e. the grain size, voids/cracks, crystallinity evolution). The sample preparation for such investigation is complex because the specimen has to be uniformly thin to allow electron transparency and for that reason, it is a destructive technique. Commonly, focused ion beam (FIB) is used for TEM specimen preparation (lamella) and a comprehensive overview can be found in reference [161]. The most critical phase of the whole preparation process is the thinning procedure that could also damage the sample.

In this thesis, cross section lamellas were prepared using a Zeiss GEMINI 1540 CrossBeam focused ion beam (FIB) high-resolution (Figure 3.7) and analyzed by TEM analysis (HR-TEM, LI-BRA 200FE with an acceleration voltage of 200 kV).

The aim was to investigate the layers stack at the illuminated side of the complete cell device to examine:

- (i)a-Si:H quality: presence of epitaxial growth, sharpness of the interface to the silicon, the effect of the subsequent layer deposition and thickness of the buffer layer.
- (p)nc-Si:H growth evolution on different (i)a-Si:H substrates, grain size and shape, influence of plasma treatment, thickness and homogeneity of the film.

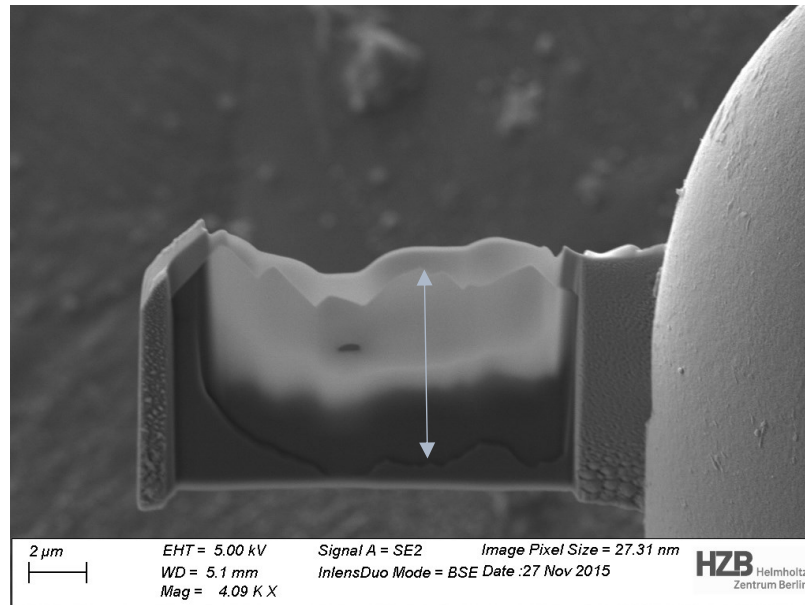


Figure 3.7. Silicon lamella taken from a cell device and fixed on the specimen holder during the thinning procedure in the FIB. The pyramid structure visible is the textured morphology of the c-Si wafers (indicated by the arrow). The gradient color of the lamella is caused by different thicknesses: the top side (pyramids) is the area of interest and for this reason is thinner than the silicon bulk. The bright top layer is a coating protective layer made of platinum. Discussion about results are given in section 5.2.2.

3.2.2. Device Characterization

Minority Carrier Lifetime Measurement

Minority carrier lifetime measurement is a standard technique for characterizing the surface passivation of treated silicon wafers. It is contactless, fast and non-destructive that makes it a routine method to control the material quality for PECVD process optimizations. Our laboratory is equipped with a lifetime tester WCT-120 by Sinton Instruments. The sample is subjected to a short pulse of light that creates excess electron-hole pairs in the silicon bulk. Then the photoconductance decay is detected as a function of the time. Analysis of the measured curve permits to extract the effective minority carrier lifetime (τ_{eff}) that gives information about how fast charge carriers recombine both at the wafer surfaces and in the bulk [25,162]. Since the wafers are of high quality, the surface recombination is the dominant phenomenon and c-Si surface treatments can drastically influence the τ_{eff} (e.g. passivation of dangling bonds as discussed in section 2.1.2). To evaluate the passivation performance, ideally, both wafer surfaces have to be treated with the same process (symmetric samples).

3. EXPERIMENTAL METHODS

If bulk recombination can be neglected, the surface quality of a semiconductor material is described by the surface recombination velocity S_{eff} (or the effective minority carrier lifetime τ_{eff}):

$$\tau_{eff} = \frac{1}{S_{eff}} = \frac{\Delta n}{U} \quad (3.3)$$

where Δn represents the excess carrier density and U is the surface recombination rate.

The lifetime is a function of minority carrier density as shown in Figure 3.8. Conventionally, a representative value for τ_{eff} is extracted at injection level of 10^{15} cm^{-3} where the recombination through defects is dominant; but the entire curve gives further information about the dominant recombination mechanism. Commonly the dominant contribution in the higher injection range can be attributed to the Auger recombination, whereas the SRH recombination influences the lower injection range.

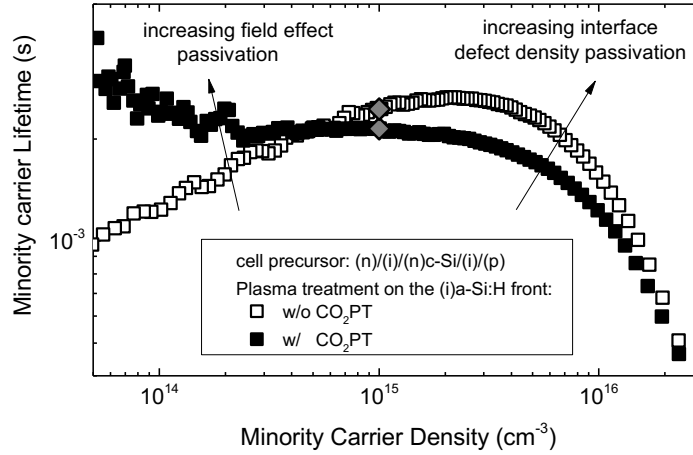


Figure 3.8. Minority carrier lifetime measurements were performed on cell precursors (p)/(i)/(n)c-Si/(i)/(n) deposited on textured c-Si with and without a CO₂ plasma treatment on the front buffer layer. Discussion about results are given in section 5.2.2.

Two more values that are extracted from a lifetime measurement can provide additional information: the implied open circuit voltage ($i-V_{oc}$) at 1 sun (injection level of approximately 10^{16} cm^{-3}). The $i-V_{oc}$ is calculated via the following equation [162]:

$$i-V_{oc} = \frac{kT}{q} \ln \left(\frac{(N_D + \Delta n)\Delta n}{n_i^2} \right) \quad (3.4)$$

where N_D is the concentration of donor atoms, Δn is the excess carrier concentration n_i is the intrinsic carrier concentration. The implied fill factor ($i-FF$) can be also extracted.

Consequently, $i-V_{oc}$ depends heavily on the wafers input parameters (i.e. thickness, resistivity, doping type etc.) and represent the upper limit that one should expect to measure in the completed device.

Symmetrical samples were fabricated to investigate the surface passivation quality of (i)a-Si:H and a-SiO_x:H films, whereas cell precursors (definition in Figure 3.1 (b)) were systematically measured directly after processing the wafers by PECVD to control the effect of the subsequent depositions and annealing steps.

To further evaluate performances of a-SiO_x:H films, the experimental minority carrier lifetime curves were fitted using a simulation model [163] that allows one to distinguish between passivation mechanisms. The model involves two fitting parameters the effective fixed charge Q_f and the interface defect density D_{it} that identify the field-effect passivation and the interface defect passivation, respectively.

Current-Voltage Characteristic

The most fundamental characterization method for analyzing solar cells performances is to test the cells under standard illumination at 25 °C and 100 mW/cm² light intensity (AM1.5g) to extract the current-voltage characteristic (J - V curve). A typical experimental curve is given in Figure 3.9 (a).

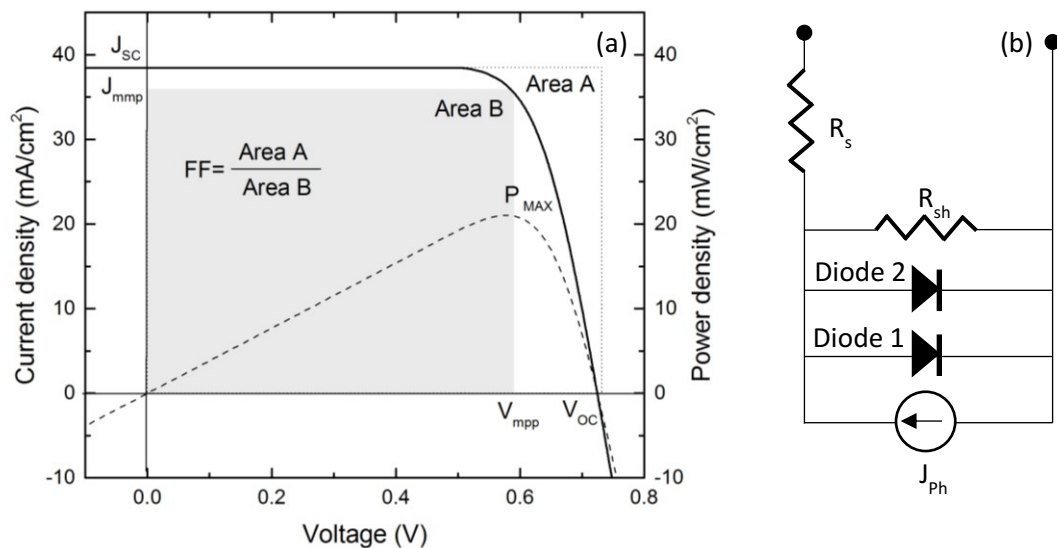


Figure 3.9. (a) Current-Voltage characteristic of a typical silicon heterojunction solar cell; correspondent cell parameters are also indicated. The dashed curve represents the power density. (b) Equivalent circuit of the solar cell described by a two-diode model.

3. EXPERIMENTAL METHODS

The most relevant parameters [19,164] are described in the following list:

- The open circuit voltage V_{OC} is the maximum voltage that occurs when the net current through the device is zero. V_{OC} up to 750 mV could be experimentally achieved for crystalline silicon solar cell [9].
- The short circuit current density J_{SC} is the current density measurable when the voltage is zero.
- The maximum power point P_{MAX} of the power density curve defines the voltage V_{mpp} and the current density J_{mpp} at the maximum power point.
- The fill factor FF is calculated as the ratio between the maximum power generated by a solar cell and the theoretical power given by the ideal squared J - V curve in absence of any losses:

$$FF = \frac{V_{mpp} J_{mpp}}{V_{OC} J_{SC}} \quad (3.5)$$

- The resistance at the short circuit current R_{SC} and at open circuit voltage R_{OC} are defined as the differential of the J - V curve for $V=0$ and $J=0$, respectively and they correlate to series resistance R_s and shunt resistance R_{sh} .
- The conversion efficiency η is the most relevant parameter and is defined as the ratio of maximum power density output (P_{MAX}) from the solar cell to power density input (P_{IN}) from the sun:

$$\eta = \frac{P_{MAX}}{P_{in}} = \frac{V_{OC} J_{SC} FF}{P_{in}} \quad (3.6)$$

The two-diode model (Figure 3.9 (b)), that includes recombination at the junction and the two resistance contributions, represents the equivalent circuit of a solar cell, the analytic expression of a J - V characteristic follows the equation [164]:

$$J = J_{Ph} - J_{01} \left[\exp\left(\frac{q(V - JR_s)}{n_1 kT}\right) - 1 \right] - J_{02} \left[\exp\left(\frac{q(V - JR_s)}{n_2 kT}\right) - 1 \right] - \frac{V - JR_s}{R_{sh}} \quad (3.7)$$

where n is the ideality factor and J_0 stands for recombination current density, both for diode 1 and 2, k is the Boltzmann constant and T is the temperature in Kelvin.

Efficiency Losses

Limitations of the cell parameters discussed above ultimately limit the conversion efficiency:

- The specific semiconductor material chosen, i.e. its band gap [19]: V_{OC} increases with the band gap while J_{SC} has an opposite tendency.
- Since J_{SC} is due to generation and collection of carriers generated by the light source, it can be limited by several factors:
 - The spectrum and power of the incident light source.
 - The cell active area that can be reduced by the presence of front metal grid.
 - The optical properties of the cell and light trapping scheme (more details can be found in section 2.2.3).
 - Collection probability of the generated carriers due to recombination in the bulk or at the wafer surfaces.
- V_{OC} is primarily limited by recombination losses both in the bulk and at the surfaces of the semiconductor material that affect the J_0 in equation (3.5). It is strongly affected by the wafer thickness and bulk quality (carrier lifetime) but also by the silicon surface passivation.
- The series resistance R_s contributes to a voltage drop and it becomes more relevant as the current increases. The causes are various and can be attributed to resistances at the contact between adjacent layers (e.g. TCO/Emitter) or to the current flow through the layer stacks and laterally to the contact grid.
- The shunt (or parallel) resistance R_{sh} is due to the presence of resistance path for the current and if a low resistance path exists across the cell, it can reduce the J_{SC} . Both resistances contribute to reduce the FF .
- FF is reduced by recombination losses and resistance contributions (R_s and R_{sh}).

A dual-source (Hg and Xe) Wacom WXS-155S-L2 solar simulator (class AAA) was used to determine the J - V parameters for characterizing the fabricated solar cells and the measurements were performed under standard test conditions (AM 1.5g). A shadow mask was aligned to the cell area to avoid illumination of the entire wafer. For the front emitter devices, a gold coated chuck assured the contact with the fully metalized rear side, whereas on the front side contacts were made by placing 4 probes in a symmetric configuration. The

3. EXPERIMENTAL METHODS

rear emitter device required individual contacting of each cell on both sides. For that purpose, two additional pins replaced the full area chuck.

SunsV_{oc}

The SunsV_{oc} equipment was used to determine the open circuit voltage at variable illumination level and obtain a *pseudo J-V* curve using the experimental J_{SC} as extracted by the *J-V* curve that is given as input. Since only the voltage is measured and no current flows across the cells, the measurement excludes the effect of the series resistance R_s . The *pseudo-cell parameters* can be defined from the *pseudo J-V curve*. Since they are limited only by recombination or shunting mechanisms, they are the potential upper limit expected for the measured solar cell. The prefix pseudo indicates that the values are not real or rather the potential upper limit for the device. In the next chapters, we will refer to *pseudo FF* to distinguish it from the *FF* extracted for the illuminated *J-V* curve.

For device characterization, it is important to determine an accurate value that is representative for the series resistance under illumination condition $R_{S,light}$. Among the experimental methods available, we calculated $R_{S,light}$ by comparing the *pseudo J-V* and the illuminated *J-V* curves according to [165]:

$$R_{S,light} = \frac{V_{pseudo\ J-V} - V_{J-V}}{J_{mmp}} \quad (3.8)$$

Quantum Efficiency and Total Reflectance

The spectral response measured from a solar cells is ratio of the generated current to the power incident on the device. From that, the external quantum efficiency (EQE) can be calculated. It gives the number of electrons generated by the solar cell compared to the number of photons incident on the device. Since no light is absorbed below the band gap of the absorber, the EQE at longer wavelengths is zero. The photocurrent density J_{SC-EQE} can be calculated by multiplying the EQE curve with the AM 1.5g spectrum and integrating over the spectral region of interest (300 - 1200 nm). This method gives useful information about loss mechanisms because the incoming light traverses several layers before reaching the absorber and the effect is clearly visible in Figure 3.10 as highlighted by the shadow areas. Moreover, the penetration depth of the light varies with its energy; this means that the layer stack at the front side of the cell absorbs photons with higher energy. In contrast, the lower energy portion of the spectra affects the rear side of the device. A discussion of the current losses in a heterojunction solar cell can be found in section 2.2.3.

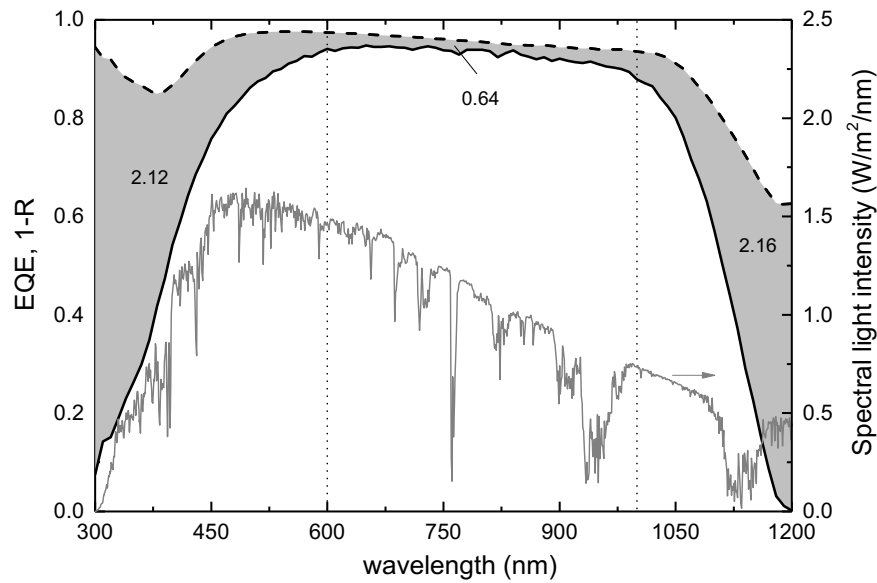


Figure 3.10. External quantum efficiency EQE (solid line) and absorbance $1-R$ (dashed line) spectra as a function of wavelength for a cells with (p)a-Si:H (10 nm) emitter. The AM1.5g standard solar spectrum used for extracting the short circuit current densities is also reported. The shaded areas indicate the parasitic absorption and the numbers are the current losses expressed in mA/cm^2 calculated in the wavelength range identified by the dotted vertical lines.

A more complete analysis of the current losses is possible calculating the internal quantum efficiency (IQE) that allows to investigate the collection of charges excluding reflectance losses from the cell. IQE was derived as:

$$IQE = \frac{EQE}{(1 - R)} \quad (3.9)$$

The spectral reflectance $R(\lambda)$ of the solar cell was measured by means of UVVis spectrophotometry using a lens to focus the beam on a small spot size. The effective absorbance of the cell was calculated as $1-R$ under the assumption that the rear side of the cell was opaque over the wavelength range of interest. From this measurement, the potential photocurrent density J_{SC-1-R} after losses due to reflection can be calculated by multiplying the $1-R$ curve with the AM 1.5g spectrum and integrating over the spectral region of interest (300 - 1200 nm). The difference between J_{SC-1-R} and J_{SC-EQE} estimates the current losses due to parasitic absorption of the incoming light in the front multilayer stack.

The spectral response measurements were performed by means of a home-built setup described in [166] using an illumination spot size of $2 \times 4 \text{ mm}^2$, with additional white bias light illuminating the whole cell area.

4. Reference Process Development for Silicon Heterojunction Solar Cells

This chapter describes the development of a reference process for silicon heterojunction (SHJ) solar cells. The PECVD and PVD deposition processes were partially transferred from small-area R & D tools to large-area production type tools and re-optimized, aiming for a uniform and reproducible reference process yielding reasonable high cell efficiencies with small run-to-run fluctuation. This is a prerequisite to study the effect of the implementation of the novel contact materials nc-Si:H and nc-SiO_x:H, as reported in chapters 5 and 6, respectively. Parts of these results have been published in [49,167,168].

The details for processing front emitter solar cells have been described in chapter 3. Here, we focus on the following four process steps discussing the cell performance and the need for optically and electrically improved contact materials in more detail:

- The optimization of the intrinsic (i)a-Si:H passivation layer relating both growth parameters and post-deposition treatments to cell results. The choice of the type of a-Si:H layer will have a great impact on the growth of nc-Si:H and nc-SiO_x:H based contacts.
- For the p-doped a-Si:H emitter, we compare trimethylboron and diborane as doping gases and correlate the layer properties to the cell performance. Later, the resulting amorphous p-doped emitter will be the reference for nc-Si:H and nc-SiO_x:H based emitters, aiming for improved transparency and reduced contact resistance.
- The transparent conductive oxide (TCO) front electrode based on (In₂O₃:Sn, ITO), and, in particular, the contact between ITO and the p-doped emitter is optimized to reach an ohmic contact with low resistance. This contact is relevant and will be the reference for the nc-Si:H and nc-SiO_x:H based emitters.
- Finally, the rear TCO layer, based on ZnO:Al, is optimized for a high infrared response maintaining a low contact resistance.

4.1. a-Si:H Passivation Layer

For this investigation, double-side polished FZ-Si wafers with bulk lifetime of above 6 ms and different lattice orientations were used. The <100> oriented Si surface is more prone to the undesired epitaxial growth of the passivation layer than the <111> oriented [86]. Hence, for this experiment, <100> lattice orientation was chosen for material optimization to avoid epitaxy on the not-<111> oriented areas on random pyramid textured wafers (see HR-TEM pictures in section 5.2.2).

Some layers were subjected to a post-deposition hydrogen plasma treatment (HPT) in order to provide an additional source of hydrogen radicals to saturate dangling bonds, as suggested in Ref. [82]. Symmetric samples were fabricated by growing 15 nm thick i-layers on both sides of the wafer.

Interface passivation performances were investigated in the as-grown condition and after an additional thermal annealing ($T_{ann} = 200$ °C, for 60 min in air atmosphere). This is done in order to verify the temperature stability of the passivation film, which is needed due to the additional thermal budget during later fabrication process.

After (i)a-Si:H development series, two different films were investigated in-depth (indicated as type A and type B in Table 4.1). The two i-layer recipes mainly differ in substrate temperature, chamber pressure and SiH₄ dilution in H₂.

Table 4.1. PECVD parameters of (i)a-Si:H, (p)a-Si:H and layers and hydrogen plasma treatment (HPT). T_{sub} : substrate temperature; P_D : plasma power density; p : chamber pressure and precursor gas flows. Doping gases were 2% diluted in H₂.

Material [Plasma treat.]	T_{sub} (°C)	P_D (mW/cm ²)	p (Pa)	SiH ₄ (sccm)	H ₂ (sccm)	TMB/B ₂ H ₆ /PH ₃ (sccm)
type A (i)a-Si:H	205	15	200	180	900	/
type B (i)a-Si:H	190	20	133	300	300	/
[HPT]	190	15	333	/	1500	/
(p)a-Si:H	175–205	15	267	55	540	90/-/-
(p)a-Si:H	205	15	267	55	540	-/50 or 90/-
*(p)a-Si:H	130–175	18	50	10	/	-/2/-
(n)a-Si:H	185	18	200	75	645	-/-/50
(n)nc-Si:H	185	200	1200	10	2000	-/-/6

* This recipe corresponds to a film deposited by the FAP tool (excitation frequency of 60 MHz, electrode area of 531 cm² and electrode spacing of 23 mm). While the others were grown in the AKT1600 with an excitation of 13.56 MHz, electrode area of 2500 cm², and electrode spacing of 16.5 mm.

Figure 4.1 summarizes implied open circuit voltage ($i-V_{oc}$) and minority carrier lifetime (τ_{eff}) derived from samples symmetrically passivated with type A or B (i)a-Si:H in as-grown condition, treated with post-deposition HPT and thermally annealed afterwards.

When grown on <100> oriented surface, type A (i)a-Si:H initially has low performance that further degrades upon annealing. This trend is a clear indication of the epitaxial nature of the layer [169]. In contrast, when the film is grown on a <111> oriented c-Si substrate, $i-V_{oc}$ and τ_{eff} reach higher values up to 718 mV and 1.5 ms, respectively.

Type B (i)a-Si:H leads to better results on <100> oriented c-Si, but is still limited by surface recombination. The passivation improves significantly after the HPT in the as-grown condition with values for τ_{eff} reaching 6 ms. Subsequent thermal treatment did not lead to further enhancement.

The same HPT is harmful for the type A film with a reduction in $i-V_{oc}$ exceeding 70 mV when compared to the same layer without HPT. We suggest that the H radicals, that penetrate the (i)a-Si:H, might provide chemical annealing with enhancement of the crystalline (epi-phase) and, hence, reduce the passivation [115,121,123]. TEM investigations presented later in chapter 5 confirmed the different morphologic nature of the type A and type B (i)a-Si:H films.

In the following, the effect of the HPT on type B passivation is investigated in more detail. It is important mentioning that the HPT is responsible for additional etching besides the main function of saturating dangling bonds. Ellipsometry measurement confirms a progressive thinning of the (i)a-Si:H with a rate of ~ 2 nm/min for the tested plasma conditions as depicted in Figure 4.2 (a). This is in agreement with observations reported by

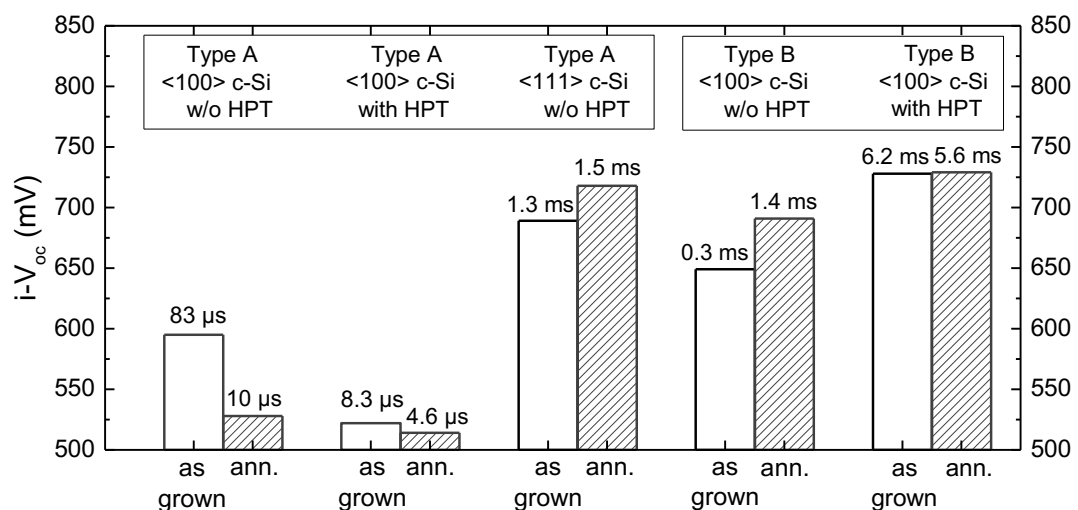


Figure 4.1. Implied open circuit voltage $i-V_{oc}$ of symmetric structures (i)/(n)c-Si/(i) (15 nm) both as-grown and after annealing (in air for 60 min at 200° C). Both types of material are tested under HPT. For comparison, also the minority carrier lifetime τ_{eff} is indicated.

Geissbühler *et al.* [138]. We accounted for this etching effect by choosing initially thicker (i)a-Si:H layers reaching the same thickness after HPT for comparison.

Figure 4.2 (b) shows τ_{eff} of the symmetrically passivated samples treated with different HPT time in the as grown condition and after thermal annealing at 200 °C. For the as-grown samples, τ_{eff} significantly increases from 0.3 up to 6.2 ms with increasing the HPT duration. The non-treated sample and for too short HPT (up to 120 s), the type B (i)a-Si:H is further improved by thermal annealing treatment. Hence, longer hydrogen exposure (240 s) is required to saturate dangling bonds in the entire layer. No further improvement upon annealing is detected for this sample (Figure 4.2 (b)). Moreover, we can conclude that this optimized sample exhibits stable performance at 200 °C which is relevant for the subsequent steps cell fabrication processes.

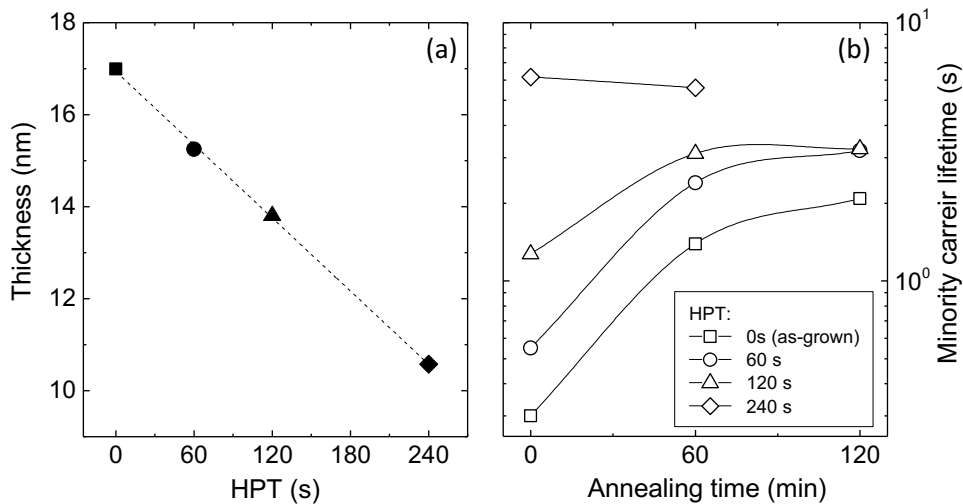


Figure 4.2. (a) Film thickness of the type B (i)a-Si:H layer as function of the HPT treatment time (see Table 4.1) measured by ellipsometry. (b) Minority carrier lifetime for the film showed in (a) measured after annealing in air at 200°C.

Solar Cell Results

The first set of solar cell results highlighted the advantage of using a fully amorphous (“non-epi”) and well-passivating (i)a-Si:H (type B) instead of the type A film. The cells had a structure as depicted in Figure 3.1 (b) and nominally the same layer thicknesses.

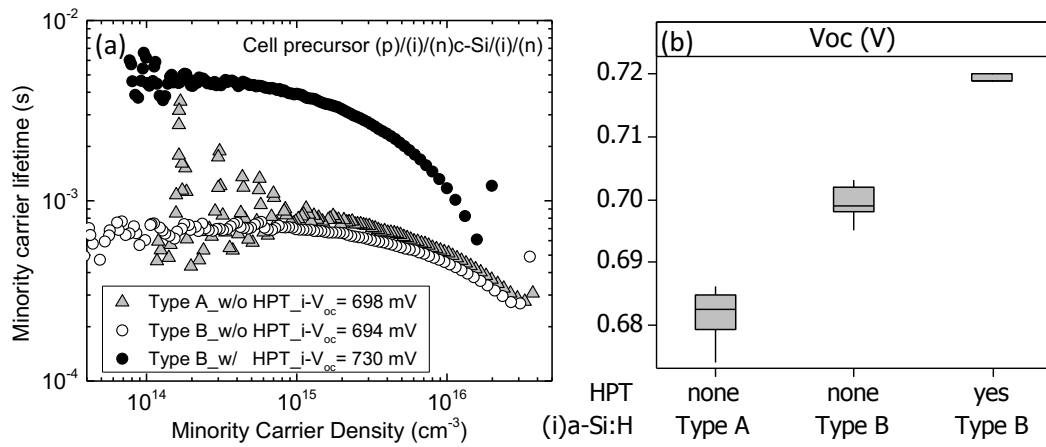


Figure 4.3. (a) Minority carrier lifetime curves of cell precursors measured in the as-grown condition. The (i)a-Si:H layer is of type A, type B with and without HPT. (b) Box plots of the open circuit voltage V_{OC} based on 7 cells for the same samples reported in (a).

Minority carrier lifetime curves measured on the cell precursors after the i-layer deposition are plotted in Figure 4.3 (a). The wafers had textured surfaces with random pyramidal facets $\langle 111 \rangle$ oriented. The results confirmed the observations made on the polished symmetric samples (Figure 4.1): Both type A and type B (without HPT) show $i-V_{OC} \leq 700$ mV leading to average V_{OC} values as extracted from the $J-V$ characteristics, of 681 and 700 mV, respectively. In contrast, the type B (i)a-Si:H film treated with the optimized HPT shows a considerable improvement in surface passivation with τ_{eff} of 3.9 ms and $i-V_{OC}$ of 730 mV, as the entire curve in Figure 4.3 (a) is shifted towards higher τ_{eff} . The open circuit voltage, extracted from the $J-V$ curve under illumination, stays on a comparably higher level (720 mV) after the entire fabrication process. Moreover, the HPT leads to reduced scatter in all the cell parameters as shown in Table 4.2.

Table 4.2. Solar cell parameters (best and average) shown in Figure 4.3 with variable (i)a-Si:H layers and with or without HPT growth on textured wafers.

(i)a-Si:H	HPT	J_{SC} (mA/cm ²)	V_{OC} (mV)	FF (%)	η (%)
type A	No	38.4 (38.2±0.2)	683 (681±5)	76.6 (75.9±1.0)	20.4 (20.1±0.3)
type B	No	37.3 (37.4±0.1)	702 (699.6±2.9)	76.3 (75.3±0.8)	20.0 (19.7±0.3)
type B	Yes	38.3 (38.2±0.2)	720 (719±0.5)	77.4 (77.1±0.3)	21.3 (21.2±0.1)

4.2. p-doped Emitter

A p-type doped amorphous film ((p)a-Si:H) was developed for use as the emitter layer. For front emitter applications, this film has to be transparent, offering selective hole collecting and good Si/TCO contact properties.

Figure 4.4 compares properties of (p)a-Si:H films grown on glass substrates in temperature ranges of 130-175 °C and 175°C-220°C using B₂H₆ and TMB gas precursors, respectively. Deposition parameters are given in Table 4.1. The different temperature range is due to the higher thermal stability of TMB than diborane gas precursors [170,171]. The effect of the doping on the optical properties is depicted in Figure 4.4 (a): B₂H₆ doped films exhibit a band gap narrowing [133] from 1.85 eV to 1.55 eV accompanied by a slight increase of the refractive index n as the deposition temperature increases. In contrast, TMB doped layers systematically exhibit values of E_{04} above 1.9 eV throughout the entire temperature range accompanied by a slight increases of the refractive index. This is in agreement with other studies [172,173]. Wu *et al.* [172] demonstrated that the widening of the band gap is related to carbon incorporation from the TMB molecule as CH_x radicals [173]. The C incorporation is also enhanced by the presence of boron [172]. Additionally, a higher H content could contribute to the higher bandgap and lower n in the case of TMB. For comparison, the intrinsic a-Si:H film deposited at $T_{sub} = 205$ °C has a slightly more narrow bandgap and a higher refractive index if compared to the corresponding TMB doped film ($n_{(i)a-Si:H} = 4.19$ and $n_{TMB} = 3.75$ at 633 nm).

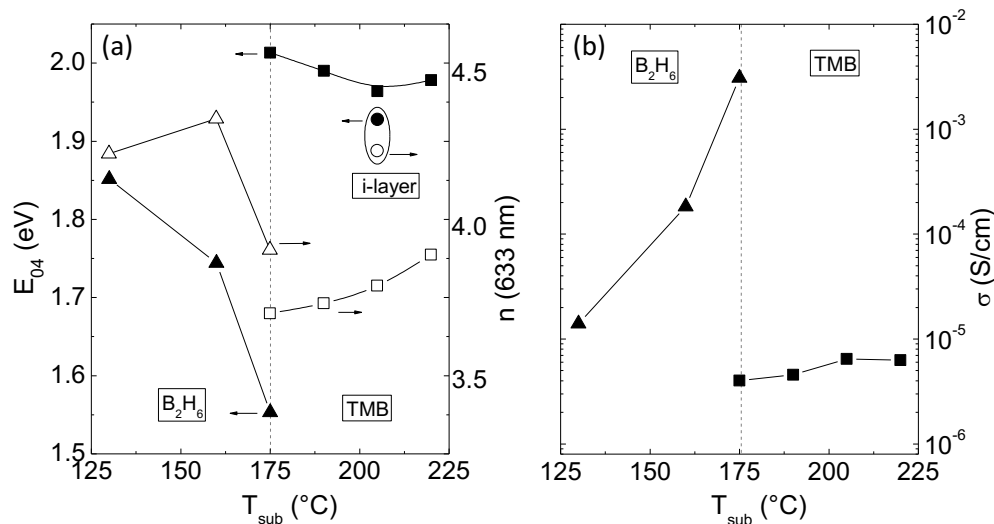


Figure 4.4. (a) Optical band gap E_{04} (full symbols), refractive index n at 633 nm (open symbols) and (b) dark conductivity σ of p-doped layers on glass substrates as a function of substrate temperature T_{sub} . The layer thicknesses are in the range of 100 – 200 nm. Triangles: B₂H₆ doped (p)a-Si:H, squares: TMB doped (p)a-Si:H and circles: (i)a-Si:H.

Figure 4.4 (b) depicts the electrical conductivity (σ) measured in the dark as function of both T_{sub} and type of doping gas. For films doped with B_2H_6 , σ rises by more than two orders of magnitude in the range of T_{sub} investigated. Similar high conductivities were reported in the study by Spear and Le Comber [124] for diborane doped amorphous films. In contrast, varying T_{sub} only slightly effects the conductivity for TMB-doped layers with values remaining nearly constant in the upper 10^{-6} S/cm range. These values are in agreement with data reported in literature [173,174].

The absorption coefficient α for selected films is plotted in Figure 4.5 (a) and compared to the undoped amorphous layer. For B_2H_6 doped layers, α is systematically above that of the undoped sample in the whole energy range analyzed. The TMB doped films show a higher α than the intrinsic film for photon energy below 1.9 eV. In the higher energy part of the spectrum, the advantage of using TMB instead of B_2H_6 is appreciable as was also observed by [173]. The considerable difference in σ for the two doping gases correlates with the absorption coefficient.

Figure 4.5 (b) shows the relation between σ and α extracted at 500 nm (~ 2.5 eV) as function of the doping gas for the material investigated in this study. The target is to obtain p-doped layers with parameters close to the upper left corner. The shaded area, in contrast, indicates a critical area as the bulk conductivity begins to contribute to the cell's series resistance. Considering a 10 nm thick (p)a-Si:H with a σ of 10^{-5} S/cm, a series resistance contribution of $0.1 \Omega \cdot cm^2$ is calculated. Hence, σ should not be much below this value.

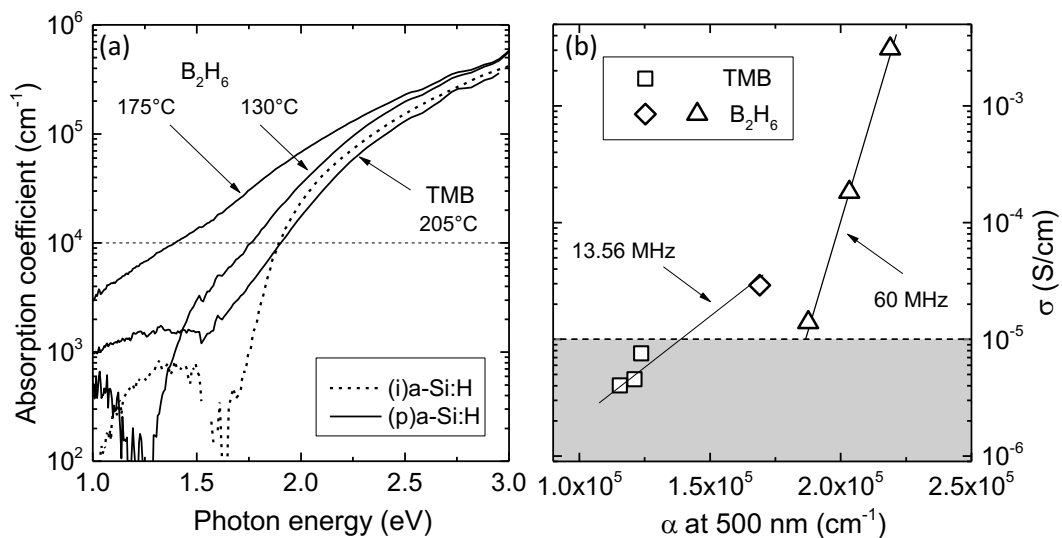


Figure 4.5. (a) Absorption coefficient α extracted by reflectance and transmittance measurements as function of photon energy for (i)a-Si:H and selected (p)a-Si:H films deposited at different substrate temperature and doping gases. The film properties are reported in Figure 4.4. (b) Dark conductivity σ as function of the absorption coefficient extracted at 500 nm for (p)a-Si:H layers: squares and diamonds indicate films deposited at excitation frequencies of 13.56 MHz (AKT1600) doped with TMB and B_2H_6 , respectively; triangles indicate B_2H_6 a-Si:H deposited at 60 MHz (FAP tool).

Table 4.3. Optoelectronic properties of the (p)a-Si:H layers selected for cell application as measured on ~200 nm thick films grown on glass substrates.

Layer	Doping gas	T_{sub} (°C)	E_{04} (eV)	σ ($\times 10^{-5}$ S/cm)	n at 633 nm	α at 500 nm ($\times 10^4$ cm $^{-1}$)
#1	B ₂ H ₆	130	1.85	1.4	4.19	18.8
#2	TMB	205	1.96	0.7	3.75	12.4

As expected, it can be generally observed that films doped with TMB have superior optical performances but lower conductivity as compared to the diborane samples. For application in solar cells, hence, the TMB doped (p)a-Si:H with the highest conductivity is compared to the B₂H₆ doped film with the best optical properties were chosen. The properties of the selected (p)a-Si:H layers are summarized in Table 4.3.

Solar Cell Results

Solar cells were fabricated passivating the wafer surface with type A (i)a-Si:H film and growing the selected emitters to have an (i)/(p) stack with thickness of 8/13 nm and 5/8 nm on polished and textured c-Si, respectively. The rear side was completed with the same (i)a-Si:H layer and an (n)a-Si:H back surface field (BSF) film of 10 nm thickness.

The resulting cell parameters are shown in Figure 4.6 (a). The data indicate similar trends both for polished and textured wafers with a systematically higher J_{sc} of cells with TMB-doped emitters. The gain in J_{sc} extracted from EQE measurements amounts to about to 2.3 and 1.5 mA/cm² for cells on polished and textured wafers, respectively (Figure 4.6 (b)).

The effect of the reduced absorption of TMB doped layers is clearly visible from the IQE curves. In Figure 4.6 (b), a systematically lower parasitic absorption is detectable particularly in the blue range of the wavelength spectrum. Moreover, the values of FF depend heavily on the doping gas used and are distinctly reduced by the use of TMB.

The J - V curve for the cell with TMB-doped emitter on polished c-Si has an S-shape character as depicted in Figure 4.6 (c). This might be caused by insufficient emitter doping affecting both the band alignment at the a-Si:H/c-Si interface and the contact to the front TCO (section 2.2.2). Emitter with reduced doping level reduces the electric field in the depletion region on the c-Si side and allows accumulation of both electrons and holes enhancing recombination probability. Van Cleef *et al.* [175] who demonstrated that the S-shape J - V characteristic with (p)a-Si:H emitters can be removed by increasing the doping and reducing the activation energy from 0.4 to 0.33 eV.

Table 4.4 summarizes the solar cell parameters for the best cells discussed in this session.

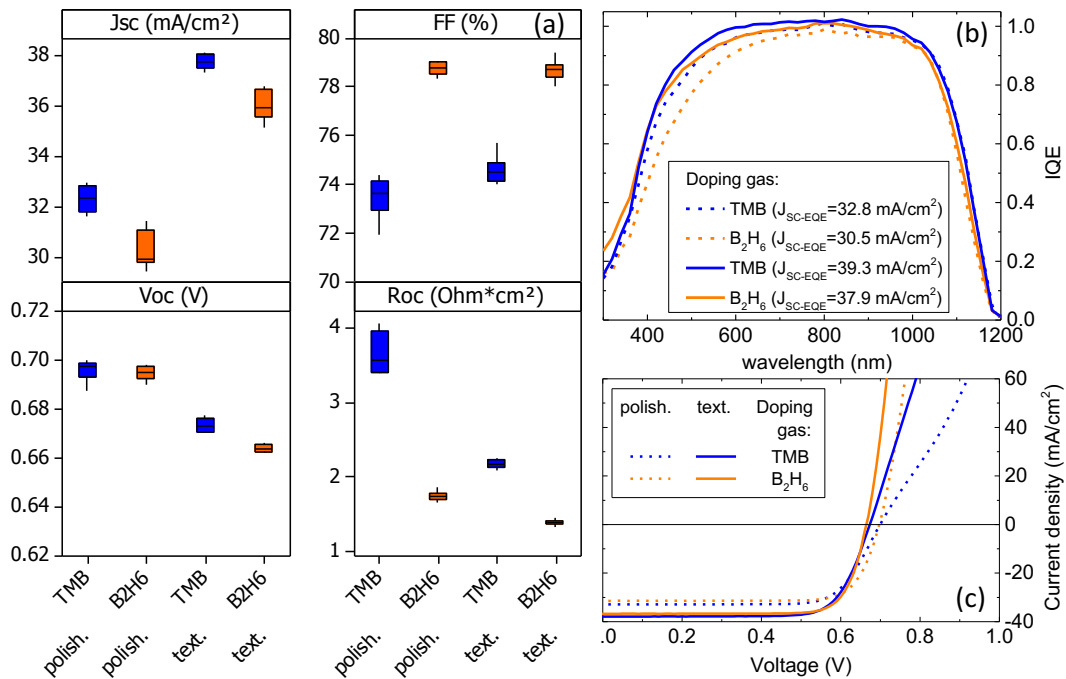


Figure 4.6. (a) Box plots of the cell characteristics based on 12 cells deposited on polished and textured wafers with type A (i)α-Si:H layers. For each group of cells the emitter was deposited with TMB or B₂H₆ as doping gas. (b) Internal quantum efficiency IQE spectra as function of wavelength and (c) $J-V$ curves for the best cells on polished and textured c-Si wafers with both emitter materials. Deposition parameters for p-doped layers are reported in Table 4.1.

Table 4.4. $J-V$ parameters of the best solar cells as shown in Figure 4.6.

Doping gas	wafer	J_{sc} (mA/cm ²)	V_{oc} (mV)	FF (%)	η (%)
TMB	polished	32.9	699	74.3	17.1
B ₂ H ₆		31.4	697	79.1	17.3
TMB	textured	38.1	673	75.7	19.3
B ₂ H ₆		36.7	664	79.3	19.4

In contrast to polished wafers, well-shaped $J-V$ curves are measured for cells on textured wafers although the TMB-doped device suffers from high R_{oc} . The difference might be caused by the increased surface area due to the pyramid pattern and by the emitter thickness. The data suggest that series resistance is the cause of the observed FF losses that is further dependent on the wafer morphology. SunsVoc measurements confirm the previous observation: pseudo- FF s of the best textured cells with B₂H₆ are 1% absolute higher than with TMB. The series resistance under illuminated condition ($R_{S,light}$) is computed from the illuminated $J-V$ curve and the SunsVoc as described in Ref. [165] and in section 3.2.2. The use of a B₂H₆ doped emitter results in lower $R_{S,light}$ (0.6 Ω·cm²) of about 40%.

4.3. Front TCO

The front TCO layer has to provide a suitable conductivity for lateral carrier transport and to act as anti-reflection film. For an effective reduction of losses, the TCO films require a fine optimization both for optical and electronic properties [58]. To ensure transparency throughout the VIS + NIR spectrum, an optical band gap above 3.5 eV is required, and high carrier mobility (Hall mobility, μ_H) is beneficial in order to allow for using low free-carrier densities (N_D) without sacrificing conductivity. The latter depends on the specific TCO material, crystalline structure and impurity density. Finally, the TCO work function (φ_{TCO}) affects the contact to the adjacent doped film as discussed in section 2.2.2. Depending on the front grid geometry and the required TCO thickness to ensure the reflectance minimum at 600 nm, the target for the sheet resistance R_{sh} is at about $40 \Omega_{sq}$.

Commonly, $\text{In}_2\text{O}_3:\text{Sn}$ (ITO) is more often used than other TCO materials due to its excellent transparency combined to high conductivity achievable at temperature below 200°C . The temperature requirement is critical for application in SHJ devices. Very highly conductive ITO material leads to considerable parasitic absorption in the near infrared region of the spectrum due to high carrier density, but high Sn doping concentration reduces the μ_H within the film. Among the deposition parameters, the oxygen fraction can influence both transparency and conductivity.

ITO transmittance $T(\lambda)$ and absorptance $A(\lambda)$ spectra are depicted in Figure 4.7 (a) for the ITO films tested in this work grown at set temperature of 220°C from highly doped 90/10 wt.% ($\text{In}_2\text{O}_3/\text{SnO}_2$) sputter target.

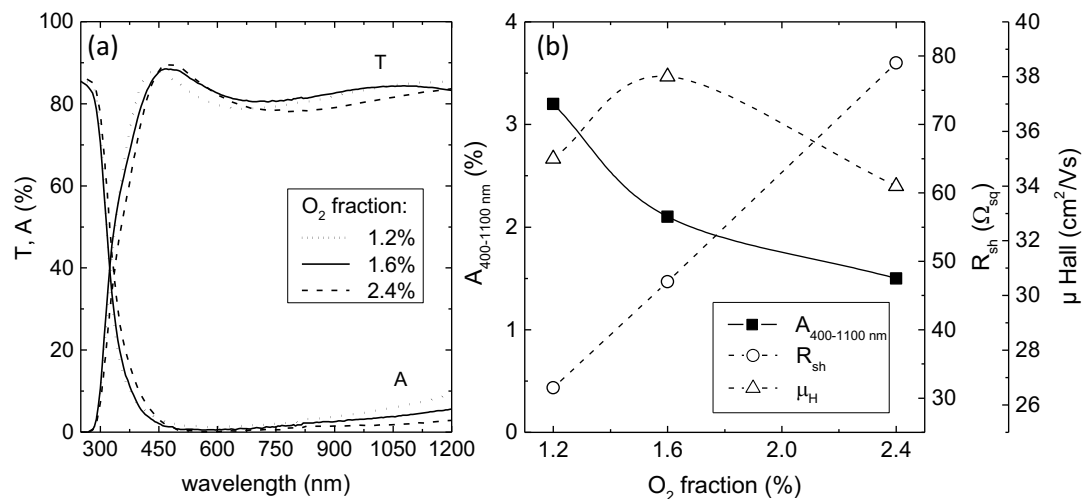


Figure 4.7. (a) Transmittance T and absorptance A spectra of ITO films on glass deposited from the same sputter target with varying oxygen fraction. (b) Optoelectronic ITO properties of the three ITO films, i.e. integrated absorptance A in the range 400 - 1100 nm, sheet resistance R_{sh} , and Hall mobility μ_H . The layer thicknesses are about 110 nm thick.

The higher oxygen fraction reduces the free-carrier absorption in the NIR region (>700 nm) but increases absorptance A for wavelengths below 450 nm, which is due to an increasing of the effective band gap with increasing N_D known as the Burstein-Moss Shift. The integrated A in the range 400 – 1100 nm weighted with the AM1.5g solar spectrum shows that the reduction in free carrier absorption overcompensates the reduction of the effective band gap (Figure 4.7 (b)). Additionally, the sheet resistance R_{sh} linearly grows up to about $80 \Omega_{sq}$. The effect of the increasing in the R_{sh} of the ITO on cell parameters results in a growth of R_s by 30% (relative) that implicates losses in fill factor of 0.7% absolute, as simulated accordingly to [176].

A trade-off between optical and electronic properties can be identified for the intermediate O_2 fraction of the $O_2 + Ar$ sputter gas mixture where the film achieves hall mobility of $\sim 38 \text{ cm}^2/\text{Vs}$ and R_{sh} of $47 \Omega_{sq}$. This is the ITO layer chosen for solar cells presented in this work.

Solar Cell Results

As noted in a report by Kanevce *et al.* [50], the mismatch in the work function of the front TCO and the p-doped emitter affects strongly the charge transport mechanisms, as also discussed in section 2.2.2. Bivour *et al.* have intensively studied the role of the (p)a-Si:H on the electrical TCO/(p) contact by means of numerical simulations [52] and experiments [177], supporting the hypothesis that high doping of the p-doped layer is required for the formation of an efficient tunneling junction. Others [51] focused on the influence of the TCO properties (commonly ITO) and reported an enhancement in cell performance when the ITO work function approached the one of the p-doped silicon film. Literature data reported for a p-type a-Si:H emitter a work function of 5.2 eV whereas the TCO should exhibit a work function above 4.8 eV to allow good ohmic contact as predicted by several simulation studies [51,52].

A study on the ITO/(p)a-Si:H contact was carried out by inserting a 10 nm thin ITO film, with variably free-carrier density, between the emitter and the bulk ITO layer (70 nm, N_D of 10^{20} cm^{-3}), by varying the O_2 fraction in the sputtering deposition chamber. The device scheme under investigation is depicted in Figure 4.8 (a).

The N_D decreased when the O_2 fraction rose and the ITO work function is assumed to follow an opposite trend to the N_D as suggested by Klein *et al.* [53]. The bulk ITO thickness ($N_D = 2 \times 10^{20} \text{ cm}^{-3}$) was fixed to 70 nm to reach the antireflection effect in combination with the thin ITO contact layer. The variable contact ITO films considerably affect the J - V characteristic from S-shaped to well-shaped curves.

4. REFERENCE PROCESS DEVELOPMENT FOR SILICON HETEROJUNCTION SOLAR CELLS

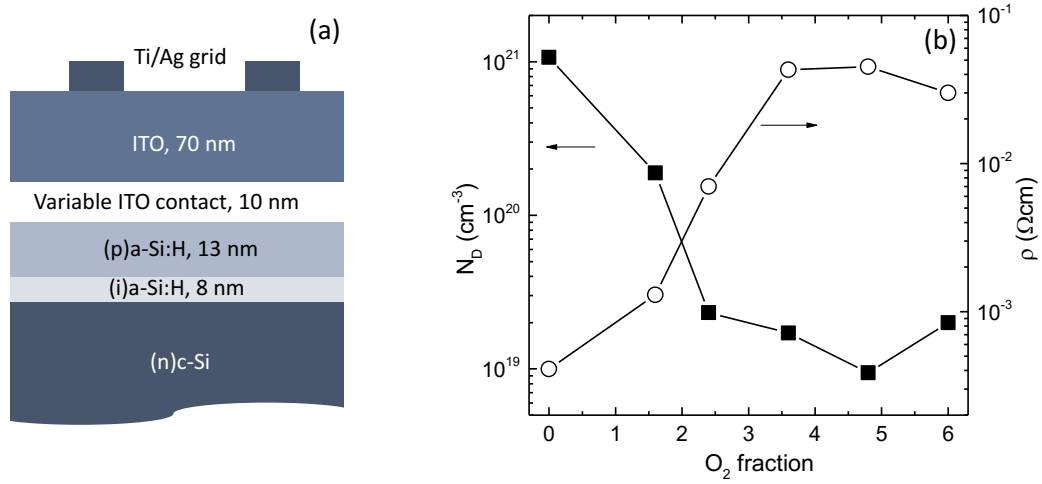


Figure 4.8. (a) The sketch of the front side of the cell fabricated indicating the variable thin ITO contact layer. (b) Free-carrier density N_D and resistivity ρ of the variable contact ITO layer as obtained from Hall measurements as a function of O_2 fraction on film grown on glass with a thickness of 160-220 nm.

To quantify this trend FF and R_{OC} are plotted in Figure 4.9 (a - b) as function of N_D of the ITO contact layer. Two clear trends emerged: for N_D lower than $2 \times 10^{19} \text{ cm}^{-3}$, R_{OC} sharply jump up to values above $7 \Omega \cdot \text{cm}^2$ and consequently the FF decreases, whereas elsewhere the cell parameters are more or less constant ($N_D > 2 \cdot 10^{19} \text{ cm}^{-3}$). *Pseudo-FF* appeared unaffected by the variation in N_D , indicating that the drop in FF is caused by a series resistance.

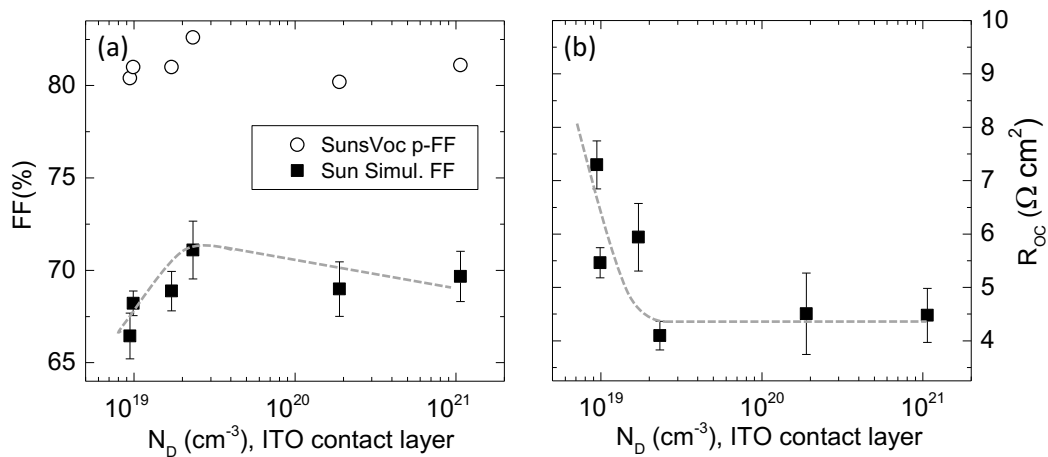


Figure 4.9. (a) Fill factor FF , pseudo fill factor $p\text{-}FF$ and (b) R_{OC} measured for variable free-carrier density in the contact ITO layer ($9.9 \times 10^{18} < N_D < 1.1 \times 10^{21} \text{ cm}^{-3}$). The dashed lines are guide to the eye.

The performance degradation contradicts the hypothesis that an increased work function caused by a lower N_D leads to an improved TCO/p contact. Alternatively, it can be attributed to the contact resistance caused by the variable ITOs that block the tunneling for very low N_D (high φ_{ITO}) because of an increased width of the space-charge region at the TCO/(p) interface.

Simulations, performed by Kirner *et al.* [49] on the same structures as shown in Figure 4.8 (a), qualitatively reproduce the experimental trends and suggest that inefficient tunneling leads to S-shape J - V characteristics caused by the above mentioned widening of the space charge region could clearly be seen in the simulated band diagrams.

4.4. Rear TCO

The rear contact (TCO + metal) influences the light management of the NIR response and its optimization can improve NIR light reflection and reduce parasitic absorption in the low energy range of the optical spectrum [59]. Similarly to the front TCO, the most common material used at the rear side is ITO [28,178].

Alternative materials have been investigated with reduced potential costs such as Al-doped ZnO (AZO) [179]. Results on SHJ, however, are rarely found in literature. In this work, we hence used AZO/Ag reflectors as originally developed for a-Si:H/ μ c-Si:H solar cells [180] and re-optimized as rear side contact in SHJ devices.

For the optimization process of the rear TCO employed in our reference process, the ZnO:Al film was deposited by DC sputtering at room temperature from ZnO:Al target doped with 1 wt.% Al₂O₃. The variables for optimization of the rear side TCO are free-carrier density N_D , and thickness. N_D is controlled by varying the oxygen gas mixture in argon during the sputtering process. More oxygen in the film reduces N_D and decreases the absorption coefficient and the refractive index in the NIR, which are positive for the reflection at the rear contact. As a drawback, it increases the resistivity ρ with values in the range 0.002 – 0.25 Ω -cm.

Considering an AZO film of 70 nm and a series-resistance contribution of $< 0.1 \Omega$ -cm², $\rho < 10^4 \Omega$ -cm is required. This value is still several orders of magnitude higher than the ρ experimentally calculated for the set of AZO films. From a-Si/ μ c-Si cell development, however, it was known that higher oxygen flows (= higher ρ) will lead to lower FF , most likely due to a poor Si/AZO contact as a result of Si surface oxidation during sputtering.

Solar Cell Results

Solar cells were fabricated on textured c-Si depositing (i)a-Si:H passivation layer of type B and the TMB doped emitter. The rear side was completed with the same (n)nc-Si:H BSF film and an AZO layer sputtered with a variable argon/oxygen mixture and a thickness of 70 and 190 nm.

Figure 4.10 (a) shows the effect of the oxygen fraction variation over the cell parameters. The nominal AZO thickness was maintained at 70 nm and the O₂ fraction was varied in the range 0.2 – 1.23%.

J_{SC} increases with an increased O₂ fraction while R_{OC} slightly decreases with a minimum at 0.7%. The J_{SC} trend is driven by the reduced carrier density in the TCO film. A further increase in O₂ fraction was detrimental and caused a degradation of R_{OC} and a consequent reduction in FF .

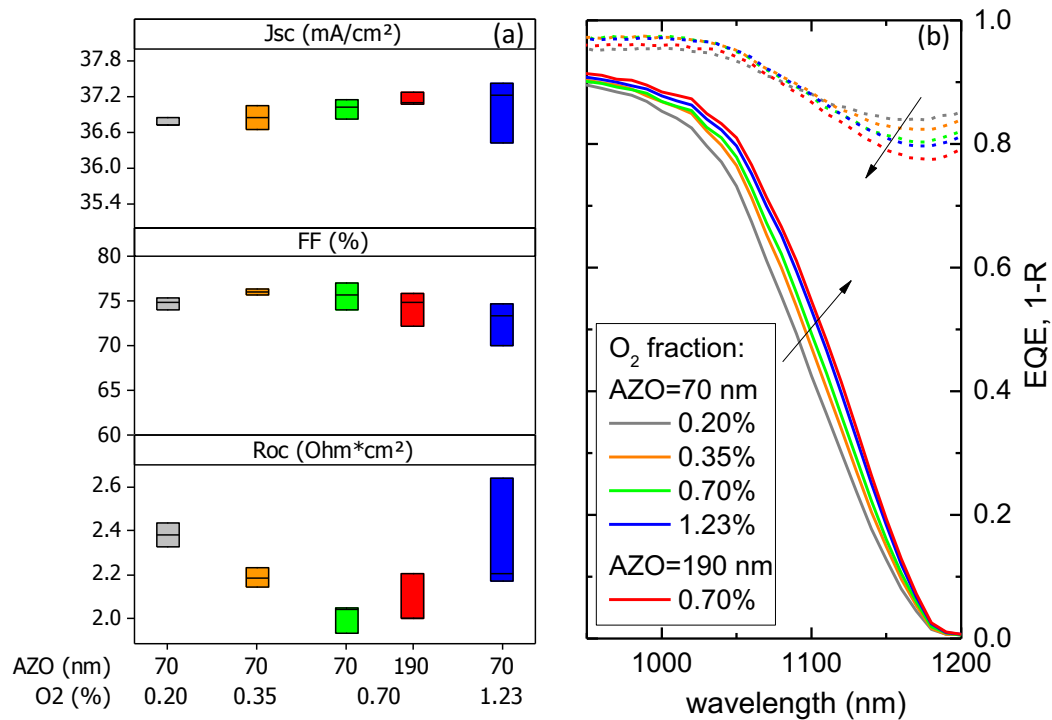


Figure 4.10. (a) Box plots of selected cell characteristics based on 7 cells for each wafers with variable AZO on the rear side in term of O₂ fraction variation and film thickness. (b) External quantum efficiency EQE (solid line) and absorbance 1-R (dashed line) curves measured on the best cells for each wafer as function of the wavelength in the range 950-1200 nm. The dashed curves in (a) and arrows in (b) indicate the direction of the trends with increasing O₂ fraction.

Table 4.5. Solar cell parameters of the best cells shown in Figure 4.10 for a variable O₂ fraction and thickness of the rear side AZO film.

O ₂ fraction (%)	AZO thickness (nm)	J_{SC-EQE} (mA/cm ²)	V_{oc} (mV)	FF (%)	η (%)
0.20	70	37.2	716	75.4	19.8
0.35	70	37.6	718	76.4	20.3
0.70	70	37.6	718	77.2	20.4
	190	38.2	710	75.9	20.0
1.23	70	37.8	708	74.7	19.8

From the EQE and 1-*R* curves in Figure 4.10 (b), an increased O₂ flow gradually reduces the parasitic absorption and, hence, increases the reflection at the rear AZO/Ag contact (see trend indicated by the arrows). This results in the progressive gain in J_{sc} as already see above with a maximum enhancement of 0.6 mA/cm².

Finally, the influence of the AZO thickness was investigated as reported in same Figure 4.10 for the oxygen fraction of 0.7%. FF and R_{oc} remained comparable for the 70 nm and 190 nm thick AZO films, whereas the J_{sc} rose to 0.6 mA/cm². This can be explained by the fact that the thicker AZO film increases the reflection according to the rule $t_{opt} = \lambda/2/n$ as also reported in [59].

Best cell's results are summarized in Table 4.5. We choose an AZO thickness of 70 nm and oxygen fraction of 0.35% as the reference process in order to allow for comparison among different series throughout this thesis. Moreover this process exhibited the most narrow FF distribution and, hence, appears to be a good choice for a robust reference process. As demonstrated, however, there is potential for J_{sc} and cell efficiency improvement by using a thicker AZO sputtered with more O₂ dilution.

4.5. Discussion and Conclusions

A stable and reproducible reference process for fabricating silicon heterojunction solar cells was established at PVcomB. Critical dependencies of the key processes and material properties were studied in more detail.

The progress in conversion efficiency η and open circuit voltage V_{oc} for the reference process having intrinsic and p-doped amorphous silicon (i)a-Si:H layers as passivation and emitter layers, respectively, is shown in Figure 4.11.

4. REFERENCE PROCESS DEVELOPMENT FOR SILICON HETEROJUNCTION SOLAR CELLS

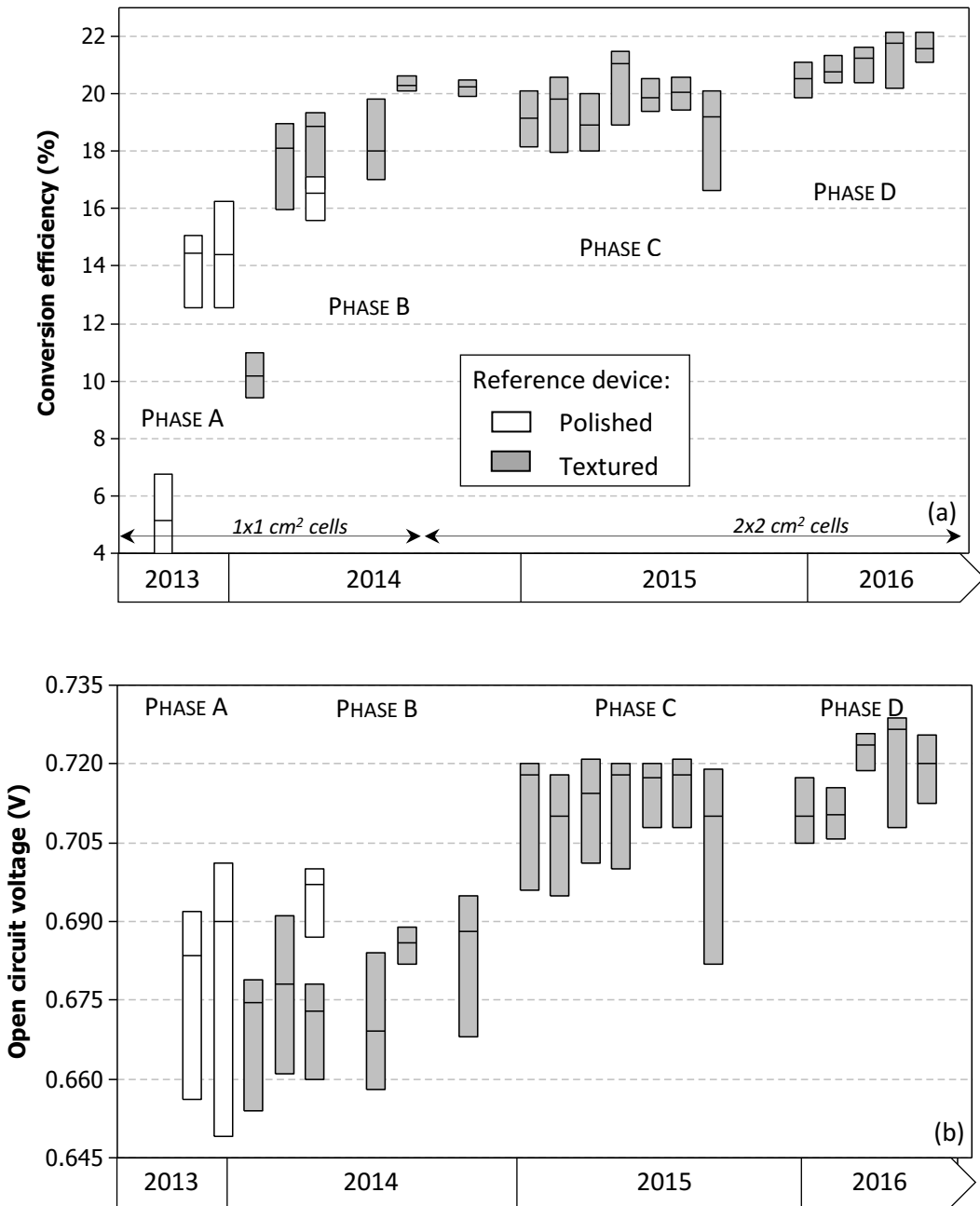


Figure 4.11. Boxplot of the evolution in (a) conversion efficiency and (b) open circuit voltage for the reference silicon heterojunction solar cells with (p)a-Si:H emitter layer in front emitter configuration.

The segment indicated as *phase A* reports data from the initial phase of setting up a complete fabrication process. These initial poor results reflect the non-optimized PECVD process with instability in the early stages. Additionally the poor yield is due to issues in handling of wafers necessary to complete the entire process. Thereafter, a sufficient degree of handling procedures and routine was reached and cells with η exceeding 16% were fabricated on polished wafers.

In *phase B* we dealt with a systematic optimization of PECVD processes and sputtering of the front TCO. Trimethylboron (TMB) was selected as doping gas to prevent a reduction of the optical band gap and increase in refractive index as compared to the diborane B_2H_6 [173]. As expected from the material optoelectronic properties, the optimized TMB doped film led to a superior optical performances with a maximum gain in short circuit current J_{SC} of 2.3 mA/cm^2 . However, the cells suffered from low FF which is attributed to the conductivity of this film, being slightly too low, as discussed above.

Reference solar cells belonging to *phase B* reached a η above 20%. The reference process was stable and, at this stage, first p-doped hydrogenated nanocrystalline materials were implemented as emitter. The relative outcomes will be discussed in chapters 5 and 6.

As shown in Figure 4.11 (b), those devices exhibited V_{OC} below 700 mV which is the main limiting factor. To address this issue the (i)a-Si:H passivation layer was further optimized in *phase C* as discussed above.

In order to enhance the surface passivation quality, both deposition parameters and post-deposition treatments were investigated. The optimized material, treated with hydrogen plasma treatment, increases passivation quality considerably to the point where only the c-Si bulk lifetime limits the minority carrier lifetime resulting in V_{OC} of 720 mV after the entire fabrication process. The now optimized reference solar cells, resulted in the best cells with J - V parameters of $J_{SC} = 38.3 \text{ mA/cm}^2$, $V_{OC} = 720 \text{ mV}$, $FF = 77.4\%$ and conversion efficiency of up to 21.3%.

After this further reference optimization, the amorphous emitter was once more replaced with p- (and also n-doped) nanocrystalline films leading to the best results as reported in chapters 5 and 6 for both front and rear emitter cells.

Finally, the work discussed in this chapter contributed to the data displayed in *phase D*. The improved solar cell parameters of those solar cells originated from further reference process optimizations carried out on industrial $125 \times 125 \text{ mm}^2$ quasi-square CZ-Si wafers. Among them, improved wafer cleaning + texturing and the use of screen-printed Ag instead of thermal evaporated Ag for the front grid fabrication. This resulted in lower series resistances and, as a results higher FF approaching 80%. This final optimization phase led to conversion efficiency of 22.2% demonstrating the potential of the PECVD and PVD processes discussed in this chapter.

The J - V parameters of our reference process are still below the record both-sides contacted SHJ solar cells by Kaneka [14] with $J_{SC} = 40.8 \text{ mA/cm}^2$, $V_{OC} = 738 \text{ mV}$, $FF = 83.5\%$ and $\eta = 25.1\%$. The comparison indicates that the conversion efficiency losses by $\sim 3\%$ is

dominated by the critical trade-off between the optical and electrical losses that reduces the J_{SC} and FF .

Both from literature and our findings discussed in this chapter, the p-doped emitter turns out as the key layer for additional optimizations. Therefore, in order to further increase the efficiency by (i) reducing the parasitic absorption in the emitter layer and (ii) by improving its electrical features for a more efficient charge separation at the junction and at the contact to the front TCO, we study the use of nanocrystalline based emitters and alternative passivation in the subsequent chapters.

5. Nucleation of p-doped Nanocrystalline Silicon Layers for SHJ Solar Cells

This chapter focuses on the integration of thin p-doped hydrogenated nanocrystalline silicon ((p)nc-Si:H) films as novel contact material in silicon heterojunction (SHJ) solar cells.

Due to their specific optoelectronic properties, nc-Si:H films are investigated to address the limitations of the reference process with p-doped a-Si:H emitters discussed in chapter 4. Concerning the electrical losses, the presence of the highly doped nanocrystalline phase offers a better carrier transport and field-effect passivation than amorphous layers do and it is promising for improving the critical contact to the front transparent conductive oxide (TCO) layer. Furthermore, the reduced parasitic absorption, due to the lower absorption coefficient in the relevant spectra range, leads to potential gain in short circuit current that are examined and discussed in chapter 6.

We investigate the (p)nc-Si:H emitter growth in stack with the (i)a-Si:H passivation layer. Key challenge is the growth of highly crystalline, *thin* layers in order to benefit from the lower parasitic absorption and enhanced electrical properties. Therefore, we address the following aspects:

- The relation among deposition regime (gas composition), optoelectronic material properties and structural features on reduced nc-Si:H film thickness.
- The substrate selectivity of nc-Si:H material towards the (i)a-Si:H layer and the effect of the substrate quality on crystalline fraction development.
- The impact of the nanocrystalline growth regime on the (i)a-Si:H layers depending on the passivation quality.

Finally, we optimize a strategy to integrate those films in SHJ cells and accomplish the requirements by oxidizing the (i)a-Si:H surface with a CO₂ plasma treatment prior the nc-Si:H emitter deposition. Part of these results have been published in [181].

5.1. Nanocrystalline Material Optimization

5.1.1. Effect of the Gas Composition

For material characterization, about 200 nm thick (p)nc-Si:H films were grown on glass substrates with deposition parameters as given in Table 5.1. Fabrication and characterization methods were described in section 3.1.2 and 3.2.1, respectively.

The deposition parameters investigated were the effect on the p-doped nc-Si:H film properties of both the H₂/SiH₄ ratio (H₂-dilution) and the dopant source-gas flows (trimethylboron TMB and diborane B₂H₆) under constant other deposition parameters.

Table 5.1. PECVD deposition parameters for the p-doped nc-Si:H materials investigated for effects of varying the doping gases and the H₂-dilution. T_{sub} : substrate temperature; P_D : plasma power density; p : chamber pressure and precursor gas flows. Electrode spacing is fixed at 16.5 mm. Doping gases are 2% diluted in H₂.

T_{sub} (°C)	P_D (mW/cm ²)	p (Pa)	SiH ₄ (sccm)	H ₂ (sccm)	H ₂ /SiH ₄ (sccm)	TMB (sccm)	B ₂ H ₆ (sccm)
205	165	667	12	4800	400	3 – 5.3	-
				6000	500	4	-
				7500	625	4	
205	165	667	12	4800	400	-	1 – 8
				6000	500	-	4
				7500	625	-	4

Experimental results of the crystalline fraction (F_C), conductivity (σ) and the refractive index at 633 nm (n) are shown in Figure 5.1 and Figure 5.2.

Regarding the H₂-dilution series, F_C and n follow the same trend for both doping gases. F_C slightly increases (Figure 5.1 (a)) and n decreases with increasing H₂-dilution (Figure 5.1 (c)). On the contrary, σ slowly reduces at higher H₂-dilution for TMB-doped films, whereas it reaches a maximum for H₂-dilution of 500 in the case of B₂H₆-doped layer (Figure 5.1 (b)).

The relation between F_C and H₂-dilution, as similarly observed elsewhere [70,182], is caused by the increase of atomic H available in the plasma for higher H₂/SiH₄ ratios that is key factor in the nc-Si:H evolution [81] (see section 2.3.2). Using TMB as doping gas, the layers exhibit values for F_C that are systematically below those of layers grown with diborane, with values up to 80% and 85%, respectively. Our data confirms the observation made by Koh *et al.* [110] who found a suppressed or delayed nucleation by adding TMB that is explained by the CH₃ radicals generated in the plasma upon dissociation of the dopant molecule.

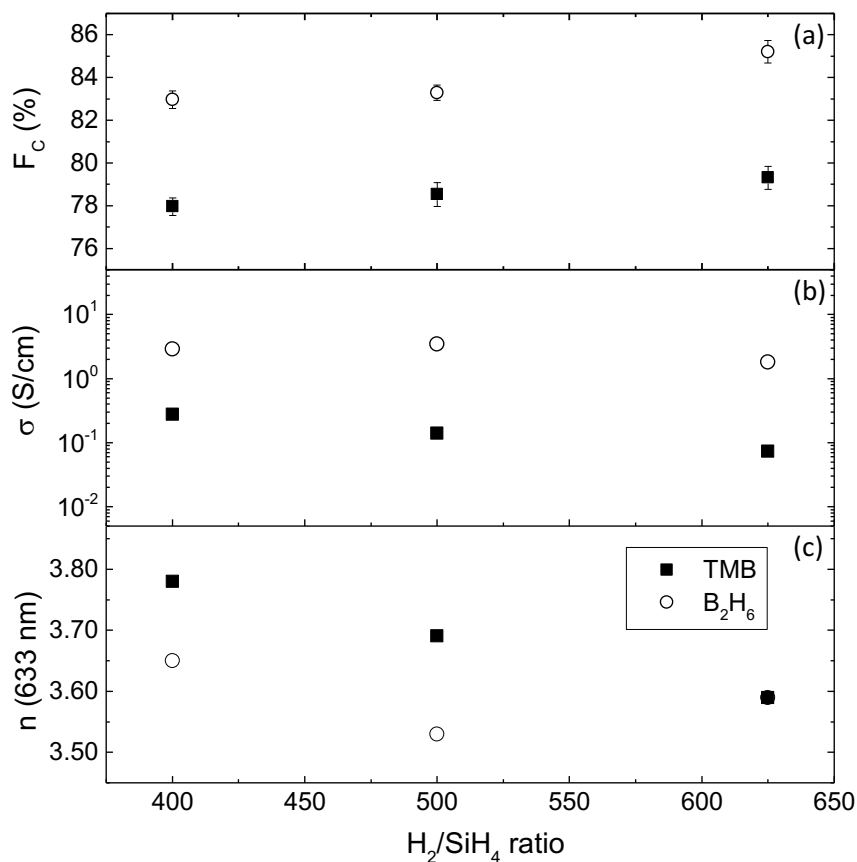


Figure 5.1 (a) Raman crystalline volume fraction F_C , (b) conductivity σ , (c) refractive index n (at 633 nm) as function of the H_2/SiH_4 ratio for (p)nc-Si:H layers doped with TMB or B_2H_6 gas (4 sccm). The layer thicknesses are of about 200 nm. The other parameters were kept constant as indicated in Table 5.1.

Concerning the conductivity, the experimental trends appear in contrast to the general observation made on nc-Si:H films that F_C was enhanced by progressively higher H_2 -dilution [70]. For higher crystalline fraction ($F_C > 70\%$) a slight decrease in σ was already observed elsewhere [183]. Interestingly, σ decreases faster when TMB is used with a reduction by one order of magnitude for the highest H_2 -dilution tested. It is worth mentioning that the conductivity discussed here is the lateral σ (measured using coplanar contacts) that is expected to be lower than the transversal σ due to the anisotropy of the nanocrystalline growth (see Figure 2.5) [126].

Another aspect that needs to be considered is the high probability that atomic H neutralizes B dopants [127]. Jiang *et al.* [127] experimentally determined that only a few percent of the total amount of boron is electrically active. This might explain the reason for the constant or even decreasing σ measured for layers that exhibit even higher crystalline phase (Figure 5.1).

In Figure 5.2, the effect of the dopant-gas flow at constant hydrogen dilution is analyzed. The H_2/SiH_4 ratio was fixed at 400 because it resulted in the highest conductivity for the TMB doped film. When comparing the two dopant sources, it is worth mentioning, that B_2H_6 delivers two boron atoms per source-gas molecule while TMB ($B(CH_3)_3$) only one. Moreover, B_2H_6 can be easily decomposed even in the absence of plasma [170], whereas TMB has a higher thermal stability with a relatively high dissociation energy for the B–C bond [184].

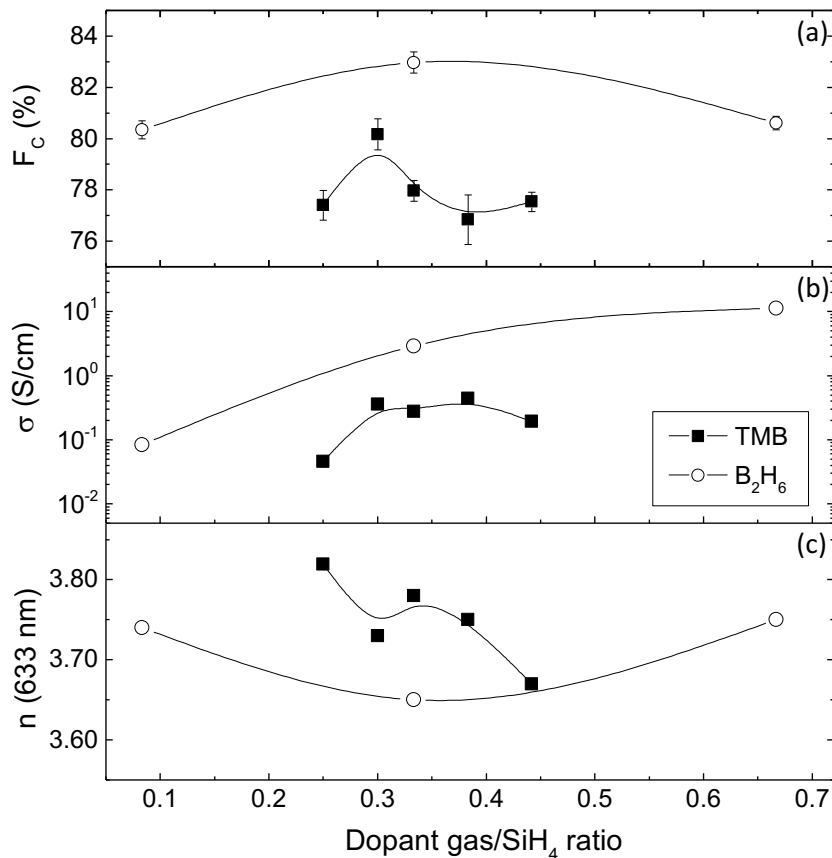


Figure 5.2. (a) Raman crystalline volume fraction F_C , (b) conductivity σ , (c) refractive index n (at 633 nm) as function of the dopant gas/ SiH_4 ratios for (p)nc-Si:H layers doped with TMB and B_2H_6 . The layer thicknesses are of about 200 nm. The other parameters were kept constant as indicated in Table 5.1. The lines are guides to the eye.

The σ is increased by two orders of magnitude for the B_2H_6 doped series reaching 10 S/cm. F_C varies slightly with a maximum for the intermediate doping gas ratio (Figure 5.2 (b) and (a)). For TMB, in contrast, σ saturates and stays below 0.5 S/cm in the range investigated whereas the F_C decreases already for TMB/ SiH_4 ratio of 0.3. For both doping gases, hence, the F_C is found to decrease with higher dopant gas flows. Concerning the optical properties, n reduces as expected ($n_{c-Si} < n_{a-Si:H}$) as the crystalline fraction F_C increases.

The observation that the boron doping hinders the crystalline growth both for B_2H_6 and TMB was discussed elsewhere [109,185,186]. Particularly, Saleh and Nickel [109] showed that the incorporation of boron atoms from B_2H_6 affects the nc-Si:H micro/nanostructure.

Moreover, the use of TMB as doping gas results in a more narrow process window for maximizing the conductivity as compared to diborane gas. Higher TMB flows are not helpful for a further increase in conductivity as it can be deduced by the data shown in Figure 5.2 (b). Also, Roschek *et al.* [185] found a similar trend for σ with comparable results for nc-Si:H films grown at H_2 -dilution below 300 with a maximum at TMB/ SiH_4 ratio of 0.3. Above this value the electrical properties rapidly degrades, in particular increasing the TMB flow by two from the optimized point leads to a decrement in σ by 2–3 order of magnitude [185].

From this comparison and from the corresponding one made on (p)a-Si:H films in section 4.2, we may draw the following conclusions. The different σ of TMB and B_2H_6 , already observed for *amorphous* films (see Figure 4.6), is detected also *nanocrystalline* layers. Both for TMB and B_2H_6 doped (p)nc-Si:H layers, the optical band gap is widened with values above 2 eV. The amorphous films selected for cell application, in comparison had E_{04} 's of 1.96 for (TMB) and 1.85 eV (B_2H_6). The optoelectronic properties of both amorphous and nanocrystalline films faster reached the saturation when TMB is used, which is believed to be caused by the presence of CH_3 radicals in both cases [110]. In conclusion, diborane appears to be the more suitable doping gas.

Preliminary Cell Results

To investigate the effect of the H_2 -dilution discussed in Figure 5.1 on the cell performance, two solar cell series were fabricated with emitter layers doped with optimized B_2H_6 and TMB gases flows. The solar cells had all the same structure (see Figure 3.1) with emitter layer thickness in the range of 15 – 20 nm.

Box plots for the fill factors (FF) are depicted Figure 5.3. All the cells have open circuit voltages in the range of 715 – 725 mV and conversion efficiency of 18 – 20%.

Despite the similar trends observed for the thick layers in Figure 5.1, the impact of the H_2 -dilution on the FF was different for the TMB and B_2H_6 doped cells.

Devices having TMB doped emitters showed FF s that increase with a maximum approaching 77% for the best device (Figure 5.3 (a)) but a sharp decay for higher dilution. On the contrary, when B_2H_6 is used as doping gas, the FF was almost independent on the H_2 -dilution with values limited to about 75%.

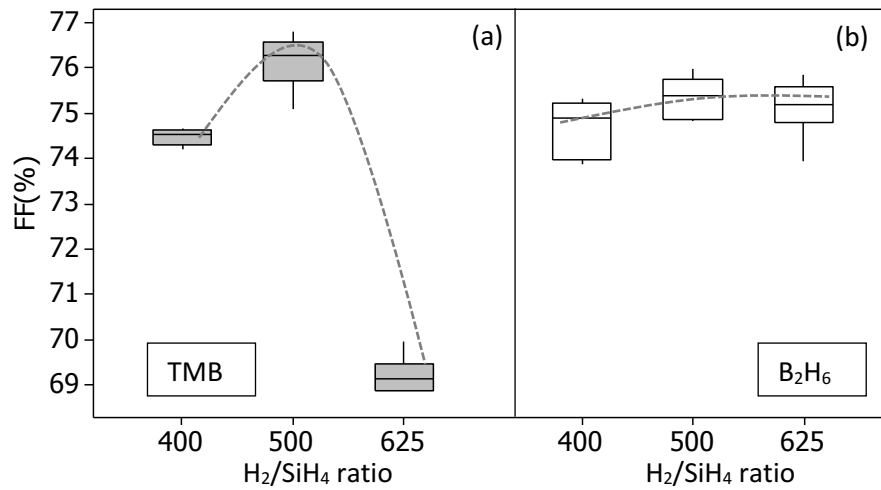


Figure 5.3. Box plots of fill factor FF of two series of solar cells (based on 7 cells) with varying the H_2/SiH_4 ratio of the (p)nc-Si:H emitters doped with (a) TMB and (b) B_2H_6 gases (4 sccm). Deposition parameters for the emitters are given in Table 5.1 and the layers are grown with a nominal thickness of 15 nm. The lines are guides to the eye.

The lower FF s found in case of B_2H_6 emitters were in contrast to our expectations based on the properties measured on (thick) single layers, i.e. the higher F_c (5% absolute) and the higher conductivity by one order of magnitude in comparison to TMB doped films.

In the following sections, cells having (p)nc-Si:H layers doped with TMB will be discussed concerning the nucleation on the underlying (i)a-Si:H film and control of the surface passivation performances.

5.2. Integration of Thin nc-Si:H Layers in SHJ Cells

In this section the development of SHJ solar cells with TMB doped nc-Si:H emitters is described. Firstly, combinations of different intrinsic passivation films with a nanocrystalline emitter are investigated (section 5.2.1). Then, sections 5.2.2 and 5.2.3 focused on the impact of the thin nc-Si:H film on the passivation. Finally, the effect of the dopant gas flow on cell performance is discussed in section 5.2.4.

Selected films were investigated in layer stacks similar to those in completed solar cell devices. The (p)nc-Si:H films were grown in a stack with the passivation layers and the emitter thickness was reduced drastically. The properties of the (i)a-Si:H layers have been discussed in section 4.1, while for the p-doped films the reader can refer to the previous section 5.1.

Table 5.2 summarizes deposition parameters and thicknesses used in the cells. For an overview of the different types of samples and corresponding investigation techniques the reader can refer to Table 3.4.

5.2. Integration of Thin nc-Si:H Layers in SHJ Cells

Table 5.2. PECVD parameters of (i)a-Si:H and (p)nc-Si:H films used for cell fabrication. t : layer thickness, T_{sub} : substrate temperature, P_D : plasma power density, p : chamber pressure and precursors gas flows. Electrode spacing was fixed at 16.5 mm.

Material	t (nm)	T_{sub} (°C)	P_D (mW/cm ²)	p (Pa)	SiH ₄	H ₂	TMB
					(sccm)		
type A (i)a-Si:H	6	205	15	200	180	900	-
type B (i)a-Si:H	6	190	20	200	300	300	-
(p)nc-Si:H	15	205	165	667	12	4800	2.7–6.0

5.2.1. Nanocrystalline Silicon Nucleation

To investigate the nanocrystalline growth, (p)nc-Si:H films doped with TMB were selected from the set of recipes analyzed in section 5.1.1, therefore the TMB/SiH₄ ratio was set at 0.25 (TMB = 3 sccm) and 0.33 (TMB = 4 sccm).

Figure 5.4 shows the Raman spectra of set of stacks grown on glass substrate.

To study the effect of a reduction in emitter thickness, a p-doped nc-Si:H film was deposited directly on the glass substrate with a nominal thickness of 25 nm, which is a reasonable layer thickness to deposit for making device.

The corresponding Raman spectrum in Figure 5.4 (a) exhibits a crystalline fraction F_C of 68.4%. The value is remarkably close to the one found for the 200 nm thicker film deposited using the same condition ($F_C = 78\%$). The small shoulder visible at about 500 cm⁻¹ originates from the very small crystals and grain boundary and it was equally detected for the thicker film (not shown here). Considering that the nc-Si:H film is only 25 nm thick and the laser used for the Raman investigation is in the blue range, we can suppose that the entire film thickness is probed. It can be indirectly deduced that thin (p)nc-Si:H layer is already in the nanocrystalline-growth regime and that the incubation zone (IZ) thickness is well below 25 nm on glass substrates. Similar values can be found in literature for about 25 nm thick films [101,108].

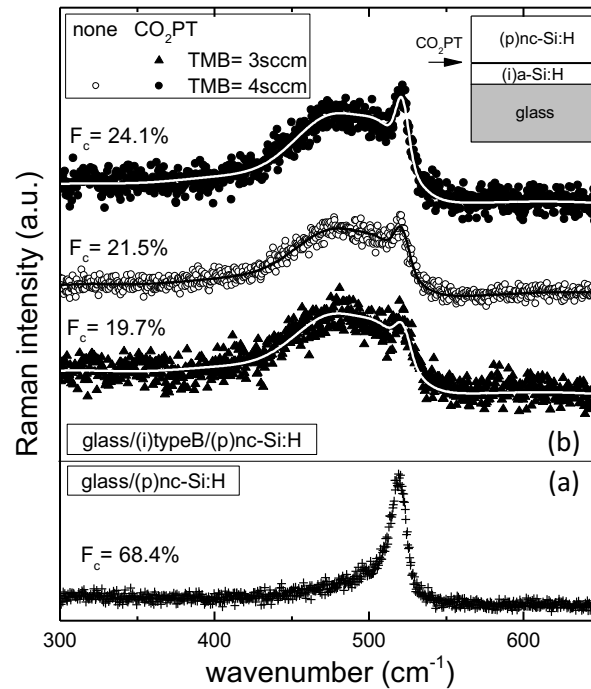


Figure 5.4. Experimental data and fitted curves obtained from Raman spectra (laser 442 nm) for (a) the reference without (i)a-Si:H layer and (b) for stacks with (i)a-Si:H layer of type B. Full symbols indicate (i)a-Si:H layer treated with CO₂PT (plasma parameters are in Table 5.3) whereas open symbols without any treatments on the i-layer surface. The variations in the (p)nc-Si:H emitter are specified in the legend. The layer stack is depicted in (b) and the arrow indicates the interface treated with CO₂PT. The corresponding crystalline fraction F_C are also indicated for each spectrum. The curves are vertically shifted for easier comparison.

Since a great influence of the (i)a-Si:H film on the F_C is expected due to the permeability of the amorphous silicon layer to the atomic H [97], different structures were fabricated by inserting a 7 nm thick (i)a-Si:H layer of type B between the glass substrate and the p-doped layer. The thickness of the (p)nc-Si:H film was again fixed at 25 nm and the resulting structures investigated by Raman.

Figure 5.4 (b) shows that the amorphous film radically reduces the crystalline fraction in the (p)nc-Si:H films down to a value below 25%. The broad peak centered at 480 cm⁻¹ is a clear indication of the increased amorphous fraction within the stack. On type B (i)a-Si:H, an F_C of 21.5% was measured for (p)nc-Si:H with TMB of 4 sccm.

Strategies have been suggested to enhance the fast crystallization of nanocrystalline silicon as discussed in section 2.3.2. Among them, CO₂ plasma treatment (CO₂PT) [114,118] or oxidation in air [117] has been reported in literature and applied in thin film silicon devices. Pernet *et al.* [119] indicated that such treatment results in SiO_x formation on the intrinsic amorphous layer underneath.

5.2. Integration of Thin nc-Si:H Layers in SHJ Cells

Figure 5.4 (b) shows the Raman spectra of stacks with an (i)a-Si:H interface oxidized by means of a CO₂PT directly performed after the i-layer deposition and prior to the (p)nc-Si:H film growth. The plasma conditions selected for the CO₂PT are reported in Table 5.3, whereas the TMB flow for the doped films are fixed at 3 and 4 sccm.

Table 5.3. PECVD parameters for the CO₂PT applied to oxidize the (i)a-Si:H surface before the (p)nc-Si:H deposition.

	T_{sub} (°C)	P_D (mW/cm ²)	p (Pa)	Electrode spacing (mm)	CO ₂ (sccm)	time (s)
CO ₂ PT	205	15	200	20	100	10

The (p)nc-Si:H layer deposited with higher TMB flow on the well passivating type B (i)a-Si:H film reaches a value of F_c of 21.5%.

A higher F_c for the (p)nc-Si:H layer grown with TMB of 4 sccm as compared to the lower TMB flow showed up similarly on thick layers (compare Figure 5.2), where the highest F_c was reached for a TMB flow of 3.6 sccm. However, it remains speculative if this is a systematic behavior as also slight thickness fluctuations might influence the results.

Applying both the CO₂PT and the higher TMB/SiH₄ ratio, the crystalline fraction was enhanced with a maximum of 24.1%.

Moreover, a lateral conductivity of $2.6 \cdot 10^{-5}$ S/cm was measured for the sample showing a F_c of 24.1% (TMB flow of 4 sccm) while a value below the measurement limit of our equipment ($< 10^{-9}$ S/cm) was found for the one grown with a TMB flow of 3 sccm. This makes the first one attractive for application as emitter in solar cells, as will be shown in the next section.

5.2.2. Impact on the Passivation

In the previous section, different i-layer/(p)nc-Si:H stacks were investigated in terms of structural properties. Next, the afore-mentioned stacks were tested on c-Si wafers to investigate the effect of the nanocrystalline growth and the CO₂PT on the (i)a-Si:H passivation film. Moreover, this investigation was expected to reveal indirect information on the nanocrystalline growth of (p)nc-Si:H films on the amorphous layer underneath.

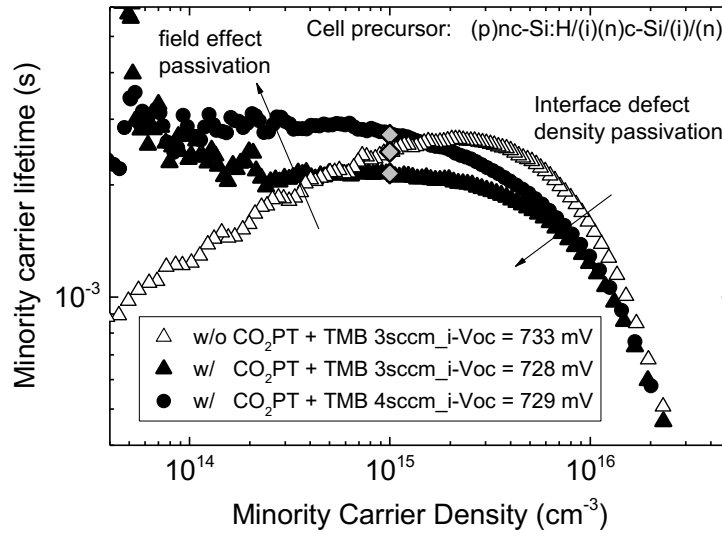


Figure 5.5. Minority carrier lifetime measurements performed on cell precursors (p)/(i)/(n)c-Si/(i)/(n) deposited on textured c-Si with a without a CO₂ plasma treatment on the front passivation layer of type B. The p-doped layer is (p)nc-Si:H deposited with TMB flows of 3 sccm or 4 sccm. τ_{eff} are extracted at minority carrier density of 10^{15} cm^{-3} as indicated in the plot by the diamond symbols.

Figure 5.5 shows the minority carrier lifetime spectra measured on three samples fabricated on textured c-Si wafers. The stacks consisted of the same (i)a-Si:H film of type B and the two different (p)nc-Si:H layers deposited with TMB at 3 sccm and 4 sccm. On the other side of the wafers the same (i)/(n) stack was deposited to focus on the variation on the p-doped side.

For the stack without the CO₂PT, the minority carrier lifetime curve is high (efficient passivation) in the high carrier density range (= efficient chemical passivation) leading to $i-V_{oc} = 733 \text{ mV}$, but drops as the minority carrier density decreases, most likely because of a poor field-effect passivation. These experimental observation might be explained by the higher hydrogen dilution combined with a high plasma power required for the nanocrystalline growth of the doped layer. Under these plasma conditions, higher precursor dissociations provide more atomic hydrogen [121] that is able to penetrate the amorphous film and passivate dangling bonds at the a-Si:H/c-Si interface such as the hydrogen plasma treatment (HPT) does.

In contrast, when the i-layer surface is treated with the CO₂PT before growing the nc-Si:H emitter, the lifetime increases in the low injection region where the field-effect becomes dominant. On the other hand, the CO₂PT causes a slight reduction in chemical passivation leading to $i-V_{oc}$ of 728 mV. Finally, the increase in TMB flow leads to even further increase in charge carrier lifetime in the low injection level whereas the $i-V_{oc}$ stays constant. The resulting i -FF reaches the highest value of 82.8% for the sample with TMB flow of 4 sccm.

To recapitulate, for a fixed type of (i)a-Si:H substrate, the CO₂PT together with higher dopant gas flow are responsible of increased crystalline fraction that allows for higher doping efficiency. It is worth noting that the type B (i)a-Si:H layer even when it was not treated with HPT, reached high values of $i-V_{oc}$ and τ_{eff} in combination with doped nano-crystalline films.

Some authors [187–189] identified, both from experiments and theoretical considerations, the so-called *percolation threshold* for p-doped nc-Si:H films at a crystalline fraction of $\sim 20 - 30\%$. The structural connection within the nc-Si:H network is usually deduced by an upward discontinuity in transport properties such as mobility and/or conductivity [187] and it also related to the overcome of the incubation zone [189]. This leads to higher space charge in the p-doped layer that results in an enhanced field-effect passivation [189], that is consistent with our findings in Figure 5.5 and the structural properties previously discussed in Figure 5.4 (b). Thus, we can infer that in the CO₂ treated sample the nc-Si:H overcomes the percolation threshold.

To further investigate this aspect, the minority carrier lifetime curves for samples with (p)nc-Si:H layer deposited on both types of i-layers were compared to similar structures with amorphous (p)a-Si:H films. The graphs of the variation of $i-V_{oc}$ with sample type and the dependence of carrier lifetime on injection level are presented in Figure 5.6 (a) and (b), respectively.

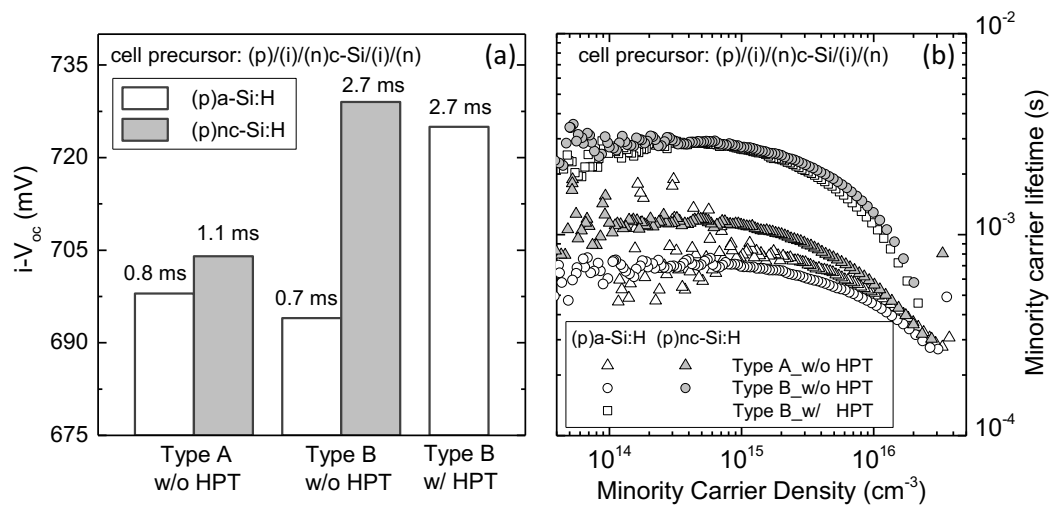


Figure 5.6. (a) Implied open circuit voltage $i-V_{oc}$ and minority carrier lifetime τ_{eff} measured on cell precursors (p)/(i)/(n)c-Si/(i)/(n) deposited on textured c-Si. Type A and B i-layers are combined with (p)a-Si:H and (p)nc-Si:H (CO₂PT and TMB= 4 sccm). (b) Corresponding minority carrier lifetime curves. Data for samples with (p)a-Si:H films are taken from Figure 4.3 in section 4.1.

It has been already exposed in section 4.1 that the type B i-layer requires HPT to reach a good passivation level and, in combination with (p)a-Si:H film, $i-V_{OC}$ of 725 mV was achieved. Instead, the curves corresponding to the optimized (p)nc-Si:H layers show higher carrier lifetime than the corresponding samples with (p)a-Si:H films. The strongest effect was observed for the type B i-layer with a τ_{eff} of 2.7 ms and $i-V_{OC}$ of 729 mV. A similar outcome has been reported in [190,191].

When type A i-layer was used, the improvements in surface passivation were more limited and were mainly driven by field-effect passivation. Olibet *et al.* [88] showed similar trend for their (p)nc-Si:H in the low injection level range whereas the surface passivation either did not improve or degraded when compared to the symmetric passivated structure with only i-layer.

The data shown in Figure 5.6 demonstrate that nanocrystalline deposition influences the interface defect density depending on the quality of the (i)a-Si:H layer. A similar effect was observed for the hydrogen plasma treatment that more effectively passivates dangling bonds if the i-layer is completely free of an epitaxial phase (section 4.1).

Solar Cell Results

Figure 5.7 shows the $J-V$ curves obtained for a nc-Si:H emitter deposited from a recipe with a TMB flow of 3 sccm prepared by using both type A and type B (i)a-Si:H films.

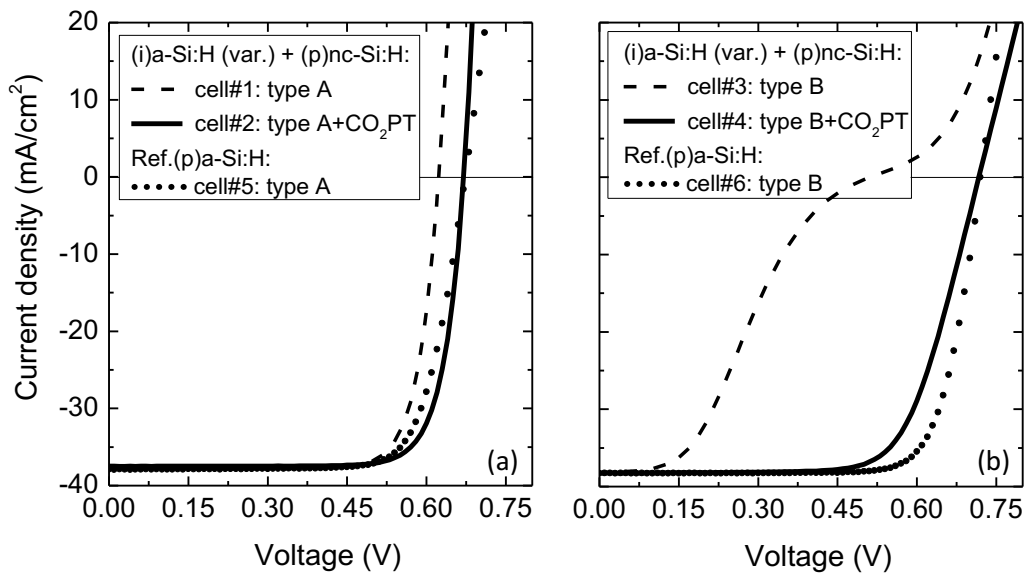


Figure 5.7. Illuminated $J-V$ characteristics for the best cells on textured c-Si wafers with 15 nm (p)nc-Si:H emitter grown on top of type A (a) and type B (b) i-layer. The passivation films were tested in stacks with and without the CO₂PT. Cell parameters are reported in Table 5.4. Cells with (p)a-Si:H emitter doped with TMB are given for both types of i-layer as references. Only for cell #6 the i-layer is treated with HPT as discussed in section 4.1.

5.2. Integration of Thin nc-Si:H Layers in SHJ Cells

The cell parameters are summarized in Table 5.4 together with those for CO₂ plasma treated i-layers for comparison. In the same picture, cells with the (p)a-Si:H emitter grown on both types of i-layers are given as reference.

Table 5.4. Solar cell parameters of the best cells shown in Figure 5.7 both with (p)nc-Si:H and (p)a-Si:H emitters. In brackets, the average values based on 7 cells for each wafers. The CO₂PT and HPT parameters are reported in Table 5.3 and Table 4.1, respectively.

Cell	(i)a-Si:H	PT	J_{sc} (mA/cm ²)	V_{oc} (mV)	FF (%)	η (%)	R_s (Ω cm ²)	
(p)nc-Si:H	#1	type A	-	37.8 (37.8±0.3)	623 (621.1±2.2)	79.1 (78.6±0.4)	18.6 (18.4±0.2)	1.48
	#2	type A	CO ₂	37.5 (37.5±0.2)	670 (672.8±1.5)	79.5 (79.1±0.3)	20.0 (19.9±0.1)	1.31
	#3	type B	-	38.2 (38.2±0.1)	512 (511.0±3.6)	32.5 (69.4±0.8)	6.4 (6.4±0.1)	> 40
	#4	type B	CO ₂	38.1 (38.0±0.2)	718 (715.9±3.5)	70.0 (69.4±0.8)	19.2 (18.9±0.3)	3.68
(p)a-Si:H	#5	type A	-	38.4 (38.2±0.2)	683 (681.0±5.3)	76.6 (75.9±1.0)	20.1 (19.8±0.3)	1.81
	#6	type B	HPT	38.3 (38.2±0.2)	720 (719±0.5)	77.4 (77.1±0.3)	21.3 (21.2±0.1)	2.05

Cell #1 grown on the type A i-layer without CO₂PT has a well-shaped light J - V curve (Figure 5.7 (a)) with a FF above 79%. As expected the passivation performance of the type A film is poor with the observed V_{oc} (623 mV) even lower than the one expected from passivation tests (see Figure 5.6). This value is about 60 mV lower than the V_{oc} measured on the reference device with a (p)a-Si:H emitter (cell #5).

Degradation of the type A i-layer passivation is a likely cause for the lower voltage observed on completed cells with such a stack and might be induced by the more aggressive plasma condition for the nanocrystalline growth of the p-type layer. Similar trend, but with more severe reduction in V_{oc} , were found after treating the type A passivation film with HPT (see Figure 4.1).

The same nc-Si:H emitter was deposited on the well-passivating (= fully amorphous) type B i-layer with completely different outcomes (cell #3 in Figure 5.7 (b)). The cell shows a strong S-shape character with a V_{oc} of 512 mV that is lower than the value expected from the i- V_{oc} (733 mV). The low built-in voltage caused by the low effective free-carrier density in the emitter due to the F_c be lower than the percolation threshold can explain the wide discrepancy in voltage [189]. Moreover, the minority carrier lifetime curve showed in Figure 5.5 confirms that the cell #3 is not limited by surface defect passivation.

The nc-Si:H grown on a completely amorphous passivation film results in a lower F_C (as confirmed by Raman investigation) that reduces the conductivity and the effective doping in the bulk emitter. Lower voltages were also observed by Pernet *et al.* for i-layers that were not treated with CO₂PT or HPT [114].

In Figure 5.7, the positive effect of the CO₂PT is visible (cell #2 and #4). For the epitaxial type A layer, the J - V curve in Figure 5.7 (a) shifts towards higher voltages (+ 50 mV) with further increase in FF (up to 79.5%). The latter value is associated with reduced series resistance R_s . The enhanced crystalline fraction in the emitter can positively influence the contact to the front transparent conductive oxide (TCO) and results in lower resistances.

The effect of the CO₂PT has an even more pronounced impact on cell #4 grown using the fully amorphous (i)a-Si:H type B (Figure 5.7 (b)). It leads to removal of the S-shape character with a V_{OC} improvement of +200 mV (V_{OC} = 718 mV). From the R_s reported in Table 5.4, the cell suffers from high series resistance problems that might be related to the still poor nucleation on the epitaxy-free i-layer.

In order to further investigate the structural properties of both (i)a-Si:H and (p)nc-Si:H, the front side stacks (c-Si/(i)a-Si:H/(p)nc-Si:H/(In₂O₃:Sn, ITO)) of completed cells were analyzed by cross sectional HR-TEM.

Micrographs of the device with type A i-layer are shown in Figure 5.8 and Figure 5.9 taken from different positions along the pyramid profile. The a-Si:H/c-Si interface is blurred primarily in the valley between two consecutive pyramids but also on the facets. The dark area in the pyramid valley demonstrates the epitaxial nature of the passivation layer. This area has lattice orientation as the c-Si substrate as indicated by the Fourier transforms in the bottom part of Figure 5.8 (insets A and B).

Along the pyramids facets, the (i)a-Si:H film appears amorphous but it is periodically interrupted by epitaxial areas (dark structures in Figure 5.8 and Figure 5.9 (b)). The epitaxy is responsible for higher interface defect density (e.g. at grain boundaries) and, thus, V_{OC} below 700 mV (see Table 5.4). The (i)a-Si:H film is about 6 nm thick even if it is difficult to identify the transition from the amorphous layer to the nanocrystalline emitter. Moreover, the a-Si:H/c-Si interface appears to be rough even in the regions where the (i)a-Si:H develops as amorphous (as indicated by the white lines in Figure 5.9 (a) and (b)). Olibet *et al.* [88] observed a not abrupt a-Si:H/c-Si interfaces when the emitter stack was deposited on textured c-Si. The growth of a nominally amorphous silicon film by PECVD on textured c-Si can lead to an epitaxial phase due to variation of the deposition rate on different substrate orientations and increased residual stress in the film [145].

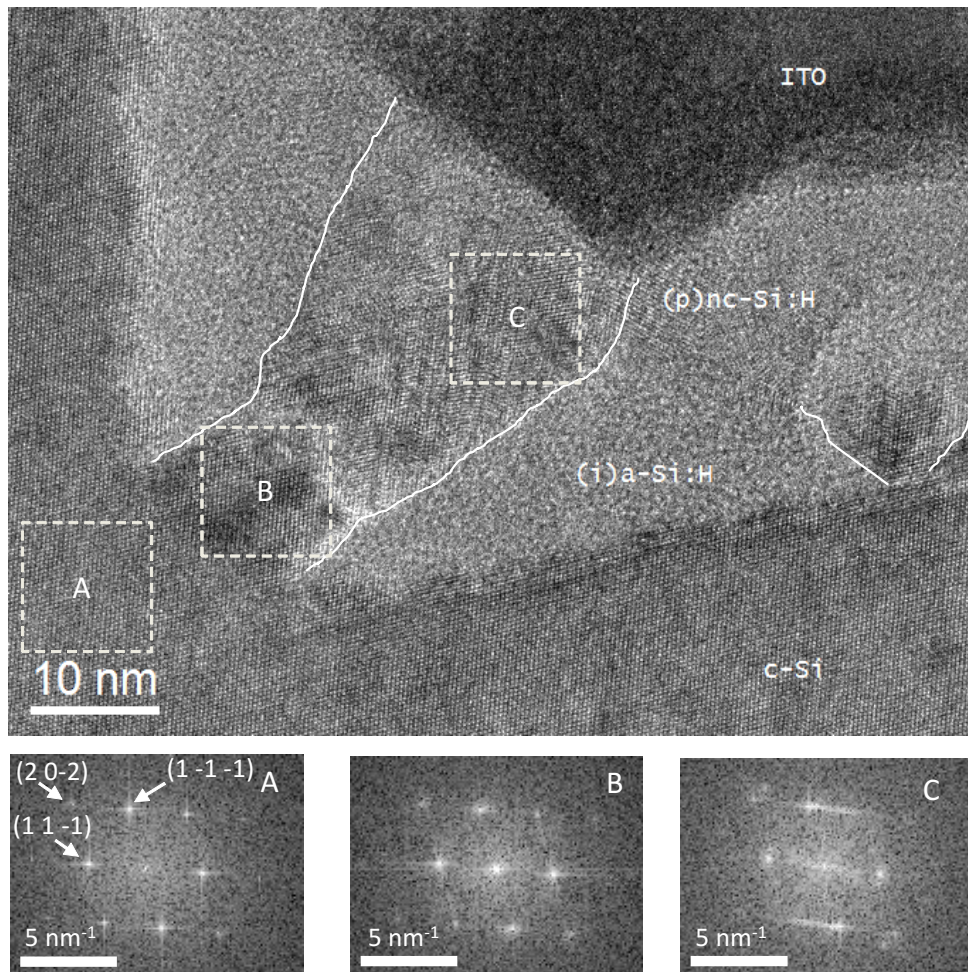


Figure 5.8. Cross sectional HR-TEM micrograph of the front side cell stack (c-Si/(i)a-Si:H/(p)nc-Si:H/ITO) in the valley for the device with type A (i)a-Si:H layer. The zone axis orientation for the Si substrate is [101]. The small insets are the Fourier transforms calculated in the area indicated by the letters. Lines highlight individual crystals.

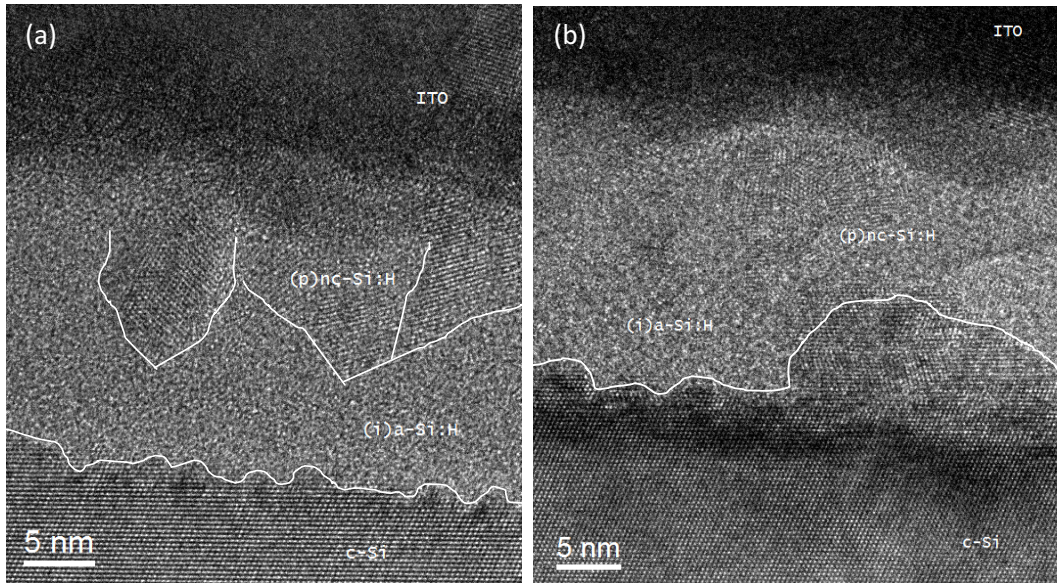


Figure 5.9. Cross sectional HR-TEM micrographs of the front side cell stack (c-Si/(i)a-Si:H/(p)nc-Si:H/ITO) on the facet for the device with type A (i)a-Si:H layer. Defined nanocrystalline grains (a) and epitaxial a-Si:H/c-Si interface in (b) The zone axis orientation for the Si substrate is [101]. Lines highlight individual crystals and the rough a-Si:H/c-Si interface.

The nc-Si:H layer, grown on top of the passivation layer, exhibits defined crystallites which evolve from the (i)a-Si:H layer (Figure 5.8 and Figure 5.9). In the valley, the nc-Si:H emitter develops with a columnar character due to the template given by the type A passivation layer not fully amorphous. It is possible to identify the related lattice orientation as indicated by the inset C in Figure 5.8. The existence of such highly crystallized and oriented grains, might explain the very low series resistance measured on this cell and the associated high *FF*.

The layer thickness appears non-uniform along the facet with an average thickness of about 15 nm.

Figure 5.10 shows a HR-TEM micrograph of the device with type B i-layer that was oxidized before the emitter growth. As expected from τ_{eff} tests, the a-Si:H/c-Si interface is abrupt with a fully amorphous and uniform (i)a-Si:H layer with a thickness of about 5 nm. The nanocrystalline emitter grows uniformly on top of it and the layer thickness is lower than the expected one by about 3 nm. The crystallites are well defined and more homogeneously distributed with various orientations in the bulk of the film. The Fourier transforms (insets in the same Figure 5.10) confirm the observations.

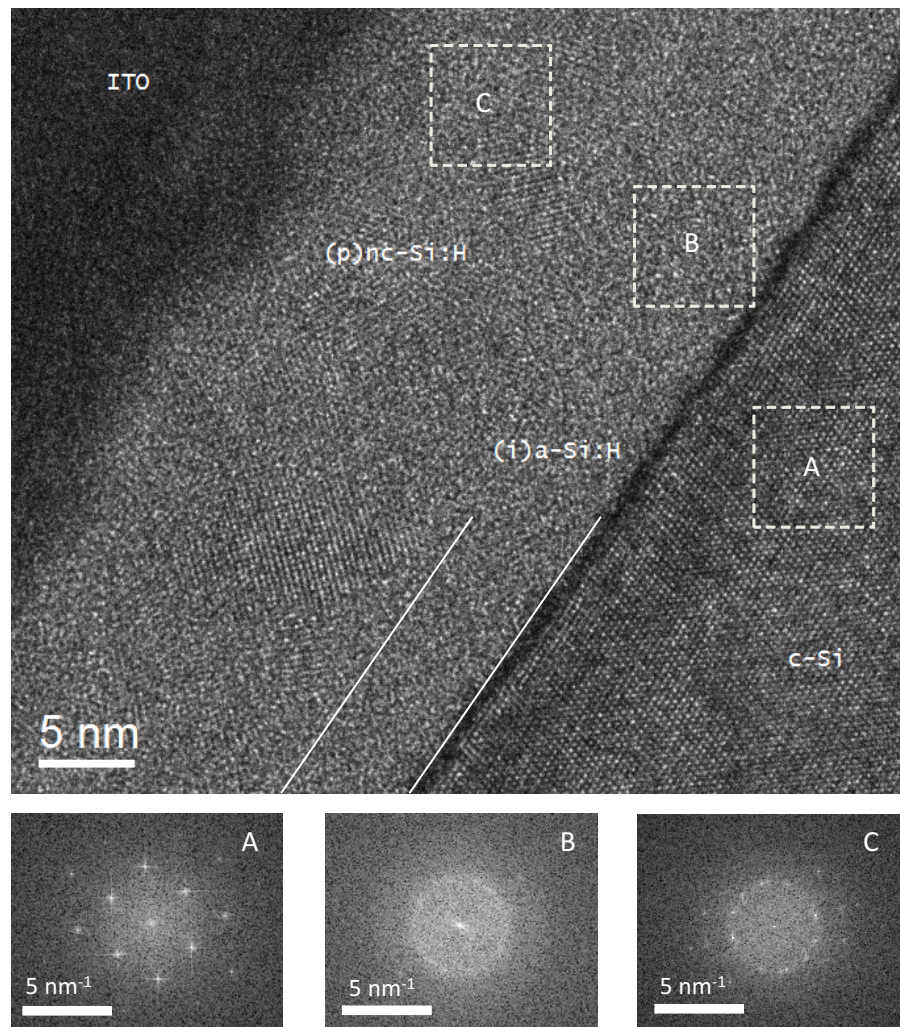


Figure 5.10. Cross sectional HR-TEM micrograph of the front side cell stack (c-Si/(i)a-Si:H/(p)nc-Si:H/ITO) on the facet for the device with type B (i)a-Si:H layer treated with CO₂PT. The zone axis orientation for the Si substrate is [101]. The small insets are the Fourier transforms calculated in the area indicated by the letters. Lines highlight the passivation layer.

5.2.3. Variation of the (i)a-Si:H Passivation Film Thickness and Morphology

In this section, the effect of the (i)a-Si:H thickness in combination with a (p)nc-Si:H emitter is investigated on polished wafers. The same variation in thickness was applied to a device having a (p)a-Si:H layer as a reference. In Figure 5.11 (a), the V_{OC} against the (i)a-Si:H deposition time is shown.

The V_{OC} progressively increases with (i)a-Si:H thickness due to the beneficial interface defect passivation [60]. A similar trend is observed for both amorphous and nanocrystalline emitters. The introduction of the CO₂PT on the i-layer surface appears to be beneficial for the (p)nc-Si:H film evolution also on polished substrate with enhanced open circuit voltages. The gain in V_{OC} is of about 100 mV for passivation layer of 15 s (~2.5 nm), while for thicker i-layer the curves approach to a closer values.

On the other hand, the values of R_{OC} is dependent on both diode quality and the (ohmic) contact resistance. In this experiment it was not possible to distinguish between each resistive contribution considering that the variation of the substrate layer influences the complete nc-Si:H evolution, from the IZ to the bulk, to the front TCO contact. R_{OC} for cells with (p)a-Si:H and (p)nc-Si:H emitters as a function of (i)a-Si:H deposition time are presented in Figure 5.11 (b).

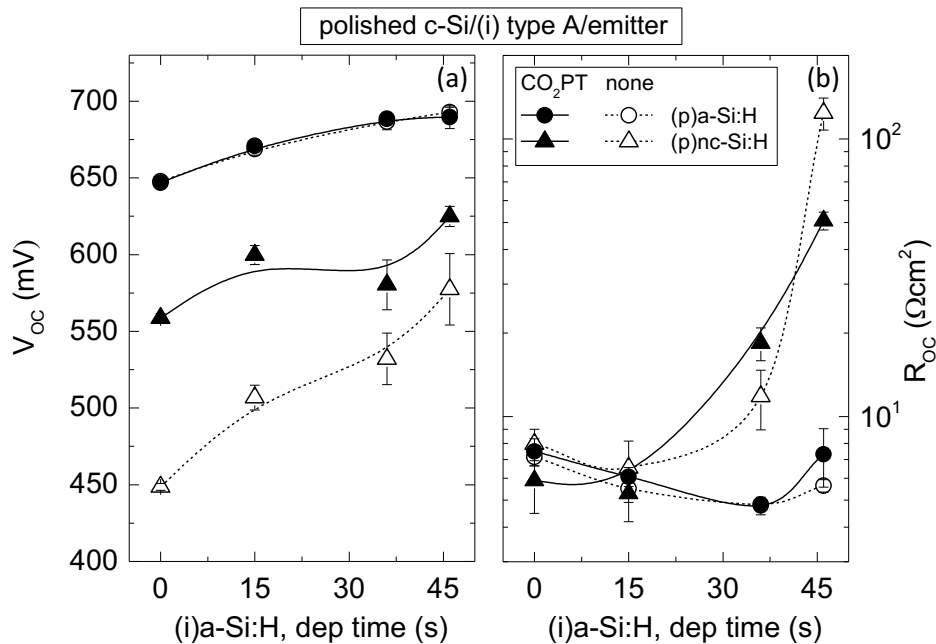


Figure 5.11. (a) V_{OC} and (b) R_{OC} extracted from illuminated J - V curves of cells growth on polished n-type $\langle 111 \rangle$ oriented c-Si wafers as function of the (i)a-Si:H deposition time. The passivation layer used is of type A and (p)a-Si:H or (p)nc-Si:H as emitter. The CO₂PT is applied directly after the i-layer grown with deposition parameters reported in Table 5.3. The values are the average based on 8 cells for each wafers. Deposition rate of type A (i)a-Si:H is 0.174 nm/s. Lines are guides to the eye.

5.2. Integration of Thin nc-Si:H Layers in SHJ Cells

For the fully amorphous emitter R_{OC} is reduced with increasing i-layer thickness up to a minimum at a deposition time of 36 s. Interestingly, the CO₂PT has a negligible effect on the (p)a-Si:H cell with a slight increase of R_{OC} . This indicates that the oxidation of the (i)a-Si:H is limited to areas close to the surface and thus being very thin, only marginally impedes the flow of charge carriers at the (i)/(p) interface.

For devices having nc-Si:H emitters, R_{OC} rises with (i)a-Si:H thickness for both the untreated and CO₂ plasma treated i-layer surfaces indication of the severe S-shape character of the J - V curves with nc-Si:H emitters. The results discussed here and in the previous section highlight that the substrate morphology plays a decisive role on the nanocrystalline evolution of the doped layers in SHJ cells. As a result, the trade-off between good passivation and low contact resistance is still limiting the cell performance.

5.2.4. Effect of the Doping Gas Dilution

It was already observed in sections 5.2.1 and 5.2.2 that a higher TMB flow (4 instead of 3 sccm) leads to nc-Si:H films with (slightly) higher crystallinity and higher conductivity as well as to better passivation, in particular for low carrier injection. Hence, it is expected that this will also result in better solar cells, with higher values for V_{OC} and FF .

To verify this, six samples with varying TMB gas flows were selected from the study on single layers discussed in Figure 5.2 and used as emitters with a thickness of 15 nm. The thickness of all the other layers and the cell design are identical for the entire series.

The resulting J - V parameter as a function of TMB gas flow are shown in Figure 5.12. The conversion efficiency gradually rises with the TMB flow with a maximum at about 4 sccm, as expected. This trend is dominated primarily by the variation in V_{OC} and FF (R_{OC}) with a maximum of 727 mV and a minimum of 2.5 Ω -cm², respectively. For the best device, moreover, a gain in J_{SC} of 0.6 mA/cm² is found.

The progressive increase in V_{OC} for the TMB flow in the range 2.7 – 4 sccm is ascribable to the progressive increment in field-effect passivation as deduced from minority carrier lifetime measurements as show in Figure 5.5 for TMB flow of 3 and 4 sccm. This trend is determined by the crystalline fraction enhancement that results in an increased electric field strength at the junction. In particular, the (i)a-Si:H/(p)nc-Si:H stacks investigated by Raman for 3 and 4 sccm showed a F_C of 19.7% and 24.1% (the correspondent Raman spectra are depicted in Figure 5.4), respectively.

The progressive increment in J_{SC} in the same doping flow range is a further consequence of the higher F_C due to both reduced parasitic absorption and improved transparency.

5. NUCLEATION OF P-DOPED NANOCRYSTALLINE SILICON LAYERS FOR SHJ SOLAR CELLS

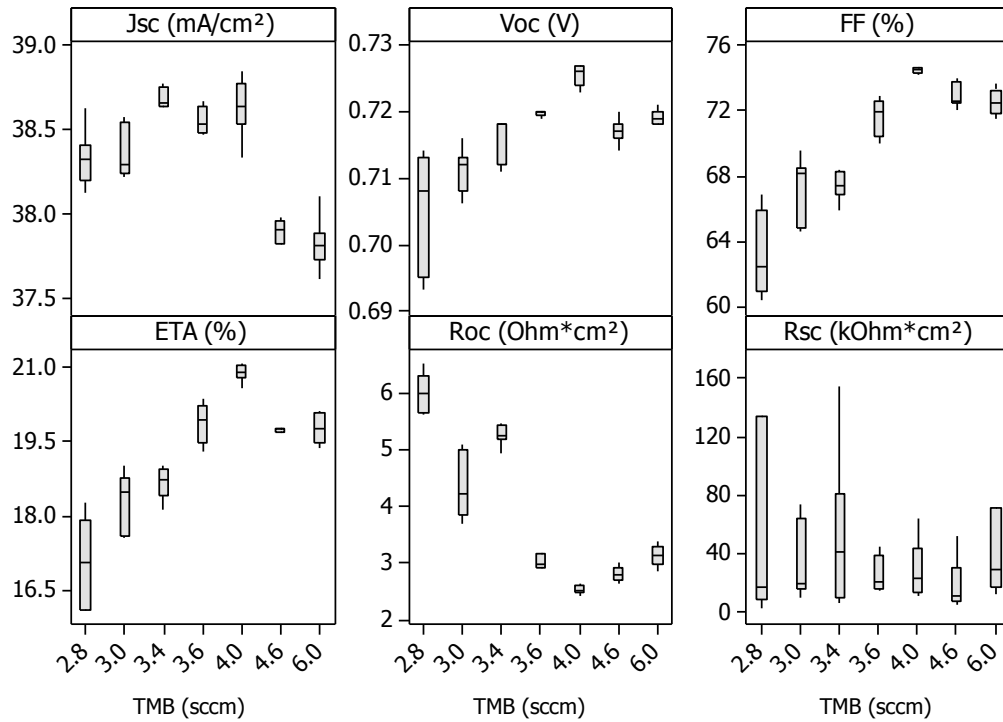


Figure 5.12. Box plots of the cell parameters based on 7 cells with varying the TMB flows of the nc-Si:H emitter with a nominal thickness of 15 nm. The cells are grown on n-type both sides textured c-Si wafers passivated with type B i-layer. Optical and electronic properties of the emitters are given in Figure 5.2.

For higher TMB flows, the boron reduces the crystalline fraction as discussed above for the single layers and in Ref.s [109,186]. This results in a reduction in σ by 60% from the maximum of 0.44 S/cm leading to a reduced V_{oc} as measured on corresponding cells.

On cell level, it can be observed that the doping flow optimum stays at 4 sccm that is the condition at which the best compromise between optical and electrical properties is found. Single layers data shown in Figure 5.2 measured on thicker single layers reveal a maximum F_c for 3.6 sccm. Such small discrepancy might be attributed to the drastically lower thickness for the layers deposited in the devices.

The J - V characteristic for the best cell of this series is depicted in Figure 5.13 and compared to the reference cell with (p)a-Si:H emitter.

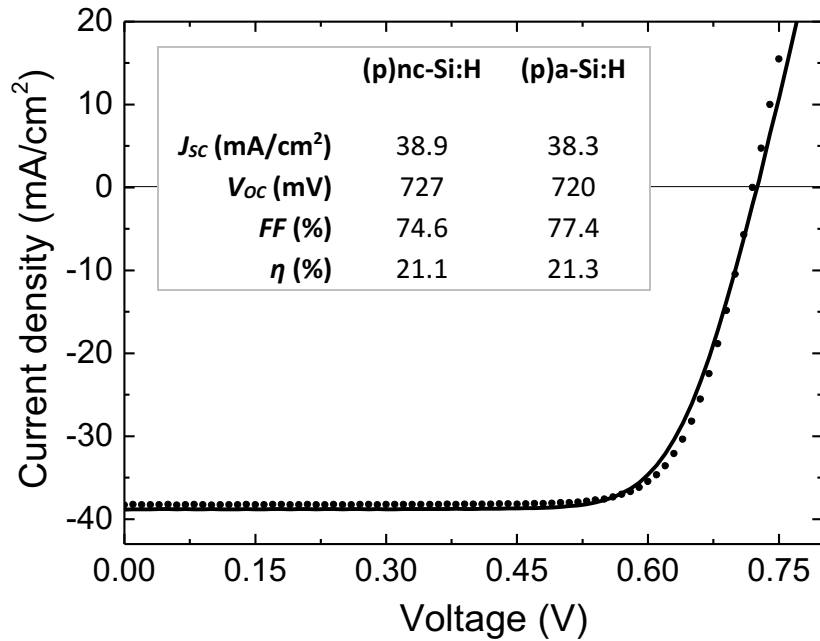


Figure 5.13. Illuminated J - V characteristics for the best cells on textured wafers with (p)nc-Si:H emitter deposited with TMB flows of 4 sccm (Figure 5.12) and (p)a-Si:H emitter given as reference. The table reports the cell parameters extracted from the J - V curves.

5.3. Discussion and Conclusions

In this chapter, p-doped hydrogenated nanocrystalline silicon (p)nc-Si:H layers were implemented as emitter in silicon heterojunction (SHJ) solar cells. We addressed how to grow *thin* (p)nc-Si:H layers with a fast nucleation resulting in high crystalline fraction F_c without deteriorating the underlying intrinsic amorphous silicon (i)a-Si:H passivation layer.

For the integration of (p)nc-Si:H layers in SHJ devices, the relation among deposition conditions, reduced film thickness and quality of the underlying (i)a-Si:H passivation layers was investigated on cell-relevant stack leading to the following results.

The study on the influence of the doping gas phase composition showed that the use of trimethylboron limits the crystalline volume fraction F_c and film conductivity as compared to diborane gas. Similar conclusions were observed by other groups [110,185] despite the different deposition regimes. Nevertheless, this difference is not observed on cell level.

The i-layer quality influences the nanocrystalline growth of (p)nc-Si:H films. A passivation layer that exhibits epitaxy promotes nucleation enhancing the crystalline fraction and leading to solar cells having fill factors approaching to 79%. HR-TEM images confirmed the

hypothesis showing the development of epitaxially-grown, highly crystalline regions throughout the i/p stack. These cells are mainly voltage limited due to the initial lower passivation quality of the i-layer that is further degraded by the emitter deposition regime as discussed in chapter 4 for the reference process (*phase B* in Figure 4.11).

In contrast, the use of a well-passivating, fully amorphous intrinsic passivation film (type B) delays the nucleation to fully developed nanocrystalline growth in the emitter, resulting in *J-V* characteristics with S-shapes. The analysis of the carrier lifetime curves showed a degradation in field-effect passivation in the low injection level range but at the same time improved interface defect density passivation with a high $i-V_{OC}$ of 733 mV. This suggests that the (p)nc-Si:H deposition is able to passivate dangling bonds in the (i)a-Si:H layer and at the a-Si:H/c-Si interface acting as a hydrogen plasma treatment.

A strategy to enhance F_c within the (p)nc-Si:H layer was found by oxidizing the (i)a-Si:H surface prior to the emitter growth by means of a short CO₂ plasma treatment. The aim is to preserve the excellent surface passivation together with higher *FF*. Solar cells fabricated with this treatment showed well-shaped *J-V* characteristic with open circuit voltage of 727 mV and *FF* up to 74.6%. A similar method was applied before only in thin film devices [114,118] where the much thicker (i)a-Si:H layer allowed for more aggressive methods.

The best device fabricated using both the CO₂PT and the fine optimized TMB gas flow for the (p)nc-Si:H growth, which was found to be a critical growth parameter, led to a conversion efficiency of 21.1%.

From the direct comparison of the cell parameters of the best cell developed here and the reference with (p)a-Si:H emitter (Figure 5.13) it can be seen that we succeeded to improve V_{OC} and J_{SC} slightly by implementing the nc-Si:H emitter, however, due to the lower *FF* the cell efficiency did not improve. Rather, the trade-off between good passivation and low contact resistance is limiting the cell performance. We ascribe this to the problems in the initial stage of the nc-Si:H growth which influence the crystalline fraction in the only 15 nm thick emitter, and, partially, to a poor contact to the front TCO.

Parts of these *FF* issues will be addressed in the next chapters, by further developing the emitter stack. Moreover, optical improvement, in order to further increase the J_{SC} gain, is addressed, both by simulations and experimentally.

6. Nanocrystalline Silicon Oxide Window Layers

This chapter addresses the minimization of current losses by using p- and n-doped hydrogenated nanocrystalline silicon oxide (nc-SiO_x:H) films as the window layers in silicon heterojunction (SHJ) solar cells. These materials exhibit improved optical properties due to the oxygen incorporation into the matrix that reduces the parasitic absorption. Furthermore, the refractive index matching with the adjacent layers allows for an enhanced antireflection effect. The benefit of such layers is well-known from their application in thin-film silicon solar cells, such as a-Si:H/ μ c-Si:H tandem cells [180,192]. In case of the applications in SHJ solar cells, however, the optical and electrical requirements, as well as the growth prerequisites, are quite different from those in above mentioned cells. In the previous chapter we developed the know-how to obtain a rapid nucleation of (p)nc-Si:H films. The key challenge here is to maintain good passivation and a low-ohmic contact with optically improved nc-SiO_x:H films.

Using experimentally extracted n & k data from single layers, we simulate the optical behavior of the multilayer stack placed on the illuminated side of the c-Si absorber. By varying the doped material (amorphous a-Si:H, nc-Si:H and nc-SiO_x:H) in the simulated stack with (i)a-Si:H passivation and (In₂O₃:Sn, ITO) layers, we identify the optimum film characteristics, both in terms of refractive index and thickness.

Deposition parameters for single layers are explored to find PECVD growth regimes that allow for refractive index reduction without sacrificing on the crystalline phase and, hence, conductivity.

Solar cells are fabricated with the p-doped emitter or n-doped front surface field layers placed on the illuminated side of the device, in front emitter or rear emitter configuration, respectively. Photocurrent loss analysis performed on completed solar cells are in agreement with the simulated photocurrent trends for both planar and random pyramids surface morphologies.

Finally, the contact between ITO and the p-doped emitter is manipulated to investigate the causes of fill factor losses and improve on these device limitations.

Parts of these results have been published in [193–195].

6.1. Optical Simulation Model

Computational Approach

The freeware program OPAL 2 [26] was used to perform an optical analysis of the front surface stack of SHJ solar cells. It computes the optical properties for any angles of incidence, that is: parasitic absorption in thin-film coatings, reflectance and transmittance into the substrate leading to the desired photocurrent [196]. Moreover, the software allows computing the equivalent currents that are lost by reflection and parasitically absorbed by the window layers stack. Finally, it calculates the photocurrent that would have been generated within the cell associated with the actual photon spectrum that reaches the absorber.

The computational approach of OPAL 2 consists of three elements, briefly summarized below. For a detailed discussion, the reader is referred to [196,197].

- Ray tracing: For the specified surface morphology, the software uses the precomputed information concerning the number of unique paths from geometric considerations (facets and angles) [198]. This approach drastically reduces the computation time since the Fresnel equations to be solved are limited only to the relevant paths. The analysis of the light paths and their probability for pyramidal textured morphologies is given in [198].
- Thin film optics: Reflectance, absorbance and transmittance spectra (*RAT*) can be calculated for each unique path using the transfer matrix formalism [199]. The user selects the front layer structure that consist of a half space of air (superstrate) followed by a multilayer stack (thin films) and finally the semi-infinite silicon substrate. Each film is defined by thickness and refractive index data ($n(\lambda)$, $k(\lambda)$) and the calculated $\alpha(\lambda)=4\pi\cdot k(\lambda)/\lambda$.
- Light trapping scheme: The internal optics are given by the optical path length enhancement factor Z and the substrate thickness W that identify the optical width ($Z\cdot W$). The Z factor indicates the efficiency of the light trapping scheme. The upper limit suggested by Yablonovitch and Cody [200] ($Z= 4n^2$) assumes an ideal solar cell structure that is isotropic, perfect internal reflection at the rear side, ideal antireflection coatings (100% transmission) and no absorption in the substrate. Those hypotheses correspond to a Z value above 50 that overestimates the light available at the optical width [201] Although Z varies with the wavelength, it can be approximated by a constant and reasonable value for c-Si cells might be chosen as the value at a long wavelength (i.e. 1050 nm) [26].
- Equivalent currents are calculated using the *RTA* spectra for a defined incident spectrum and the specific path enhancement Z . The generation current, i.e. the current absorbed into the substrate J_{c-Si} is defined by the integral over all λ :

$$J_{c-si} = \int I(\lambda) \cdot T(\lambda) \cdot [1 - e^{-\alpha(\lambda) \cdot z \cdot W}] \cdot d\lambda$$

where q is the charge of an electron, $I(\lambda)$ is the photon flux of the incident spectrum, $\alpha(\lambda)$ is the absorption coefficient of the substrate, $T(\lambda)$ is the transmitted spectrum. Similarly, the generation currents lost by reflection (J_{ref}) and absorption (J_{abs}) in the layer stack are quantified by replacing the $T(\lambda)$ quantity with $R(\lambda)$ or $A(\lambda)$, respectively.

Assumptions and Simulated Stack

The following assumptions were made:

- $n(\lambda)$ and $k(\lambda)$ spectra were extracted from transmittance and reflectance curves measured on thicker layer grown on glass substrates as described in section 3.2.1 and material derived in section 6.2. While the optical properties of the c-Si substrate were taken from literature data [202]. Figure 6.1 (a) gives an example of experimental refractive index data used to simulate the window stack of the front emitter device.
- $I(\lambda)$ is the standard AM1.5g incident spectrum.
- The surface morphologies of interest were planar and random upright pyramids that represent the polished and the textured samples investigated in this thesis, respectively.

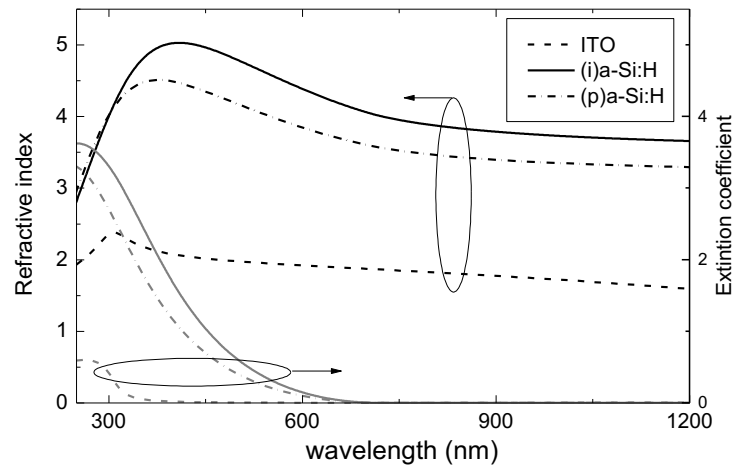


Figure 6.1. Refractive index n and extinction coefficient k as function of the wavelength experimentally extracted from transmittance and reflectance curves for the sputtered ITO film and for amorphous PECVD layers (~ 200 nm on glass).

6. NANOCRYSTALLINE SILICON OXIDE WINDOW LAYERS

- For layers with thicknesses in the range of light wavelengths, the propagation of light is coherent, resulting in interference phenomena in the *RAT* spectra, while thick substrate layers are assumed as incoherent [199].
- The layers were assumed to grow conformal in terms of thickness and properties independently of the surface pattern. For nanocrystalline films, also the crystalline volume fraction was assumed to remain constant with the film thickness.
- The *Z* factor was kept constant at 2 for the planar morphology (perfect back reflector) and at 35 for the textured pattern [201] to take into account the light trapping enhancement. These settings lead to a current available at the optical width of 41.3 and 44.5 mA/cm² on planar and random pyramids surface, respectively, for a substrate thickness (*W*) of 270 μm.

The sketch of the multilayer stack representing the illuminated side of the cell is depicted in Figure 6.2 showing the range of materials and film thicknesses selected for this investigation. It consists of a half space of air followed by an ITO, doped and passivation layers and lastly, the crystalline silicon substrate.

The following sections examine and discuss the equivalent photocurrents lost due to reflection (J_{ref}) and parasitic absorption (J_{abs}) in two distinct multilayer stacks: (i) with p-doped emitters and (ii) n-doped front surface field layers. The calculations were performed for planar surface morphology and a random upright pattern and are expressed as the difference to the value calculated with 0 nm of emitter (Δ).

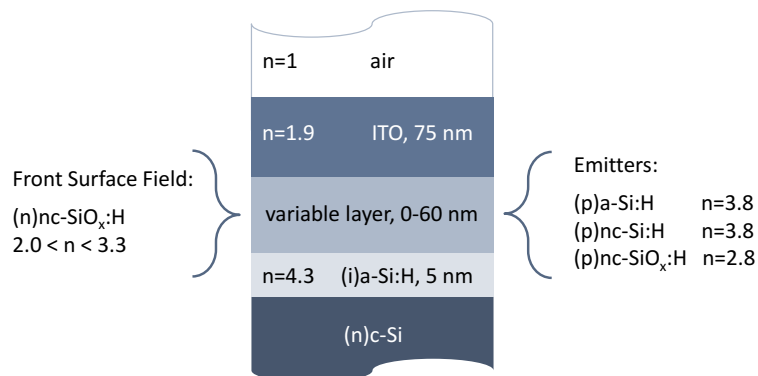


Figure 6.2. Sketch of the modeled structure that represents the layer stack placed at the front side of a SHJ solar cells. The thickness and refractive index for the substrate, passivation layer and ITO were kept constant. The simulations were performed both in front and rear emitter cell configuration using optical data from p- and n-doped a-Si:H, nc-Si:H or nc-SiO_x:H films, respectively. The refractive index values added for each layer are extracted at 633 nm.

Validation of the Model

The validation of the optical simulation model was conducted for the two morphologies investigated. Figure 6.3 shows the comparison between experimental and simulated reflectance spectra of the reference (p)a-Si:H emitter with a nominal thickness of 13 and 8 nm on polished and textured substrates, respectively. The curves are in good agreement with the simulated ones that were computed for layer stack with nominal thicknesses. In the comparison, the reader should consider that the experimental curves are measured on completed devices with front metal grid and back contact. Therefore, the simulated curves were corrected to take into account the additional reflection from the silver grid⁶. Moreover, the absence of reflection at the rear reflector in the model is visible at wavelengths above 1000 nm, thus experimental and simulated curves diverge significantly in this range, as highlighted in Figure 6.3 by the shaded area.

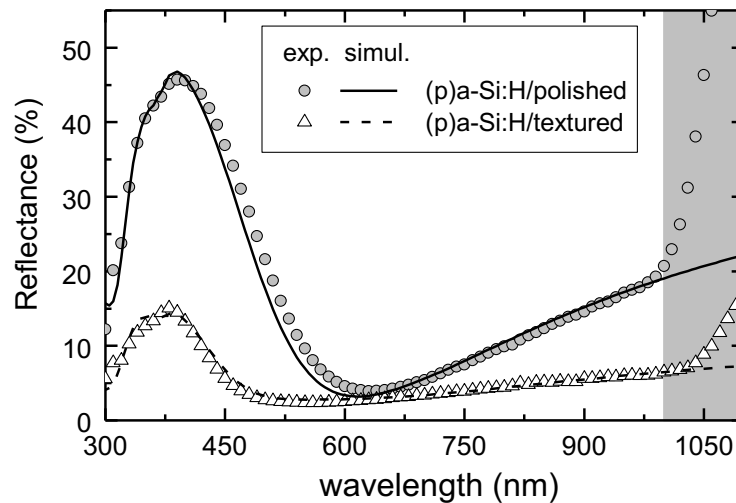


Figure 6.3. Experimental and simulated reflectance spectra of solar cells on polished and textured substrate with nominally 13 and 8 nm (p)a-Si:H emitter, respectively. The simulated structure is depicted in Figure 6.2. The nominal thicknesses for the ITO/(p)a-Si:H/(i)a-Si:H stack are: 75/13/10 nm on polished and 75/8/6 nm on textured wafers. The simulations were performed using the nominal values. The shadowed area highlights the absence of reflection at the rear side for the simulated spectra.

⁶ Formula: $R_{stack} * 0.97 + R_{Ag} * 0.03$

6.2. Nanocrystalline Silicon Oxide Material

A nc-Si:H film alloyed with oxygen can be grown using PECVD by adding a source of oxygen (e.g. CO₂). The effect of the CO₂/SiH₄ ratio on the nc-SiO_x:H material properties has been intensively investigated in literature both for undoped [203] and doped films [135,136,204,205]. In this section, we investigate the effect of deposition parameters variation (gas pressure and power density) on the optoelectronic properties of p- and n-doped nc-SiO_x:H films.

6.2.1. Introduction

In order to allow more sunlight to enter the c-Si absorber, a window stack with wider optical band gap than crystalline silicon is required in SHJ solar cells. The commonly used doped and undoped a-Si:H films are responsible for parasitic absorption [58] and consequently alternative materials alloyed with oxygen or carbon have been suggested to enhance transparency. Concerning the (p)a-Si:H film, doping by trimethylboron (TMB) has drawn attention as an alternative to diborane (B₂H₆) [173] allows for band gap increasing and consequently high blue spectral response in SHJ solar cells (see chapter 4, section 4.2). Zhang *et al.* [131] reported, for cells with intentionally carbon alloyed (p)a-SiC:H emitter, short circuit current density J_{SC} values of 35.0 and 40.3 mA/cm² on polished and textured surfaces, respectively and conversion efficiency of 20.8% for the textured surface cell. For comparison, the J_{SC} achieved by the $\eta = 25.1\%$ record cell [14] with similar device structure on textured surfaces is of above 40 mA/cm².

Besides that, a nanocrystalline window film allows for further widening of the optical band gap. Richter *et al.* [206] have applied (n)nc-SiO_x:H film as a front surface field (FSF) in the rear emitter configuration giving a cell with fill factor FF , J_{SC} and conversion efficiency η of 77%, 35.7 mA/cm² and 20.4%, respectively (measured on probed area of 2 mm² without fingers) on polished c-Si. Others [207,208] use the nc-SiO_x:H as window emitter layer on p-type c-Si wafers with a maximum J_{SC} of 35.8 mA/cm², FF of 79.6% and η of 19% (active area of 0.67 cm²) but V_{OC} of 667 mV [209].

6.2.2. p-doped Layers

Effect of Power and Pressure on p-doped nc-SiO_x:H Films

The optical and electrical properties of (p)nc-SiO_x:H were investigated by varying both pressure p and power density P_D of the PECVD process, whereas the process gas flow was kept constant. The deposition parameters selected for the study are given in Table 6.1. The results show a similar tendency as discussed in Ref. [210] and by Kirner [211] for n-doped nc-SiO_x:H films developed in the same AKT1600 PECVD tool.

6.2. Nanocrystalline Silicon Oxide Material

Table 6.1 PECVD deposition parameters for the p-doped nc-SiO_x:H material deposited for the study of the power and pressure on the material properties. P_D : plasma power density; p : chamber pressure; precursor gas flows. Electrode spacing was fixed at 16.5 mm.

T_{sub} (°C)	P_D (mW/cm ²)	p (Pa)	SiH ₄ (sccm)	H ₂ (sccm)	CO ₂ (sccm)	TMB (sccm)
205	165	667 – 1200	15	7500	10	3.75
	233	933				
	250	800				
	300	667 – 933 – 1200				
	350	933–1200				

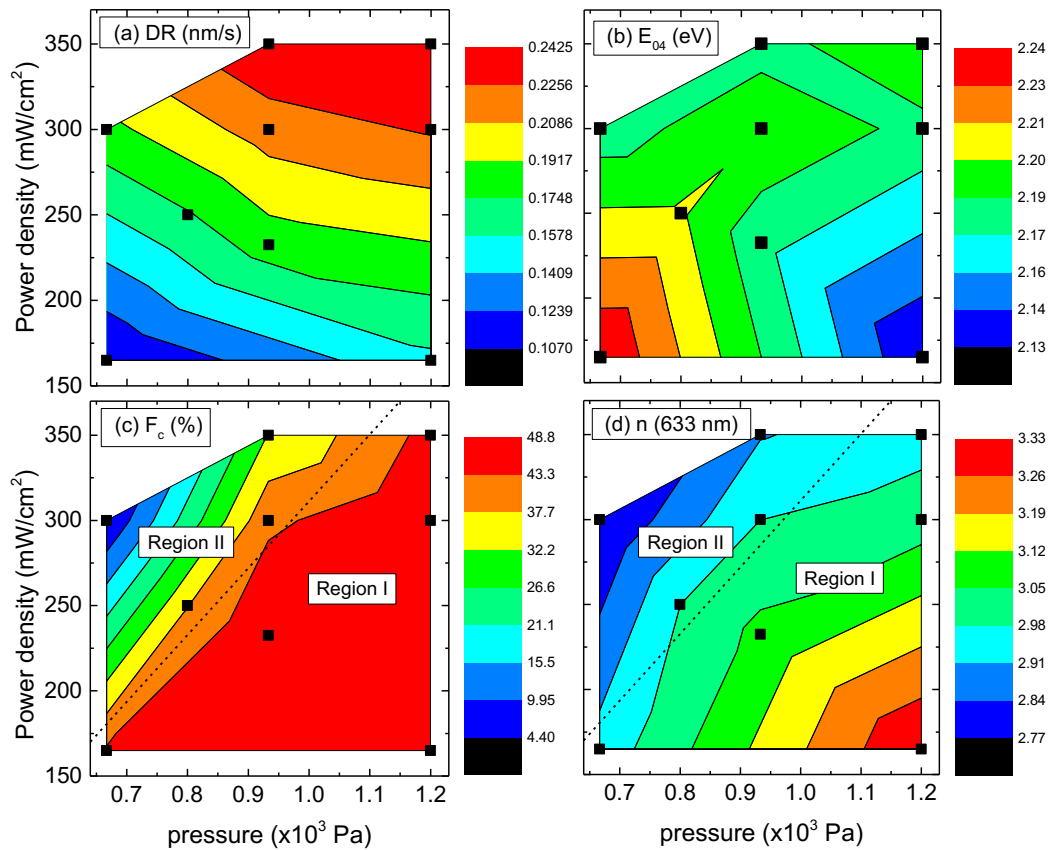


Figure 6.4. Contour plots of the film properties as function of both pressure and power density: (a) deposition rate DR, (b) electrical conductivity σ , (c) Raman crystalline fraction F_c and (d) refractive index n . The dashed line in (c) and (d) indicates the deposition regime I and II. Black squares indicate experimental data extracted from single layers deposited on glass substrates.

In Figure 6.4, contour plots showing the variation of (a) deposition rate, (b) conductivity, (c) crystalline fraction F_c and (d) refractive index n at 633 nm as a function of power density P_D and deposition pressure p are presented.

For higher power density, increased gas dissociation is expected therefore the deposition rate rises progressively. Moreover, dissociation energy required to split off the O from the CO_2 molecule is lower than the energy required to dissociate the C-O bond. Consequently there is a very low probability to find carbon in the growing layer since the remaining CO will be pumped out of the chamber. Investigation conducted by secondary ion mass spectrometry revealed C content below 1% [157]. The oxygen is expected to be mainly incorporated in the amorphous fraction as an amorphous silicon oxide phase [203,212].

As shown in Figure 6.4 (c) for Raman crystalline fraction, two parameter regions are identified. In region I, F_c shows only a slight dependence on p and P_D , whereas for high P_D -low p (region II) amorphous phase formation is promoted. In situ mass spectrometry measurements, discussed in Ref. [210], revealed that CO_2 depletion gradually increased with a square root function of the power density while it is only slightly independent on the pressure. This leads to the conclusion that the observed trend in film properties is caused by increased oxygen incorporation [210]. Besides that, n linearly decreases from 3.3 (high p and low P_D) to 2.8 (low p and high P_D) with an opposite tendency to the F_c (Figure 6.4 (d)).

The described relation between F_c and n in the range investigated shows a difference in the two regimes: For the films deposited at lower pressure both parameters increase, whereas, for higher pressure the F_c increases and at the same time more oxygen is incorporated leading to a reduction of n .

Accordingly to the plasma analysis discussed in Ref. [210], the different trends are related to the hydrogen radicals dissociation and electron density that control the nanocrystalline growth. For higher pressure, the electron density is low and strongly depends on the power in the plasma, while in high P_D -low p of regime II the much higher electron density leads to higher dissociation rate of the precursor gases and in particular CO_2 .

6.2.3. n-doped Layers

The optical, structural and electrical properties of (n)nc-SiO_x:H single layers grown, with thickness of about 200-250 nm, on glass substrates were investigated. Table 6.2 summarizes the deposition parameters varied in this work.

Figure 6.5 (a) and (b) show the effect of power and pressure variation on F_c and n . Similarly to what was discussed in [210] and above for (p)nc-SiO_x:H material, two clear trends are identified. Region I consists of deposition conditions that do not affect the F_c whereas the refractive index can be lowered down to 2.4 thanks to more oxygen incorporation in the amorphous phase. For increasing P/p values, the crystalline fraction reduces rapidly and the amorphous fraction becomes prevalent. In the same Figure 6.5, the dashed lines

indicate the effect of the increased CO₂ gas flow on the material properties. More CO₂ in the gas mixture reduces both n and F_c but the impact on the nanostructure is less pronounced for nc-SiO_x:H films n-doped with PH₃ than for those p-doped with TMB [213]. Interestingly, Ding *et al.* [204] measured an equal oxygen content in p- and n-doped nc-SiO_x:H films that exhibited strong differences in F_c (i.e. below 20% and above 60% for p- and n-type, respectively). This indicates that the doping gas nature plays a role in the nanocrystalline evolution.

Table 6.2. PECVD parameters for the n-doped nc-SiO_x:H material. P_D : plasma power density; p : chamber pressure; precursors gas flows. Electrode spacing was fixed at 16.5 mm.

T_{sub} (°C)	P_D (mW/cm ²)	p (Pa)	SiH ₄ (sccm)	H ₂ (sccm)	CO ₂ (sccm)	PH ₃ (sccm)
185	175	800 – 1200	10	3000	12 – 18	8 – 32
	250	800 – 1200				
	300	1200				

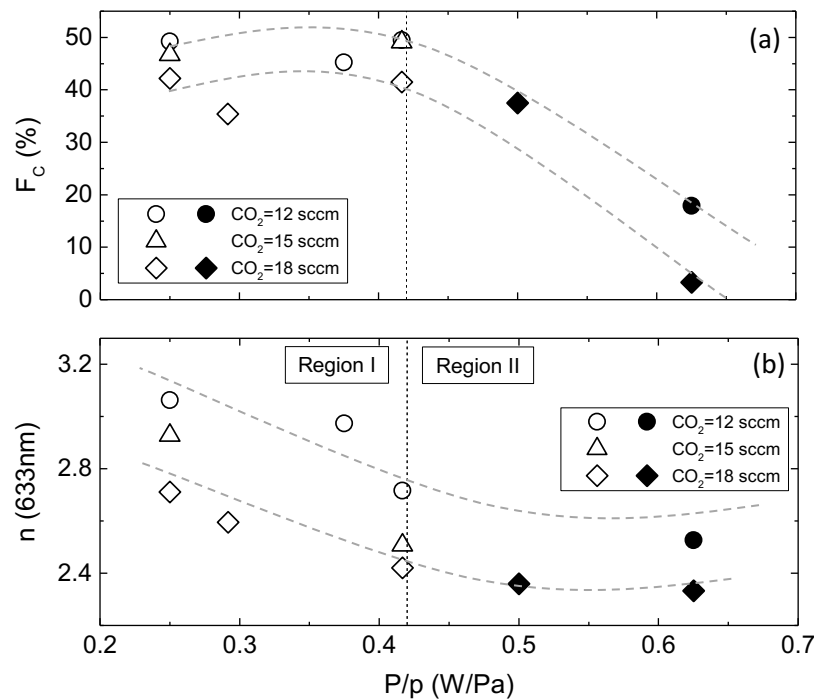


Figure 6.5. (a) Raman crystalline volume fraction F_c and (b) refractive index n (at 633 nm) as function of the Power/pressure P/p ratio and for variable CO₂ flow. The two deposition regimes are indicated as Region I and II. The PH₃ flow was kept constant at 8 sccm for all the films. The film thickness is in the range 200-250 nm. The lines are guides to the eye.

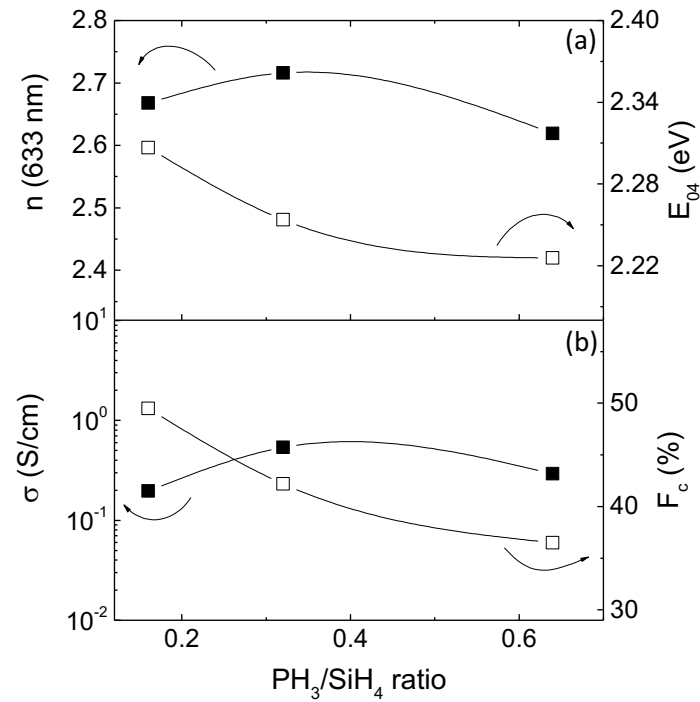


Figure 6.6. (a) Refractive index n and optical band gap E_{04} , (b) conductivity σ and Raman crystalline volume fraction F_c as function of the PH_3/SiH_4 ratio. The other deposition parameters were kept constant: $p=1200$ Pa, $P_D=250$ mW/cm² and $\text{CO}_2=12$ sccm. Film thickness is in the range 200-250 nm. The lines are guides to the eye.

Thanks to the beneficial P/p ratio, a film with refractive index of 2.4 and a crystalline volume fraction of 40% can be grown for a CO_2/SiH_4 ratio of 1.8.

The effect of the PH_3 gas flow on the material properties is depicted in Figure 6.6.

Despite the wide range investigated, the structural and optical properties change only slightly upon variation of the PH_3/SiH_4 ratio [209,211]. The comparison of this experiment to the similar one presented for p-doped nc-SiO_x:H elsewhere [204,213] confirms that the PH_3 gas flow in precursor mixture has a weaker impact on the crystalline fraction compared to TMB.

6.2.4. Comparison of nc-Si:H and nc-SiO_x:H

For application as emitter or FSF layer, the ideal material should have both higher conductivity and Raman crystalline fraction, whereas for window application, the optical properties depend on how the entire multilayer stack interacts with the incoming light. To enhance antireflection effect and significantly reduce the reflection, it is useful to create a stack in which the refractive index consecutively decreases from silicon to the ambient air.

For the specific SHJ device investigated in this work (see Figure 6.2), the refractive index of the c-Si substrate and front ITO layer represent fixed parameters ($n_{c-Si} = 3.8$ and $n_{ITO} = 1.9$ at 633 nm). While, both passivating and the doped layers might be chosen to better adjust their n to the adjacent materials. Usually silicon films alloyed with oxygen or carbon atoms are used to the aim (cf. section 6.2.1).

Figure 6.7 (a) and (b) illustrate the relation between optical and electrical properties for the nc-Si:H and nc-SiO_x:H films developed in this work. Looking at the p-doped layers, conductivities in the range of $\sim 10^{-1}$ S/cm can be obtained, as found for the non-oxidic nc-Si:H, but the optical transparency only slightly increases with oxygen incorporation. Improved E_{04} and n , due to higher oxygen content, lead to progressively degradation of electrical properties with σ below 10^{-4} S/cm partially caused by reduced crystalline fraction or due to lower doping efficiency within the film. Concerning the n-doped films, a similar trend is detected but, as expected from the values of F_c reported in the Figure 6.5, most of the films exhibit σ above 10^{-3} S/cm even for the highest CO₂ gas flow. Lambertz *et al.* [205] observed similar tendencies as the ones reported in Figure 6.7 (a-b) for nc-SiO_x:H films deposited at comparable H₂-dilution and doping gases.

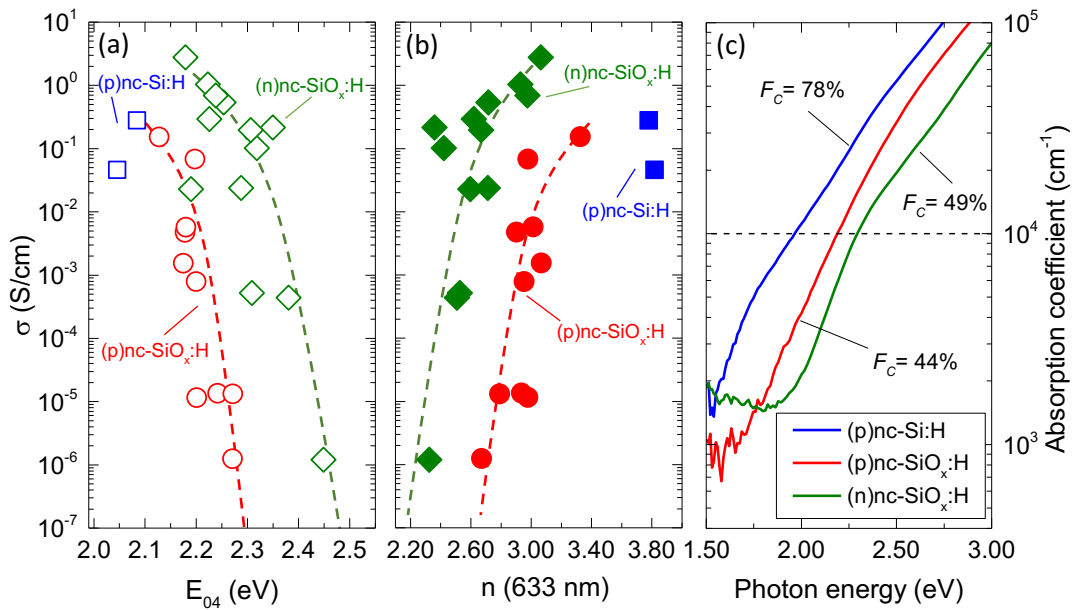


Figure 6.7. Electrical conductivity σ as function of (a) optical band gap E_{04} and (b) refractive index n for the p- and n-doped nc-SiO_x:H films. p-doped nc-Si:H layers deposited with TMB flow of 3 and 4 sccm are given as reference. The lines are guides to the eye. (c) Absorption coefficient as function of photon energy measured on (p)nc-Si:H, (p)nc-SiO_x:H and (n)nc-SiO_x:H films selected for their optoelectronic properties and grown using (p)nc-Si:H: TMB/SiH₄=0.33 and H₂-dilution=500. (p)nc-SiO_x:H: 667 Pa, 165 mW/cm² and H₂-dilution= 500. (n)nc-SiO_x:H: 1200 Pa, 250 mW/cm² and H₂-dilution= 300.

A graph of the absorption coefficient α of selected (p)nc-Si:H, (p)nc-SiO_x:H and (n)nc-SiO_x:H films, as function of photon energy, is presented in Figure 6.7 (c). The spectra were extracted from optical measurements as described in section 3.2.1. The layers exhibit a progressively lower refractive index: 3.82, 2.87 and 2.51, respectively. The widening of the optical band gap for the oxygen-alloyed film is clearly visible with a shift of α towards higher photo energies.

It can be summarized that, as the oxygen content in the amorphous fraction increases, wide band gap films can be grown both for p- and n-doping. The layers became more transparent with strong reduction in refractive index approaching $n=2$ or even below as reported in [136]. Commonly, the increasing of oxygen content compromises the film nanostructure with the amorphous fraction becoming predominant. This was observed for the films belonging to region II as discussed above for both doping types and also elsewhere [204,214]. Literature data [135,204,215] showed conductivities that degraded by 10 orders of magnitude for highly CO₂ diluted plasma conditions. Furthermore, the use of higher plasma excitation frequency might lead to better optoelectronic performances for both p- and n-type nc-SiO_x:H [137]. This particular aspect was not investigated in the present work since the constraints of our PECVD tool did not allow the exploration of different plasma excitation frequencies.

6.3. Integration of (p)nc-SiO_x:H in Front Emitter Cells

This section involves simulations of photocurrents that are lost by reflection or parasitically absorbed in the multilayer stack and the current photogenerated in the device. Different p-doped amorphous and nanocrystalline materials with variable thickness are applied as window stack (6.3.1). Section 6.3.2 compares experimental results for SHJ solar cells having amorphous and nanocrystalline emitters, whereas section 6.3.3 discusses the effect of a thickness variation of (p)nc-SiO_x:H layer on cell performance. Finally, sources of losses that causes reduction of fill factor are addressed for the (p)nc-SiO_x:H emitter and related to the charge carrier transport at the emitter/ transparent conductive oxide (TCO) contact (section 6.3.3).

6.3.1. Simulation Results

Front emitter cell structures were simulated using OPAL 2 by varying the p-doped emitter material. Experimental optical data obtained from transmittance and reflectance curves measured on (p)a-Si:H, (p)nc-Si:H and (p)nc-SiO_x:H films were used for the computational analysis. A schematic of the front stack is reported in Figure 6.2. The (p)nc-SiO_x:H layer selected had a refractive index of 2.87 at 633 nm which is a trade-off between the optical/electrical and structural properties discussed in section 6.2.2.

The evolution of photocurrent loss due to light that is reflected or absorbed in the multilayer stack and therefore cannot contribute to the generated photocurrent is shown in Figure 6.8 as function of the emitter thickness and material for planar (a-b) and random pyramids morphologies (c-d).

The fraction of current parasitically absorbed by the emitter (J_{emi}) increases almost linearly with increasing the thickness but much more rapidly for the (p)a-Si:H film. The reason can be attributed to the different optical band gap of the material used. A value for E_{04} of 1.96 eV was measured for the amorphous film used here and above 2 eV for the nanocrystalline materials. The corresponding absorption spectra are shown in Figure 2.6. The (p)nc-SiO_x:H emitter accounts for the lowest parasitic absorption (J_{emi}) for the entire range of thicknesses simulated. J_{emi} follows the same trend as described above for the n-doped films but increases slowly in comparison to the other two materials without oxygen. Additionally, the reflected fraction of the losses (J_{ref}) for (p)a-Si and (p)nc-Si:H layers is quite similar. For the first nanometers, the values of J_{ref} increase slightly as a consequence of the negative reflection effect in introducing such layer in the stack.

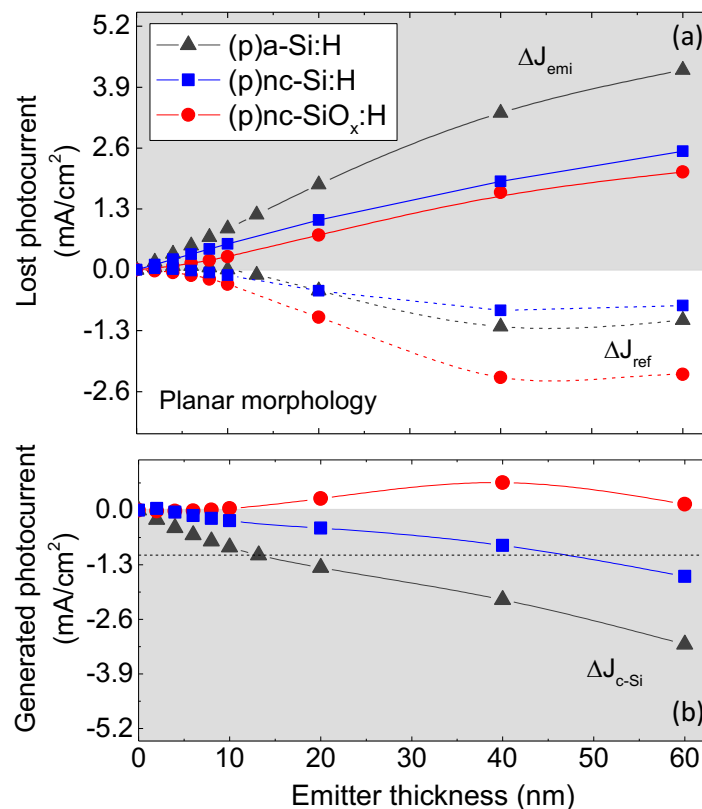


Figure 6.8. Simulated implied photocurrents that are (a) reflected from the entire front structure J_{ref} , absorbed in the emitter J_{emi} and (b) absorbed in the c-Si wafer J_{c-Si} as a function of emitter thickness on planar morphology. The values are expressed as a difference relative to the structure with a 0 nm thick emitter. Black triangles represent the (p)a-Si:H emitter, blue squares are the (p)nc-Si:H layer while red circles indicate the (p)nc-SiO_x:H film. The reader can refer to Figure 6.2 for the thickness of the other layers of the simulated stack. The curves are guides to the eye.

At a specific film thickness, the emitter layer improves the optics and less current is lost to reflection as shown in Figure 6.8 (a) that indicates more light enters the silicon absorber. The turning point is at about 5 nm for (p)nc-Si:H whereas above 10 nm for (p)a-Si:H. As a result, the photocurrent generated in the absorber J_{c-si} drops monotonously both for (p)a-Si:H and (p)nc-Si:H as depicted in Figure 6.8 (b).

The situation is completely different for the (p)nc-SiO_x:H emitter due to the more pronounced antireflection effect (Figure 6.8 (a)). The more transparent oxide emitter and the front ITO layer form a stack with refractive indexes that progressively increase from air to the c-Si substrate. Both J_{ref} and J_{emi} contribute to the superior trend shown in Figure 6.8. (b) where J_{c-si} rapidly increases with the (p)nc-SiO_x:H emitter thickness. The significant antireflection effect overcompensates the parasitic absorption within the layer. The simulations indicate that the advantage of the progressive increase in refractive index from the ambient air to the silicon substrate (see Figure 6.2) can be maximized for a 40 nm thick (p)nc-SiO_x:H film. The dotted line just above -1.3 mA/cm² represents the generated photocurrent for a stack with 13 nm (p)a-Si:H emitter. It is useful to evaluate the potential benefits in terms of photogenerated by using nc-Si:H and nc-SiO_x:H layers.

Figure 6.9 shows the results of a similar simulation study performed on a random pyramid morphology.

The trends for J_{emi} and J_{ref} are qualitatively similar to the planar one; however, the current parasitically absorbed J_{ref} in the front layers is much less thanks to the texturing that reduces the first reflection and enhance the light path of the refracted light. Moreover, J_{emi} increases faster with increasing emitter thickness because of the multiple internal reflections that enhance the light absorption probability into the front stack. Therefore, the photocurrent generated in the silicon absorber goes down linearly for all the emitters with increasing the thickness but much faster for (p)a-Si:H than for (p)nc-Si:H and (p)nc-SiO_x:H (Figure 6.9 (b)). It can be observed that the slope is more pronounced if compared to the planar morphology for the same material/thickness. Once more, the dotted line represents the generated photocurrent for a stack with 8 nm (p)a-Si:H is visible in Figure 6.9 (b). It highlights the advantage of using nc-Si:H or nc-SiO_x:H emitters over the (p)a-Si:H reference film.

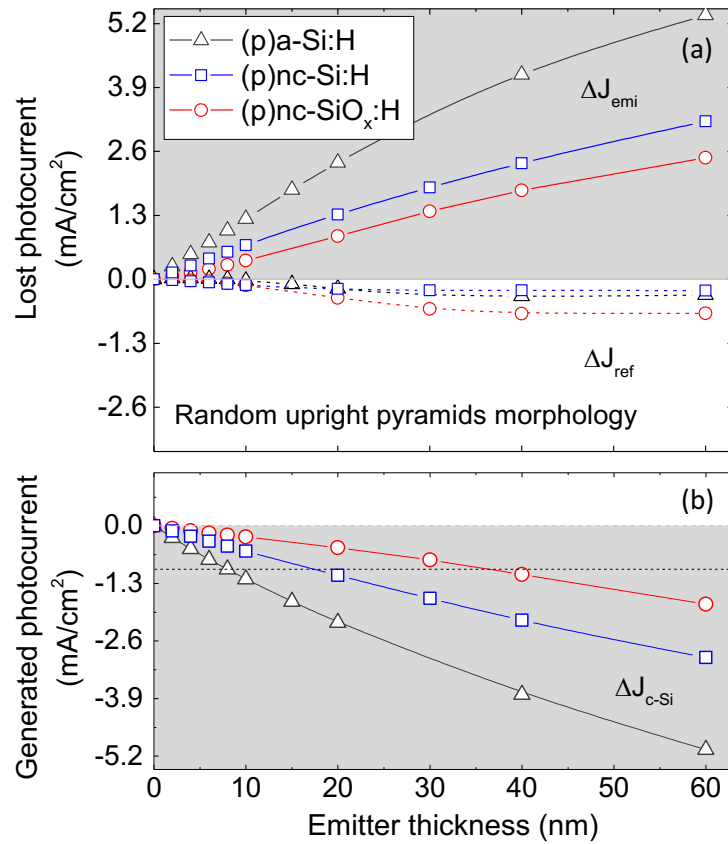


Figure 6.9. Simulated implied photocurrents that are (a) reflected from the entire front structure J_{ref} , absorbed in the emitter J_{emi} and (b) absorbed in the c-Si wafer J_{c-Si} as a function of emitter thickness on random upright pyramids morphology. The values are expressed as a difference relative to the structure with a 0 nm thick emitter. Black triangles represent the (p)a-Si:H emitter, blue squares are the (p)nc-Si:H layer while red circles indicate the (p)nc-SiO_x:H film. The reader can refer to Figure 6.2 for the thickness of the other layers of the simulated stack. The curves are guides to the eye.

6.3.2. Photocurrent Analysis

Figure 6.10 shows the experimental external quantum efficiency EQE and absorbance $1-R$ spectra for devices grown on polished and textured wafers having different emitters doped with TMB gas: (p)a-Si:H, (p)nc-Si:H and (p)nc-SiO_x:H. They were processed following the procedures described in sections 3.1, information about deposition parameters are summarized in Table 6.3. Details about film properties were discussed in sections 4.2, 5.1.1 and 6.2.2. The emitter layer thicknesses are different for polished and textured wafers and are specified in the text, whereas the (i)a-Si:H layer is 6 nm thick.

6. NANOCRYSTALLINE SILICON OXIDE WINDOW LAYERS

Table 6.3. PECVD parameters of (i)a-Si:H, (p)a-Si:H, (p)nc-Si:H and (p)nc-SiO_x:H films used for cell fabrication. T_{sub} : substrate temperature, P_D : plasma power density, p = chamber pressure, precursors gas flows. Electrode spacing was fixed at 16.5 mm.

Material	T_{sub} (°C)	P_D (mW/cm ²)	p (Pa)	SiH ₄	H ₂	TMB	CO ₂
				(sccm)			
type A (i)a-Si:H	205	15	200	180	900	-	-
(p)a-Si:H	205	15	267	55	540	90	-
(p)nc-Si:H	205	165	667	12	4800	4	-
(p)nc-SiO _x :H	205	165	667	15	7500	3.75	10

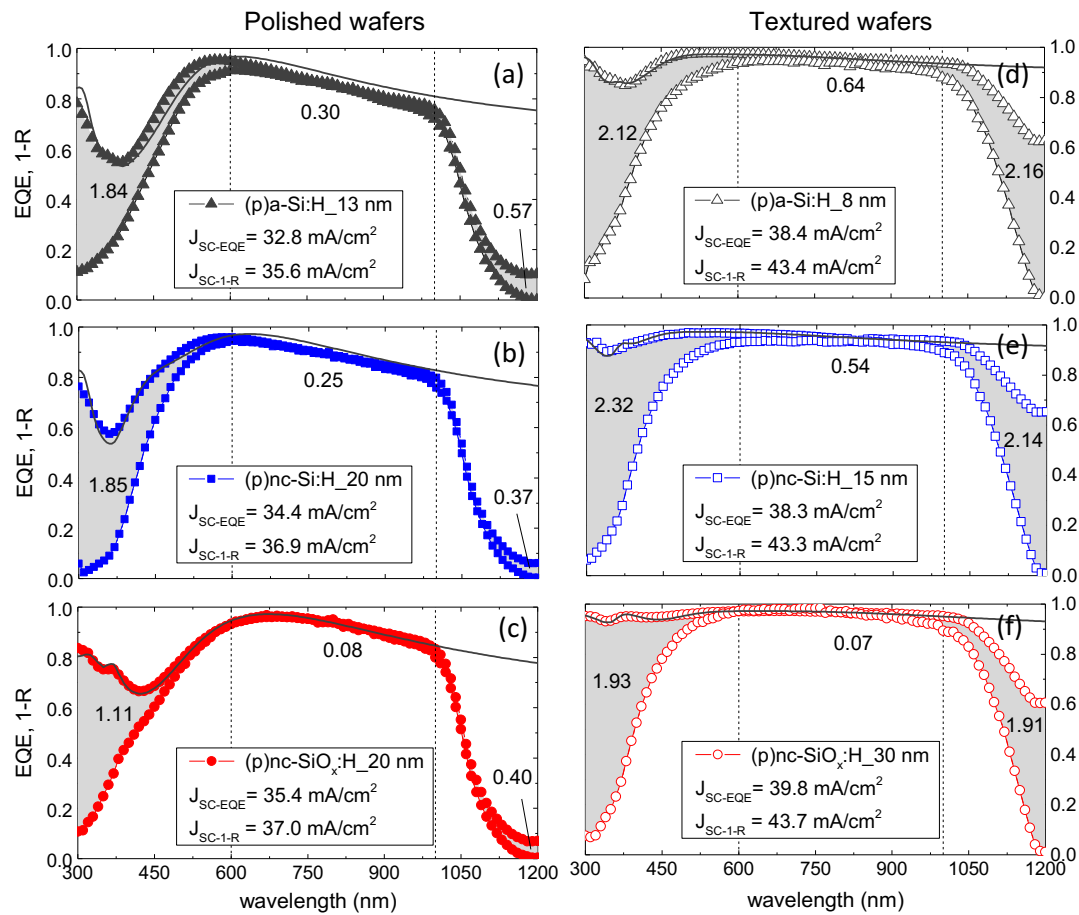


Figure 6.10. Experimental (symbols) and simulated (solid line) absorbance spectra 1-R and external quantum efficiency EQE curves as function of wavelength for the cells with (a-d) (p)a-Si:H, (b-e) (p)nc-Si:H and (c-f) (p)nc-SiO_x:H emitter growth on polished and textured wafers. In each plot is indicated the short circuit current integrated over the wavelength spectrum both for EQE and 1-R curves. The shaded areas indicate the parasitic absorption and the numbers the current losses expressed in mA/cm² calculated in the wavelength range identified by the dotted vertical lines.

6.3. Integration of (p)nc-SiO_x:H in Front Emitter Cells

As expected, the window stack benefits from the better refractive index match and layer thickness by using nanocrystalline films instead of the reference amorphous emitter thus enhancing the amount of light that enters the cell. Consequently, the potential photocurrent density J_{SC-1-R} calculated from the 1-R curve as described in section 3.2.2, increases with a total gain of 1.4 mA/cm² as compared to the cell with (p)a-Si:H layer. The use of the nc-SiO_x:H layer additionally shifts the 1-R curve at higher wavelengths and, at the same time, reduces the reflectance losses both in the blue range and above 600 nm. Concerning the parasitic absorption at the front stack indicated by the shaded areas (Figure 6.10 (a-c)), it can be concluded that only the (p)nc-SiO_x:H emitter leads to a concrete advantage. The J_{SC-EQE} benefits from the improved graded refractive index series and increased E_{04} . The current loss analysis indicates a net gain +0.73 mA/cm² for wavelengths below 600 nm and +0.22 mA/cm² in the range 600 – 1000 nm as compared to the amorphous emitter. In the infrared, the optical performance is unchanged since the three compared devices had an identical rear side stack.

A similar study was carried out on a textured c-Si wafer and the EQE and 1-R spectra are shown in Figure 6.10 (d-f). As predicted from simulations in Figure 6.9, the use of (p)a-Si:H and (p)nc-Si:H results in a similar J_{SC-EQE} due to comparable reflection and parasitic absorption for the selected thicknesses. The (p)nc-SiO_x:H emitter allows for reduced losses below 1000 nm with a total gain of +0.38 mA/cm² as compared to the (p)a-Si:H device.

6.3.3. Solar Cell Results

The effect of the emitter thickness was firstly investigated for the (p)nc-SiO_x:H film deposited in cell precursor structures grown on textured c-Si wafers as shown in Figure 6.11. The deposition time was adjusted to deposit progressively thicker p-doped layers from deposition conditions as specified in Table 6.3.

The minority carrier lifetime curves show an enhancement of the passivation performances as the emitter thickness increases for the entire range (Figure 6.11). A double effect caused by the doped films and the nanocrystalline growth regime can be identified. The longer deposition time, necessary to grow thicker films, exposes the i-layer to plasma conditions that allows H atoms to more efficiently passivate dangling bonds improving the interface defect passivation.

On the other side, the carrier lifetime in the low injection region increases when emitter thickness is increased from 17 up to 30 nm due to improved field-effect passivation. The enhanced crystalline fraction for the 30 nm thick emitter layer compared to the thinner one results in a higher conductivity of the minority carriers (holes) in the p-emitter.

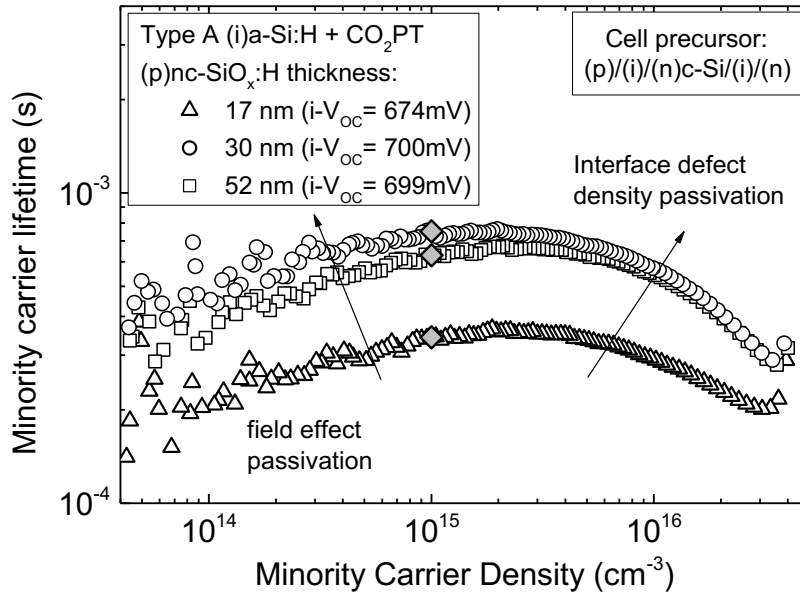


Figure 6.11. Minority carrier lifetime measurements performed on cell precursors (p)/(i)/(n)c-Si/(i)/(n) deposited on textured c-Si for a variable thickness of the (p)nc-SiO_x:H emitter deposited on a (i)a-Si:H of type A treated with CO₂PT. τ_{eff} are extracted at a minority carrier lifetime of 10¹⁵ cm⁻³ as indicated by the diamond symbols.

The gain in $i-V_{oc}$, as measured on cell precursors with thicker emitters, amounts to about 30 mV. The cell substructure with a roughly 50 nm thick emitter shows a saturation in the field-effect passivation that might be due to no further increase in the F_c and doping density.

Similarly, Ghahfarokhi *et al.* [190] reported an increase in τ_{eff} (at low injection level) for progressively thicker nc-Si:H films. They concluded that the higher F_c and enhanced conductivities for thicker films increased the electric field strength and thus improved passivation.

To support this hypothesis, Raman crystallinity was measured on the same stack deposited on glass substrates: type A (i)a-Si:H + CO₂PT + 50 nm (p)nc-SiO_x:H. The F_c reaches the same value measured for the 200 nm thick film, 43.5 and 44%, respectively. These observations lead to the conclusion that further increase in emitter thickness is not beneficial since no electrical improvements are expected and that probably a value of 44% is the maximum possible F_c for the deposition conditions optimized for such film. The end of the incubation zone (IZ) is supposed to be between 17 and 30 nm since the F_c does not increase further. On the other side, the prolonged exposure to the plasma leads to better passivation clearly visible in the higher injection range.

The emitter stacks discussed above were tested on complete devices with process described in section 3.1.

6.3. Integration of (p)nc-SiO_x:H in Front Emitter Cells

Boxplots of the J_{SC} , FF , V_{OC} and R_{OC} as a function of emitter thickness are presented in Figure 6.12. The J-V curves of the best cell for each emitter thickness are plotted in Figure 6.13. As expected, the 17 nm thick emitter is limited by the incomplete evolution of the film nanostructure. The cells exhibit J-V curves with S-shape character that drastically reduces the FF . Increasing the emitter thickness to 30 nm raises V_{OC} by more than 80 mV and then it remains steady at 675 mV also for the 52 nm emitter, following the trend discussed for the i - V_{OC} in Figure 6.11.

These values correlate with the observed passivation quality of the type A i-layer used in this experiment. A similar trend was observed by others [216] with a maximum in FF for a 20 nm thick film. The lower optimum thickness as compared to the findings in [216] can be explained by the diborane gas used that allow higher crystalline volume fraction and conductivities.

The EQE and 1- R spectra extracted from the best cells grown on textured wafers with (p)nc-SiO_x:H emitters of different thickness are shown in Figure 6.14.

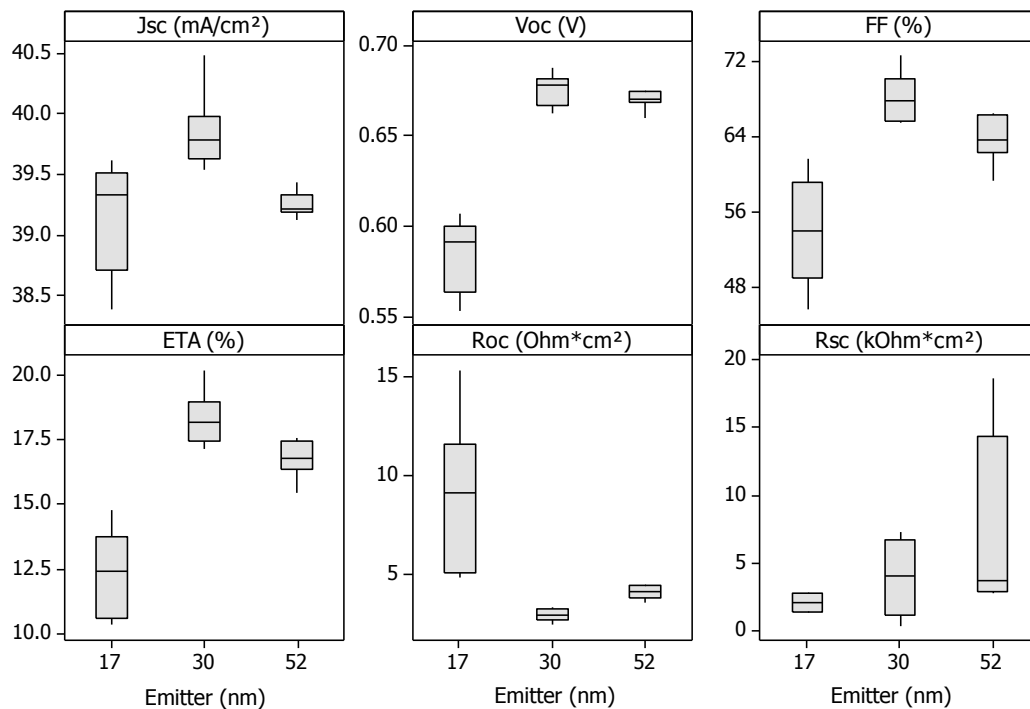


Figure 6.12. Box plots of the cell parameters based on 8 cells for variable (p)nc-SiO_x:H emitter thickness. The cells are grown on n-type both sides textured c-Si wafers with type A (i)a-Si:H passivation layer.

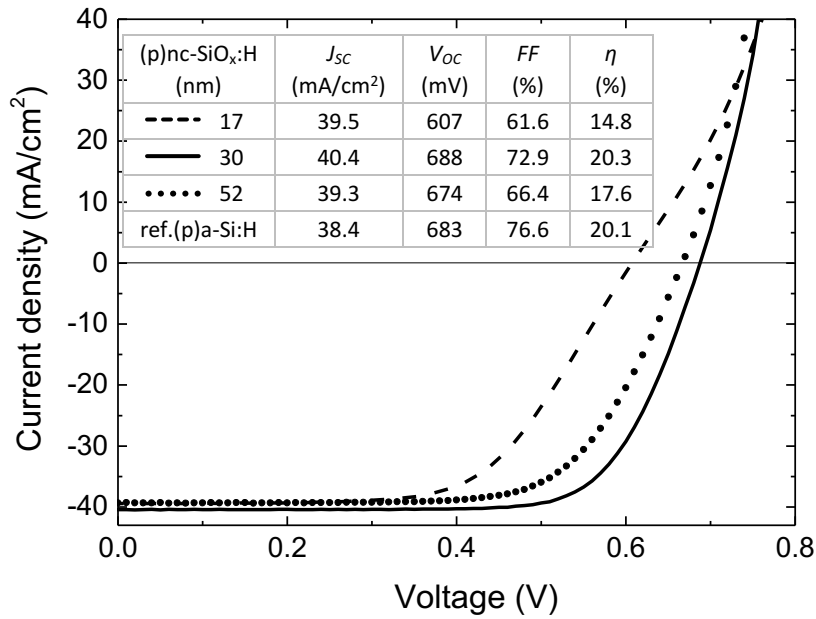


Figure 6.13. Illuminated J - V characteristics and solar cell parameters for the best cells with variable (p)nc-SiO_x:H emitter thickness as reported in Figure 6.12. Type A (i) a-Si:H passivation layer was used, explaining the low V_{oc} 's (compare section 4.1).

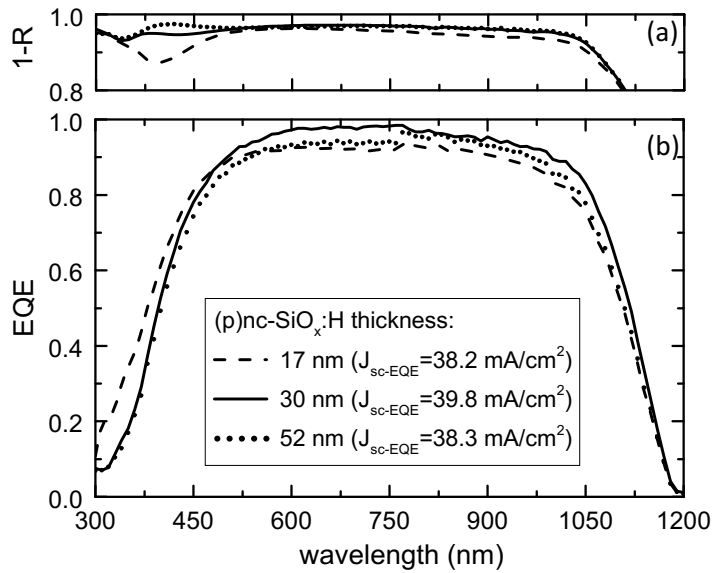


Figure 6.14. (a) Experimental absorbance $1-R$ and (b) external quantum efficiency EQE as a function of the wavelength for cells with 17, 30 and 52 nm of (p)nc-SiO_x:H emitter grown on textured wafers.

As predicted by simulation, the losses due to reflection decrease both in the 300-600 nm and 600 – 1000 nm ranges as the emitter thickness increases from 17 to 30 nm, whereas for thicker films both values stabilize (see Figure 6.14 (a)). The EQE spectra instead account for the increased parasitic absorption of the incoming light that is pronounced for wavelengths below 450 nm. The device with a nominally 30 nm thick emitter shows J_{SC} of 39.8 mA/cm² with a gain of about 1.4 mA/cm² as compared to the reference cell with (p)a-Si:H emitter.

The data in Figure 6.12 confirms the observation on the F_c evolution, after a minimum at 30 nm the R_{oc} arises again. The R_{oc} trend dominates the measured FF and conversion efficiency. It can be seen that the FF ($\sim 72\%$) is the main limiting factor if compared to the value reported for a-Si:H and nc-Si:H emitter cells (cf. sections 4.2 and 5.2.1). The pseudo- FF , measured on these cells, returns values above 80% confirming that series resistance primarily causes the losses. The next section investigates this aspect in more detail.

6.3.4. Charge Carrier Transport at the TCO/(p)nc-SiO_x:H Contact

In the previous sections of this chapter and in chapter 5, strategies to integrate thin nc-Si:H and nc-SiO_x:H films in device have been discussed. We have shown how the i-layer nature and its surface oxidation can reduce the IZ and help to develop faster the nanocrystalline growth of the doped layers (section 5.2.2). Furthermore, we have discussed above that the bulk F_c might be limited by the emitter thickness. Nevertheless, the devices with nanocrystalline emitters discussed both in the previous sections and in section 5.2 shown reduction in FF in comparison to the reference (p)a-Si:H emitters. This issue was particularly evident for the (p)nc-SiO_x:H films where FF are limited up to about 73%. The high series resistances observed probably originate from an insufficient transversal transport and are the primary cause of fill factor losses.

The sketch in Figure 6.15 illustrates a model for the current transport mechanism that is based on *in situ* ellipsometry analysis [97] and transmission electron microscopy studies by Cuony *et al.* [136] and Ding *et al.* [217]. The possible sources of losses are listed below:

- The incubation zone is completely amorphous with lower doping efficiency and reduced carrier mobility.
- The bulk of the nc-Si:H or nc-SiO_x:H layer might offer too high resistivity. Electronic properties are controlled by the existence of a percolation path within three-dimensional nanocrystalline layer (schematically indicated in Figure 6.15). If the film exhibits a F_c below the percolation threshold, low conductivity and carrier mobility are measured [187]. The presence of grain boundary can be additional source of reduced mobility due to impurities segregation, as discussed by J. Seto in [218] for polycrystalline silicon films.

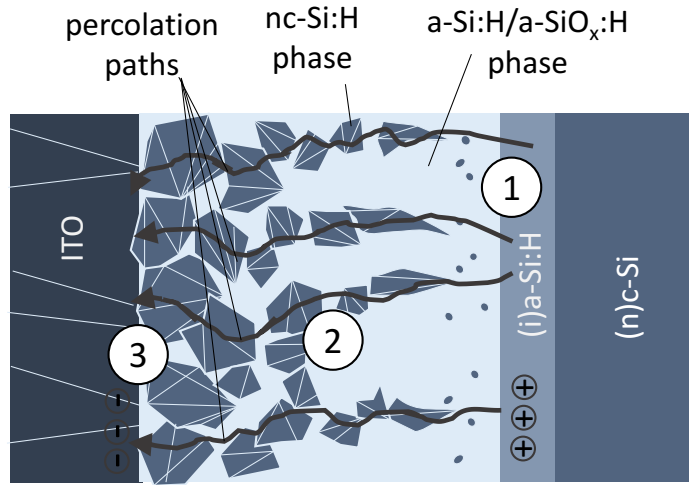


Figure 6.15. Schematic model of the current transport mechanism at the illuminated side of a SHJ device with (p)nc-Si:H or (p)nc-SiO_x:H emitter. The numbers indicate the possible losses: (1) incubation zone at the (i)a-Si:H/(p)nc-SiO_x:H contact, (2) lacking in crystalline volume fraction in the emitter bulk and (3) insufficient (p)/ITO tunnel contact caused by sub optimal doping and/or crystalline volume fraction at the interface.

- The F_C and doping efficiency of the nc-SiO_x:H film at the (i)/(p)/TCO interface impede the tunneling at the (p)emitter/TCO contact. Reasons for that can be found in the sub-optimal crystalline volume fraction of the p-doped film and consequently lower conductivity.

The three problems are in an interdependent relation since the IZ determines the crystalline evolution in the bulk and, later on, the final structural properties and the contact to the adjacent film. The effects of the first two aspects have been discussed in the previous sections, while the latter is discussed in the next subsection focused on the emitter/TCO contact.

As discussed in section 2.2.2 and experimentally discussed for the (p)a-Si:H emitter cells in section 4.3, the (p)emitter/TCO contact is identified as source of losses that potentially reduce the FF [50,52]. Thus, the use of highly conductive/doped nc-Si:H material should be beneficial due to the higher dopant density (lower activation energy) [185], which causes a narrow space charge region at the TCO/p interface and result in increased tunnel probability of holes through it (see band diagram in Figure 6.16).

This aspect is further investigated in this section for a device with (p)nc-SiO_x:H emitter by modifying the contact to the front ITO film. To this end, a non-oxidic (p)nc-Si:H film was inserted between the (p)nc-SiO_x:H emitter and the front ITO with deposition conditions giving both higher F_C and dopant density than the nc-SiO_x:H emitter. The outcomes of this study were published in [194,195] and [193] for device results and the transport mechanism, respectively. Figure 6.16 depicts the band diagram scheme for a device with (a) and without (b) contact layer.

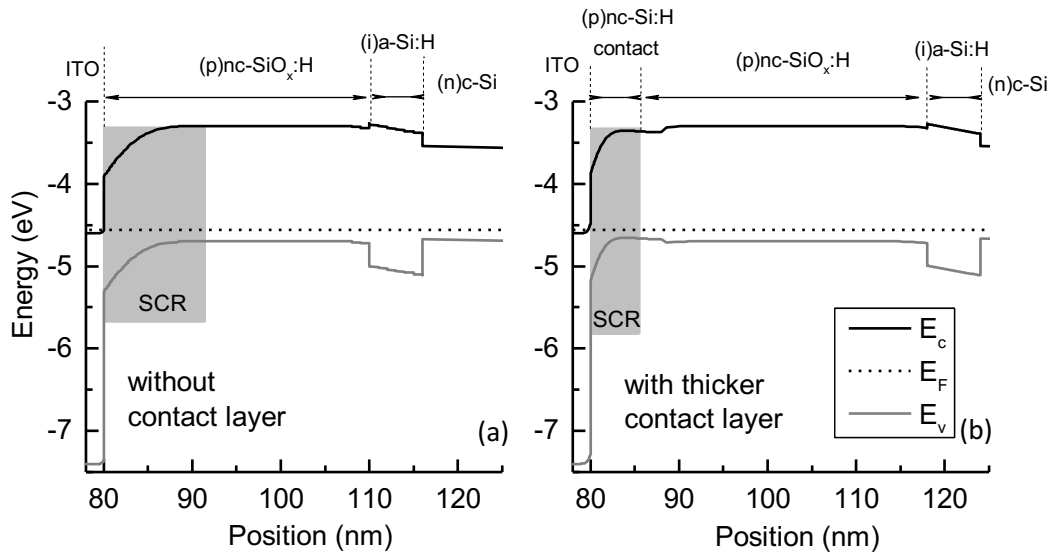


Figure 6.16. 1-D band diagram for the cell with (p)nc-SiO_x:H emitter depicted in Figure 6.15 (a) without and (b) with a 8 nm thick additional non-oxidic contact layer simulated with AFORS-HET. Layer input parameters are reported in Ref. [194] (SCR= space charge region).

Solar cells were fabricated using the same (i)/(p) stack composed of a type A (i)a-Si:H film and a 30 nm thick (p)nc-SiO_x:H emitter (deposition parameters reported in Table 6.3). Afterwards, a p-doped contact layer was deposited under similar PECVD conditions but without the addition of CO₂ in the precursor gas mixture. The thickness of the nc-Si:H contact layer was varied in a wide range adjusting the deposition time (0 – 80 s). The growth rate was determined from a thicker film (~ 200 nm) deposited on glass substrate under the same conditions. The calculated thickness on textured wafers is in the range 0 – 10 nm although a larger error margin is expected due to the discrepancy in growth rate between the early stage and the bulk film. It is moreover difficult to estimate the crystalline fraction and conductivity of such a thin contact layer, thus, the values measured on the thicker single layer are given for completeness: $F_c = 72\%$ and $\sigma = 21 \text{ S/cm}$.

Figure 6.17 shows the average η , J_{sc} , FF and R_s obtained from J - V characteristics under standard illumination conditions for contact layers of different thicknesses. Both η and FF progressively rise with increasing contact layer thickness and above roughly 4 nm settle at a constant value. The gradual approach of the J - V values to the pseudo ones with increasing contact layer thickness indicates the presence of contact problems for thinner contact layers. In effect, the R_s in Figure 6.17 (b) rapidly decreases towards a minimum ($1.1 \Omega\text{-cm}^2$) for the emitter stack with a non-oxidic layer thicker than 5 nm. This indicates that the (p)/ITO interface changes by inserting the contact layer which assists tunneling with a lower ohmic contact.

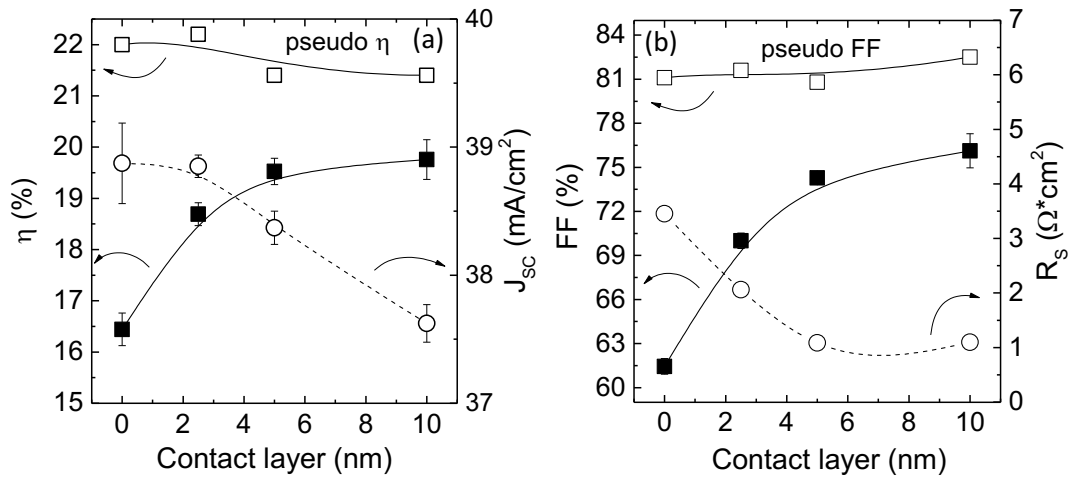


Figure 6.17. Cell parameters obtained as an average of 12 cells for each wafer as a function of the contact layer thickness. (a) Conversion efficiency η and short circuit current density J_{sc} and (b) fill factor FF were extracted from J - V characteristics and pseudo efficiency and pseudo fill factor from SunsVoc measurements. The series resistance R_s , calculated from light and pseudo J - V , is shown in (b). The lines are guides to the eye.

Electrical simulations reported earlier in Figure 6.16 confirm this hypothesis [193]. Furthermore, the pseudo parameters obtained from SunsVoc measurements add helpful information. The pseudo η is above 22% in absence of contact layer and only slightly decreases with a 2.5 nm thick contact layer due to increased parasitic absorption that reduces J_{sc} . In Figure 6.17 (b), the pseudo FF remains constant and is thus independent of the contact layer thickness. The residual difference in FF (as discussed in section 3.2.2) and η to the SunsVoc values might be attributed to the losses caused by the thicker incubation zone, the sub-optimal crystalline fraction in the bulk of the film and of the ITO/grid.

6.4. Integration of (n)nc-SiO_x:H in Rear Emitter Cells

This section starts with simulations to investigate how the light lost by reflection and parasitically absorbed in the window multilayer stack affects the generated photocurrents for rear emitter cells. Refractive index data were extracted from the n-doped single layers fabricated in section 6.2.3 for variable CO₂ flow oxygen: to an higher oxygen content in the layer correspond progressively reduced $n(\lambda)$ and $k(\lambda)$. The thickness of the layer were varied and applied as window stack (section 6.4.1). Finally, preliminary experimental results are presented in section 6.4.2.

6.4.1. Simulation Results

Simulations were performed using the OPAL 2 software on planar and pyramidal surface morphology for a multilayer stack having an (n)nc-SiO_x:H film as FSF as modeled in the sketch depicted in Figure 6.2. The modeled structure and the relative input parameters are given in section 6.1. This type of doping was chosen for this investigation since the experimental optical data were available in a wide range. Moreover, most of the corresponding films exhibited a crystalline volume fraction above 40% that makes these materials interesting for cell application (see section 6.2.3). The simulations represented a good tool for analyzing the effect of both refractive index and thickness on the losses due to reflection or parasitic absorption in the multilayer stack.

Figure 6.18 shows the computed data for the planar substrate. A characteristic trend is clearly visible for the photocurrent lost in the window stack (J_{FSF}) that progressively rises with increasing the refractive index of the film. The lower oxygen content in the layer leads to the progressively higher extinction coefficient (k) (Figure 6.18 (a)). Also, the J_{FSF} values increases among the entire set of thicknesses simulated with a current loss of above 1 mA/cm² for a 60 nm thick FSF. More interestingly, the reflection trend in Figure 6.18 (b) shows that the most transparent layer ($n = 2.0$) is the worst choice since the reflected fraction of the losses (J_{ref}) rapidly rises with decreasing n . This happens because the lower refractive index approaches that of the adjacent ITO layer whereas the optimum is in between n_{ITO} and n_{c-Si} .

Besides that, for higher n , the J_{ref} is reduced due to an improved antireflection effect caused by the better n matching of the entire stack that progressively increases from air to the c-Si substrate. It can be observed that thicker films lead to reduced J_{ref} losses for n above 2 with a minimum for n about 3. This value represents the geometric mean between the two adjacent films, i.e. ITO and (i)a-Si:H. Consequently, the photocurrent generated in the c-Si (J_{c-Si}) in Figure 6.18 (c) increases rapidly with n up to the optimal balance between J_{FSF} losses and J_{ref} gains at n of about 2.7 for the entire set of thickness investigated. Furthermore, the J_{c-Si} peak becomes broader for thinner FSF films and reaches its highest point for a thickness of 30 – 40 nm.

Figure 6.19 reports results from a similar simulation performed on random pyramids morphology. The outcomes are qualitatively similar and J_{FSF} and J_{ref} have a similar trend as discussed for the planar case (Figure 6.18 (a - b)). The antireflection effect is much less pronounced due to the improved light management and a broad minimum in J_{ref} appears again but is shifted to lower n (2.7 for film above 30 nm). The minimum stays at higher refractive index ($n=3$) for thinner films. Lastly, the outcomes for J_{c-Si} show a reduced generated photocurrent in the entire refractive index range investigated because J_{FSF} is the dominant loss phenomenon on textured morphology. The trend identified for J_{ref} is also visible in the J_{c-Si} with a minimum losses at about $n = 2.4$.

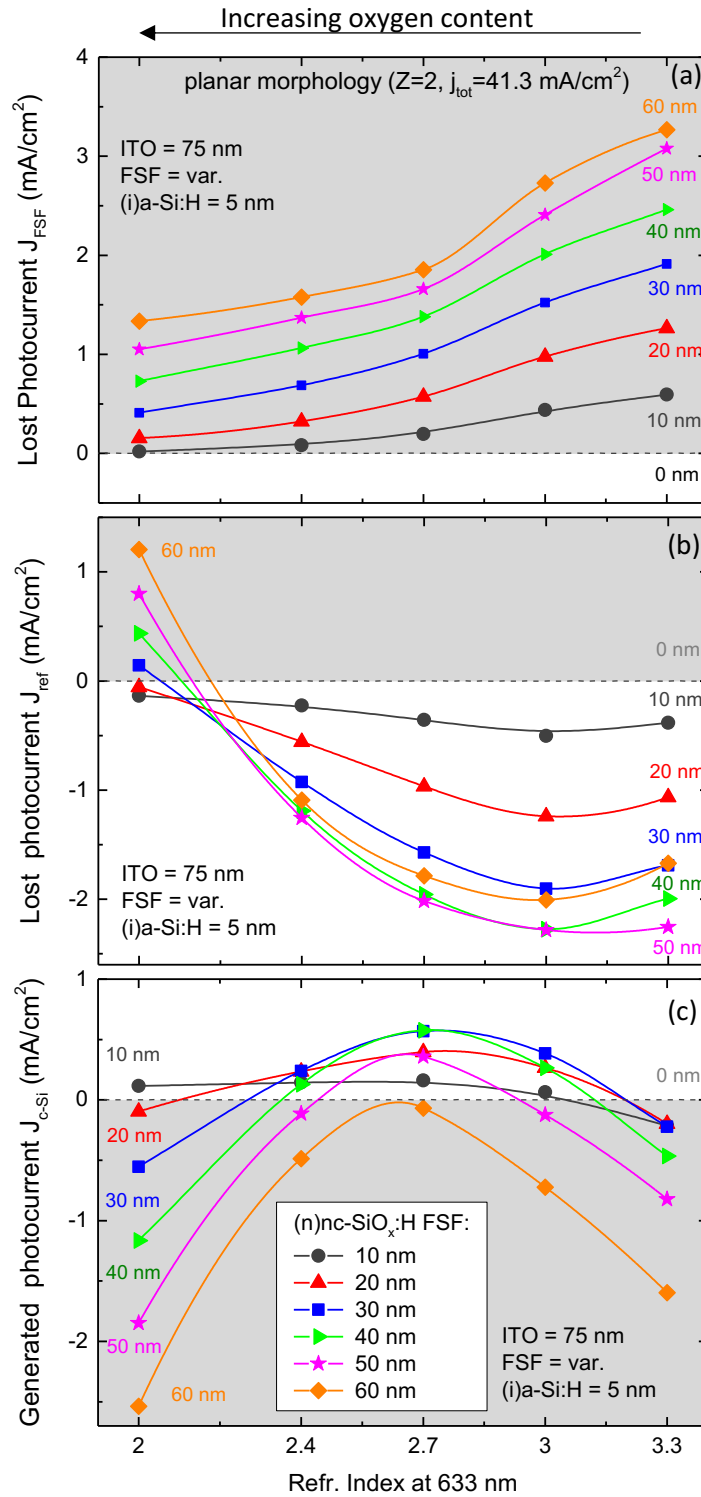


Figure 6.18. Simulated implied photocurrents that are (a) absorbed in the front surface field FSF doped layer J_{FSF} , (b) reflected from the entire front structure J_{ref} , and (c) absorbed in the c-Si wafer J_{c-Si} as a function of FSF refractive index that varies in a wide range ($2.0 < n_{633\text{nm}} < 3.3$). The values are expressed as a difference relative to the structure with a 0 nm thick (n)nc-SiO_x:H layer. The layer thickness was varied from 0 to 60 nm. The simulation were performed on planar surface morphology for the simulated stack reported in Figure 6.2. The curves are guides to the eye.

6.4. Integration of (n)nc-SiO_x:H in Rear Emitter Cells

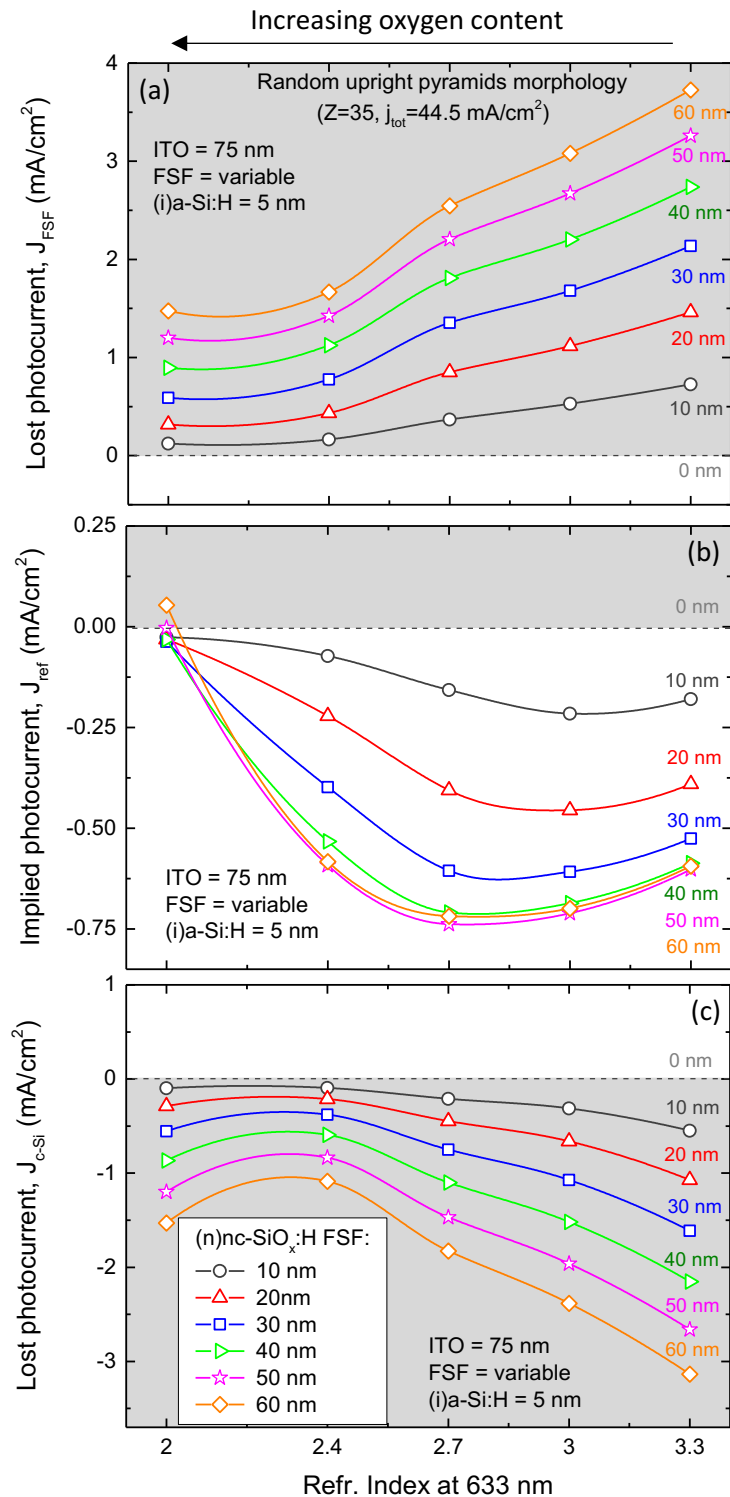


Figure 6.19. Simulated implied photocurrents that are (a) absorbed in the front surface field FSF doped layer J_{FSF} , (b) reflected from the entire front structure J_{ref} , and (c) absorbed in the c-Si wafer J_{c-Si} as a function of FSF refractive index that varies in a wide range ($2.0 < n_{633nm} < 3.3$). The values are expressed as difference relative to the structure with 0 nm thick (n)nc-SiO_x:H. The layer thickness was varied from 0 to 60 nm. The simulations were performed on random upright pyramids surface morphology for the simulated stack reported in Figure 6.2. The curves are guides to the eye.

It can be summarized, accordingly to the simulation performed here, that the optimized layer should have a refractive index of 2.7 and a thickness of 30 – 40 nm on planar surfaces. Instead, for textured morphologies the ideal features of the FSF layer are n equal to 2.4 and as thin as possible compatible with the nanocrystalline evolution of the films.

6.4.2. Solar Cell Results

The experimental results presented in this section are a preliminary attempt to apply (n)nc-SiO_x:H films on SHJ in a rear emitter configuration. More investigations are required for a better control of the material properties in terms of homogeneity and crystalline fraction on reduced thickness and concerning passivation optimization of the window stack.

The cell structure is depicted in Figure 3.1 and both polished and textured wafers were used to validate the simulated trends. The ITO and type B passivation layers were grown with nominal thicknesses of 75 nm and 10 nm, respectively. The p-doped emitter used in this study was the (p)a-Si:H doped with diborane and it was placed at the rear side of the cell.

Effect of Refractive Index

Three recipes were selected from the material investigation reported in section 6.2.3 to grow films with refractive index varied in the range between 2.4 and 2.7 in agreement with the simulation study reported in the previous section 6.4.1. The CO₂ gas flow was varied to control the oxygen incorporation whereas the other deposition parameters were kept constant as shown in Figure 6.5. The material properties of the selected recipes are summarized in Table 6.4 and the films exhibit F_c above 40%.

Table 6.4. Deposition parameters and optoelectronic properties of selected single layers for application as FSF on cell level. The film thickness is in the range 200-250 nm. The other deposition parameters were kept constant: $P_D= 250$ mW/cm² and $p= 1200$ Pa.

(n)nc-SiO _x :H	CO ₂ (sccm)	PH ₃ (sccm)	n (at 633 nm)	E_{04} (eV)	F_c (%)	σ (S/cm)
#1	12	8	2.67	2.31	49.5	$2.0 \cdot 10^{-1}$
#2	15		2.51	2.38	49.1	$4.4 \cdot 10^{-4}$
#3	18		2.37	2.45	41.5	$1.2 \cdot 10^{-6}$

Figure 6.20 shows the experimental results extracted from illuminated J - V curves for both types of substrate morphologies and compared to the J_{c-Si} simulated for the corresponded cell structure.

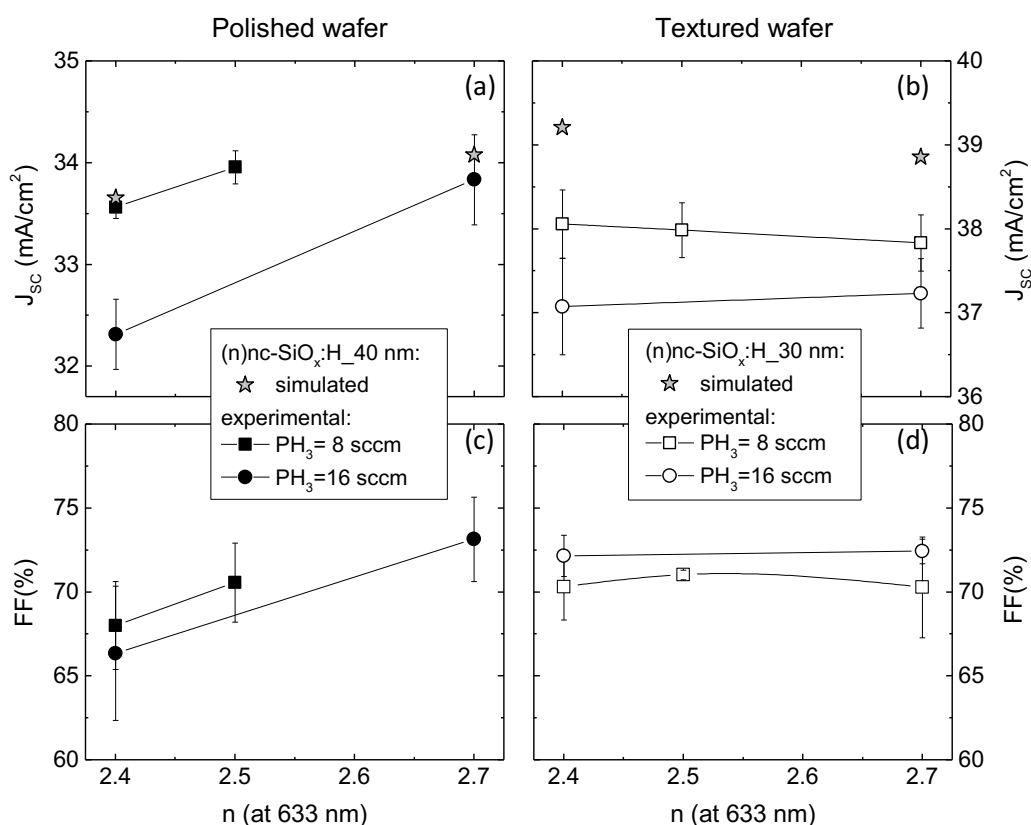


Figure 6.20. (a-b) Short circuit current density J_{sc} and (c-d) fill factor FF extracted from illuminated J - V curves as a function of the refractive index n at 633 nm of the (n)nc-SiO_x:H front surface field FSF layer grown with variable CO₂ flow (12, 15 and 18 sccm) and for two PH₃ flows (8 and 16 sccm). The cells were deposited on both polished and textured wafers with type B i-layer (8 nm) and FSF as indicated in the label. The values are an average of a set of 5 cells measured on the same samples. The stars indicate J_{c-Si} values simulated for the device structure discussed in this experiment. Other deposition parameters were: $P_D = 250$ mW/cm² and $p = 1200$ Pa. The lines are guides to the eye.

In Figure 6.20 (a), J_{sc} progressively rises with increasing refractive index of the FSF layer up to 34 mA/cm². The reduced oxygen content in the film improved the electrical properties of the film, as indicated by the σ in Table 6.4, and resulted in a higher FF on polished substrate. The FSF grown with a higher PH₃ flow resulted in current density losses of about 1 mA/cm² as expected by the narrowing of E_{04} (compare cells with $n = 2.4$). The improved FF in Figure 6.20 (c) is related to the increased conductivity within the FSF layer deposited with higher PH₃ flow.

On textured wafers, the J_{sc} rose slowly for increased oxygen content in the film (lower n) as revealed in the simulations (cf. Figure 6.19 (c)) and consequently no appreciable differences was detected concerning FF .

It can be observed that the J_{sc} measured on those solar cells are lower than the values showed in section 6.3.2 for the device having (p)nc-SiO_x:H emitters. The reason stays in the thicker (i)a-Si:H passivation layers deposited for this first set of solar cells.

By comparing the measured J_{sc} to the simulated ones, it can be concluded that the simulated trends are reproducible on cell level for both polished and textured substrates (see Figure 6.18 and Figure 6.19).

To analyze further the effect of a variation in the refractive index of the FSF layer, 1-R and EQE spectra measured on selected cells from the study discussed above are presented in Figure 6.21. The FSF film with $n=2.5$ allows lower reflection losses due to the improved

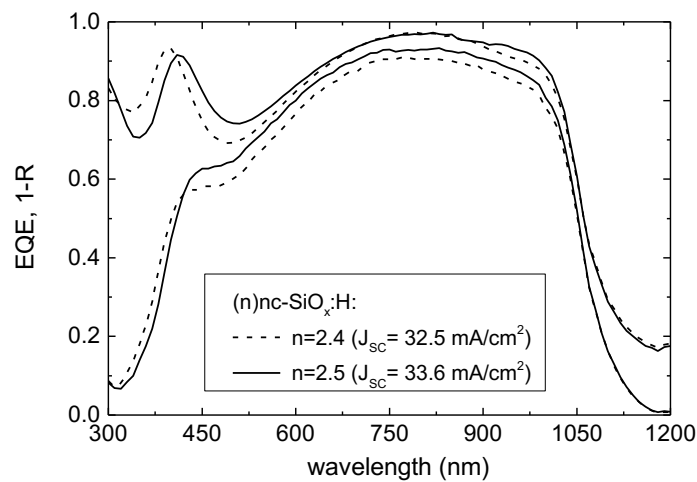


Figure 6.21. Experimental absorbance 1-R and external quantum efficiency EQE spectra as function of wavelength measured on the best cell with variable oxygen content in the 40 nm thick (n)nc-SiO_x:H front surface field layer. The cells were deposited on polished wafers.

index matching at the front stack as clearly indicated by the 1-R spectra in Figure 6.21 (a) for wavelength below 600 nm. The EQE curves in Figure 6.21 (b) indicate that the improved optics overcompensate the losses due to higher parasitic absorption ($\lambda < 450$ nm).

The cell parameters extracted from illuminated J - V curves are summarized in Table 6.5.

Effect of the FSF Thickness

The effect of the FSF thickness on J_{SC} and FF for cell with a (n)nc-SiO_x:H front surface field layer is presented in Figure 6.22. The deposition times were selected to span a range of thicknesses wide enough to evaluate the presence of trends comparable to the simulations. Moreover, the thickness of the thinnest film was carefully chosen to avoid the negative effect of the suboptimal nanocrystalline growth on the cell performance.

On polished substrates, the antireflection effect improved for a 40 nm thick FSF layer which in turn overcompensated the increased absorption due to the thicker film resulting in a maximum in J_{SC} (Figure 6.22 (a)). The influence of the (n)nc-SiO_x:H thickness was investigated elsewhere [209], where the nc-SiO_x:H was used as emitter film for a p-type c-Si substrate. Interestingly, in this publication no significant effect on the J_{SC} was measured even if reduced reflected losses were detected for thicker film. In contrast, it was noticed a strong degradation of cell performance (FF and η) for (n)nc-SiO_x:H film of 30 nm possibly caused by the predominant amorphous phase of TEM image show [209]. Furthermore,

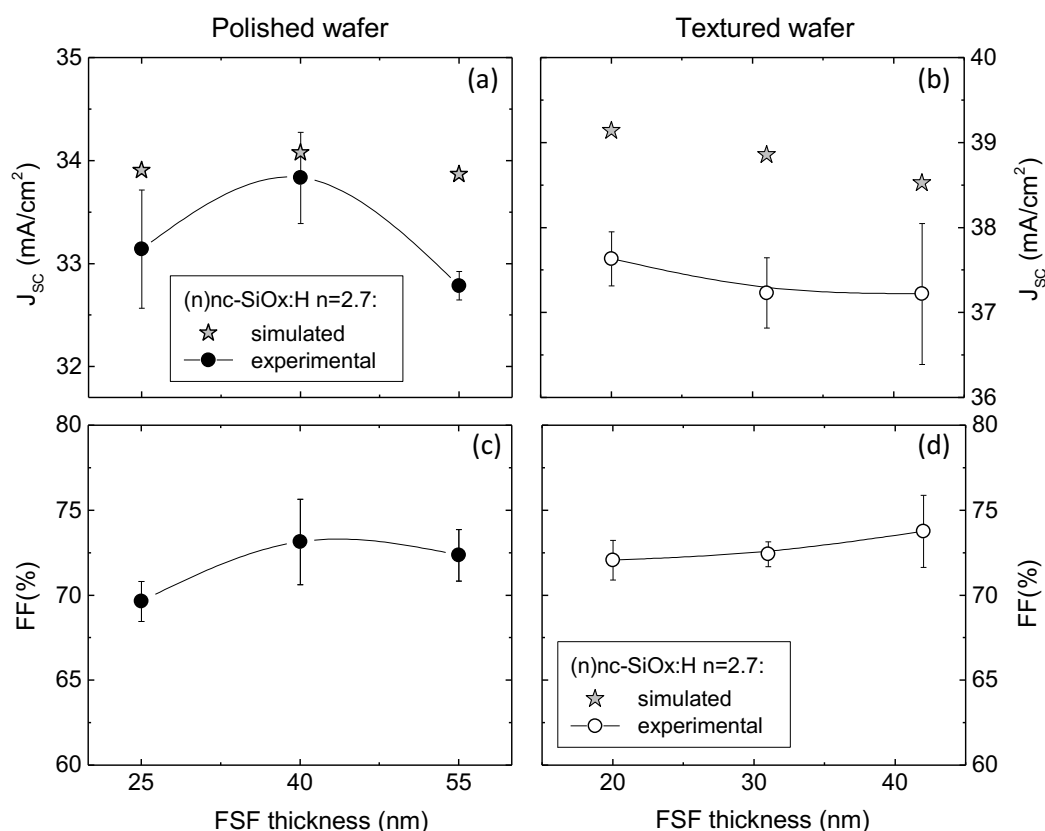


Figure 6.22. (a-b) Short circuit current density J_{SC} and (c-d) fill factor FF extracted from illuminated J-V curves as function of the (n)nc-SiO_x:H front surface field (FSF) thickness on polished and textured wafers. The values are an average of a set of 5 cells measured on the same samples. The cells were deposited on both polished and textured wafers with type B i-layer (8 nm). The values are an average of a set of 5 cells measured on the same samples. The stars indicate J_{c-sj} values simulated for the device structure discussed in this experiment. Other deposition parameters are: CO₂= 12 sccm, PH₃= 16 sccm, P_D = 250 mW/cm² and p = 1200 Pa. The lines are guides to the eye.

Raman measurements performed on our cell structures (deposited on glass) exhibited F_c around 20%.

On textured substrates, J_{sc} progressively reduced with thicker FSF layers due to the increased parasitic absorption within the film. Contrary to the observations for the (p)nc-SiO_x:H emitter in section 6.2.2, the FF improved only slightly for both substrates. The best cells measured within this series are reported in Table 6.5.

Table 6.5. Solar cell parameters of the best cells with (n)nc-SiO_x:H front surface field layers shown in Figure 6.20 and Figure 6.22.

substrate	PH ₃ /thick. (sccm)/(nm)	n (633 nm)	J_{sc} (mA/cm ²)	V_{oc} (mV)	FF (%)	η (%)	R_{oc} (Ω cm ²)
polished	8/40	2.7	34.3	704	72.2	17.4	3.18
polished	16/40	2.5	34.1	705	71.5	17.2	3.45
textured	16/31	2.4	38.3	696	71.7	19.1	2.43
textured	16/20	2.7	38.1	691	73.7	19.4	1.87

This suggests that the (n)nc-SiO_x:H film overcomes the incubation zone faster than the p-doped ones. The cells show well-shaped J - V curves independent of the FSF thickness and substrate type. Nevertheless, more detailed investigations are required to understand the influence of PH₃ on the incubation zone and nanocrystalline evolution of (p)nc-SiO_x:H films.

Further Fill Factor Improvements

Considering the studies reported in chapter 5 and in section 6.3.4, two more variations were tested in order to explore the potential of (n)nc-SiO_x:H FSF. Some adjustments to the solar cell structure were necessary, namely:

- Replacement of the AZO on the rear side with ITO since the (p)a-Si:H emitter optimization was conducted in contact with an ITO layer.
- Use of a thicker (n)nc-Si:H contact layer between the n-FSF and the front ITO.

The solar cell parameters for different (n)nc-SiO_x:H FSF layers are summarized in Table 6.6. Looking at Table 6.6, we can conclude that the low open circuit voltages is the main limitation of the cells. The carrier lifetime measurements on the cell precursors, reported in Table 6.6, suggest that the reduced V_{oc} is caused by either etching of/damage to the passivation layer during the FSF depositions or by the low conductivity of the thin FSF film.

Table 6.6. Solar cell parameters of the best cells with (n)nc-SiO_x:H deposited for PH₃=16 sccm and CO₂=15 sccm with refractive index of 2.7.

(n)nc-SiO _x :H (nm)	TCO emi.	J_{sc} (mA/cm ²)	$i-V_{oc}$ (mV)	V_{oc} (mV)	FF (%)	η (%)	R_{oc} ($\Omega \cdot \text{cm}^2$)
40	ITO	33.7	711	708	74.6	17.8	2.57
30	ITO	37.7	706	693	75.2	19.7	1.68
30 + contact layer 20s	AZO	38.2	702	705	77.1	20.8	1.49

Nevertheless, the values of FF , which reach 77% and 74.6% on textured and polished wafers, respectively, are promising for further optimization on cell level which was beyond the scope of this work. We believe that the plasma treatment of the (i)a-Si:H surface prior to the FSF deposition (i.e. CO₂PT) might lead to better control of the nanocrystalline evolution as shown for the nc-Si:H emitter layers in section 5.2.1.

6.5. Discussion and Conclusions

P- and n-doped nanocrystalline silicon oxide (nc-SiO_x:H) were investigated to minimize the current losses at the illuminated side of a silicon heterojunction solar cells.

The opportunity of control the oxygen incorporation into the matrix by an appropriate variation of PECVD deposition regime was studied. The impact of power and gas pressure on the film optoelectronic properties shows a similar trend independently of the doping types. As expected from literature data [205,213], for a fixed refractive index, higher conductivities by several orders of magnitude are measured for n-doped nc-SiO_x:H films as compared to the p-doped ones.

Photocurrent loss analysis was carried out for devices both in front and rear emitter configuration having different types of contact layers (a-Si:H, nc-Si:H and nc-SiO_x:H) in stack with (i)a-Si:H and ITO films. Optical simulations shown that a stack with refractive index that progressively increases from the air to the silicon absorber leads to a significant reduction of losses due to reflection and parasitic absorption.

The following conclusions were drawn.

On planar morphology, the antireflection effect of the doped film depends both on the film thickness and refractive index. For nc-SiO_x:H emitter layers, the reduced reflectance losses overcompensate the parasitic absorption with a maximum current gain for a layer that is 3-6 times thicker than the commonly used 5 – 10 nm (p)a-Si:H, with an optimum refractive index for nc-SiO_x:H to be at 2.7. On the contrary, a-Si:H and nc-Si:H films accounted for a progressive reduction in current density due to their refractive index approaching 4 and stronger parasitic absorption.

On textured Si wafers, the improved light trapping due to the random pyramids reduces the potential for the anti-reflection effect, thus, the benefit of using nc-SiO_x:H films is limited to the reduced parasitic absorption.

The short circuit density J_{SC} measured on completed devices with different emitter layers are summarized in Table 6.7 and compared to the simulated ones. J_{SC} is maximized for a (p)nc-SiO_x:H film with a J_{SC} of 40.4 mA/cm² with a gain of 2 mA/cm² as compared to the amorphous emitter (compare Fig. 6.13), but at the cost of FF, as will be discussed in the following.

Table 6.7. Simulated generated photocurrent J_{c-Si} and experimental J_{SC-EQE} for different emitter layers both on planar and pyramid surface morphologies. The emitter thicknesses t are in agreement with the analysis performed in the previous session. The experimental J_{SC} s are measured on devices with front metal grids, whereas the simulated J_{c-Si} s are corrected to take into account the estimated 5% grid shadowing.

Surface morphology	Emitter	t (nm)	J_{c-Si} (mA/cm ²) Simulated	$J_{SC-light\ J-V}$ (mA/cm ²) Experimental
polished	(p)a-Si:H	13	33.7	32.9
	(p)nc-Si:H	20	34.2	34.1
	(p)nc-SiO _x :H	20	35.3	35.1
textured	(p)a-Si:H	8	38.8	38.3
	(p)nc-Si:H	15	38.9	38.8
	(p)nc-SiO _x :H	30	40.0	40.4

The lower conductivities measured on (p)nc-SiO_x:H single layers resulted in lower fill factors ($FF = 72.9\%$) as compared to the reference cells. We suggest that sources of fill factor FF losses originates from (i) the thicker incubation zone, (ii) too low crystalline fraction in the bulk of the emitter and (iii) too highly resistive contact to the front TCO. The last aspect appears to be the main reason and was investigated by inserting a highly conductive (p)nc-Si:H film (“contact layer”) between the emitter and the TCO. For both p- and n-type nc-SiO_x:H emitters introduction of a non-oxidic contact layer resulted in a reduced series resistance and, hence, improved FF almost to the reference level for thick enough contact layer. However, by introducing the contact layer, the optical benefit was almost completely lost.

To sum up, based on the results presented here, neither p- nor n-type nc-SiO_x:H did fulfill our expectations to improve the efficiency of Si heterojunction solar cells completely yet. While the optical advantages could be clearly demonstrated both from simulations and experiments, the poor electrical performance compensated the optical gain, so far.

Therefore, a new approach to improve both optics and electrics by using an ultra-thin a-SiO_x layer for c-Si passivation *and* nucleation enhancement of the nc-Si:H emitter is explored in the subsequent chapter.

7. Exploratory Study on Thin Silicon Dioxide Passivation Layers

In the previous chapters 5 and 6, we investigated the integration of thin doped hydrogenated nanocrystalline silicon and nanocrystalline silicon oxide (nc-Si:H and nc-SiO_x:H) layers in silicon heterojunction (SHJ) solar cells aiming to enhance the solar cell current (J_{sc}). Structural characterizations and solar cell results demonstrated that a fast and fully developed nanocrystalline growth on top of the intrinsic amorphous passivation layer is challenging. Although an increased J_{sc} value was achieved, increased series resistance and low fill factors limited the cell conversion efficiency and therefore the application of such materials in this configuration.

In this chapter, we explore an alternative approach with the aim to circumvent the unfavorable substrate dependence of nc-Si:H layer growth on the underlying (i)a-Si:H layer. Motivated by the beneficial effect of treating the (i)a-Si:H surface with CO₂ plasma prior to the nc-Si:H emitter deposition (chapter 5) and by the recent results with oxide passivated contact shown in Ref. [68], we develop a PECVD process for growing an ultra-thin amorphous silicon oxide a-SiO_x:H film acting as both passivation and nucleation enhancement for the doped nanocrystalline silicon films.

Furthermore, optical improvements are expected on cell level, due to reduced parasitic absorption resulting both from the removal of the (i)a-Si:H film and the increased crystalline fraction in the (p)nc-Si:H layer. Ideally, if the nc-Si:H layer exhibits a drastically higher F_c , its thickness can be more freely adjusted.

Parts of the results have been published in [219].

7.1. Introduction

The growth of an a-SiO_x:H passivation & nucleation-enhancement film by plasma enhanced chemical vapor deposition (PECVD) is attractive, since we can use the same deposition tool employed for the other silicon layers and process them without vacuum break. For best passivation, we aim for stoichiometric silicon dioxide (SiO₂) material. The SiO₂ film has to

fulfil some requirements, namely due to its isolating nature, it has to be ultra-thin (below 2 nm) to allow carrier tunneling. Furthermore, it has to be of high purity and stoichiometric for optimal passivation, and it must be uniformly deposited on the Si surface [63]. Usually such films have been grown by wet-chemical [63] or by thermal oxidation [220] methods.

Some groups have reported on a-SiO_x:H films grown by PECVD as passivation film in SHJ solar cells for reducing parasitic absorption [62], or to prevent epitaxial growth at the interface with c-Si [221]. Recent investigations [62,222], performed in combination with (p)a-Si:H emitters, reveal that the contact performance degraded with the oxygen content in the amorphous intrinsic film leading to both losses in V_{OC} and FF . The alloying process increases the valence band offset at the hole contact, progressively increasing the transport barrier for holes. The solution suggested in both studies is a combination of thin (i)a-Si:H and a-SiO_x:H films instead of a thicker a-SiO_x:H film. On the other hand, PECVD a-SiO_x:H films are preferred as passivation film instead of the reference (i)a-Si:H in devices having nanocrystalline emitter [208,209,223,224]. This combination is slightly beneficial for improving FF , but the V_{OC} is generally limited compared to devices with conventional (i)a-Si:H passivation layer.

SiO₂, thermally-grown at temperatures as high as 1000 °C [225] or wet-chemically-grown [31], is well-known in the microelectronics as passivation layer as it allows for extremely low effective surface recombination velocity due to low surface defect density ($D_{it} \sim 10^{10} \text{ cm}^{-2} \text{ eV}^{-1}$). Earlier applications in solar cells are found in the studies of Yablonovitch *et al.* [226] and Kawabata *et al.* from Mitsubishi Electric Corporation [227], where an ultra-thin oxide layer reduced the surface defect density and allowed for V_{OC} improvements in combination with nc-Si:H emitters. In the past years, a passivated contact scheme consisting of an ultra-thin SiO₂ layer have regained the attention of the community, for their high potential in passivation performance [220,228,229] and compatibility with standard high temperature screen printing.

Recently, the TOPcon solar cell with diffused front boron emitter and rear passivated SiO₂ contact covered by a n-type doped poly-Si film achieved a conversion efficiency of 25.1% [68]. Films, grown by thermal, wet chemically or ozone oxidation, have achieved $i-V_{OC}$ of above 740 mV [220]. In contrast to thermal oxides, such dry- or wet-chemically growth oxides usually need a high-temperature annealing (activation) step to enhance the passivation performance.

Other techniques that have been used to grow quasi-stoichiometric SiO₂ films include electron cyclotron resonance [230], remote plasma [231] and PECVD [152,232].

7.2. Material Optimization

In this section, the effect of precursor gas composition on the optical and structural properties is investigated. Therefore, passivation performances of the optimized a-SiO_x:H layer are tested using cell relevant thicknesses.

a-SiO_x:H films were deposited by PECVD with a precursor gas mixture of SiH₄, N₂O and H₂ (Table 7.1). The N₂O/SiH₄ ratio was varied in a wide range with the aim to grow a stoichiometric silicon dioxide film, whereas power and pressure were kept constant. The power density P_D was chosen to be as low as possible to avoid any surface damage when the film is grown on a c-Si wafer while ensuring plasma stability [138].

Several types of samples were fabricated to allow the use of different characterization methods. Both polished and textured n-type wafers with <100> and <111> lattice orientation, respectively, were selected for the investigation. The sample structures are presented in Figure 7.1.

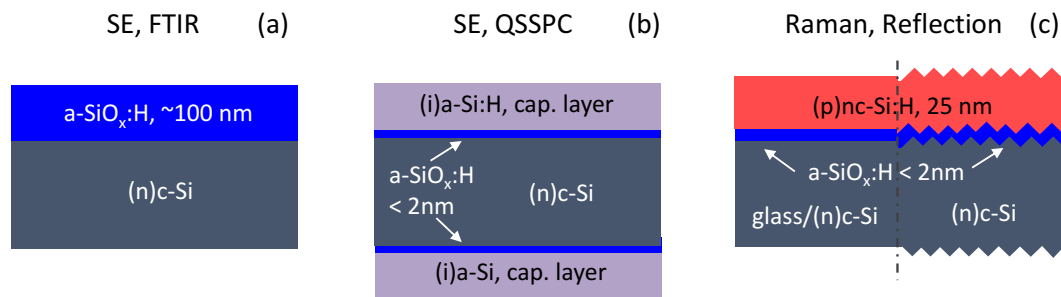


Figure 7.1. Overview of samples fabricated for material characterization. For each structure, the type of study possible is also indicated. The film thickness is referred to the planar morphology.

Table 7.1. Deposition parameters for the a-SiO_x:H material. P_D : plasma power density; p : chamber pressure; T_{sub} : substrate temperature and precursor gas flows. Electrode spacing was fixed at 16.5 mm.

P_D (mW/cm ²)	p (Pa)	T_{sub} (°C)	N ₂ O (sccm)	SiH ₄ (sccm)	H ₂ (sccm)
15	200	185	60	120	900
			120	60	
			170	10	
			175	5	
			500	4.5	-

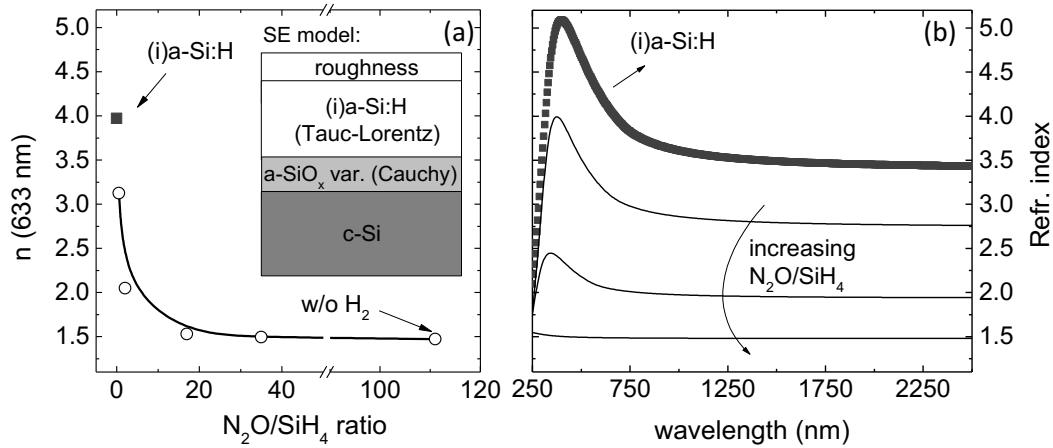


Figure 7.2. (a) Refractive index n at 633 nm as function of the N_2O/SiH_4 ratio and (b) the entire spectra as function of wavelength for selected ratios as indicated. The data are measured by ellipsometry for ultra-thin a-SiO_x:H capped with (i)a-Si:H protective film. The sample sketch and the SE model used to fit the experimental curves is indicated in (a).

Samples with ultra-thin oxide films were capped with a 15 nm thick (i)a-Si:H film to protect the a-SiO_x from further oxidation in air atmosphere. Thermal annealing steps were performed in forming gas (FG) atmosphere used for its well-known properties to enhance passivation properties [232]. The samples were treated in a rapid thermal annealing oven (RTA) for 30 min with a ramp of 150 °C/min at a variable temperature up to 650 °C.

7.2.1. Optical and Structural Properties

The a-SiO_x:H films were initially 10 nm thick and progressively the thickness was reduced to below 2 nm that represents the target for application in a device. As consequence of the optimization process, the a-SiO_x:H deposition was reproducible and the film properties were controlled independently of thickness. The dispersion spectra for the different a-SiO_x:H films are shown in Figure 7.2. The refractive index reduced with increasing the N_2O/SiH_4 ratio in the gas mixture. For the highest diluted condition, n extracted at 633 nm approaches the stoichiometric value ($n_{SiO_2} = 1.461$) [233]. The refractive index trend is in agreement with literature [234], this might be explained by more oxygen incorporation in the film and/or by porosity. In contrast to the findings of Ref. [234] the deposition rate in our experiment remains unchanged and only slightly drops for $N_2O/SiH_4 = 35$.

Structural characterization is required to investigate the material quality and stoichiometry, thus, Fourier transform infrared (FTIR) transmission spectra were measured on layers deposited at N_2O/SiH_4 ratios of 17, 35 and 110 (sample structure in Figure 7.1 (a)).

The absorption coefficient spectra determined for the as-grown condition at room temperature are depicted in Figure 7.3 (a). The (i)a-Si:H reference film shows the typical vibration modes of the Si-Si bond centered at 600 cm⁻¹ and of Si-H bonds at

2000 – 2100 cm^{-1} . The latter is a characteristic indication of the hydrogen content [150,155] that is beneficial for the dangling bonds passivation. Looking at the a-SiO_x:H sample growth with the lower N₂O/SiH₄ ratio (curve b), the typical vibration modes of silicon oxide nitride material (a-SiO_xN_x:H) are clearly visible at 870 cm^{-1} and 3390 cm^{-1} caused by Si-N and N-H stretching modes, respectively. Moreover, the film contains H, probably bonded to N, as deduced from the shift of the Si-H stretching regime to higher frequencies [151].

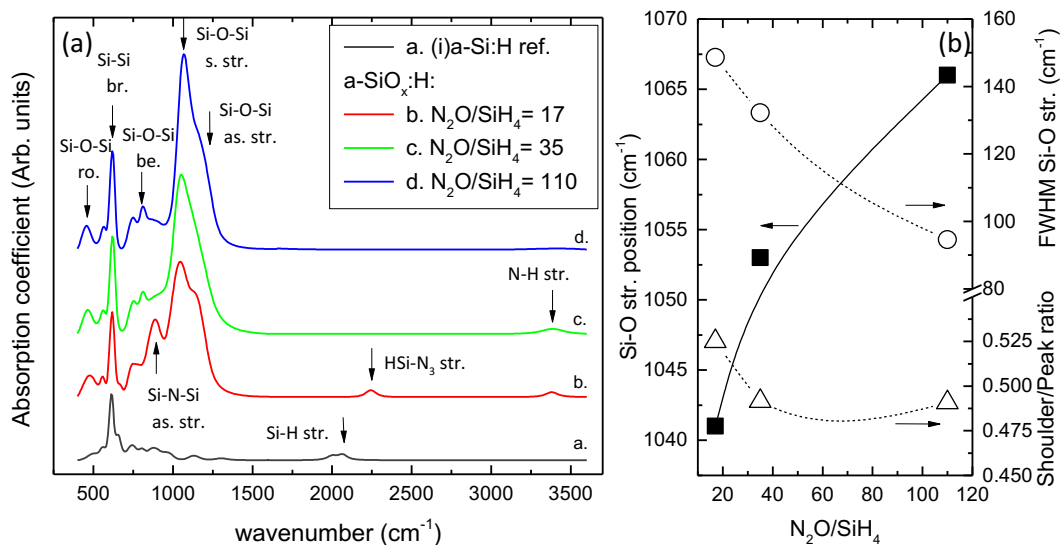


Figure 7.3. (a) Absorption coefficient as function of wavenumber for variable N₂O/SiH₄ ratios measured at room temperature in the as-grown condition. The spectrum of (i)a-Si:H is given as reference. The relevant modes are identified by arrows (ro.=rocking, be.=bending, br.=breathing, str.=stretching, as.=asymmetric, s.=symmetric) with the associated bonds. The curves are vertically shifted for easier comparison. (b) Evolution of the Si-O stretching mode peak position, the corresponding full width at half maximum FWHM and the shoulder/peak ratio for the symmetric and asymmetric modes as function of N₂O/SiH₄ ratio. Lines are guides to the eye.

Date *et al.* [75] investigated the dissociation of N₂O molecules in PECVD discharge and revealed that NO and N represent minor by-products besides the more abundant N₂ and O₂. Figure 7.3 (a) shows that the incorporation of undesired species can be lowered by (i) increasing the N₂O flow [235] and (ii) removing the H₂ flow from the gas mixture. Pai *et al.* [153] have shown that N and H impurity content can be reduced by adding He to the gas mixture.

Looking at the curve c in Figure 7.3 (a), the film grown with higher N₂O gas flow has considerably reduced modes associated to Si-N and N-H bonds. In addition, the Si-H peak completely vanishes and the Si-O stretching regime becomes more intense and shifts to higher wavenumbers. Finally, the film deposited without H₂ flow and at the highest N₂O/SiH₄ ratio (curve d) leads to a spectrum very close to the one typical of SiO₂ [236]. The much lower amount of nitrogen and hydrogen might be explained by the lower SiH₄ gas

flow and the removal of H₂ in the gas mixture. This strongly lowers the possible interactions of NO and N species with H. Only a broad and low intensity N-H peak at 3400 cm⁻¹ was detected (not visible in Figure 7.3 (a) due to the scale).

The Si-O stretching absorption peak shifts towards higher wavenumbers (1070 cm⁻¹) as compared to the spectra grown with lower N₂O/SiH₄ ratio (Figure 7.3 (b)), furthermore a clear shoulder appears at around 1150 cm⁻¹. Both features suggest that the O content approaches to the stoichiometry ($x = 2$) as discussed by He *et al.* [237] for a a-SiO_x:H deposited by PECVD and as compared to the spectrum of thermally grown SiO₂ [236].

Moreover, Figure 7.3 (b) shows the full width at half maximum (FWHM) for the Si-O stretching mode as function of the N₂O/SiH₄ ratio and consecutively of the oxygen content in the film. Qualitatively and quantitatively, similar tendency has been observed elsewhere [237] for x above 1. The reduction of the FWHM values indicates that the Si-O stretching peak becomes progressively sharper. The shoulder/peak ratio of the Si-O (asymmetric/symmetric) stretching regime follows a decreasing trend as well, that describes the progressive rising of the out-of-phase Si-O peak and the approach to stoichiometry [152].

The bond densities of the relevant peaks for the three a-SiO_x:H films are presented in Table 7.2 and indicated by square brackets. The [Si-N] bond density is gradually reduced as the N₂O/SiH₄ ratio increases, while the [Si-H] was only detected for the film with the lowest oxygen content. It can be seen that the Si-O bond density exceeds 6×10^{22} cm⁻³ for all the films and it seems to be independent of the N₂O/SiH₄ ratio, i.e. of the oxygen source available in the deposition chamber during the PECVD process. The substantial reduction of H₂/SiH₄ decreases the bonding probability of Si with nitrogen species.

Comparing the three materials with literature data [238] grown from different gas mixtures, we confirmed that the film deposited at the lowest N₂O flow is an a-SiO_xN_y:H oxygen-rich as indicated by the refractive index below 1.75 and low [Si-N]. Whereas, for higher N₂O/SiH₄, the material progressively approaches SiO₂ even if low nitrogen impurities are detectable.

As highlighted above, the (i)a-Si:H reference shows a significant Si-H bond density. The low, but still detectable, [Si-O] might originate from unintentional surface oxidation once the sample was exposed to the air atmosphere after the deposition.

Table 7.2. Bond densities of (i)a-Si:H reference and a-SiO_x:H films grown using different N₂O/SiH₄ ratios during PECVD deposition.

N ₂ O/SiH ₄ ratio	n (633 nm)	bond density ($\times 10^{22}$ cm ⁻³)			
		[Si-N]	[Si-O]	[Si-H]	[N-H]
0 (ref.)	3.97	0	0.17	1.10	0
17	1.531	1.75	6.50	0.82	0.28
35	1.495	1.14	6.50	0	0.42
110	1.473	0.86	6.76	0	0.13

Effect of Annealing on the Structural Properties

The annealing effect on the structural properties of a-SiO_x:H was investigated under forming gas atmosphere at two temperatures (300 and 650 °C).

The peak positions of the Si-O stretching mode and the corresponding FWHM are plotted against the annealing temperature T_{ann} in Figure 7.4. The Si-O stretching peak position shifts toward higher wavenumbers with increasing annealing temperature [239] independent of the N₂O/SiH₄ ratio (Figure 7.4 (a)). In the case of the FWHM parameter, a different trend is detectable. For the oxygen richer samples (N₂O/SiH₄ = 35 and 110), the Si-O peak becomes sharper as the annealing temperature increases, while that for a-SiO_xN_y:H broadens (Figure 7.4 (b)). Considering both components, the thermal annealing increases the structural order and/or induces thermal relaxation of the lattice and, finally, improves the film quality for the oxygen richer films that approach the spectra of the stoichiometric SiO₂ [233].

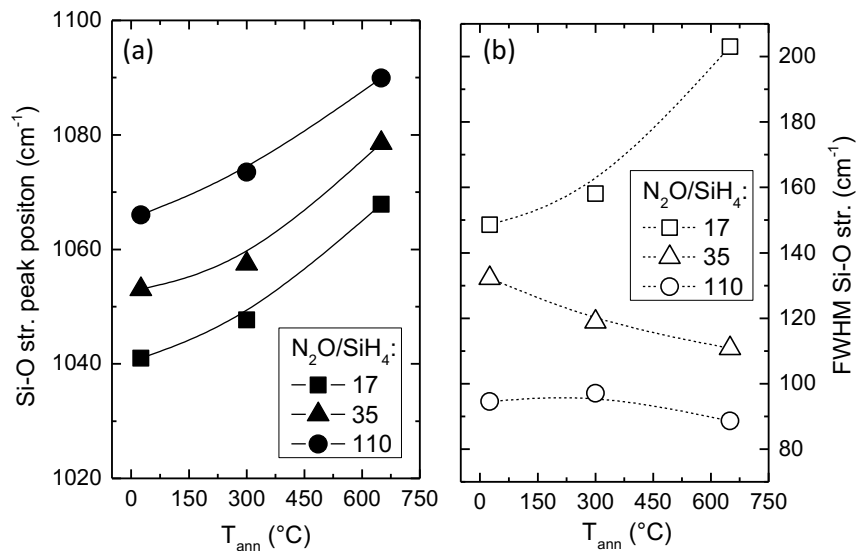


Figure 7.4. (a) Evolution of the stretching Si-O peak position and (b) the corresponding full width at half maximum FWHM as function of the annealing temperature T_{ann} for variable N₂O/SiH₄ ratio. Lines are guides to the eye.

The bond densities plotted as a function of the annealing temperature for selected a-SiO_x:H films are presented in Figure 7.5. The evolution of the N-H stretching peak, centered at 3380 cm⁻¹, reveals that at the highest temperature investigated, the bond density is lower than in the as-grown state, suggesting H release. In the literature [230] a-SiN_x films, have been reported to show a similar tendency at much higher temperature (above 900°C), this difference indicates that N is less strongly bonded in our films.

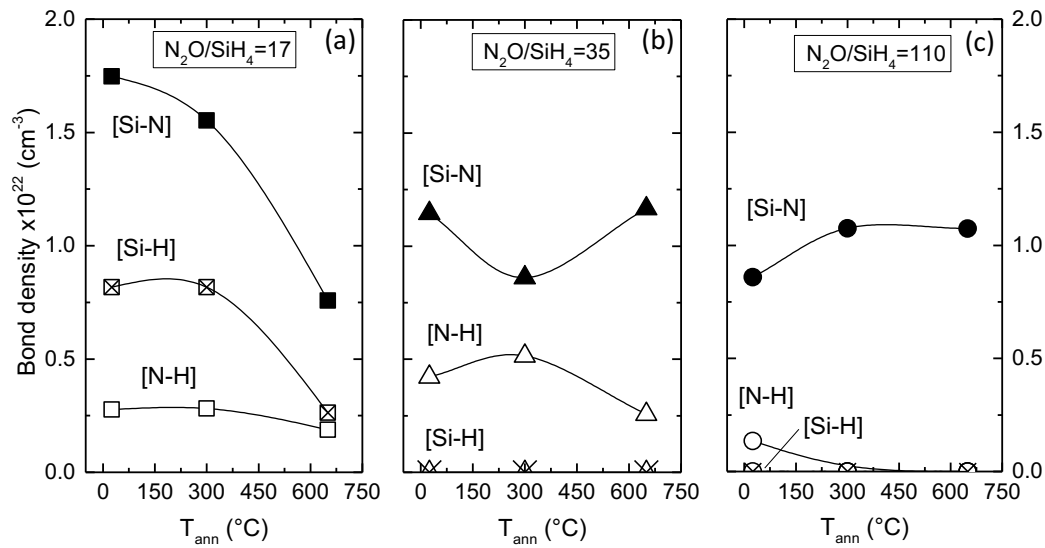
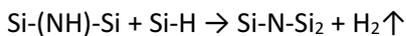
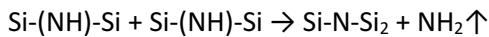


Figure 7.5. Evolution of the bond densities for the [Si-N], [N-H] and [Si-H] as a function of the annealing temperature T_{ann} for variable $\text{N}_2\text{O}/\text{SiH}_4$ ratio, as extracted from FTIR data. Lines are guides to the eye.

In the case of the most stoichiometric film in Figure 7.5 (c), the [N-H] vanishes completely after the treatment at 300 $^{\circ}\text{C}$. For the film deposited at $\text{N}_2\text{O}/\text{SiH}_4$ of 35, the annealing at 300 $^{\circ}\text{C}$ increases the N-H concentration (Figure 7.5 (b)). San Andrés *et al.* [230] explain the observed tendency by the non-bonded H atoms that form new N-H bonds. This hypothesis is consistent with the deposition condition used for growing this sample. Effectively, the presence of non-bonded H is possible in both materials since they were deposited using a high H_2 flow, whereas the probability is drastically lower for the film having the $\text{N}_2\text{O}/\text{SiH}_4$ of 110. For the latter, the only source of hydrogen comes from the silane gas that is below 5 sccm (see Table 7.1). Moreover the Si-N bond density, in Figure 7.5 (b), symmetrically follows the [N-H] trend and suggests that Si-N bond formation by the following reaction [240]:

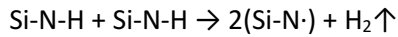


For the film in Figure 7.5 (a), the presence of the shifted peak at 2300 cm^{-1} indicates a possibility of the reaction below with release of volatile NH_2 species [240]:



Moreover, for this layer the bond density analysis in Figure 7.5 (a) indicates N losses.

Finally, for the most stoichiometric film the previous mechanisms appears unlikely since no Si-H bonds are detected and no net reduction of N bond density is measured. This observation leads to the same conclusions as drawn in [230], that is the release of H comes from the rupture of the N-H bonds without subsequent formation of other bonds as indicated below:



As highlighted by the authors in [230], the reaction leads to material degradations.

Considering the structural investigations, the best a-SiO_x:H is the film grown at N₂O/SiH₄= 110.

7.2.2. Passivation Performances

The passivation performance of the a-SiO_x:H films on <100> oriented c-Si surfaces were further investigated and the results are shown in Figure 7.6. The sample consisted in an ultra-thin a-SiO_x:H film covered with an (i)a-Si:H protective layer (15 nm). The schematic view is given in Figure 7.1 (b).

Considering the as-grown values in Figure 7.6 (a), it can be seen a much better passivation of the (i)a-Si:H reference and, as expected, the *i-V_{oc}* is enhanced by the low temperature annealing up to 250 °C. The H atoms diffuse and better passivate dangling bonds at the a-Si/c-Si interface. Above 250° C, the (i)a-Si:H film degraded due to hydrogen effusion out of the amorphous network [90].

The a-SiO_x:H samples exhibit a rapid degradation of *i-V_{oc}* with increasing the oxygen content (or N₂O/SiH₄ ratio in the PECVD process) in Figure 7.6 (a) as reported in [222] but a higher thermal stability. The analyzed samples show the same tendency with a pronounced improvement in passivation performance at 300 °C (not shown for all the a-SiO_x:H films).

The maximum *i-V_{oc}* and τ_{eff} were measured for the a-SiO_x:H material closest to stoichiometric SiO₂ with values of 686 mV and 1.6 ms, respectively, as the entire curve Figure 7.6 (b) in is shifted towards higher τ_{eff} . At higher T_{ann} , the passivation reverted to the as-grown condition. The degradation is detected at much lower temperature than typically experimented for thermally or chemically SiO₂ grown [228]. A similar temperature range was shown to be optimal for 10 nm thick PECVD a-SiO_x:H layer with a higher τ_{eff} of 5.5 ms detected on highly resistive wafers [232].

Figure 7.6 (b) shows the injection dependence of the minority carrier lifetime curves measured on the sample deposited at the N₂O/SiH₄ ratio of 110 in the as-deposited condition and after annealing treatments. The experimental curves were fitted as described in [163] to extract the defect density (D_{it}) and fixed-charge density (Q_f) presented in Figure 7.6 (c). The curve changes drastically after the first annealing and both fitting parameters need to be reduced. At T_{ann} of 300 °C, D_{it} decreases by two orders of magnitude, which indicates a reduction of a-SiO_x:H/c-Si interface defect density with a shift of the entire curve towards higher carrier lifetime. Considering the structural investigation discussed above, the vanishing of weakly bonded N atoms and the lattice re-organization might contribute to the improved electrical properties.

To test the role of the intrinsic capping layer on the passivation process during the annealing, a symmetric sample with a thicker a-SiO_x:H was deposited and annealed in the same range of temperature. The results are displayed in Figure 7.6 (a) with a similar trend. This proves that the FG atmosphere is required [229,232] but indicates that the intrinsic capping layer also plays a role in enhancing the passivation performances of the a-SiO_x:H film. We suggest that the a-SiO_x:H takes advantage of H atoms that diffuse out of the (i)a-Si:H network thanks to the temperature and the FG external pressure.

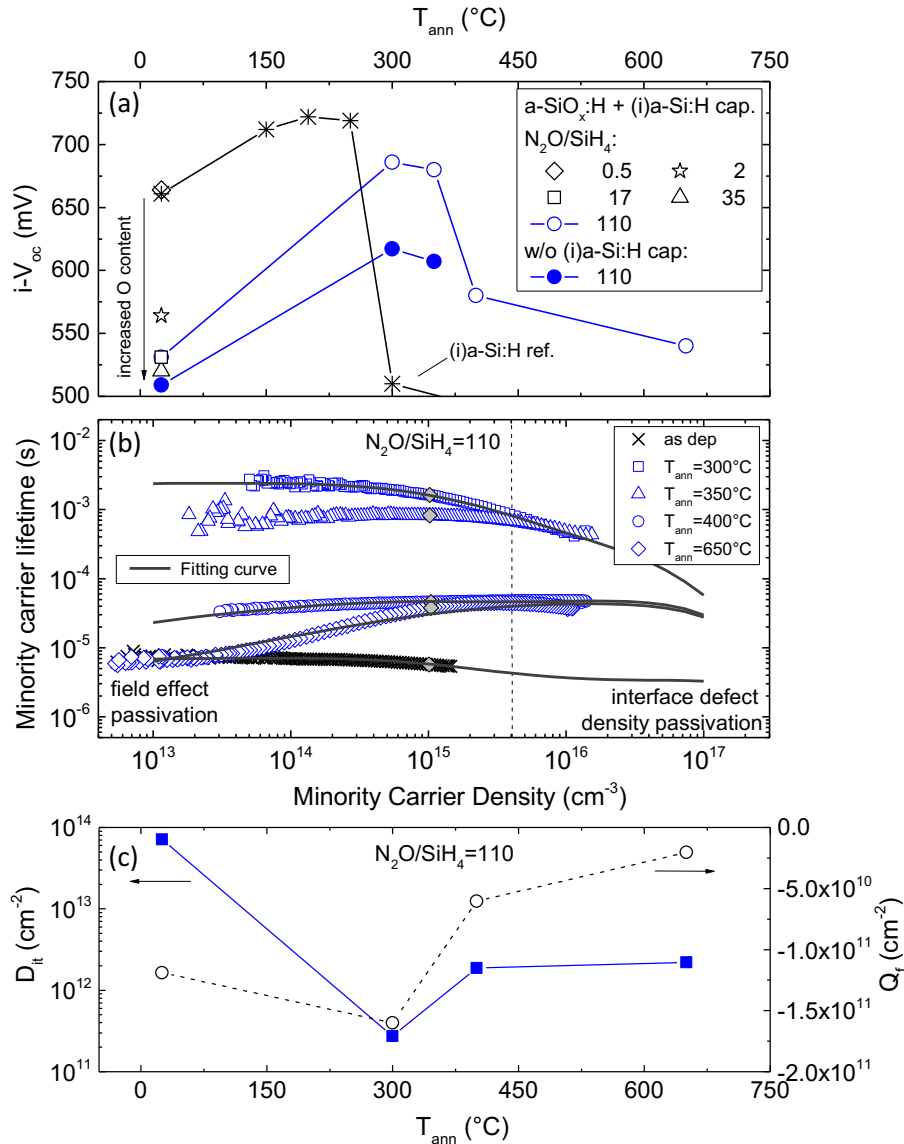


Figure 7.6. (a) Implied open circuit voltage $i-V_{oc}$ as a function of annealing temperature of a-SiO_x:H symmetric samples with varying the N_2O/SiH_4 ratio from 0.5 to 110. The a-SiO_x:H film is 1.5 nm thick. The (i)a-Si:H sample with a layer thickness of 15 nm was added as a reference (b) Experimental minority carrier lifetime curves (symbols) as a function of minority carrier density for the symmetric structure deposited at $N_2O/SiH_4=110$ and treated at different annealing temperatures T_{ann} . The lines indicate the curve fitted as described in [163]. (c) a-SiO_x:H/c-Si interface defect density and fixed-charge density extracted from the fitting curves reported in (a). Lines in (a) and (c) are guides to the eye.

In the following we implemented the here optimized a-Si_x:H in solar cells. As it was found to be close to stoichiometry, we use the common denotation SiO₂.

7.3. Integration in SHJ Solar Cells

7.3.1. Nanocrystalline Growth Enhancement

Layer stacks were fabricated by depositing a 25 nm thick (p)nc-Si:H film on top of a SiO₂ layer on both c-Si and glass substrates (structure in Figure 7.1 (b - c)). The advantage of using these structures was the opportunity to investigate the window layer stacks with thicknesses compatible with the final device. A sample with (i)a-Si:H as passivation layer represents the typical front side of a SHJ.

The samples deposited on glass substrates were analyzed by Raman spectroscopy to extract the crystalline fraction (F_c) as function of the substrate material underneath. The reflectance spectra R were also measured on the same layer stacks grown on polished c-Si substrates. The results for different window layer stacks are presented in Figure 7.7.

The Raman spectra for the sample without passivation layer and the one with (i)a-Si:H were already discussed in section 5.2.1. Briefly, when the (p)nc-Si:H layer is deposited directly on the substrate surface (in this case glass) without any coating, the Raman spectrum in

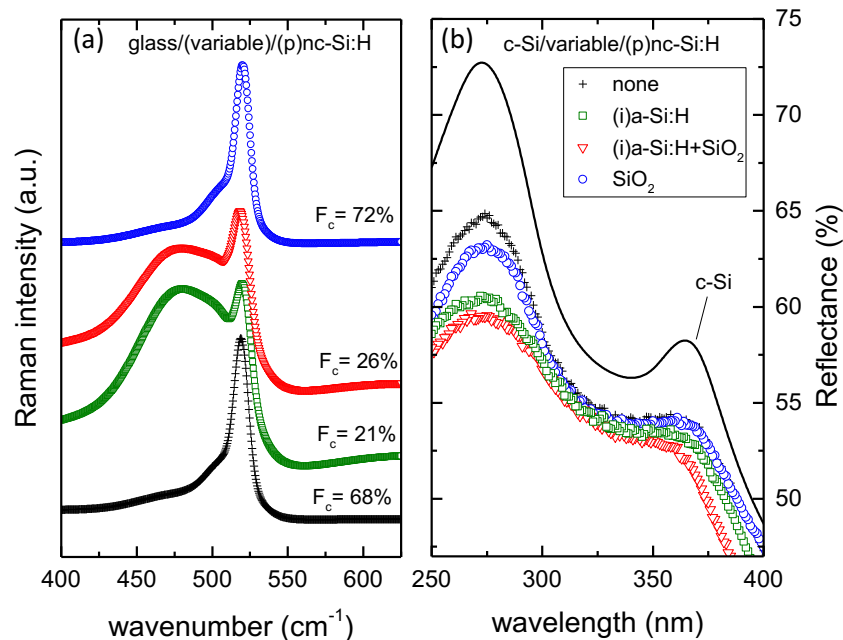


Figure 7.7. (a) Raman shift as function of wavenumber and (b) the correspondent reflectance curves as function of wavelength for samples with variable substrate layers and coated with 25 nm thick (p)nc-Si:H film. The extracted Raman crystalline fraction (F_c) are indicated in (a) and reflection spectra for untreated c-Si and (p)a-Si:H in (b) are given as a reference.

Figure 7.7 (a) reveals a narrow peak at 520 cm^{-1} giving a crystalline fraction of 68%. The R curve shows the two maxima characteristic of c-Si at 275 nm and 365 nm (Figure 7.7 (b)). The entire R curve has a lower intensity if compared with the reference one depicted in the same picture for only c-Si due to the presence of the amorphous fraction. The peak positions and shapes are comparable.

The amorphous phase is drastically increased to the detriment of the nanocrystalline fraction if an (i)a-Si:H film is inserted (squared scatter line) and the F_c reduces to 21%. We were able to increase the F_c to about 26% by combining an (i)a-Si:H layer with an ultra-thin SiO_2 film. The corresponding R curve in Figure 7.7 (b) still shows the two relevant peaks but their intensity is further reduced.

The last sample, grown with only an ultra-thin SiO_2 layer, has again a significant crystalline fraction of 72%. The small discrepancy between the Raman and reflectance trends can be explained by the different substrate (glass and c-Si, respectively) that affect the passivation layer and, consequently, the nc-Si:H evolution in term of crystalline fraction and/or layer thickness as discussed also in Ref. [100]. In agreement with literature [97,98,102], we can summarize that the c-Si, glass and SiO_2 behave similarly as substrate for the nanocrystalline growth of (p)nc-Si:H film.

7.3.2. Cell Results on Polished Wafers

The SiO_2 film optimized in the previous section was tested in SHJ devices. The ultra-thin film was grown on the illuminated side followed by 25 nm of (p)nc-Si:H emitter. The wafers selected for these experiments were both sides polished c-Si to check if the improved F_c on the oxidized substrate can be beneficial on the planar morphology. It was shown in section 5.2.3 that the devices having (p)nc-Si:H grown on non-textured wafers were dominated by S-shaped J - V characteristics.

Figure 7.8 shows J - V curves and extracted FF and R_{oc} for cells grown with different passivation layers. The reference device fabricated with 7 nm (i)a-Si:H passivation layer shows an S-shape character that is related to the nc-Si:H growth on such planar substrates that is covered with amorphous silicon films. Additional devices without a passivation layer and with SiO_2 layer of variable thickness were fabricated. At this stage it was not possible to anneal the SiO_2 /(p)nc-Si:H stack in the FG atmosphere as discussed above, since the rear side of the device was kept as for the reference device, i.e. the passivation consists in (i)a-Si:H layer. This implicates that lower V_{oc} is expected if compared to the lifetime data shown in Figure 7.6. The shape of the J - V curves in Figure 7.8 indicates that the SiO_2 is beneficial for the nanocrystalline evolution of a p-doped emitter. Using optimized deposition parameters, it is possible to uniformly cover the c-Si surface with an ultra-thin film SiO_2 . The thickness series in the same Figure 7.8 shows how critical the thickness of the dielectric film is in order not to impede the charge flow and allow tunneling. Interestingly, the R_{oc} extracted from the illuminated curves, indicated in Figure 7.8, reveals values of $1.5 \Omega \cdot \text{cm}^2$ for the cell with SiO_2 layer of 1.5 nm.

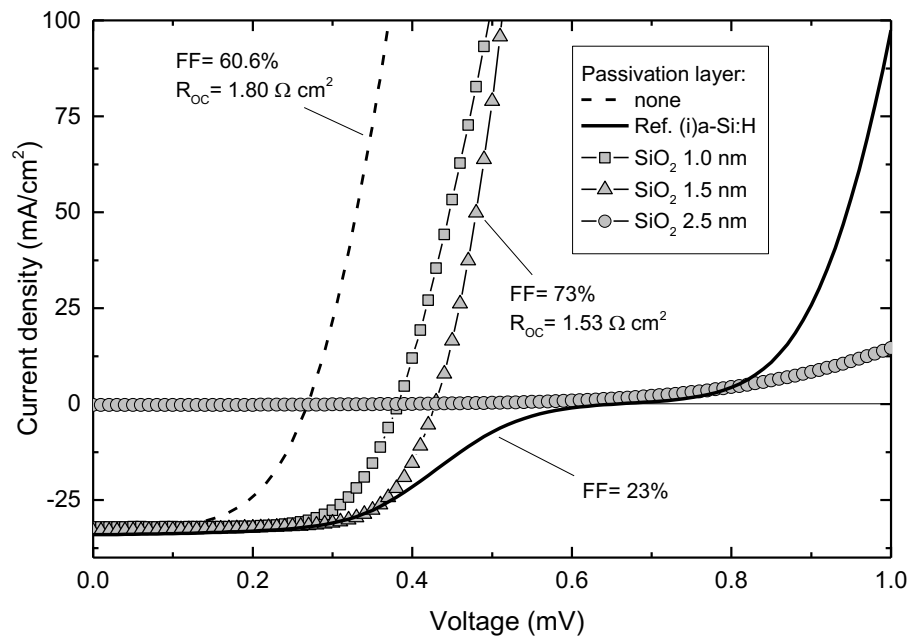


Figure 7.8. (a) Illuminated J - V characteristics for the best cells on polished c -Si wafers with 25 nm (p)nc-Si:H emitter grown on top of variable passivation layers. Fill factor FF and resistance at the open circuit voltage R_{OC} are also indicated.

In order to improve the V_{OC} , preliminary annealing tests were done on the $\text{SiO}_2/(\text{p})\text{nc-Si:H}$ stack with the optimized conditions discussed above (300°C, 30 minutes) in the FG atmosphere. The passivation performances were unsuccessful and not comparable to the samples having the (i)a-Si:H capping film showed in Figure 7.6. The reasons for that were not yet fully understood but we suggest that they might be related to the deposition conditions of the doped layer or to the doping impurities that diffuses from the p-doped emitter.

Optical Improvements

The impact of the (i)a-Si:H film on the short circuit current density has been discussed in section 2.2.3. According to our estimation, the (i)a-Si:H film employed, reduces the J_{c-Si} linearly by about 0.155 mA/cm² per nanometer added resulting in about 0.9 mA/cm² lost for a 7 nm thick (i)a-Si:H film grown on planar cells. In this section the consequences of the replacement of the passivation layer with a SiO_2 film are discussed.

The external quantum efficiency EQE measured on the solar cells shown above are depicted in Figure 7.9. The use of a wider band gap and ultra-thin films like SiO₂ results in reduced parasitic absorption in the blue wavelength range with a gain in short circuit density of almost 1 mA/cm² if compared to the reference device with (i)a-Si:H passivation film.

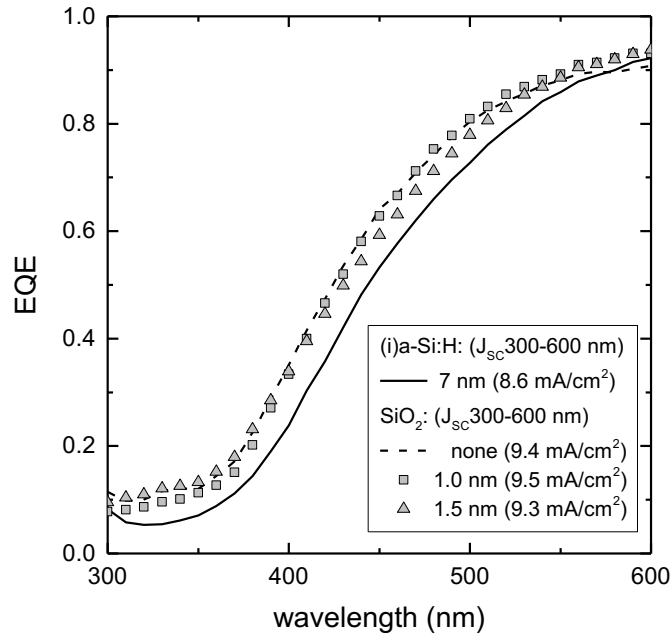


Figure 7.9. External quantum efficiency EQE curves in the range 300 – 600 nm as function of wavelength measured on cells with variable SiO₂ thickness. The reference device with 7 nm (i)a-Si:H as passivation film is given as reference. *J-V* curves of this set of samples are reported in Figure 7.8.

These layer stacks were further investigated by measuring both Raman and reflectance curves on dedicated samples and by the support of the optical simulation tool (OPAL 2, further details are given in chapter 6). The results are reported in Table 7.3 and indicate a completely different trend between simulations and experimental data. All the curves exhibit a characteristic peak at 275 nm indication of the F_C within the nc-Si:H film.

Table 7.3. Simulated and experimental reflectance intensity peak extracted at 275 nm R_{275nm} and Raman crystalline fraction F_C measured on the SiO₂ + 25 nm (p)a-Si:H stack deposited on polished wafers and on glass, respectively.

SiO ₂ (nm)	R_{275nm} simul. (%)	R_{275nm} exp. (%)	F_C exp. (%)
0	61.11	64.61	68
1.0	61.14	63.19	72
1.5	61.50	61.87	69
2.5	61.60	51.52	63
4.0	61.58	49.56	60

The peak intensity extracted from reflectance simulations remain stable, whereas the experimental one rapidly declines with thicker SiO₂ films (2.5 and 4.0 nm). Concurrently, the crystalline fraction measured on the same stack grown on glass decreases as well. This suggests that the nanocrystalline evolution depends on the thickness of the SiO₂ film similarly to what was found in section 5.2.3 for the intrinsic a-Si:H.

The effect of replacing the a-Si:H passivation film with SiO₂ results that is associated with two factors. Firstly, the reduced parasitic absorption is primarily due to the SiO₂ but also by the increased crystalline volume fraction in the (p)nc-Si:H emitter enhanced by the oxidized substrate.

7.4. Discussion and Conclusions

Silicon dioxide films deposited by PECVD were investigated as a replacement of the (i)a-Si:H passivation layer to further enhance the nanocrystalline growth evolution of doped nc-Si:H contacts. As compared to the (i)a-Si:H passivation layer, oxidized surfaces offer a more favorable substrate to reduce the incubation zone drastically [97]. In the following we discuss the main issues, challenges and outcomes related to the integration of SiO₂ layers in SHJ device.

We systematically investigated the influence of the PECVD source-gas composition with the aim to grow an a-SiO_x:H film close to the stoichiometry. FTIR and ellipsometry measurements suggested that higher N₂O flow in SiH₄ and the omission of H₂ from the gas phase is beneficial for avoiding N and H incorporation. Furthermore the power density was kept on the lowest value possible to sustain the plasma, in order to avoid damage of the c-Si surface [138].

We related the deposition growth regime of ultra-thin SiO₂ layer to the passivation performance. The films exhibited low surface passivation as the oxygen contented is increased, as expected from literature [222]. On the contrary, temperature treatment in forming gas strongly increased the surface passivation with a maximum at 1.6 ms after annealing at 300 °C. The lower thermal stability of our silicon dioxide material as compared to the wet-chemically/thermally grown one [63] might be related to the lattice structure obtained by a PECVD process. At this stage it is not clear, if PECVD growth can fulfill the required SiO₂ material quality, e.g. by further improving the post-treatment, or if we have to move to a classical dry- or wet-oxide.

The structural investigation of cell-relevant samples confirmed that the crystalline fraction of the (p)nc-Si:H film drastically increases when it is grown on an SiO₂ substrate layer similarly to the growth on glass or c-Si substrates. Therefore, the *J-V* characteristic of completed cell show that, up to now, the open circuit voltage is the main limitation as expected from the minority carrier lifetime measurements but highlighted that the SiO₂/(p)nc-Si:H stack is able to drastically reduce the series resistance on polished wafer and led to *FF* above 70%.

7. EXPLORATORY STUDY ON THIN SILICON DIOXIDE PASSIVATION LAYERS

We can conclude that the proposed device scheme has potential to overcome the nanocrystalline nucleation issue and it has the advantage of further reducing current losses due to the reduced parasitic absorption of the passivation and doped nc-Si:H layers, but further efforts are needed to exploit the full potential of the SiO₂ passivation.

8. Conclusions and Outlook

This thesis addressed the integration of nanocrystalline silicon (nc-Si:H) and silicon oxide (nc-SiO_x:H) contact materials grown by plasma enhanced chemical vapor deposition (PECVD) in silicon heterojunction (SHJ) solar cells. The aim is to take advantage of the favorable optoelectronic properties of nc-Si:H and nc-SiO_x:H layers that are originated from their two-phase structure composed of Si crystallites embedded in an amorphous silicon(oxide) matrix.

Besides the knowledge on nanocrystalline materials developed in thin-film silicon solar cells in our institute in the past years [180,191], the applications of those layers to SHJ solar cells need different optical and electrical requirements, as well as growth prerequisites. In particular, the challenges are: (i) the underlying intrinsic amorphous silicon (i)a-Si:H film has to be preserved from potential passivation damages and (ii) develop a fast nucleation to ensure the carrier transport towards the contacts without parasitically absorbing the incoming light and to provide a low ohmic contact to the adjacent transparent conductive oxide (TCO) layer.

As a prerequisite to study the implementation of the novel contact materials, we established a reference process for SHJ solar cells with an amorphous emitter. Materials and process steps were re-optimized and/or developed *ex novo* to set a stable and reproducible reference device. The reference process exhibited a progressive evolution in performance (see Figure 4.11 in chapter 4) from the instability in the early stages, which coincided with the initial phase of this thesis, to the final optimization that led to conversion efficiency of 22.2% still under development.

We showed that the morphology of the (i)a-Si:H passivation layer influences the growth of (p)nc-Si:H films. In particular, a passivation layer that exhibits slightly epitaxy promotes nucleation enhancing the crystalline fraction in the growing nc-Si:H emitter as confirmed by HR-TEM images. As a consequence, high fill factors (*FFs*) approaching to 79% were obtained, but the open circuit voltage is low due to poor passivation of this a-Si:H.

On the contrary, an improved passivation layer was optimized for the reference process and tested in combination with (p)nc-Si:H emitters. Solar cells exhibited *J-V* characteristics

8. CONCLUSIONS AND OUTLOOK

dominated by S-shapes. We ascribed the poor performance to the reduced crystallinity fraction that compromised the field-effect passivation.

In order to overcome this limitation and combine both good passivation and rapid nucleation, we worked on the well-known substrate selectivity of nc-Si:H towards (i)a-Si:H substrates [97,100,103]. A short CO₂ plasma treatment (CO₂PT) was optimized to oxidize the (i)a-Si:H surface prior to the emitter deposition. The positive effect was confirmed by Raman, minority carrier lifetime measurements and *J-V* characteristics on completed cells. Device fabricated with CO₂PT and a fine optimization of the doping gas flow (trimethylboron) led to open circuit voltage V_{oc} of 727 mV and *FF* of 74.6%, short circuit current density J_{sc} of 38.9 mA/cm² and conversion efficiency of 21.1%.

Next, we addressed the minimization of current losses by implementing p- and n-doped hydrogenated nanocrystalline silicon oxide (nc-SiO_x:H) films as window layers. We assessed on the advantage of creating a stack with refractive indexes (*n*) that consecutively decreased from silicon to the ambient air that enhances antireflection effect. Optical simulations, where used to identify the optimal film thickness and refractive index for different doped materials (amorphous and nanocrystalline).

In the case of nc-SiO_x:H film we identified two different trends as function of the substrate morphology. Flat surfaces showed the strongest gain in photocurrent due to reduced reflectance losses that overcompensated the parasitic absorption in the film. Additionally the losses were minimized for a layer thickness of ~ 35 – 40 nm and *n* equal to 2. Contrarily, on textured morphology the beneficial effect was only limited to the reduced parasitic absorption leading to a required lower optimized *n* of about 2.4. The simulated optical advantages were confirmed by experimental cell results.

The potential for high current density was demonstrated for (p)nc-SiO_x:H emitters grown on polished and textured substrates with J_{sc} values of 35.1 and 40.4 mA/cm², respectively. As compared to the optimized amorphous emitter, the gain amounted to more than 2 mA/cm² for the best device accompanied by a conversion efficiency of 20.3%, limited by a low *FF* of 72.9%.

From these findings, we can conclude that doped nanocrystalline layers did not completely fulfilled our expectations to improve the efficiency of SHJ solar. Analyzing the cell characteristics, the causes were found in the poor *FFs* especially for cells fabricated with (p)nc-SiO_x:H emitters that we ascribed to contact issues at the (p)emitter/ transparent conductive oxide (TCO) interface caused by lower crystalline volume fraction. To support this hypothesis, a highly conductive/doped contact nc-Si:H layer was inserted at the Si/TCO interface showing an improvement in *FF*.

Experiments with (n)nc-SiO_x:H used as front surface field layer in rear emitter cells confirmed that easier control of the nanostructure for n-doped material in comparison to p-doped one. Preliminary solar cells showed fill factor of 77% and conversion efficiency of 20.8%.

Motivated by recent works on SiO₂ passivated tunnel-contacts [68] and the positive effect of the CO₂PT on the nanocrystalline growth in this work, we explored SiO₂ as passivation layer to (i) overcome the substrate selectivity of nc-Si:H layer towards the underlying (i)a-Si:H layer and (ii) further minimization of current losses. PECVD was chosen as deposition technique to allow for growing the entire silicon layer stack in one step process. We optimized an ultra-thin SiO₂ film close to the stoichiometry that is able to passivate the wafer surfaces after an annealing at 300 °C in forming gas (implied- V_{oc} of 686 mV). Raman crystalline volume fraction of 72% was measured on *thin* cell-relevant stack that is close to the values usually measured on much thicker single layers. As a consequence, preliminary cells results on polished wafers with SiO₂ layer in range of 1 – 2 nm showed improved fill factors with low series resistance as compared to the (i)a-Si:H/(p)nc-Si:H stacks. Furthermore, the device showed, as expected, a current gain by up to 1 mA/cm² in the blue range of the wavelength spectrum as compared to reference cell with a-Si:H films.

To sum up, based on the results presented here, both nc-Si:H and nc-SiO_x:H were successfully applied as thin contact layers in SHJ device (Table 8.1). However, besides the optical advantages that could be clearly demonstrated both from simulations and experiments, the materials did not yet improved the efficiency of the reference device.

Table 8.1. Solar cell parameters for the best cells fabricated on textured wafers with different emitter or front surface field.

Emitter/FSF (Front)	Device scheme	J_{sc} (mA/cm ²)	V_{oc} (mV)	FF (%)	η (%)
(p)a-Si:H	FE	38.3	720	77.4	21.3
(p)nc-Si:H	FE	38.9	727	74.6	21.1
(p)nc-SiO _x :H	FE	40.4	688	72.9	20.3
(n)nc-SiO _x :H	RE	38.2	702	77.1	20.8
*(p)a-Si:H	FE	38.3	726	79.3	22.2

*This solar cell is originated from further reference process optimizations that are not part of this thesis as discussed in chapter 4.

Outlook

Based on the results shown in this work and in literature, the following approached can be suggested to further improve conversion efficiencies by addressing the fill factor issues.

A first approach consists in placing the (p)nc-Si:H layer in *rear emitter configuration*. Improvements are expected considering the following:

- On the not illuminated side, more degrees of freedom for enhancing the nanocrystalline growth are allowed due to the lower requirements concerning the film optics. Among the options possible, we can mention the use of a seed layer

8. CONCLUSIONS AND OUTLOOK

and/or thicker emitter films. The nc-Si:H emitter will improve the contact resistance to the rear TCO.

- The use of (n)nc-SiO_x:H films on the front side to benefit from the lower parasitic absorption as showed in chapter 6. In order to better control the oxygen incorporation in the layer and the nanostructure, higher pressure regimes will be investigated (this regime was temporary not assessable during this work), as suggested by the experimental results reported here and in Ref. [210].

The second, more exploratory, approach is the proposed device scheme with the SiO₂ based passivation and nc-Si:H doped layers:

- The much higher crystalline fraction together with the extremely low series resistance found on cell fabricated are promising for application on textured device in combination with both nc-Si:H and nc-SiO_x:H films.
- The gain in short circuit current is expected to be further enhanced due to the removal of the (i)a-Si:H films J_{SC} .

The voltage is the main limitations to overcome. To exploit the full potential of the SiO₂ passivation, alternative (more common) SiO₂ deposition methods, such as thermal, chemical or ozone oxidation [63,220], will be implemented and combined with thin PECVD nc-Si:H contact layers.

List of Acronyms and Symbols

Gas/Tool	
PECVD	Plasma Enhanced Chemical Vapor Deposition
PT	Plasma treatment
SiH ₄	Silane
H ₂	Hydrogen
B(CH ₃) ₃ , TMB	Trimethylboron
B ₂ H ₆	Diborane
PH ₃	Phosphine
CO ₂	Carbon dioxide
N ₂ O	Dinitrogen monoxide

Characterization	
FTIR	Fourier Transform Infrared Spectroscopy
<i>J-V</i> curve	Current-voltage characteristic
SE	Spectral ellipsometry
HR-TEM	High Resolution Transmission Electron Microscopy

Material/cell	
(i)	Intrinsic
(p)	p-doped
(n)	n-doped
(p)/(i)/(n)c-Si/(i)/(n)	Cell precursor
a-Si:H	Hydrogenated amorphous silicon
a-SiO _x	Amorphous silicon oxide
BSF	Back Surface Field
c-Si, N	Crystalline silicon
DB	Dangling bonds
FE	Front emitter cell
FSF	Front surface Field
HF	Hydrofluoric acid
In ₂ O ₃ :Sn, ITO	Indium tin oxide
IZ	Incubation zone

nc-Si:H	Hydrogenated nanocrystalline silicon
nc-SiO _x :H	Hydrogenated nanocrystalline silicon oxide
PT	Plasma treatment
RCA	Radio Corporation of America (cleaning procedure)
RE	Rear emitter cell
SHJ	Silicon heterojunction
TCO	Transparent Conductive Oxide
ZnO:Al, AZO	Aluminum doped zinc oxide

	Name	Unit
1-R	Absorbance	/
α	Absorption coefficient	cm ⁻¹
η	Conversion efficiency	%
λ	wavelength	nm
μ	Hall mobility	cm ² /Vs
σ	Electrical conductivity	S/cm
τ_{eff}	Effective carrier lifetime	s
D_{it}	Interface defect density	cm ⁻²
DR	Deposition rate	nm/s
E_{04}	Optical band gap (Photon energy for $\alpha > 10^4$)	eV
E_g	Band gap	eV
EQE	External Quantum Efficiency	%
F_C	Raman crystalline fraction	%
FF	Fill factor	%
IQE	Internal Quantum Efficiency	%
J_{SC}	Short circuit current density	mA/cm ²
k	Extinction coefficient	-
n	Refractive index	-
N_D	Free-carrier density	cm ⁻³
p	Chamber pressure	Pa
P_D	Power density	mW/cm ²
Q_f	Fixed charge density	cm ⁻²
R	Reflectance	%
R_{OC}	Series resistance at the open circuit voltage	$\Omega \cdot \text{cm}^2$
R_S	Series resistance	$\Omega \cdot \text{cm}^2$
R_{sh}	Shunt resistance	$\Omega \cdot \text{cm}^2$
t	Thin film thickness	nm
T_{sub}, T_{ann}	Substrate, annealing temperature	°C
T	Transmittance	%
$V_{OC}, i-V_{OC}, p-V_{OC}$	Open circuit voltage, implied-V _{OC} , pseudo-V _{OC}	V
W	Substrate width	cm
Z	Enhancement factor	-
[Si-H] (example)	Bond density	cm ⁻³

Bibliography

- [1] United Nation Climate Change Conference, "Paris Agreement", <http://www.cop21.gouv.fr/en>, 2015.
- [2] "RENEWABLES 2016 GLOBAL STATUS REPORT", <http://www.ren21.net/>
- [3] S. Mann, M. de Wild-Scholten, V. Fthenakis, W. van Sark and W. Sinke, "The energy payback time of advanced crystalline silicon PV modules in 2020: A prospective study", *Progress in Photovoltaics: Research and Applications*, 22, pp. 1180–1194, 2014.
- [4] B. Burger, "Photovoltaics Report", www.ise.fraunhofer.de, 2016.
- [5] A. Metz, "International Technology Roadmap for Photovoltaic (ITRPV)", 2014.
- [6] NREL, "Best research-cell efficiencies chart: Rapport technique", http://www.nrel.gov/ncpv/images/efficiency_chart.jpg, 2016.
- [7] M. Green, "The path to 25% silicon solar cell efficiency: History of silicon cell evolution", *Progress in Photovoltaics: Research and Applications*, 17, pp. 183–189, 2009.
- [8] M. Tanaka, M. Taguchi, T. Matsuyama, T. Sawada, S. Tsuda, S. Nakano, H. Hanafusa and Y. Kuwano, "Development of New a-Si/c-Si Heterojunction Solar Cells: ACJ-HIT (Artificially Constructed Junction-Heterojunction with Intrinsic Thin-Layer)", *Japanese Journal of Applied Physics*, 31, pp. 3518–3522, 1992.
- [9] M. Taguchi, A. Yano, S. Tohoda, K. Matsuyama, Y. Nakamura, T. Nishiwaki, K. Fujita and E. Maruyama, "24.7% Record Efficiency HIT Solar Cell on Thin Silicon Wafer", *IEEE Journal of Photovoltaics*, 4, pp. 96–99, 2014.
- [10] M. Taguchi, E. Maruyama and M. Tanaka, "Temperature Dependence of Amorphous/Crystalline Silicon Heterojunction Solar Cells", *Japanese Journal of Applied Physics*, 47, pp. 814–818, 2008.
- [11] M. Taguchi, Y. Tsunomura, H. Inoue, S. Taira, T. Nakashima, T. Baba and E. Maruyama, "High-efficiency HIT solar cell on thin (< 100 μm) silicon wafer", *Proceedings of the 24th European Photovoltaic Solar Energy Conference*, pp. 1690–1693, 2009.
- [12] K. Masuko, M. Shigematsu, T. Hashiguchi, D. Fujishima, M. Kai, N. Yoshimura, T. Yamaguchi, Y. Ichihashi, T. Mishima, N. Matsubara, T. Yamanishi, T. Takahama, M. Taguchi, E. Maruyama and S. Okamoto, "Achievement of More Than 25% Conversion Efficiency With Crystalline Silicon Heterojunction Solar Cell", *IEEE Journal of Photovoltaics*, 4, pp. 1433–1435, 2014.

- [13] New Energy and Industrial Technology Development Organization (NEDO), Kaneka Corporation, "http://www.nedo.go.jp/english/news/AA5en_100109.html", Sept 2016.
- [14] D. Adachi, J. Hernández and K. Yamamoto, "Impact of carrier recombination on fill factor for large area heterojunction crystalline silicon solar cell with 25.1% efficiency", *Applied Physics Letters*, 107, p. 233506, 2015.
- [15] T. Watahiki, T. Furuhashi, T. Matsuura, T. Shinagawa, Y. Shirayanagi, T. Morioka, T. Hayashida, Y. Yuda, S. Kano, Y. Sakai, H. Tokioka, Y. Kusakabe and H. Fuchigami, "Rear-emitter Si heterojunction solar cells with over 23% efficiency", *Applied Physics Express*, 8, p. 21402, 2015.
- [16] P. Campbell and M. Green, "Light trapping properties of pyramidally textured surfaces", *Journal of Applied Physics*, 62, p. 243, 1987.
- [17] T. Koida, H. Fujiwara and M. Kondo, "High-mobility hydrogen-doped In₂O₃In₂O₃ transparent conductive oxide for a-Si: H/c-Si heterojunction solar cells", *Solar Energy Materials and Solar Cells*, 93, pp. 851–854, 2009.
- [18] S. Sze and K. Ng, "Physics of semiconductor devices", *Wiley-Interscience; 3rd edition*, 2006.
- [19] M. Green, "Solar cells: Operating principles, technology, and system applications", *series in solid state physical electronics*. Prentice Hall, 1981.
- [20] M. Kerr and A. Cuevas, "General parameterization of Auger recombination in crystalline silicon", *Journal of Applied Physics*, 91, p. 2473, 2002.
- [21] W. Shockley and W. Read, "Statistics of the Recombinations of Holes and Electrons", *Physical Review*, 87, pp. 835–842, 1952.
- [22] W. Shockley and H. Queisser, "Detailed Balance Limit of Efficiency of p-n Junction Solar Cells", *Journal of Applied Physics*, 32, p. 510, 1961.
- [23] T. Tiedje, E. Yablonovitch, G. Cody and B. Brooks, "Limiting efficiency of silicon solar cells", *IEEE Transactions on Electron Devices*, 31, pp. 711–716, 1984.
- [24] A. Richter, M. Hermle and S. Glunz, "Reassessment of the Limiting Efficiency for Crystalline Silicon Solar Cells", *IEEE Journal of Photovoltaics*, 3, pp. 1184–1191, 2013.
- [25] A. Cuevas and D. Macdonald, "Measuring and interpreting the lifetime of silicon wafers", *Solar Energy*, 76, pp. 255–262, 2004.
- [26] "PV lighthouse OPAL2", <https://www2.pvlighthouse.com.au/calculators/OPAL%202/OPAL%202.aspx>
- [27] S. Kasap and P. Capper, "Springer handbook of electronic and photonic materials", *Springer*, 2007.
- [28] A. Descoedres, Z. Holman, L. Barraud, S. Morel, S. de Wolf and C. Ballif, ">21% Efficient Silicon Heterojunction Solar Cells on n- and p-Type Wafers Compared", *IEEE Journal of Photovoltaics*, 3, pp. 83–89, 2013.
- [29] S. Glunz, J. Benick, D. Biro, M. Bivour, M. Hermle, D. Pysch, M. Rauer, C. Reichel, A. Richter, M. Rudiger, C. Schmiga, D. Suwito, A. Wolf and R. Preu, "n-type silicon - enabling efficiencies > 20% in industrial production", Honolulu, HI, USA, pp. 50–56, 2010.

- [30] E. Yablonovitch, D. Allara, C. Chang, T. Gmitter and T. Bright, "Unusually low surface-recombination velocity on silicon and germanium surfaces", *Physical review letters*, 57, pp. 249–252, 1986.
- [31] H. Angermann, "Characterization of wet-chemically treated silicon interfaces by surface photovoltage measurements", *Analytical and bioanalytical chemistry*, 374, pp. 676–680, 2002.
- [32] A. Descoedres, L. Barraud, S. de Wolf, B. Strahm, D. Lachenal, C. Guérin, Z. Holman, F. Zicarelli, B. Demaurex, J. Seif, J. Holovsky and C. Ballif, "Improved amorphous/crystalline silicon interface passivation by hydrogen plasma treatment", *Applied Physics Letters*, 99, p. 123506, 2011.
- [33] M. Mews, T. Schulze, N. Mingirulli and L. Korte, "Hydrogen plasma treatments for passivation of amorphous-crystalline silicon-heterojunctions on surfaces promoting epitaxy", *Applied Physics Letters*, 102, p. 122106, 2013.
- [34] B. Hoex, J. Gielis, van de Sanden, M. C. M. and W. Kessels, "On the c-Si surface passivation mechanism by the negative-charge-dielectric Al₂O₃", *Journal of Applied Physics*, 104, p. 113703, 2008.
- [35] S. Glunz, D. Biro, S. Rein and W. Warta, "Field-effect passivation of the SiO₂/Si interface", *Journal of Applied Physics*, 86, p. 683, 1999.
- [36] J. Fossum, "Physical operation of back-surface-field silicon solar cells", *IEEE Transactions on Electron Devices*, 24, pp. 322–325, 1977.
- [37] H. Goldbach, A. Bink and R. Schropp, "Thin p++ μ c-Si layers for use as back surface field in p-type silicon heterojunction solar cells", *Journal of Non-Crystalline Solids*, 352, pp. 1872–1875, 2006.
- [38] D. Chapin, C. Fuller and G. Pearson, "A New Silicon p-n Junction Photocell for Converting Solar Radiation into Electrical Power", *Journal of Applied Physics*, 25, p. 676, 1954.
- [39] W. Fuhs, K. Niemann and J. Stuke, "Heterojunctions of Amorphous Silicon and Silicon Single Crystals", Yorktown Heights, New York (USA), pp. 345–350, 1974.
- [40] C. Battaglia, A. Cuevas and S. de Wolf, "High-efficiency crystalline silicon solar cells: Status and perspectives", *Energy Environ. Sci.*, 9, pp. 1552–1576, 2016.
- [41] W. van Sark, L. Korte and F. Roca, "Physics and technology of amorphous-crystalline heterostructure silicon solar cells", *Engineering Materials. Springer*, 2011.
- [42] S. de Wolf, A. Descoedres, Z. Holman and C. Ballif, "High-efficiency Silicon Heterojunction Solar Cells: A Review", *green*, 2, 2012.
- [43] R. Anderson, "Experiments on Ge-GaAs heterojunctions", *Solid-State Electronics*, 5, pp. 341–351, 1962.
- [44] A. Fantoni, Y. Vigranenko, M. Fernandes, R. Schwarz and M. Vieira, "Influence of the band offset on the performance of photodevices based on the c-Si/a-Si: H heterostructure", *Thin Solid Films*, 383, pp. 314–317, 2001.
- [45] T. Schulze, L. Korte, E. Conrad, M. Schmidt and B. Rech, "Electrical transport mechanisms in a-Si: H/c-Si heterojunction solar cells", *Journal of Applied Physics*, 107, p. 23711, 2010.

- [46] V. Fthenakis, "Sustainability of photovoltaics: The case for thin-film solar cells", *Renewable and Sustainable Energy Reviews*, 13, pp. 2746–2750, 2009.
- [47] A. Froitzheim, R. Stangl, L. Elstner, M. Schmidt and W. Fuhs, "Interface recombination in amorphous/crystalline silicon solar cells, a simulation study", New Orleans, LA, USA, pp. 1238–1241, 2002.
- [48] R. Varache, J. Kleider, M. Gueunier-Farret and L. Korte, "Silicon heterojunction solar cells: Optimization of emitter and contact properties from analytical calculation and numerical simulation", *Materials Science and Engineering: B*, 178, pp. 593–598, 2013.
- [49] S. Kirner, M. Hartig, L. Mazzarella, L. Korte, T. Frijnts, H. Scherg-Kurmes, S. Ring, B. Stannowski, B. Rech and R. Schlatmann, "The Influence of ITO Dopant Density on J-V Characteristics of Silicon Heterojunction Solar Cells: Experiments and Simulations", *Energy Procedia*, 77, pp. 725–732, 2015.
- [50] A. Kanevce and W. Metzger, "The role of amorphous silicon and tunneling in heterojunction with intrinsic thin layer (HIT) solar cells", *Journal of Applied Physics*, 105, p. 94507, 2009.
- [51] L. Zhao, C. Zhou, H. Li, H. Diao and W. Wang, "Role of the work function of transparent conductive oxide on the performance of amorphous/crystalline silicon heterojunction solar cells studied by computer simulation", *Physica Status Solidi a*, 205, pp. 1215–1221, 2008.
- [52] M. Bivour, S. Schröer and M. Hermle, "Numerical Analysis of Electrical TCO/a-Si:H(p) Contact Properties for Silicon Heterojunction Solar Cells", *Energy Procedia*, 38, pp. 658–669, 2013.
- [53] A. Klein, C. Körber, A. Wachau, F. Säuberlich, Y. Gassenbauer, S. Harvey, D. Proffit and T. Mason, "Transparent Conducting Oxides for Photovoltaics: Manipulation of Fermi Level, Work Function and Energy Band Alignment", *Materials*, 3, pp. 4892–4914, 2010.
- [54] E. Centurioni and D. Iencinella, "Role of front contact work function on amorphous silicon/crystalline silicon heterojunction solar cell performance", *IEEE Electron Device Letters*, 24, pp. 177–179, 2003.
- [55] M. Bivour, S. Schröer, M. Hermle and S. Glunz, "Silicon heterojunction rear emitter solar cells: Less restrictions on the optoelectrical properties of front side TCOs", *Solar Energy Materials and Solar Cells*, 122, pp. 120–129, 2014.
- [56] P. CAMPBELL, S. Weham and M. Green, "Light trapping and reflection control in solar cells using tilted crystallographic surface textures", *Solar Energy Materials and Solar Cells*, 31, pp. 133–153, 1993.
- [57] S.-Y. Lien, C.-H. Yang, C.-H. Hsu, Y.-S. Lin, C.-C. Wang and D.-S. Wu, "Optimization of textured structure on crystalline silicon wafer for heterojunction solar cell", *Materials Chemistry and Physics*, 133, pp. 63–68, 2012.
- [58] Z. Holman, A. Descoedres, L. Barraud, F. Fernandez, J. Seif, S. de Wolf and C. Ballif, "Current Losses at the Front of Silicon Heterojunction Solar Cells", *IEEE Journal of Photovoltaics*, 2, pp. 7–15, 2012.
- [59] Z. Holman, M. Filipič, A. Descoedres, S. de Wolf, F. Smole, M. Topič and C. Ballif, "Infrared light management in high-efficiency silicon heterojunction and rear-passivated solar cells", *Journal of Applied Physics*, 113, p. 13107, 2013.

- [60] H. Fujiwara and M. Kondo, "Effects of a-Si:H layer thicknesses on the performance of a-Si:H/c-Si heterojunction solar cells", *Journal of Applied Physics*, 101, p. 54516, 2007.
- [61] L. Barraud, Z. Holman, N. Badel, P. Reiss, A. Descoedres, C. Battaglia, S. de Wolf and C. Ballif, "Hydrogen-doped indium oxide/indium tin oxide bilayers for high-efficiency silicon heterojunction solar cells", *Solar Energy Materials and Solar Cells*, 115, pp. 151–156, 2013.
- [62] P. Seif, A. Descoedres, M. Filipič, F. Smole, M. Topič, Z. Charles Holman, S. de Wolf and C. Ballif, "Amorphous silicon oxide window layers for high-efficiency silicon heterojunction solar cells", *Journal of Applied Physics*, 115, p. 24502, 2014.
- [63] A. Moldovan, F. Feldmann, M. Zimmer, J. Rentsch, J. Benick and M. Hermle, "Tunnel oxide passivated carrier-selective contacts based on ultra-thin SiO₂ layers", *Solar Energy Materials and Solar Cells*, 142, pp. 123–127, 2015.
- [64] C. Battaglia, S. Martin de Nicolas, S. de Wolf, X. Yin, M. Zheng, C. Ballif and A. Javey, "Hole selective MoOx contact for silicon heterojunction solar cells", Denver, CO, USA, pp. 968–970
- [65] M. Bivour, H. Steinkemper, J. Jeurink, S. Schröer and M. Hermle, "Rear Emitter Silicon Heterojunction Solar Cells: Fewer Restrictions on the Optoelectrical Properties of Front Side TCOs", *Energy Procedia*, 55, pp. 229–234, 2014.
- [66] J. Nakamura, N. Asano, T. Hieda, C. Okamoto, H. Katayama and K. Nakamura, "Development of Heterojunction Back Contact Si Solar Cells", *IEEE Journal of Photovoltaics*, 4, pp. 1491–1495, 2014.
- [67] A. Tomasi, B. Paviet-Salomon, D. Lachenal, Nicolas, S. de Martin, M. Ledinsky, A. Descoedres, S. Nicolay, S. de Wolf and C. Ballif, "Photolithography-free interdigitated back-contacted silicon heterojunction solar cells with efficiency >21%", Denver, CO, USA, pp. 3644–3648, 2014.
- [68] S. Glunz, F. Feldmann and A. Richter, M. Bivour, C. Reichel, H. Steinkemper, J. Benick, M. Hermle, "The irresistible charm of a simple current flow pattern – 25% with a solar cell featuring a full-area back contact", *Proceedings of the 31th European Photovoltaic Solar Energy Conference*, 2015.
- [69] A. V. Shah, "Thin-film silicon solar cells", *Engineering Sciences: Micro- And Nanotechnology. Taylor & Francis*, 2010.
- [70] O. Vetterl, F. Finger, R. Carius, P. Hapke, L. Houben, O. Kluth, A. Lambertz, A. Mück, B. Rech and H. Wagner, "Intrinsic microcrystalline silicon: A new material for photovoltaics", *Solar Energy Materials and Solar Cells*, 62, pp. 97–108, 2000.
- [71] A. Shah, J. Meier, E. Vallat-Sauvain, N. Wyrsh, U. Kroll, C. Droz and U. Graf, "Material and solar cell research in microcrystalline silicon", *Solar Energy Materials and Solar Cells*, 78, pp. 469–491, 2003.
- [72] P. Roca i Cabarrocas, "New approaches for the production of nano-, micro-, and polycrystalline silicon thin films", *physica status solidi (c)*, 1, pp. 1115–1130, 2004.
- [73] K. Choy, "Chemical vapour deposition of coatings", *Progress in Materials Science*, 48, pp. 57–170, 2003.

- [74] J. Perrin, O. Leroy and M. Bordage, "Cross-Sections, Rate Constants and Transport Coefficients in Silane Plasma Chemistry", *Contributions to Plasma Physics*, 36, pp. 3–49, 1996.
- [75] L. Date, K. Radouane, B. Despax, M. Yousfi, H. Caquineau and A. Hennad, "Analysis of the N₂O dissociation in a RF discharge reactor", *Journal of Physics D: Applied Physics*, 32, pp. 1478–1488, 1999.
- [76] L. Spencer and A. Gallimore, "Efficiency of CO₂ Dissociation in a Radio-Frequency Discharge", *Plasma Chemistry and Plasma Processing*, 31, pp. 79–89, 2011.
- [77] H. Sterling and R. Swann, "Chemical vapour deposition promoted by r.f. discharge", *Solid-State Electronics*, 8, pp. 653–654, 1965.
- [78] S. Usui and M. Kikuchi, "Properties of heavily doped GD · Si with low resistivity", *Journal of Non-Crystalline Solids*, 34, pp. 1–11, 1979.
- [79] J. Schmitt, "Fundamental mechanisms in silane plasma decompositions and amorphous silicon deposition", *Journal of Non-Crystalline Solids*, vol. 59-60, pp. 649–657, 1983.
- [80] J. Knights, "Effects of inert gas dilution of silane on plasma-deposited a-Si: H films", *Applied Physics Letters*, 38, p. 331, 1981.
- [81] A. Matsuda, "Formation kinetics and control of microcrystallite in $\mu\text{c-Si:H}$ from glow discharge plasma", *Journal of Non-Crystalline Solids*, vol. 59-60, pp. 767–774, 1983.
- [82] J. Pankove and M. Tarng, "Amorphous silicon as a passivant for crystalline silicon", *Applied Physics Letters*, 34, p. 156, 1979.
- [83] D. Staebler and C. Wronski, "Reversible conductivity changes in discharge-produced amorphous Si", *Applied Physics Letters*, 31, p. 292, 1977.
- [84] H. Fujiwara and M. Kondo, "Impact of epitaxial growth at the heterointerface of a-Si:H/c-Si solar cells", *Applied Physics Letters*, 90, p. 13503, 2007.
- [85] T. Wang, E. Iwaniczko, M. Page, D. Levi, Y. Yan, H. Branz and Q. Wang, "Effect of emitter deposition temperature on surface passivation in hot-wire chemical vapor deposited silicon heterojunction solar cells", *Thin Solid Films*, 501, pp. 284–287, 2006.
- [86] M. Burrows, U. Das, R. Opila, S. de Wolf and R. Birkmire, "Role of hydrogen bonding environment in a-Si: H films for c-Si surface passivation", *Journal of Vacuum Science & Technology A: Vacuum, Surfaces, and Films*, 26, p. 683, 2008.
- [87] B. Demarex, R. Bartlome, J. Seif, J. Geissbühler, D. Alexander, Q. Jeangros, C. Ballif and S. de Wolf, "Low-temperature plasma-deposited silicon epitaxial films: Growth and properties", *Journal of Applied Physics*, 116, p. 53519, 2014.
- [88] S. Olibet, E. Vallat-Sauvain, L. Fesquet, C. Monachon, A. Hessler-Wyser, J. Damon-Lacoste, S. de Wolf and C. Ballif, "Properties of interfaces in amorphous/crystalline silicon heterojunctions", *physica status solidi (a)*, 207, pp. 651–656, 2010.
- [89] R. Rizzoli, E. Centurioni, J. Plá, C. Summonte, A. Migliori, A. Desalvo and F. Zignani, "Open circuit voltage in homojunction and heterojunction silicon solar cells grown by VHF-PECVD", *Journal of Non-Crystalline Solids*, vol. 299-302, pp. 1203–1207, 2002.
- [90] J. Schüttauf, C. van der Werf, I. Kielen, W. van Sark, J. Rath and R. Schropp, "Improving the performance of amorphous and crystalline silicon heterojunction solar cells by

- monitoring surface passivation", *Journal of Non-Crystalline Solids*, 358, pp. 2245–2248, 2012.
- [91] S. de Wolf and M. Kondo, "Nature of doped a-Si: H/c-Si interface recombination", *Journal of Applied Physics*, 105, p. 103707, 2009.
- [92] S. de Wolf and M. Kondo, "Abruptness of a-Si:H/c-Si interface revealed by carrier lifetime measurements", *Applied Physics Letters*, 90, p. 42111, 2007.
- [93] E. Vallat-Sauvain, U. Kroll, J. Meier, A. Shah and J. Pohl, "Evolution of the microstructure in microcrystalline silicon prepared by very high frequency glow-discharge using hydrogen dilution", *Journal of Applied Physics*, 87, p. 3137, 2000.
- [94] T. Itoh, K. Yamamoto, K. Ushikoshi, S. Nonomura and S. Nitta, "Characterization and role of hydrogen in nc-Si:H", *Journal of Non-Crystalline Solids*, vol. 266-269, pp. 201–205, 2000.
- [95] L. Houben, M. Luysberg, P. Hapke, R. Carius, F. Finger and H. Wagner, "Structural properties of microcrystalline silicon in the transition from highly crystalline to amorphous growth", *Philosophical Magazine A*, 77, pp. 1447–1460, 1998.
- [96] S. Miyazaki, Y. Osaka and M. Hirose, "Effects of growth rate on the microcrystalline characteristics of plasma-deposited $\mu\text{c-Si:H}$ ", *Solar Energy Materials*, 11, pp. 85–95, 1984.
- [97] P. Roca i Cabarrocas, N. Layadi, T. Heitz, B. Drévillon and I. Solomon, "Substrate selectivity in the formation of microcrystalline silicon: Mechanisms and technological consequences", *Applied Physics Letters*, 66, p. 3609, 1995.
- [98] J. Koh, A. Ferlauto, P. Rovira, C. Wronski and R. Collins, "Evolutionary phase diagrams for plasma-enhanced chemical vapor deposition of silicon thin films from hydrogen-diluted silane", *Applied Physics Letters*, 75, p. 2286, 1999.
- [99] N. Layadi, P. Roca i Cabarrocas, B. Drévillon and I. Solomon, "Real-time spectroscopic ellipsometry study of the growth of amorphous and microcrystalline silicon thin films prepared by alternating silicon deposition and hydrogen plasma treatment", *Physical Review B*, 52, pp. 5136–5143, 1995.
- [100] M. Bailly, J. Carpenter, Z. Holman and S. Bowden, "Substrate dependent growth of microcrystalline silicon", *IEEE Journal of Photovoltaics*, pp. 1201–1205, 2014.
- [101] Z. Zuo, G. Cui, Y. Wang, J. Wang, L. Pu and Y. Shi, "Substrate-thickness Dependence of Hydrogenated Microcrystalline Silicon Nucleation Rate on Amorphous Silicon Layer", *Chemical Vapor Deposition*, 19, pp. 363–366, 2013.
- [102] E. Vallat-Sauvain, J. Bailat, J. Meier, X. Niquille, U. Kroll and A. Shah, "Influence of the substrate's surface morphology and chemical nature on the nucleation and growth of microcrystalline silicon", *Thin Solid Films*, 485, pp. 77–81, 2005.
- [103] J. Bailat, E. Vallat-Sauvain, L. Feitknecht, C. Droz and A. Shah, "Influence of substrate on the microstructure of microcrystalline silicon layers and cells", *Journal of Non-Crystalline Solids*, vol. 299-302, pp. 1219–1223, 2002.
- [104] M. Python, O. Madani, D. Dominé, F. Meillaud, E. Vallat-Sauvain and C. Ballif, "Influence of the substrate geometrical parameters on microcrystalline silicon growth for thin-film solar cells", *Solar Energy Materials and Solar Cells*, 93, pp. 1714–1720, 2009.

- [105] C. Lin, Y. Fang, S. Chen, C. Lin, T. Chou, S. Hwang, J. Hwang and K. Lin, "Preferential coalescence of nanocrystalline silicon on different film substrates", *Journal of Non-Crystalline Solids*, 352, pp. 44–50, 2006.
- [106] E. Dirani, A. Andrade, L. Noda, F. Fonseca and P. Santos, "Effect of the substrate on the structural properties of low temperature microcrystalline silicon films – a Raman spectroscopy and atomic force microscopy investigation", *Journal of Non-Crystalline Solids*, 273, pp. 307–313, 2000.
- [107] S. Saha, J. Rath, S. Kshirsagar and S. Ray, "The thickness dependences of the electronic and structural properties of n-type microcrystalline silicon films deposited under various powers", *Journal of Physics D: Applied Physics*, 30, pp. 2686–2692, 1997.
- [108] S. Filonovich, H. Águas, T. Busani, A. Vicente, A. Araújo, D. Gaspar, M. Vilarigues, J. Leitão, E. Fortunato and R. Martins, "Hydrogen plasma treatment of very thin p-type nanocrystalline Si films grown by RF-PECVD in the presence of $B(CH_3)_3$ ", *Science and Technology of Advanced Materials*, 13, p. 45004, 2016.
- [109] R. Saleh and N. Nickel, "Raman spectroscopy of B-doped microcrystalline silicon films", *Thin Solid Films*, 427, pp. 266–269, 2003.
- [110] J. Koh, H. Fujiwara, R. Koval, C. Wronski and R. Collins, "Real time spectroscopic ellipsometry studies of the nucleation and growth of p-type microcrystalline silicon films on amorphous silicon using B_2H_6 , $B(CH_3)_3$ and BF_3 dopant source gases", *Journal of Applied Physics*, 85, p. 4141, 1999.
- [111] J. Seif, A. Descoedres, G. Nogay, S. Hanni, S. Nicolas, N. Holm, J. Geissbuhler, A. Hessler-Wyser, M. Duchamp, R. Dunin-Borkowski, M. Ledinsky, S. de Wolf and C. Ballif, "Strategies for Doped Nanocrystalline Silicon Integration in Silicon Heterojunction Solar Cells", *IEEE Journal of Photovoltaics*, pp. 1–9, 2016.
- [112] O. Vetterl, M. Hülsbeck, J. Wolff, R. Carius and F. Finger, "Preparation of microcrystalline silicon seed-layers with defined structural properties", *Thin Solid Films*, 427, pp. 46–50, 2003.
- [113] J.-H. Zhou, K. Ikuta, T. Yasuda, T. Umeda, S. Yamasaki and K. Tanaka, "Growth of amorphous-layer-free microcrystalline silicon on insulating glass substrates by plasma-enhanced chemical vapor deposition", *Applied Physics Letters*, 71, p. 1534, 1997.
- [114] P. Pernet, M. Goetz, H. Keppner and A. Shah, "Growth of thin μ c-Si:H on intrinsic a-Si:H for μ c-Si:H solar cell application", *MRS Proceeding*, 452, pp. 889–894, 1996.
- [115] S. Sriraman, S. Agarwal, E. Aydil and D. Maroudas, "Mechanism of hydrogen-induced crystallization of amorphous silicon", *Nature*, 418, pp. 62–65, 2002.
- [116] J. Rath, F. Rubinelli and R. Schropp, "Effect of oxide treatment at the microcrystalline tunnel junction of a-Si: H/a-Si:H tandem cells", *Journal of Non-Crystalline Solids*, vol. 266-269, pp. 1129–1133, 2000.
- [117] L. Gui-Jun, H. Guo-Fu, H. Xiao-Yan, Y. Yu-Jie, W. Chang-Chun, S. Jian, Z. Yin and G. Xin-Hua, "The study of a new n/p tunnel recombination junction and its application in a-Si: H/ μ c-Si:H tandem solar cells", *Chinese Physics B*, 18, pp. 1674–1678, 2009.
- [118] N. Pellaton Vaucher, B. Rech, D. Fischer, S. Dubail, M. Goetz, H. Keppner, N. Wyrsh, C. Beneking, O. Hadjadj, V. Shklover and A. Shah, "Controlled nucleation of thin

- microcrystalline layers for the recombination junction in a-Si stacked cells", *Solar Energy Materials and Solar Cells*, 49, pp. 27–33, 1997.
- [119] P. Pernet, M. Hengsberger, C. Hof, M. Goetz and A. Shah, "Growth of Thin $\mu\text{c-Si:H}$ Layers for pin Solar Cells: Effect of the H_2 - or CO_2 -Plasma Treatments", *16th EC Photovoltaic Solar Energy Conference*, p. 498-501, pp. 498–501, 2000.
- [120] J.-L. Guizot, K. Nomoto and A. Matsuda, "Surface reactions during the a-Si: H growth in the diode and triode glow-discharge reactors", *Surface Science*, 244, pp. 22–38, 1991.
- [121] A. Matsuda, "Growth mechanism of microcrystalline silicon obtained from reactive plasmas", *Thin Solid Films*, 337, pp. 1–6, 1999.
- [122] C. Tsai, G. Anderson, R. Thompson and B. Wacker, "Control of silicon network structure in plasma deposition", *Journal of Non-Crystalline Solids*, 114, pp. 151–153, 1989.
- [123] K. Nakamura, K. Yoshino, S. Takeoka and I. Shimizu, "Roles of Atomic Hydrogen in Chemical Annealing", *Japanese Journal of Applied Physics*, 34, pp. 442–449, 1995.
- [124] W. Spear and P. Le Comber, "Substitutional doping of amorphous silicon", *Solid State Communications*, 17, pp. 1193–1196, 1975.
- [125] R. Street, "Doping and the Fermi Energy in Amorphous Silicon", *Physical Review Letters*, 49, pp. 1187–1190, 1982.
- [126] J. Kočka, J. Stuchlík, H. Stuchlíková, V. Švrček, P. Fojtík, T. Mates, K. Luterová and A. Fejfar, "Amorphous/microcrystalline silicon superlattices—the chance to control isotropy and other transport properties", *Applied Physics Letters*, 79, p. 2540, 2001.
- [127] X. Jiang, Y. He and H. Zhu, "The effect of passivation of boron dopants by hydrogen in nano-crystalline and micro-crystalline silicon films", *Journal of Physics: Condensed Matter*, 6, pp. 713–718, 1994.
- [128] Y. Tawada, M. Kondo, Okamoto H. and Y. Hamakawa, "Hydrogenated amorphous silicon carbide as a window material for high efficiency a-Si solar cells", *Solar Energy Materials*, 6, pp. 299–315, 1982.
- [129] R. Janssen, A. Janotta, D. Dimova-Malinovska and M. Stutzmann, "Optical and electrical properties of doped amorphous silicon suboxides", *Physical Review B*, 60, pp. 13561–13572, 1999.
- [130] M. W. M. van Cleef, J. Rath, F. Rubinelli, van der Werf, C. H. M., R. Schropp and W. F. van der Weg, "Performance of heterojunction p+ microcrystalline silicon n crystalline silicon solar cells", *Journal of Applied Physics*, 82, p. 6089, 1997.
- [131] D. Zhang, D. Deligiannis, G. Papakonstantinou, R. A. C. M. M. van Swaaij and M. Zeman, "Optical Enhancement of Silicon Heterojunction Solar Cells With Hydrogenated Amorphous Silicon Carbide Emitter", *IEEE Journal of Photovoltaics*, 4, pp. 1326–1330, 2014.
- [132] M. Green, "Self-consistent optical parameters of intrinsic silicon at 300K including temperature coefficients", *Solar Energy Materials and Solar Cells*, 92, pp. 1305–1310, 2008.

- [133] A. Hadjadj, P. Cabarrocas and B. Equer, "Mobility-edge shift during diborane doping in hydrogenated amorphous silicon and hydrogenated amorphous silicon carbide", *Philosophical Magazine Part B*, 80, pp. 1317–1326, 2000.
- [134] W. Beyer, "Structural and electrical properties of silicon-based amorphous alloys", *Journal of Non-Crystalline Solids*, vol. 97-98, pp. 1027–1034, 1987.
- [135] A. Lambertz, V. Smirnov, T. Merdzhanova, K. Ding, S. Haas, G. Jost, R. Schropp, F. Finger and U. Rau, "Microcrystalline silicon–oxygen alloys for application in silicon solar cells and modules", *Solar Energy Materials and Solar Cells*, 119, pp. 134–143, 2013.
- [136] P. Cuony, D. Alexander, I. Perez-Wurfl, M. Despeisse, G. Bugnon, M. Boccard, T. Söderström, A. Hessler-Wyser, C. Hébert and C. Ballif, "Silicon Filaments in Silicon Oxide for Next-Generation Photovoltaics", *Advanced Materials*, 24, pp. 1182–1186, 2012.
- [137] A. Richter, Lei Zhao, F. Finger and K. Ding, "Microstructure model for nanocrystalline hydrogenated silicon oxide thin films in silicon heterojunction solar cells", *Proceeding of the 42rd IEEE Photovoltaics Specialists Conference*, pp. 1–4, 2015.
- [138] J. Geissbühler, S. de Wolf, B. Demareux, J. Seif, D. Alexander, L. Barraud and C. Ballif, "Amorphous/crystalline silicon interface defects induced by hydrogen plasma treatments", *Applied Physics Letters*, 102, p. 231604, 2013.
- [139] B. Demareux, S. de Wolf, A. Descoeurdes, Z. Charles Holman and C. Ballif, "Damage at hydrogenated amorphous/crystalline silicon interfaces by indium tin oxide overlayer sputtering", *Applied Physics Letters*, 101, p. 171604, 2012.
- [140] J. Kegel, H. Angermann, U. Stürzebecher and B. Stegemann, "IPA-free Texturization of n-type Si Wafers: Correlation of Optical, Electronic and Morphological Surface Properties", *Energy Procedia*, 38, pp. 833–842, 2013.
- [141] W. Kern, "The Evolution of Silicon Wafer Cleaning Technology", *Journal of The Electrochemical Society*, 137, p. 1887, 1990.
- [142] O. Gabriel, S. Kirner, M. Klick, B. Stannowski and R. Schlatmann, "Plasma monitoring and PECVD process control in thin film silicon-based solar cell manufacturing", *EPJ Photovoltaics*, 5, p. 55202, 2014.
- [143] O. Cubero, F.-J. Haug, Y. Ziegler, L. Sansonnens, P. Couty, D. Fischer and C. Ballif, "Reduction of the phosphorous cross-contamination in n–i–p solar cells prepared in a single-chamber PECVD reactor", *Solar Energy Materials and Solar Cells*, 95, pp. 606–610, 2011.
- [144] Tobias Henschel, "Herstellung und Optimierung von effizienten Frontkontakten für HIT-Solarzellen". Bachelorarbeit, Hochschule für Technik und Wirtschaft, 2014.
- [145] S. Olibet, C. Monachon, A. Hessler-Wyser, E. Vallat-Sauvain, S. de Wolf, L. Fesquet, J. Damon-Lacoste and C. Ballif, "Textured Silicon Heterojunction Solar Cells With Over 700 mV Open-Circuit Voltage Studied by Transmission Electron Microscopy", 2008.
- [146] W. Theiss, "Scout Tutorial 1", 2012.
- [147] G. Jellison and F. Modine, "Parameterization of the optical functions of amorphous materials in the interband region", *Applied Physics Letters*, 69, p. 371, 1996.
- [148] J. Tauc, R. Grigorovici and A. Vancu, "Optical Properties and Electronic Structure of Amorphous Germanium", *physica status solidi (b)*, 15, pp. 627–637, 1966.

- [149] M. Wojdyr, "Fityk: A general-purpose peak fitting program", *Journal of Applied Crystallography*, 43, pp. 1126–1128, 2010.
- [150] A. Langford, M. Fleet, B. Nelson, W. Lanford and N. Maley, "Infrared absorption strength and hydrogen content of hydrogenated amorphous silicon", *Physical Review B*, 45, pp. 13367–13377, 1992.
- [151] E. Bustarret, M. Bensouda, M. Habrard, J. Bruyère, S. Poulin and S. Gujrathi, "Configurational statistics in a - SixNyHz alloys: A quantitative bonding analysis", *Physical Review B*, 38, pp. 8171–8184, 1988.
- [152] L. He, T. Inokuma, Y. Kurata and S. Hasegawa, "Vibrational properties of SiO and SiH in amorphous SiOx: H films ($0 \leq x \leq 2.0$) prepared by plasma-enhanced chemical vapor deposition", *Journal of Non-Crystalline Solids*, 185, pp. 249–261, 1995.
- [153] P. Pai, "Infrared spectroscopic study of SiOx films produced by plasma enhanced chemical vapor deposition", *Journal of Vacuum Science & Technology A: Vacuum, Surfaces, and Films*, 4, p. 689, 1986.
- [154] G. Sasaki, M. Kondo, S. Fujita and A. Sasaki, "Properties of Chemically Vapor-Deposited Amorphous SiNx Alloys", *Japanese Journal of Applied Physics*, 21, pp. 1394–1399, 1982.
- [155] H. Shanks, F. Jeffrey and M. Lowry, "Bonding in hydrogenated amorphous silicon", *Le Journal de Physique Colloques*, 42, pp. C4-773-C4-777, 1981.
- [156] C. Smit, R. A. C. M. M. van Swaaij, H. Donker, A. M. H. N. Petit, W. Kessels and M. C. M. van de Sanden, "Determining the material structure of microcrystalline silicon from Raman spectra", *Journal of Applied Physics*, 94, p. 3582, 2003.
- [157] M. Klingsporn, S. Kirner, C. Villringer, D. Abou-Ras, I. Costina, M. Lehmann and B. Stannowski, "Resolving the nanostructure of plasma-enhanced chemical vapor deposited nanocrystalline SiOx layers for application in solar cells", *Journal of Applied Physics*, 119, p. 223104, 2016.
- [158] C. Droz, E. Vallat-Sauvain, J. Bailat, L. Feitknecht, J. Meier and A. Shah, "Relationship between Raman crystallinity and open-circuit voltage in microcrystalline silicon solar cells", *Solar Energy Materials and Solar Cells*, 81, pp. 61–71, 2004.
- [159] M. Ledinský, L. Fekete, J. Stuchlík, T. Mates, A. Fejfar and J. Kočka, "Characterization of mixed phase silicon by Raman spectroscopy", *Journal of Non-Crystalline Solids*, 352, pp. 1209–1212, 2006.
- [160] M. Tzolov, F. Finger, R. Carius and P. Hapke, "Optical and transport studies on thin microcrystalline silicon films prepared by very high frequency glow discharge for solar cell applications", *Journal of Applied Physics*, 81, p. 7376, 1997.
- [161] J. Mayer, L. Giannuzzi, T. Kamino and J. Michael, "TEM Sample Preparation and FIB-Induced Damage", *MRS Bulletin*, 32, pp. 400–407, 2007.
- [162] R. Sinton and A. Cuevas, "Contactless determination of current–voltage characteristics and minority-carrier lifetimes in semiconductors from quasi-steady-state photoconductance data", *Applied Physics Letters*, 69, p. 2510, 1996.
- [163] C. Leendertz, N. Mingirulli, T. Schulze, J. Kleider, B. Rech and L. Korte, "Discerning passivation mechanisms at a-Si:H/c-Si interfaces by means of photoconductance measurements", *Applied Physics Letters*, 98, p. 202108, 2011.

- [164] I. Martil and G. Diaz, "Determination of the dark and illuminated characteristic parameters of a solar cell from I-V characteristics", *European Journal of Physics*, 13, pp. 193–197, 1992.
- [165] A. Pysch, A. Mette and S. Glunz, "A review and comparison of different methods to determine the series resistance of solar cells", *Solar Energy Materials and Solar Cells*, 91, pp. 1698–1706, 2007.
- [166] Tobias Hänel, "Spannungs- und intensitätsabhängige spektrale Empfindlichkeit von poly-Si Duenschichtszellen". Diplomarbeit, FHTW, 2008.
- [167] M. Hendrichs, A. Morales-Vilches, L. Mazzarella, S. Kirner, M. Zelt, H. Rhein, S. Calnan, L. Korte, B. Stannowski and R. Schlatmann, "Process development for silicon heterojunction solar cells", *Proceeding of the EUPVSEC 2016*, 2016.
- [168] L. Mazzarella, S. Kirner, M. Mews, E. Conrad, L. Korte, B. Stannowski, B. Rech and R. Schlatmann, "Comparison of TMB and B₂H₆ as Precursors for Emitter Doping in High Efficiency Silicon Hetero Junction Solar Cells", *Energy Procedia*, 60, pp. 123–128, 2014.
- [169] S. de Wolf, C. Ballif and M. Kondo, "Kinetics of a -Si: H bulk defect and a-Si:H/c-Si interface-state reduction", *Physical Review B*, 85, 2012.
- [170] P. Roca i Cabarrocas, S. Kumar and B. Drevillon, "In situ study of the thermal decomposition of B₂H₆ by combining spectroscopic ellipsometry and Kelvin probe measurements", *Journal of Applied Physics*, 66, p. 3286, 1989.
- [171] W. Zongyan, A. Lloret, J.-M. Siefert, P. Cabarrocas and B. Equer, "Is B(CH₃)₃ An Interesting Alternative to B₂H₆ for a-Si:H p Doping?", *MRS Proceedings*, 149, 1989.
- [172] Z. Wu, B. Drevillon, M. Fang, A. Gheorghiu and C. Senemaud, "The incorporation of carbon in a-Si: H enhanced by boron doping", *Journal of Non-Crystalline Solids*, vol. 137-138, pp. 863–866, 1991.
- [173] A. Lloret, Z. Wu, M. Theye, I. Zawawi, J. Siefert and B. Equer, "Hydrogenated amorphous silicon p-doping with diborane, trimethylboron and trimethylgallium", *Applied Physics A Solids and Surfaces*, 55, pp. 573–581, 1992.
- [174] B. Yan, L. Zhao, B. Zhao, J. Chen, H. Diao, G. Wang, Y. Mao and W. Wang, "Wide bandgap p-type window layer prepared by trimethylboron doping at high temperature for a-Si:H superstrate solar cell", *Journal of Non-Crystalline Solids*, 358, pp. 3243–3247, 2012.
- [175] M. W. M. van Cleef, F. Rubinelli, R. Rizzoli, R. Pinghini, R. Schropp and W. F. van der Weg, "Amorphous Silicon Carbide/Crystalline Silicon Heterojunction Solar Cells: A Comprehensive Study of the Photocarrier Collection", *Japanese Journal of Applied Physics*, 37, pp. 3926–3932, 1998.
- [176] T. Fellmeth, F. Clement and D. Biro, "Analytical Modeling of Industrial-Related Silicon Solar Cells", *IEEE Journal of Photovoltaics*, 4, pp. 504–513, 2014.
- [177] M. Bivour, C. Reichel, M. Hermle and S. Glunz, "Improving the a-Si:H (p) rear emitter contact of n-type silicon solar cells", *Solar Energy Materials and Solar Cells*, 106, pp. 11–16, 2012.
- [178] M. Balestrieri, D. Pysch, J.-P. Becker, M. Hermle, W. Warta and S. Glunz, "Characterization and optimization of indium tin oxide films for heterojunction solar cells", *Solar Energy Materials and Solar Cells*, 95, pp. 2390–2399, 2011.

- [179] S. Nicolás, D. Muñoz, A. Ozanne, N. Nguyen and P. Ribeyron, "Optimisation of doped amorphous silicon layers applied to heterojunction solar cells", *Energy Procedia*, 8, pp. 226–231, 2011.
- [180] B. Stannowski, O. Gabriel, S. Calnan, T. Frijnts, A. Heidelberg, S. Neubert, S. Kirner, S. Ring, M. Zelt, B. Rau, J.-H. Zollondz, H. Bloess, R. Schlatmann and B. Rech, "Achievements and challenges in thin film silicon module production", *Solar Energy Materials and Solar Cells*, 119, pp. 196–203, 2013.
- [181] L. Mazzarella, S. Kirner, O. Gabriel, S. Schmidt, L. Korte, B. Stannowski, B. Rech and R. Schlatmann, "Nanocrystalline silicon emitter optimization for Si-HJ solar cells: Substrate selectivity and CO₂ plasma treatment effect", *physica status solidi (a)*, 2016.
- [182] A. Funde, N. Bakr, D. Kamble, R. Hawaldar, D. Amalnerkar and S. Jadkar, "Influence of hydrogen dilution on structural, electrical and optical properties of hydrogenated nanocrystalline silicon (nc-Si:H) thin films prepared by plasma enhanced chemical vapour deposition (PE-CVD)", *Solar Energy Materials and Solar Cells*, 92, pp. 1217–1223, 2008.
- [183] J. Kočka, T. Mates, H. Stuchlíková, J. Stuchlík and A. Fejfar, "Characterization of grain growth, nature and role of grain boundaries in microcrystalline silicon—review of typical features", *Thin Solid Films*, 501, pp. 107–112, 2006.
- [184] K.-K. Lew, L. Pan, T. Bogart, S. Dilts, E. Dickey, J. Redwing, Y. Wang, M. Cabassi, T. Mayer and S. Novak, "Structural and electrical properties of trimethylboron-doped silicon nanowires", *Applied Physics Letters*, 85, p. 3101, 2004.
- [185] T. Roschek, J. Müller, S. Wieder, B. Rech and H. Wagner, "Microcrystalline p-Layers Prepared by RF-PECVD for Silicon Thin Film Solar Cells with Zinc Oxide Front Contact", *Proceedings of the 16th European Photovoltaic Solar Energy Conference*, 2000.
- [186] T. Matsui, M. Kondo and A. Matsuda, "Doping properties of boron-doped microcrystalline silicon from B₂H₆ and BF₃: Material properties and solar cell performance", *Journal of Non-Crystalline Solids*, vol. 338-340, pp. 646–650, 2004.
- [187] K. Shimakawa, "Percolation-controlled electronic properties in microcrystalline silicon: Effective medium approach", *Journal of Non-Crystalline Solids*, vol. 266-269, pp. 223–226, 2000.
- [188] D. Kim, R. A. C. M. M. van Swaaij and M. Zeman, "Optical and Electrical Simulation of $\mu\text{c-Si:H}$ Solar Cells: Effect of Substrate Morphology and Crystalline Fraction", *IEEE Journal of Photovoltaics*, 4, pp. 22–27, 2014.
- [189] S. Hamma and P. Roca i Cabarrocas, "Low-temperature growth of thick intrinsic and ultrathin phosphorous or boron-doped microcrystalline silicon films: Optimum crystalline fractions for solar cell applications", *Solar Energy Materials and Solar Cells*, 69, pp. 217–239, 2001.
- [190] O. Madani Ghahfarokhi, K. von Maydell and C. Agert, "Enhanced passivation at amorphous/crystalline silicon interface and suppressed Schottky barrier by deposition of microcrystalline silicon emitter layer in silicon heterojunction solar cells", *Applied Physics Letters*, 104, p. 113901, 2014.

- [191] J. Ge, Z. Ling, J. Wong, T. Mueller and A. Aberle, "Optimisation of Intrinsic a-Si: H Passivation Layers in Crystalline-amorphous Silicon Heterojunction Solar Cells", *Energy Procedia*, 15, pp. 107–117, 2012.
- [192] M. Rohde, M. Zelt, O. Gabriel, S. Neubert, S. Kirner, D. Severin, T. Stolley, B. Rau, B. Stannowski and R. Schlatmann, "Plasma enhanced chemical vapor deposition process optimization for thin film silicon tandem junction solar cells", *Thin Solid Films*, 558, pp. 337–343, 2014.
- [193] S. Kirner, L. Mazzarella, L. Korte, B. Stannowski, B. Rech and R. Schlatmann, "Silicon Heterojunction Solar Cells With Nanocrystalline Silicon Oxide Emitter: Insights Into Charge Carrier Transport", *IEEE Journal of Photovoltaics*, 5, pp. 1601–1605, 2015.
- [194] L. Mazzarella, S. Kirner, O. Gabriel, L. Korte, B. Stannowski, B. Rech and R. Schlatmann, "Nanocrystalline Silicon Oxide Emitters for Silicon Hetero Junction Solar Cells", *Energy Procedia*, 77, pp. 304–310, 2015.
- [195] L. Mazzarella, S. Kirner, B. Stannowski, L. Korte, B. Rech and R. Schlatmann, "p-type microcrystalline silicon oxide emitter for silicon heterojunction solar cells allowing current densities above 40 mA/cm²", *Applied Physics Letters*, 106, p. 23902, 2015.
- [196] S. Baker-Finch and K. McIntosh, "A freeware model for precise optical analysis of the front surface of a solar cell", *Proceeding of the 35th IEEE Photovoltaics Specialists Conference*, 530, pp. 2184–2187
- [197] K. McIntosh and S. Baker-Finch, "OPAL 2: Rapid optical simulation of silicon solar cells", Austin, TX, USA, pp. 265–271
- [198] S. Baker-Finch and K. McIntosh, "Reflection of normally incident light from silicon solar cells with pyramidal texture", *Progress in Photovoltaics: Research and Applications*, 19, pp. 406–416, 2011.
- [199] B. Harbecke, "Coherent and incoherent reflection and transmission of multilayer structures", *Applied Physics B Photophysics and Laser Chemistry*, 39, pp. 165–170, 1986.
- [200] E. Yablonovitch and G. Cody, "Intensity enhancement in textured optical sheets for solar cells", *IEEE Transactions on Electron Devices*, 29, pp. 300–305, 1982.
- [201] F.-J. Haug and C. Ballif, "Light management in thin film silicon solar cells", *Energy Environ. Sci.*, 8, pp. 824–837, 2015.
- [202] M. Green and M. Keevers, "Optical properties of intrinsic silicon at 300 K", *Progress in Photovoltaics: Research and Applications*, 3, pp. 189–192, 1995.
- [203] D. Das, S. Mandal and A. Barua, "Intrinsic hydrogenated microcrystalline silicon oxide films prepared by RF glow discharge", *Journal of Materials Science Letters*, 17, pp. 2097–2100, 1998.
- [204] K. Ding, U. Aeberhard, A. Lambertz, V. Smirnov, B. Holländer, F. Finger and U. Rau, "Impact of doped microcrystalline silicon oxide layers on crystalline silicon surface passivation 1", *Canadian Journal of Physics*, 92, pp. 758–762, 2014.
- [205] A. Lambertz, F. Finger, B. Holländer, J. Rath and R. Schropp, "Boron-doped hydrogenated microcrystalline silicon oxide ($\mu\text{c-SiOx:H}$) for application in thin-film silicon solar cells", *Journal of Non-Crystalline Solids*, 358, pp. 1962–1965, 2012.

- [206] A. Richter, F. Lentz, M. Meier, F. Finger and K. Ding, "Light management in planar silicon heterojunction solar cells via nanocrystalline silicon oxide films and nano-imprint textures", *physica status solidi (a)*, 213, pp. 1976–1982, 2016.
- [207] S. Dhar, S. Mandal, G. Das, S. Mukhopadhyay, P. Ray, C. Banerjee and A. Barua, "Silicon heterojunction solar cells with novel fluorinated n-type nanocrystalline silicon oxide emitters on p-type crystalline silicon", *Japanese Journal of Applied Physics*, 54, p. 08KD03, 2015.
- [208] C. Banerjee, J. Sritharathikhun, A. Yamada and M. Konagai, "Fabrication of heterojunction solar cells by using microcrystalline hydrogenated silicon oxide film as an emitter", *Journal of Physics D: Applied Physics*, 41, p. 185107, 2008.
- [209] K. Ding, U. Aeberhard, V. Smirnov, B. Holländer, F. Finger and U. Rau, "Wide Gap Microcrystalline Silicon Oxide Emitter for a-SiO_x:H/c-Si Heterojunction Solar Cells", *Japanese Journal of Applied Physics*, 52, p. 122304, 2013.
- [210] O. Gabriel, S. Kirner, M. Klingsporn, F. Friedrich, B. Stannowski and R. Schlatmann, "On the Plasma Chemistry During Plasma Enhanced Chemical Vapor Deposition of Microcrystalline Silicon Oxides", *Plasma Processes and Polymers*, 12, pp. 82–91, 2015.
- [211] S. Kirner, "Development of wide band gap materials for thin film silicon solar cells", Technische Universität Berlin, 2014.
- [212] A. Sarker, C. Banerjee and A. Barua, "Preparation and characterization of n-type microcrystalline hydrogenated silicon oxide films", *Journal of Physics D: Applied Physics*, 35, pp. 1205–1209, 2002.
- [213] S. Kirner, S. Neubert, C. Schultz, O. Gabriel, B. Stannowski, B. Rech and R. Schlatmann, "Quadruple-junction solar cells and modules based on amorphous and microcrystalline silicon with high stable efficiencies", *Japanese Journal of Applied Physics*, 54, p. 08KB03, 2015.
- [214] K. Schwanitz, S. Klein, T. Stolley, M. Rohde, D. Severin and R. Trassl, "Anti-reflective microcrystalline silicon oxide p-layer for thin-film silicon solar cells on ZnO", *Solar Energy Materials and Solar Cells*, 105, pp. 187–191, 2012.
- [215] R. Biron, C. Pahud, F.-J. Haug, J. Escarré, K. Söderström and C. Ballif, "Window layer with p doped silicon oxide for high Voc thin-film silicon n-i-p solar cells", *Journal of Applied Physics*, 110, p. 124511, 2011.
- [216] J. Sritharathikhun, F. Jiang, S. Miyajima, A. Yamada and M. Konagai, "Optimization of p-Type Hydrogenated Microcrystalline Silicon Oxide Window Layer for High-Efficiency Crystalline Silicon Heterojunction Solar Cells", *Japanese Journal of Applied Physics*, 48, p. 101603, 2009.
- [217] K. Ding, U. Aeberhard, F. Finger and U. Rau, "Optimized amorphous silicon oxide buffer layers for silicon heterojunction solar cells with microcrystalline silicon oxide contact layers", *Journal of Applied Physics*, 113, p. 134501, 2013.
- [218] J. Seto, "The electrical properties of polycrystalline silicon films", *Journal of Applied Physics*, 46, p. 5247, 1975.
- [219] L. Mazzarella, S. Kolb, S. Kirner, C. Calnan, L. Korte, B. Stannowski, B. Rech and R. Schlatmann, "Optimization of PECVD process for ultra-thin tunnel SiO_x film as

- passivation layer for silicon heterojunction solar cells", *Proceeding of the 43rd IEEE Photovoltaics Specialists Conference*, 2016.
- [220] R. Peibst, Y. Larionova, S. Reiter, M. Turcu, R. Brendel, D. Tetzlaff, J. Krügener, T. Wietler, U. Höhne, J.-D. Kähler, H. Mehlich and S. Frigge, "Implementation of n+ and p+ polo junctions on front and rear side of double-side contacted industrial silicon solar cells", *Proceeding of the EUPVSEC 2016*, 2016.
- [221] H. Fujiwara, T. Kaneko and M. Kondo, "Application of hydrogenated amorphous silicon oxide layers to c-Si heterojunction solar cells", *Applied Physics Letters*, 91, p. 133508, 2007.
- [222] M. Mews, M. Liebhaber, B. Rech and L. Korte, "Valence band alignment and hole transport in amorphous/crystalline silicon heterojunction solar cells", *Applied Physics Letters*, 107, p. 13902, 2015.
- [223] T. Mueller, J. Wong and A. Aberle, "Heterojunction Silicon Wafer Solar Cells using Amorphous Silicon Suboxides for Interface Passivation", *Energy Procedia*, 15, pp. 97–106, 2012.
- [224] J. Sritharathikhun, H. Yamamoto, S. Miyajima, A. Yamada and M. Konagai, "Optimization of Amorphous Silicon Oxide Buffer Layer for High-Efficiency p-Type Hydrogenated Microcrystalline Silicon Oxide/n-Type Crystalline Silicon Heterojunction Solar Cells", *Japanese Journal of Applied Physics*, 47, pp. 8452–8455, 2008.
- [225] E. Nicollian and A. Goetzberger, "The Si-SiO₂ Interface - Electrical Properties as Determined by the Metal-Insulator-Silicon Conductance Technique", *Bell System Technical Journal*, 46, pp. 1055–1133, 1967.
- [226] E. Yablonovitch, T. Gmitter, R. Swanson and Y. Kwark, "A 720 mV open circuit voltage SiOx: C-Si:SiOx double heterostructure solar cell", *Applied Physics Letters*, 47, p. 1211, 1985.
- [227] K. Kawabata, H. Morikawa, T. Ishihara, K. Sato, H. Sasaki, T. Itagaki, M. Deguchi, S. Hamamoto and M. Aiga, "Formation of PN junction with hydrogenated microcrystalline silicon", *Proceeding of the 21th IEEE Photovoltaics Specialists Conference*, pp. 659–663, 1990.
- [228] F. Feldmann, M. Bivour, C. Reichel, M. Hermle and S. Glunz, "Passivated rear contacts for high-efficiency n-type Si solar cells providing high interface passivation quality and excellent transport characteristics", *Solar Energy Materials and Solar Cells*, 120, pp. 270–274, 2014.
- [229] K. Ding, M. Pomaska, A. Singh, F. Lentz, F. Finger and U. Rau, "Mechanism for crystalline Si surface passivation by the combination of SiO₂ tunnel oxide and μ c-SiC: H thin film", *physica status solidi (RRL) - Rapid Research Letters*, 10, pp. 233–236, 2016.
- [230] E. San Andrés, A. del Prado, F. Martínez, I. Mártil, D. Bravo and F. López, "Rapid thermal annealing effects on the structural properties and density of defects in SiO₂ and SiNx:H films deposited by electron cyclotron resonance", *Journal of Applied Physics*, 87, p. 1187, 2000.
- [231] C. Courtney, "Remote Plasma-Enhanced Chemical Vapor Deposition of SiO₂ Using Ar/N₂O and SiH₄", *Journal of The Electrochemical Society*, 145, p. 3957, 1998.

- [232] Z. Chen, S. Pang, K. Yasutake and A. Rohatgi, "Plasma-enhanced chemical-vapor-deposited oxide for low surface recombination velocity and high effective lifetime in silicon", *Journal of Applied Physics*, 74, p. 2856, 1993.
- [233] W. Pliskin and R. Esch, "Refractive Index of SiO₂ Films Grown on Silicon", *Journal of Applied Physics*, 36, p. 2011, 1965.
- [234] V.-A. Dao, V.-D. Nguyen, J. Heo, H. Choi, Y. Kim, N. Lakshminarayan and J. Yi, "Effect of N₂O/SiH₄ flow ratios on properties of amorphous silicon oxide thin films deposited by inductively-coupled plasma chemical vapor deposition with application to silicon surface passivation", *Vacuum*, 84, pp. 410–414, 2009.
- [235] J. Batey and E. Tierney, "Low-temperature deposition of high-quality silicon dioxide by plasma-enhanced chemical vapor deposition", *Journal of Applied Physics*, 60, p. 3136, 1986.
- [236] W. Pliskin, "Comparison of properties of dielectric films deposited by various methods", *Journal of Vacuum Science and Technology*, 14, p. 1064, 1977.
- [237] L.-N. He, D.-M. Wang and S. Hasegawa, "A study of plasma-deposited amorphous SiO_x:H films using infrared spectroscopy", *Journal of Non-Crystalline Solids*, 261, pp. 67–71, 2000.
- [238] S. Calnan, O. Gabriel, I. Rothert, M. Werth, S. Ring, B. Stannowski and R. Schlatmann, "Influence of Chemical Composition and Structure in Silicon Dielectric Materials on Passivation of Thin Crystalline Silicon on Glass", *ACS applied materials & interfaces*, 7, pp. 19282–19294, 2015.
- [239] E. San Andrés, A. del Prado, I. Mártil, G. González-Díaz, D. Bravo and F. López, "Thermally induced modifications on bonding configuration and density of defects of plasma deposited SiO_x:H films", *Journal of Applied Physics*, 92, p. 1906, 2002.
- [240] Z. Lu, P. Santos-Filho, G. Stevens, M. Williams and G. Lucovsky, "Fourier transform infrared study of rapid thermal annealing of a-SiN:H(D) films prepared by remote plasma-enhanced chemical vapor deposition", *Journal of Vacuum Science & Technology A: Vacuum, Surfaces, and Films*, 13, p. 607, 1995.

List of Publications

Publications as First Author:

- [A] L. Mazzearella, S. Kirner, M. Mews, E. Conrad, L. Korte, B. Stannowski, B. Rech and R. Schlatmann, "Comparison of TMB and B₂H₆ as Precursors for Emitter Doping in High Efficiency Silicon Hetero Junction Solar Cells", *Energy Procedia*, 60, pp. 123–128, 2014.
- [B] L. Mazzearella, S. Kirner, B. Stannowski, L. Korte, B. Rech and R. Schlatmann, "P-type microcrystalline silicon oxide emitter for silicon heterojunction solar cells allowing current densities above 40 mA/cm²", *Applied Physics Letters*, 106, p. 23902, 2015.
- [C] L. Mazzearella, S. Kirner; O. Gabriel, L. Korte, B. Stannowski, B. Rech, R. Schlatmann, "Nanocrystalline Silicon Oxide Emitters for Silicon Hetero Junction Solar Cells", *Energy Procedia*, 77, pp. 304-310, 2015.
- [D] L. Mazzearella, S. Kolb, S. Kirner, C. Calnan, L. Korte, B. Stannowski, B. Rech and R. Schlatmann, "Optimization of PECVD process for ultra-thin tunnel SiO_x film as passivation layer for silicon heterojunction solar cells", *Proceeding of the 43rd IEEE Photovoltaics Specialists Conference*, 2016.
- [E] L. Mazzearella, S. Kirner, O. Gabriel, S. S. Schmidt, L. Korte, B. Stannowski, B. Rech, R. Schlatmann, "Nanocrystalline silicon emitter optimization for Si-HJ solar cells: substrate selectivity and CO₂ plasma treatment effect", *Physics Status Solidi A*, pp. 1-7, 2016.

Publications as Co-Author:

- [F] S. Kirner, M. Hartig, L. Mazzearella, L. Korte, T. Frijnts, H. Scherg-Kurmes, S. Ring, B. Stannowski, B. Rech and R. Schlatmann, "The Influence of ITO Dopant Density on J-V Characteristics of Silicon Heterojunction Solar Cells: Experiments and Simulations", *Energy Procedia*, 77, pp. 725–732, 2015.
- [G] S. Kirner, L. Mazzearella, L. Korte, B. Stannowski, B. Rech, R. Schlatmann, "Silicon Heterojunction Solar Cells With Nanocrystalline Silicon Oxide Emitter. Insights Into Charge Carrier Transport", *IEEE Journal of Photovoltaics*, 5, pp. 1601-1605, 2015.
- [H] M. Hendrichs, A. Morales-Vilches, L. Mazzearella, S. Kirner, M. Zelt, H. Rhein, S. Calnan, L. Korte, B. Stannowski, R. Schlatmann, "Process development for silicon heterojunction solar cells", *Proceeding of the EUPVSEC 2016*.

Acknowledgments

First and foremost I wish thank Prof. Dr. Bernd Rech for being my supervisor and for the inspiring guidance during the entire thesis.

I am deeply grate to Prof. Dr. Rutger Schlatmann for the great opportunity gave me to be part of the PVcomB.

I would like to thank the members of the commission, in particular Prof. Dr. Roca Pere i Cabarrocas for accepting to be my evaluator.

My sincere thanks go to Dr. Bernd Stannowski for creating a stimulating working atmosphere in the silicon group. I thank you for precious suggestions, ideas and encouragement.

Dr. Lars Korte is acknowledged for his expertise, suggestions and ideas for experiments and interpretation of results.

My sincere gratitude is due to Dr. Simon Kirner, for his warm welcome on my first day and his contribution to my professional growing. His help, inspiration and encouragement were precious for me in the good and the bad times. I thank him for his contagious enthusiasm.

A special thank goes to Dr. Sonya Calnan for the support and precious help in many circumstances. She introduced me to the FTIR measurements supporting in my experiments, data analysis and interpretation.

I would like to thanks Dr. Onno Gabriel for the support in the PECVD experiments and for sharing his expertise and knowledge with me.

For the HR-TEM micrographs, I express gratitude to Dr. Sebastian Schmidt for the time dedicated in acquiring the images and helping in the interpretation. Holger Kropf deserves a special acknowledge for his perseverance and competence in lamellas fabrication. Dr. Marc Gluba and Karolina Mack were precious in Raman measurements, Florian Ruske for introducing me in the ellipsometry technique and Karola Kimm for acquiring SEM images.

My thanks also go to those collaborated in cells fabrication: Kerstin Jacob and Mona Wittig for taking care of the wafer cleaning and texturing as well as for doing and teaching me

photolithography process; Manuel Hartig for TCO deposition; Matthias Zelt for keeping the PECVD running; Tobias Henschel, Khalid Bhatti and Iris Dorbandt for their patience in the long evaporation processes, Paul Sonntag for sharing with me his photolithography tricks and Erhard Conrad and Matthias Mews for a-Si:H depositions with the FAP tool. Max Hendrichs, Anna Belen Morales Vilches and Holger Rein for the effort on the reference process in the last year. But also Sven Ring and Andreas Opitz.

Furthermore I thank Sebastian Neubert and Natalie Preissler especially for the support in the last moments of writing.

A special acknowledgments go to all the members of PVcomB that contributed in different ways to my work. In particular: Tobias Hänel and Karolina Mack for introducing me to equipment, providing assistance and keeping the characterization labs running. They are always present and available to solve problems.

Dr. Björn Rau for his dedication in taking care of our safety and for is surveillance.

I also would like to thank the many students that in different ways helped in the daily work measuring samples or helping in cell fabrication. In particular my student Sophie Kolb for in SE characterization, annealing treatments, data analysis and cell measurements.

My sincere gratitude is due to Bernd, Sonya, Simon, Lars and Rutger for reviewing and proofreading my thesis and for their fast and precious feedbacks and helpful ideas.

Finally, I thank my parents for their love, my sister for being always at my side.

